SOURCES AND TRANSPORT MECHANISMS OF CONTAMINANTS DURING FLOODING EVENTS

by

Rakiba Sultana

A Dissertation Submitted in

Partial Fulfillment of the

Requirements for the Degree of

Doctor of Philosophy

in Geosciences

at

The University of Wisconsin-Milwaukee

August 2025

ABSTRACT

SOURCES AND TRANSPORT MECHANISMS OF CONTAMINANTS
DURING FLOODING EVENTS
by

Rakiba Sultana

The University of Wisconsin-Milwaukee, 2025
Under the Supervision of Professor Charles J Paradis

Persistent contaminant concentrations in groundwater, especially uranium, present significant challenges, as flooding events can remobilize these contaminants from subsurface hydrogeological compartments. Despite the critical role of these events in contaminant mobilization, the precise sources of residual solid-phase contaminants and their specific transport mechanisms during infiltration remain poorly understood and difficult to quantify. Through a combination of microscale characterization, controlled field-tracer infiltration experiments, and mathematical modeling, this dissertation addresses the **fundamental scientific question**: What are the mass transport mechanisms that control the fate of contaminants during recharge of contaminant-poor groundwater or surface water to contaminant-rich groundwater? The first chapter identified trace-level solid-phase uranium associations in sediments using fission-track radiography, scanning electron microscopy, and energy-dispersive X-ray spectroscopy. This work revealed that residual solid-phase uranium in source zone aquifer sediments primarily co-occurred with amorphous aluminum-rich and iron-rich coatings, suggesting specific geochemical controls on its persistence. The subsequent chapter elucidated mass and transport mechanisms of contaminants released during flooding through controlled in-situ tracer experiments. This research highlighted the mobilization of contaminant-rich pore water ahead of floodwater and the dissolution of contaminant-rich evaporites with floodwater as key mechanisms, emphasizing the

significant role of the vadose zone as a storage and release compartment for contaminants. The final chapter employed a one-dimensional mathematical model to inversely simulate the field data from the infiltration experiments, quantifying the relative contributions of the identified mobilization mechanisms. The modeling results confirmed that advection and dispersion of contaminant-rich pore water, followed by the dissolution of contaminant-rich evaporites (often coupled with desorption), were the dominant transport pathways from the vadose zone. This chapter further solidified the understanding that the vadose zone is the primary source of contaminant release during infiltration events, while transport in the saturated zone is predominantly advection- and dispersion-dominated. Overall, this dissertation significantly deepened our understanding of the complex behavior of contaminants in the vadose zone during flooding events.

Dedicated to my beloved grandparents

TABLE OF CONTENTS

LIST OF FIGURES

LIST OF TABLES

ACKNOWLEDGEMENTS

First and foremost, I would like to express my deepest gratitude to my supervisor, Dr. Charles Paradis, for giving me the opportunity to join his lab and for generously keeping the position open when I had to defer a semester during the COVID-19 pandemic. Thank you for your unwavering support throughout this journey - your mentorship, the opportunities you provided, the financial support, and above all, your ability to always see the positive in every situation have been invaluable to me.

I am also sincerely thankful to my co-supervisor, Dr. Raymond Johnson, for his steadfast support, insightful guidance, and for always making time to help me, especially during the early field shifts, which you somehow managed to make both productive and fun.

My heartfelt thanks go to my committee members, Dr. Lindsay McHenry and Dr. Shangping Xu, for your flexibility with my often last-minute meeting requests and for generously sharing your expertise. I am also grateful to Dr. Julie Bowles for being a wonderful and supportive graduate coordinator—I always felt I had someone to turn to.

I am immensely grateful to Dr. Michael Fienen for mentoring me in numerical modeling with such openness and encouragement. It was truly an honor to work in the same building as so many brilliant minds.

This project would not have been possible without the incredible collaborators who supported it. My sincere thanks go to Aaron Tigar, Tim Wahl, Kendyl Hoss, Cullen Meurer, Jiyan Hatami, and Jena Choi for their invaluable contributions. I am also thankful to Lauren Wieczorek and Charles Rojas for always being there to help me navigate administrative hurdles.

I would like to acknowledge the generous funding that supported this research. This work was supported by the National Science Foundation (NSF) under Award No. 2229869, the Geological Society of America (GSA) Graduate Student Research Grant (Award No. 13597-22), and the U.S. Department of Energy Office of Legacy Management. I am especially thankful for the field access, technical assistance, and funding provided through contract #DE-LM0000421 with Navarro Research and Engineering, Inc. (through March 30, 2021) and contract #89303020DLM000001 with RSI EnTech, LLC (after April 1, 2021).

My family is the core of all that I am. I am deeply grateful to my parents, husband, aunt, uncle, mother-in-law, brother, and friends for their unwavering love, patience, and support throughout this journey. Their belief in me, especially during moments when I struggled to believe in myself, has been my greatest source of strength. I carry the memory of my grandparents and father-in-law with me, and I know they would be proud and smiling through joyful tears.

I am immensely grateful to have met so many wonderful people along the way and am hopeful to carry these relationships forward as I continue my journey. Thank you for being the foundation of my growth.

Page intentionally left blank

CHAPTER 1 - Introduction

Persistent groundwater contamination poses significant environmental and public health challenges worldwide. Contaminants, including heavy metals, radionuclides, and soluble salts, persist in subsurface environments due to complex interactions with aquifer materials, creating long-term risks to groundwater quality (Campbell et al., 2012; Yabusaki et al., 2017). Dynamic hydrological events, such as flooding, exacerbate these risks by mobilizing contaminants from subsurface reservoirs, yet the precise sources and transport mechanisms remain poorly understood.

The persistence of contaminants in the subsurface is governed by their interactions with mineral surfaces, amorphous phases, and organic matter under varying geochemical conditions (Bone et al., 2017; Jové Colón et al., 2006). At sites like Riverton, Wyoming, a former uranium mill tailings site, trace-level uranium associated with secondary mineral coatings and coprecipitated phases serves as a significant secondary source, releasing contaminants into groundwater when conditions favor dissolution or desorption (Duff et al., 2002; Luo et al., 2009). Flooding events introduce additional complexity by driving contaminant mobilization through the vadose zone, comprising the unsaturated zone and capillary fringe (Freeze and Cherry, 1979). The interplay between hydrogeological compartments - saturated zone, capillary fringe, and unsaturated zone controls water movement and contaminant transport (Dahan et al., 2009; Ponting et al., 2021). Controlled in-situ experiments simulating flooding provide critical insights into these processes, yet few studies have focused on reactive contaminants like uranium and sulfate under field conditions, limiting the ability to extrapolate laboratory findings to real-world scenarios (Hooda, 2010). Mathematical modeling offers a powerful approach to quantify contaminant transport mechanisms under dynamic, non-steady-state conditions like flooding.

While numerical models such as HYDRUS and MODFLOW 6 provide detailed simulations, their computational demands and extensive parameterization can hinder generalizability (Šimůnek et al., 2008; Langevin et al., 2017). Analytical models, on the other hand offer a computationally efficient alternative, enabling the isolation of advection, hydrodynamic dispersion, and geochemical release processes during infiltration events.

Dissertation Scope and Objectives

This dissertation addresses these critical knowledge gaps through an integrated approach combining advanced analytical techniques, controlled field experiments, and mathematical modeling to investigate contaminant transport during flooding, with a particular focus on uranium at the Riverton, Wyoming, uranium mill tailings site.

Chapter 2 characterizes trace-level uranium associations in natural sediments using fission-track radiography, SEM, and EDS, identifying secondary mineral phases as persistent contaminant reservoirs and providing key parameters for reactive transport models.

Chapter 3 presents novel in-situ flooding experiments designed to elucidate the hydrogeological compartments and mobilization mechanisms driving uranium and sulfate release, contrasting reactive contaminants with non-reactive tracers.

Chapter 4 applies the Wexler (1992) one-dimensional analytical model to inversely simulate field data from infiltration experiments, quantifying the relative roles of advection, hydrodynamic dispersion, and geochemical release mechanisms in contaminant mobilization.

Overall, these chapters advance the mechanistic understanding of contaminant fate and transport during flooding, providing a multidisciplinary framework for improving conceptual models, refining transport simulations, and designing more effective remediation strategies at contaminated sites with dry climate. The findings contribute to the broader field of contaminant

hydrogeology by elucidating the complex behavior of reactive contaminants in the vadose zone under dynamic hydrological conditions.

References

Bone, S.E., Dynes, J.J., Cliff, J., Bargar, J.R., 2017. Uranium(IV) adsorption by natural organic matter in anoxic sediments. Proc Natl Acad Sci USA 114, 711–716. https://doi.org/10.1073/pnas.1611918114

Campbell, K.M., Kukkadapu, R.K., Qafoku, N.P., Peacock, A.D., Lesher, E., Williams, K.H., Bargar, J.R., Wilkins, M.J., Figueroa, L., Ranville, J., Davis, J.A., Long, P.E., 2012. Geochemical, mineralogical and microbiological characteristics of sediment from a naturally reduced zone in a uranium-contaminated aquifer. Applied Geochemistry 27, 1499–1511. https://doi.org/10.1016/j.apgeochem.2012.04.013

Dahan, O., Talby, R., Yechieli, Y., Adar, E., Lazarovitch, N., Enzel, Y., 2009. In Situ Monitoring of Water Percolation and Solute Transport Using a Vadose Zone Monitoring System. Vadose Zone Journal 8, 916–925. https://doi.org/10.2136/vzj2008.0134

Duff, M.C., Coughlin, J.U., Hunter, D.B., 2002. Uranium co-precipitation with iron oxide minerals. Geochimica et Cosmochimica Acta 66, 3533–3547. https://doi.org/10.1016/S0016-7037(02)00953-5

Freeze, R.A., Cherry, J.A., 1979. Groundwater. Prentice-Hall, Englewood Cliffs, N.J.

Hooda, P.S. (Ed.), 2010. Trace Elements in Soils, 1st ed. Wiley. https://doi.org/10.1002/9781444319477

Jové Colón, C.F., Sanpawanichakit, C., Xu, H., Cygan, R.T., Davis, J.A., Meece, D.M., Hervig, R.L., 2006. A Combined Analytical Study to Characterize Uranium Soil and Sediment

Contamination: The Case of the Naturita UMTRA Site and the Role of Grain Coatings (No. NUREG/CR-6898). Rockville, MD.

Langevin, C.D., Hughes, J.D., Banta, E.R., Niswonger, R.G., Panday, Sorab, Provost, A.M., 2017. Documentation for the MODFLOW 6 Groundwater Flow Model: U.S. Geological Survey Techniques and Methods, book 6, chap. A55, 197 p., https://doi.org/10.3133/tm6A55.

Luo, W., Kelly, S.D., Kemner, K.M., Watson, D., Zhou, J., Jardine, P.M., Gu, B., 2009. Sequestering Uranium and Technetium through Co-Precipitation with Aluminum in a Contaminated Acidic Environment. Environ. Sci. Technol. 43, 7516–7522. https://doi.org/10.1021/es900731a

Ponting, J., Kelly, T.J., Verhoef, A., Watts, M.J., Sizmur, T., 2021. The impact of increased flooding occurrence on the mobility of potentially toxic elements in floodplain soil – A review. Science of The Total Environment 754, 142040. https://doi.org/10.1016/j.scitotenv.2020.142040

Šimůnek, J., Bradford, S.A., 2008. Vadose Zone Modeling: Introduction and Importance. Vadose Zone Journal 7, 581–586. https://doi.org/10.2136/vzj2008.0012

Yabusaki, S.B., Wilkins, M.J., Fang, Y., Williams, K.H., Arora, B., Bargar, J., Beller, H.R., Bouskill, N.J., Brodie, E.L., Christensen, J.N., Conrad, M.E., Danczak, R.E., King, E., Soltanian, M.R., Spycher, N.F., Steefel, C.I., Tokunaga, T.K., Versteeg, R., Waichler, S.R., Wainwright, H.M., 2017. Water Table Dynamics and Biogeochemical Cycling in a Shallow, Variably-Saturated Floodplain. Environ. Sci. Technol. 51, 3307–3317. https://doi.org/10.1021/acs.est.6b04873

CHAPTER 2 - Combining fission-track radiography and scanning electron microscopy to identify uranium host phases

Abstract

Residual solid-phase uranium from former mill tailings leachate can contribute to persistent concentrations of uranium in groundwater that exceed regulatory levels. Microscale characterization of uranium-contaminated sediment samples is lacking due to the challenges of detecting uranium at the parts-per-million level and identifying its associations with co-occurring elements. An emerging methodology, fission-track radiography, was applied to detect the low-level solid-phase uranium in sediments. Scanning electron microscopy and energy-dispersive X-ray spectroscopy were used to elucidate the uranium associations with co-occurring aluminum, and iron. Uranium-contaminated sediments were collected from upgradient source zone aquifer sediments in Riverton, Wyoming, USA, where the residual uranium was present. The combined microscopic analyses revealed that in the water-saturated layers, solid-phase uranium primarily co-occurred with amorphous aluminum (Al)-rich and iron (Fe)-rich coatings in the source zone. The unique geochemical associations of solid-phase uranium with the co-occurring Al-rich and Fe-rich coatings suggest that a select suite of equilibrium and kinetic reactions controls its persistence in groundwater. The identification of the uranium co-associations at a former uranium mill tailings site indicates that fission-track radiography with spectroscopic methods can be utilized in uranium-contaminated sites that contain trace-level solid-phase uranium and can inform conceptual and geochemical models for further mechanistic insight.

2.1 Introduction

Uranium (U) is a long-term environmental concern at sites impacted by the legacy of uranium mining and radioactive waste disposal. Groundwater contamination of uranium by

former mine and mill tailings continues to pose a challenge to site restoration efforts even after the primary sources of contamination have been removed due to the persistence of residual uranium associated with aquifer materials (Campbell et al. 2012). Site assessments often rely on site conceptual models to inform clean-up approaches of the secondary sources. Uncertainty regarding the behavior or location of additional uranium sources can cause significant risks to stakeholders. Consequently, accurate characterization of secondary sources and their potential for uranium mobilization is needed to develop effective remediation strategies and time frames.

It is long-established that the dominant factor for the retention of uranium in the subsurface under oxic and anoxic conditions is sorption to mineral surfaces, amorphous phases, and organic matter (Bone et al. 2017; Fenton and Waite 1996; Jové Colón et al. 2006; Stubbs et al. 2009). It is challenging to apply sorption models to mixtures of minerals found in natural sediments because of the insufficient knowledge of the chemical composition of surface regions and their interaction with uranium. Micron-thick coatings of secondary mineral phases and organic matter can form on mineral surfaces and serve as efficient sorption sites with a higher adsorption capacity than the substrate (Jové Colón et al. 2006). Thus, the presence of coating can potentially affect uranium sorption and transport in porous media, and this knowledge gap can add substantial uncertainty to radionuclide desorption predictions from sediments (Davis et al. 2004). In addition, uranium can coprecipitate with iron oxides (Duff et al. 2002) and aluminum hydroxides (Luo et al. 2009) which can produce elevated dissolved uranium concentrations if geochemical conditions become favorable toward mineral dissolution (Noubactep et al. 2005). Accurately predicting uranium fate and transport requires conceptual models consistent with molecular to macro-scale experimental evidence (Arai et al. 2007). Identifying the solid-phase

sinks for uranium is crucial for conceptual modeling and successful remediation approaches (Jové Colón et al. 2006; Stubbs et al. 2009).

A variety of sophisticated spectroscopic and diffraction techniques have been used to analyze uranium associations with complex mineral assemblages in sediments from some of the U.S. Department of Energy's legacy sites, e.g., the Naturita site (e.g., Jové Colón et al. 2006; Noël et al. 2017), Rifle site (Noël et al. 2017, 2019); Shiprock site (Noël et al. 2019), and Hanford site (e.g., Arai et al. 2007; Catalano et al. 2004; Singer et al. 2009; Stubbs et al. 2009). X-ray absorption near-edge structure (XANES) and extended X-ray absorption fine structure (EXAFS) (Noël et al. 2017, 2019), in addition to micro-X-ray absorption spectroscopy (XAS), micro-X-ray fluorescence (μ-XRF), micro-synchrotron X-ray fluorescence (μSXRF), and conventional bulk- and micro X-ray diffraction (XRD) (Arai et al. 2007; Catalano et al. 2004; Jové Colón et al. 2006; Singer et al. 2009), have been primarily employed for identifying uranium phase associations and microscopic distributions, as well as uranium speciation within the contaminated sediments. However, uranium concentrations in most of these studies were relatively higher (> 15 mg/kg) than those of Riverton (0.2–5.5 mg/kg) (U.S. Department of Energy 2016); 16–126 mg/kg (Arai et al. 2007), 173–356 mg/kg (Catalano et al. 2004), 70–140 mg/kg (Singer et al. 2009), 84–15 mg/kg (Stubbs et al. 2009), and an average of 245.6 mg/kg (Noël et al. 2019). As an alternative method, secondary-ion mass spectrometry (SIMS) has been applied in combination with other techniques to determine the presence and concentration of uranium in the micron-scale surface coatings (Jové Colón et al. 2006), but a limitation of SIMS is that molecular ion interference caused by other elements in other particles may induce biased isotope abundance ratio results (Esaka et al. 2012). To identify uranium particles within a thin section prepared from sediments with trace-level uranium concentrations, fission-track

radiography (Wollenberg 1971; Zielinski and Budahn 1998) has been used as a preprocessing step and later combined with SIMS (Esaka et al. 2012) and thermal ionization mass spectrometry (TIMS) (Esaka et al. 2015) to measure isotope ratio. Fission-track method has the detection limit for uranium up to a few tens of ppb level (Shin and Park 1989) and been applied to various geological problems (Galagher et al. 1998), e.g., Quaternary geochronology (Dumitru and Stockli 1998), thermochronology (Wolf et al. 1997), and provenance studies (Hurford and Carter 1991). Despite the potential advantages of fission-track methods for elucidating trace uranium associations in natural sediments, this technique has not been extensively employed in uranium mill tailings sites to inform conceptual site models. Johnson et al. (2021) applied fission-track radiography at a former uranium pilot mill, Grand Junction, Colorado, to identify trace-level uranium in sediments and further characterized the uranium associations by scanning electron microscopy (SEM) and point map analysis in energy-dispersive X-ray spectroscopy (EDS).

In this study, however, the conjunction of fission-track radiography and SEM–EDS was utilized on samples analyzed from a transect of cores at the upgradient source zone at a different uranium mill tailings site in Riverton, Wyoming, USA. Fission-track radiography was used to pinpoint trace-level uranium in sediments below the detection limit of SEM and EDS (0.1% mass concentration). The locations of elevated uranium in the sediments, identified by fission-track radiography, were further analyzed with backscattered electron (BSE) image in SEM. Then, the associations of uranium were characterized with both the point map and elemental map analysis in EDS to investigate the spatial distribution of major reservoirs for trace uranium within natural sediments at the site more efficiently. The objectives of this study were to (1) investigate whether the combination of fission- track radiography and SEM–EDS (point map and elemental map analysis) methods can identify significant hosts for trace-level solid-phase

uranium within natural sediments in Riverton, Wyoming, and (2) determine probable secondary sources for the uranium release in groundwater. The results of this study will aid in modifying conceptual models and surface adsorption approaches in reactive transport models applied in different uranium mill tailings sites.

2.2 Materials and methods

2.2.1 Site description

The study location is a former uranium mill tailings site located 3.9 km southwest of Riverton, Wyoming, United States of America. The mill processed 816,470 tons of uranium ore from 1958 to 1963 (Merritt 1971). The milling operations created radioactive mill tailings containing sandy materials with residual uranium and the tailings pile was located at the upgradient in Riverton, Wyoming (Fig. 2.1). The tailings slurry from the uranium mill tailings was the primary source that contaminated the shallow groundwater beneath the site (Narasimhan et al. 1986; White et al. 1984). The uranium in the plume in the surficial aquifer is mill- related, as confirmed by uranium activity ratios ($^{234}U/^{238}U$) (U.S. Department of Energy 2016). The Riverton site has been influenced by periodic flooding, as it is on an alluvial terrace between the Wind River in the north and the Little Wind River in the East (Fig. 2.1). Annual monitoring and the flood in 2010 indicated that the uranium concentrations were not declining as predicted (Dam et al. 2015) in the site conceptual model formulated in the 1990s. Subsequent work (Dam et al. 2015; Johnson et al. 2016; U.S. Department of Energy 2016) focused on the secondary source

characterizations by lab-scale analyses and new conceptual model construction for residual uranium.

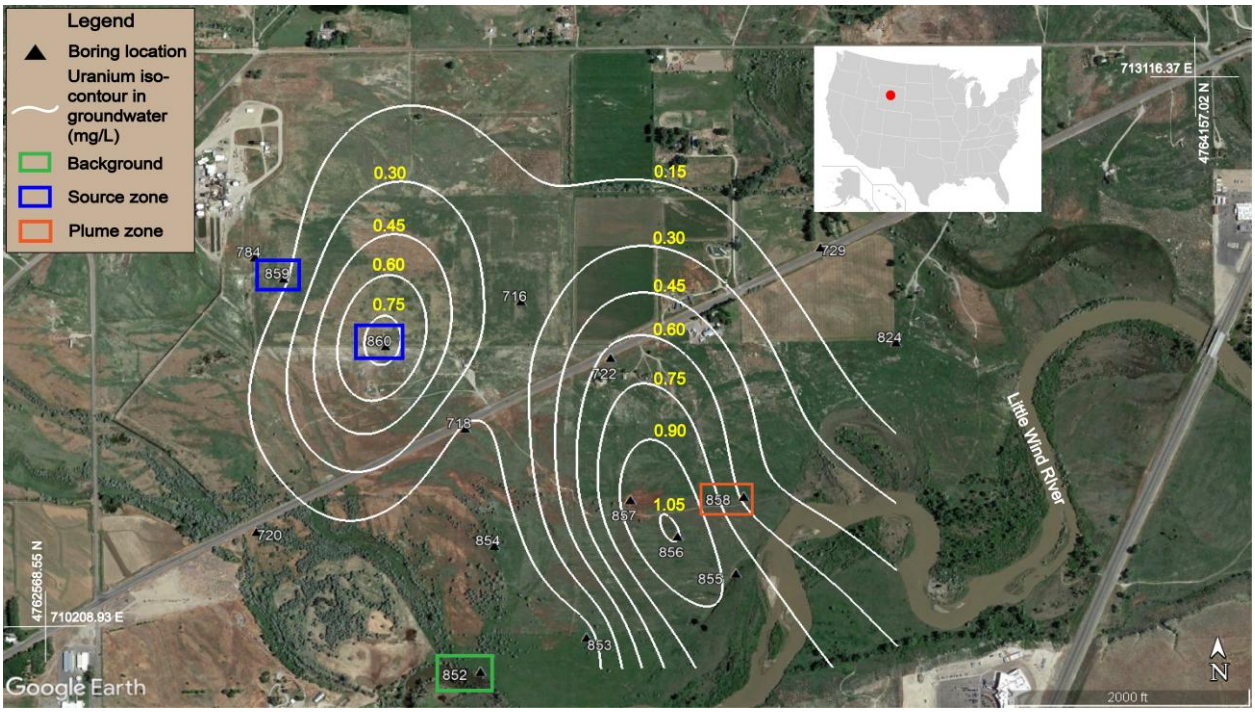

Fig. 2.1 Site map (WGS 84 UTM Zone) at Riverton, Wyoming, showing the spatial distribution of uranium concentration in the aquifer. The inset shows the USA state map where the red dot represents Riverton in Wyoming. The area bounded by orange box is depicted as source zone. Borings 859 (blue rectangle) and 860 (blue rectangle) represent the source zone, and boring 852 (green rectangle) represents the plume edge zone. Groundwater flows from the northwest to the southeast, and the aquifer depth is approximately 19.6 feet (ft) (U.S. Department of Energy 2016). Image source: Google Image, 2014 (site map)

The samples for this study were collected from the former tailings area where the tailings pile that resulted from the uranium extraction process at the uranium mill was located (Dam et al. 2015). The area is depicted as source zone in this study and defines the most upgradient area with remaining solid-phase uranium contamination (Fig. 2.1). The borings 859 and 860 (the blue rectangles in Fig. 2.1) have been analyzed from the source zone due to their location at the head of the plume. The area outside uranium plume is depicted as a plume edge zone and boring 852 (green rectangle in Fig. 2.1) represents this location in this study. Since boring 852 is located outside the plume, it has been referenced as background in this study.

2.2.2 Sample collection and uranium extraction

Sonic drilling was used to collect 6-inch diameter continuous core samples from borings 852, 859, and 860, starting from the ground surface to the top of the first confining zone, which is the top of the bedrock (U.S. Department of Energy 2016). The core from the drilling was vibrated out of the drill stem, placed in a plastic core sleeve, and then cut open to attain lithologic information. Each core was first subdivided at approximately 1 ft sediment depth intervals to obtain geochemical parameters. Then, to collect a sufficient sample volume for laboratory analyses, approximately 3 inches in thickness within each 1 ft sediment depth interval of the core was selected and thoroughly mixed in a pan to homogenize the sample. The sample volume necessary for lab analyses was placed in a plastic bottle, and the rest was preserved in a plastic bag. Soil samples were analyzed by a Department of Energy Consolidated Audit Program (DOECAP)-approved laboratory for U.S. Nuclear Regulatory Commission (NRC)- approved Contaminants of Potential Concern (COPC) (uranium [U]). Total acid digestion using EPA method SW-846 3050B was used for uranium analyses. EPA methods SW-846 6010B and SW-846 6020 were used for analyses of metals and major cations (U.S. Environmental Protection Agency 2014). All the well logs, lithologic descriptions, and final data are available from the U.S. Department of Energy (2016).

2.2.3 Thin-section preparation

A thin section of an epoxy-impregnated sample of interest was polished to prepare the glass slides. Thin- section glass slides were first prepared in standard size (27 × 46 mm [mm]). Later, the slides were modified to a size of 25 × 46 mm by grinding the edges slightly to fit in plastic containers for irradiation. The thin sections were polished to obtain close planar contact between the thin-section surface and detector, thus producing a high spatial resolution of

uranium sites and a clear image of fission tracks during irradiation (Johnson et al. 2021; U.S. Department of Energy 2018).

2.2.4 Fission-track radiography

Fission-track radiography is a method that determines the abundance and location of uranium up to a few tens of ppb levels (Wollenberg 1971; Zielinski and Budahn 1998) with an exposure of a thin section to a reactor neutron. First, a muscovite mica sheet was placed over each thin section of interest. Muscovite mica is a preferable track detector, because tracks in mica are easy to recognize (U.S. Department of Energy 2018; Wollenberg 1971). The thin-section slides with the overlying mica sheet were then placed in polyethylene tubes and irradiated in a research reactor (Fig. 2.2 a–c) at the U.S. Geological Survey in Denver, Colorado. Samples were irradiated at a neutron flux of 2×10^{12} neutrons per square centimeter per second for 8 h for a total maximum neutron dose of ~ 11.6×10^{16} neutrons (less time or a lower neutron flux [or both] is required for higher concentrations of uranium). The irradiation with a flux of thermal neutrons caused induced fission of the highly fissionable uranium-235 isotope in the uranium-bearing thin sections. The samples were then allowed to undergo radioactive decay in storage for about 6 weeks or more to allow for the decay of some shorter-lived neutron activation products. Fission tracks created from the original thin-section surface by uranium-235 can be detected on the corresponding mica sheet (Fig. 2.2d; Online Resource-1 Figs. S1, S21, and S29) placed above the thin section. The muscovite mica detector was removed from the thin section after irradiation. The mica was then washed with a strong stream of water, followed by alcohol, and then dried before mounting on a fresh glass slide to facilitate handling during analysis under micro- scopes (Fig. 2.2e). The mica was mounted original side down with the fission tracks on top, and in the same orientation as during irradiation. The images of the entire thin sections and

associated mica plates were completed for documentation (Online Resource-1 Figs. S1, S2, S21 and S22) using a high-resolution scanner (Epson Perfection V800 Photo) and to facilitate locating fission-track areas compared to grains in the thin-section areas later with the following methods. A more detailed methodology of fission-track radiography is given by Johnson et al. (2021) and U.S. Department of Energy (2018).

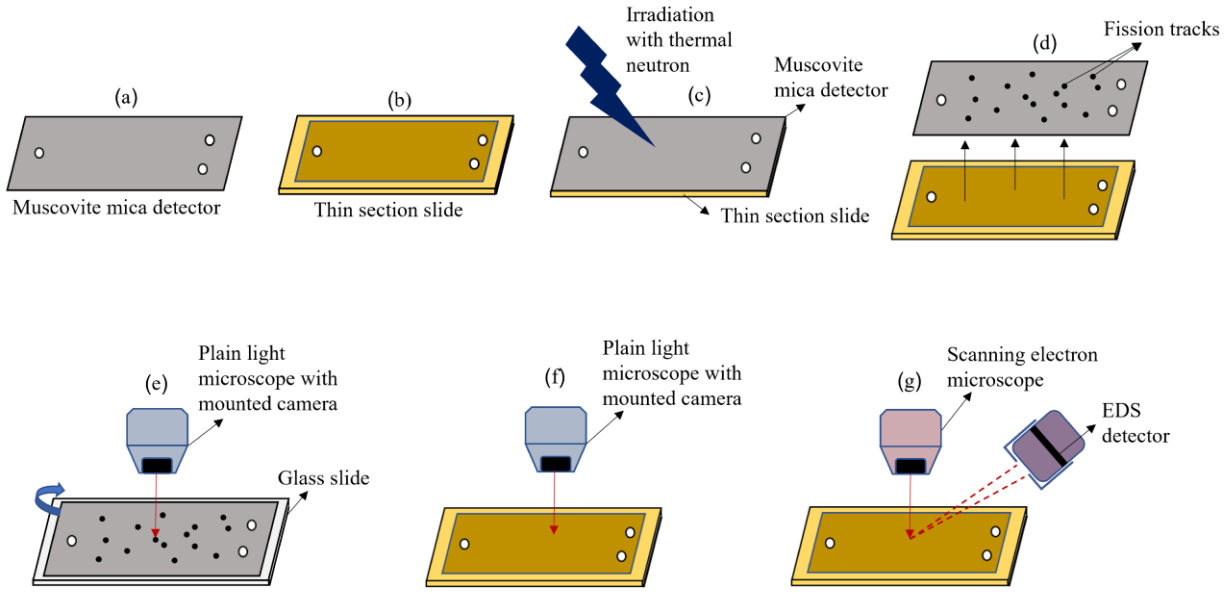

Fig. 2.2 Sample preparation and analysis steps in fission-track radiography and SEM–EDS. a, b Before irradiation; c, d during irradiation; e, g after irradiation. a Muscovite mica detector to detect uranium fission tracks. b Original thin-section slide. c The mica detector plate was placed over the thin-section slide and was run under nuclear reactor. d Uranium fission tracks formed on mica plate. e Mica plate was mounted original side down on a glass slide; in the same orientation during irradiation to compare with paired thin section; later, it was observed and imaged under the plain light microscope. f Simultaneously the thin section was observed and imaged under the plain light microscope to locate corresponding grains to the fission tracks. g Using the fission tracks as a guide, the corresponding grains were characterized in SEM–EDS

Then, the entire mica plate and concurrent thin-section slides were thoroughly examined in parallel with a micro- scope under plain polarized light (PPL) to locate individual micro-scale areas exhibiting fission-track signal, regardless of the signal strength, that could correspond to a grain on each thin section (Fig. 2.2e–f). The underside of the mounted mica, which was the surface in contact with the thin section, was adjusted in the focus of the microscope. Paired areas

of fission tracks with a significant signal on the mica plate and their corresponding grains on the thin sections were photo- graphed using cameras mounted to microscopes for docu- mentation and further analysis in SEM–EDS. Subsequently, a total of 11 micro-scale areas (Online Resource-1 Figs. S1 and S2, and Online Resource-2) showing fission-track signals corresponding to a grain on the thin section were identified in boring 859, whereas a total of eight (Online Resource-1 Figs. S21 and S22, and Online Resource-2) were observed in boring 860 during plain light microscopy. Among these, a total of seven (boring 859) and six (boring 860) micro-scale areas that had strong fission-track signals with associated grains, were documented during spectroscopic imaging and were further studied in SEM–EDS (Online Resource-1 Figs. S1, S2, S21 and S22, and Online Resource-2). Since this study is focused on secondary uranium associations, petrography and spectroscopy focused more on the identification of mineral coatings and cements rather than primary uranium association with the mineral grains. Therefore, two micro-scale areas (referred as Spot- 01 and Spot-02 in Online Resource-1 Figs. S1, S2, S21 and S23) from each boring (859 and 860) showing the strongest fission tracks as coatings around grains are discussed in this study.

2.2.5 SEM–EDS analysis

The irradiated thin sections were first carbon coated using an Edwards 306A vacuum coater fitted with carbon fiber (Cata- log #91202, Ted Pella Inc.) A Hitachi S-4800 Ultra High-Resolution Cold Cathode Field Emission Scanning Electron Microscope (FE-SEM) equipped with a photodiode back- scattered electron (PD-BSE) detector and a Bruker Quantax Energy-Dispersive X-Ray Spectroscopy (EDS) system was used to examine the thin sections after coating (Fig. 2.2g). The FE-SEM parameters during the analysis varied depending on the samples. In general, a 15 kilovolt (kV) accelerating voltage, a 15 mm WD (the analytical

working distance), and a 15-micro ampere (μA) emission current were used to analyze the slides. After a region of interest (ROI) was found within the individual thin sections, guided by fission-track radiography images as described above, a BSE image of the location was captured. The BSE image was used as a guide to analyze bright spots, which indicated the presence of high-Z elements. The same ROI was analyzed with EDS to determine the elemental composition of the sample. Elemental mapping was first performed to provide an overall idea of the types and distribution of the elements in the ROI; afterward, a point map analysis was performed to identify mineral composition based on the spectrum generated. The EDS spectra from point map analysis show intensity as a function of energy (counts per second per electron volt [cps/ eV]) and energy (kiloelectron volts [keV]) for respective elemental occurrences. The chemical composition obtained by EDS spectra can be used to indicate a possible mineralogical composition of areas with high fission-track intensity.

2.3 Results and discussion

2.3.1 Macroscale solid-phase uranium associations

A total acid digestion extraction method was used to measure total sediment-associated uranium. More detailed soil chemistry data by parameter are available in U.S. Department of Energy's (2016) report. The digestion results of the solids indicate that the uranium concentrations range from 0.2 to 5.5 mg/kg in sediment. A summary of uranium concentrations (mg/kg) with depths (ft) for borings 852, 859, and 860 is provided in Fig. 2.3. The solid-phase uranium concentration in boring 852 ranges from 0.26 mg/kg to 1.9 mg/kg. Since uranium is commonly found at an average of 2.76 mg/ kg in sediments (Herring 2013), the maximum solid-phase uranium concentration (1.9 mg/kg) observed in boring 852 that is located outside the plume (Fig. 2.1) is considered the background concentration in this paper (Fig. 2.3). The water

table depth, shown in Fig. 2.3, is susceptible to the Little Wind River stage and varying seasons. Thus, in this paper, water table depth refers to the lower depth of the water table variations above which sediments are variably water-saturated or unsaturated and under which sediments are permanently water-saturated.

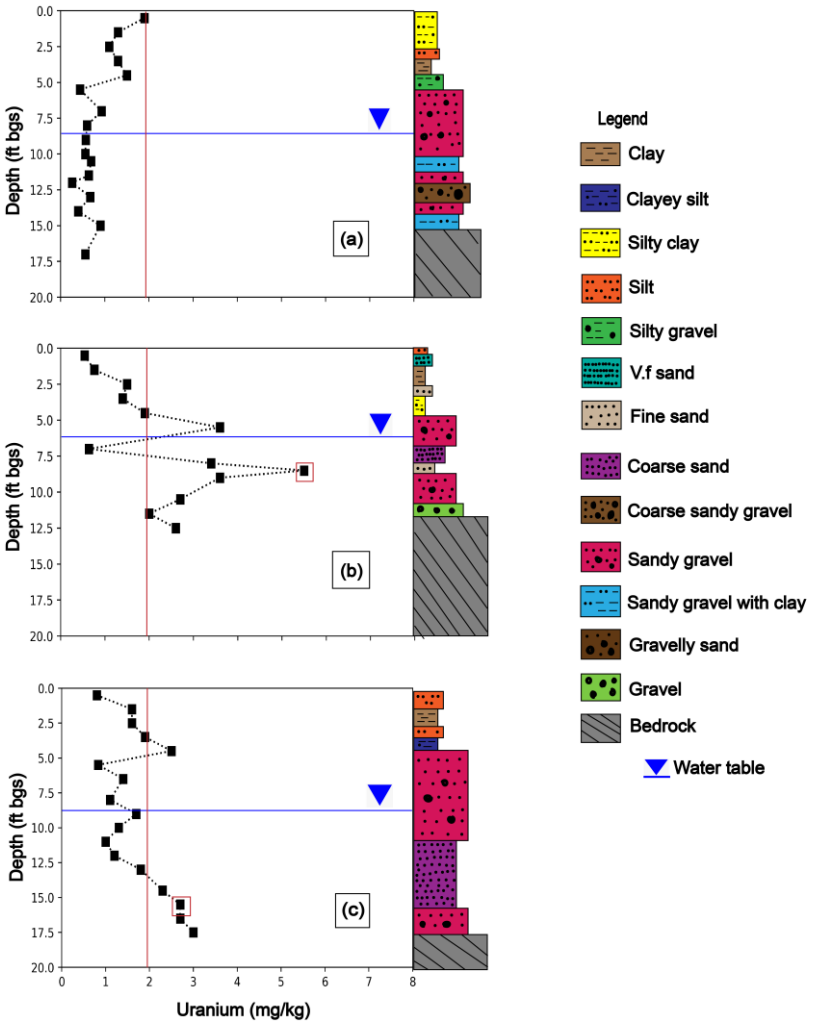

Fig. 2.3 Uranium solid-phase concentrations with depth below the ground surface (U.S. Department of Energy 2016) is shown for borings: a 852, b 859, and c 860. The red rectangle in each boring shows the target sample depth locations. The water table (blue horizontal line) and the approximate back-ground uranium concentration (red vertical line) are shown in the graph for each boring in solid phase

The macro-scale uranium concentration data from total digestions indicate a variation in the patterns of solid-phase uranium distribution along the profiles (as shown with depths,

stratigraphy, and water table location in Fig. 2.3). The sediment depth intervals with above-background and the highest solid-phase uranium concentration in each profile and below the water table, were selected for analysis using microscopic methods (shown as red rectangles in Fig. 2.3). The reasoning behind the selection of sediments below the water table is discussed in detail in the following paragraph.

Borings 859 and 860, located in the source zone (Fig. 2.1), exhibit above the background uranium concentrations below the water table (Fig. 2.3). A sample from boring 859 was collected at 8.5 ft depth (below the water table) showing uranium concentrations of 5.5 mg/kg in fine sand (Fig. 2.3). Similarly, a sample from boring 860 was collected at 15.5 ft (below the water table), exhibiting uranium concentrations of 2.7 mg/kg in coarse sand (Fig. 2.3). As a part of the DOE reclamation program (U.S. Department of Energy 2016), the tailings and 3.9 ft of sub-pile material from the unsaturated layer of the source zone were removed and later replaced with clean fill material (consisting of mostly silt), which extends up to approximately 4ft bgs in both borings. Consequently, the unsaturated layer of the source zone cannot fully represent sediments containing mill-related uranium. Therefore, this paper does not discuss the unsaturated layers of these two borings.

2.3.2 Microscale uranium associations: uranium hosts

In the source zone, two contrasting hosts for uranium are identified in aquifer sediments: Aluminum (Al)-rich coatings followed by Iron (Fe)-rich coatings. The amorphous coatings do not contain sufficient uranium to be detected using EDS in the electron microprobe. However, fission- track analysis collected in the same thin sections exhibited spatial distribution of uranium that worked as a useful guide in SEM/EDS analysis. It is to be noted that the

backscattered electron (BSE) image, fission-track radiography image, transmitted light image, and elemental maps are generated from the same ROI.

2.3.2.1 Al-rich coating

Al-rich coating as a uranium host: The aquifer sediments from boring 859 (Figs. 2.1 and 2.3) located in the source zone contain Al-rich coatings with a significant amount of Si and some amounts of Ca, S, and P (Figs. 2.4 and 2.5), as described below. Figures 4 and 5 depict two different sample points from the same thin section (Online Resource-1 Fig. S1) prepared from boring 859 (source zone). The BSE images in Figs. 2.4 and 2.5 show amorphous coatings around feldspar and quartz with a dried gel appearance and a distinct shrinkage crack (Online Resource-1 Fig. S14, S15, S19, and S20). These rim coatings are nearly continuous (Fig. 2.4) or irregular (Fig. 2.5) around both feldspar and quartz and are observed to be a few microns in width and up to a few tens of microns long (Figs. 2.4 and 2.5). The conspicuous presence of the rim coatings surrounding the grains are evidenced in the BSE images (Figs. 2.4 and 2.5) by their consistent morphology. The EDS elemental maps obtained from the same region of the coatings in Figs. 2.4 and 2.5 show a stronger signal of the Al than that of Si. The EDS spectra acquired in the same coating regions around feldspar (Figs. 2.4 and 2.5) and quartz (Online Resource-1 Fig. S4 and Fig. S17) also exhibit a prominent Al peak. In addition, the mass percentage of Al in the coating around the grains shown in Fig. 2.4 is consistently higher than that of Si (Fig. 4, Online Resource-1 Table S1, Table S4, and Table S5). Although the mass percentage of Al in the coating around the grains in Fig. 2.5 is not higher than that of Si, it is still very prominent (Fig. 2.5 and Online Resource-1 Table. S6). The consistent coating morphology and the prominent signature of Al in the coatings both suggest that the coatings are Al-rich.

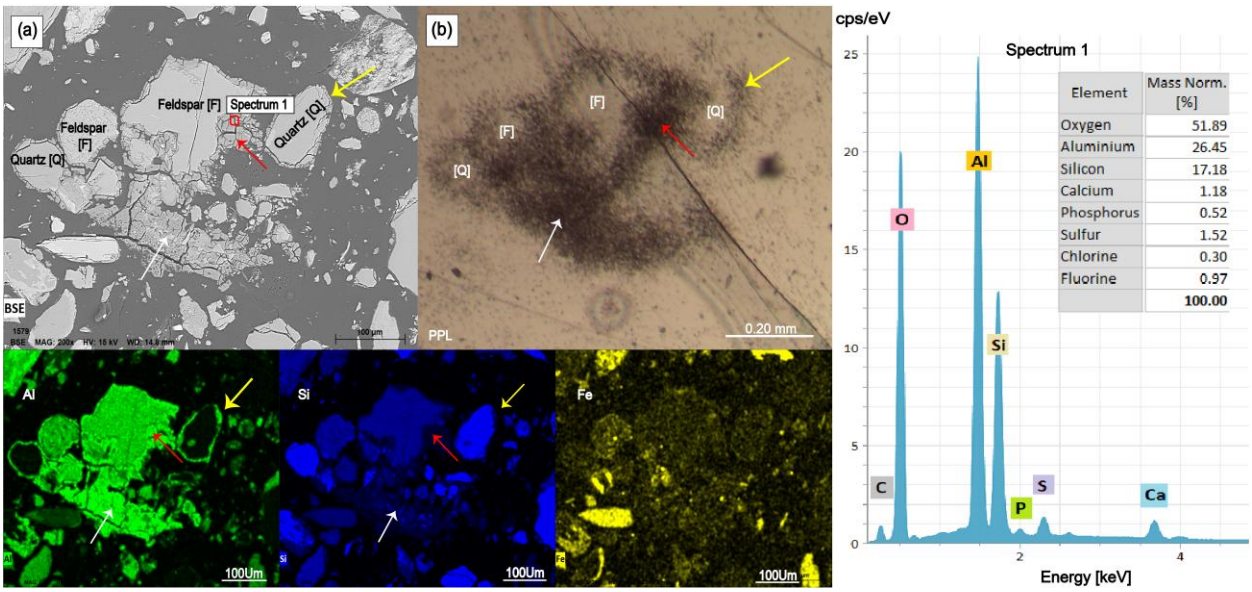

Fig. 2.4 Boring 859-1: a BSE image of Al-rich coating on feldspar (Spectrum 1) and quartz. (b) Fission-track radiography image of the same ROI in a shows uranium-enriched areas positively correlated with the coating. The elemental maps (bottom) of aluminum (Al), silicon (Si), and iron (Fe) correspond to images. a and b. Red and yellow arrows depict the uranium fission track's correlation with comparative Al and Si signals in the coating around feldspar and quartz, respectively. The white arrows show elongated Al-rich coating

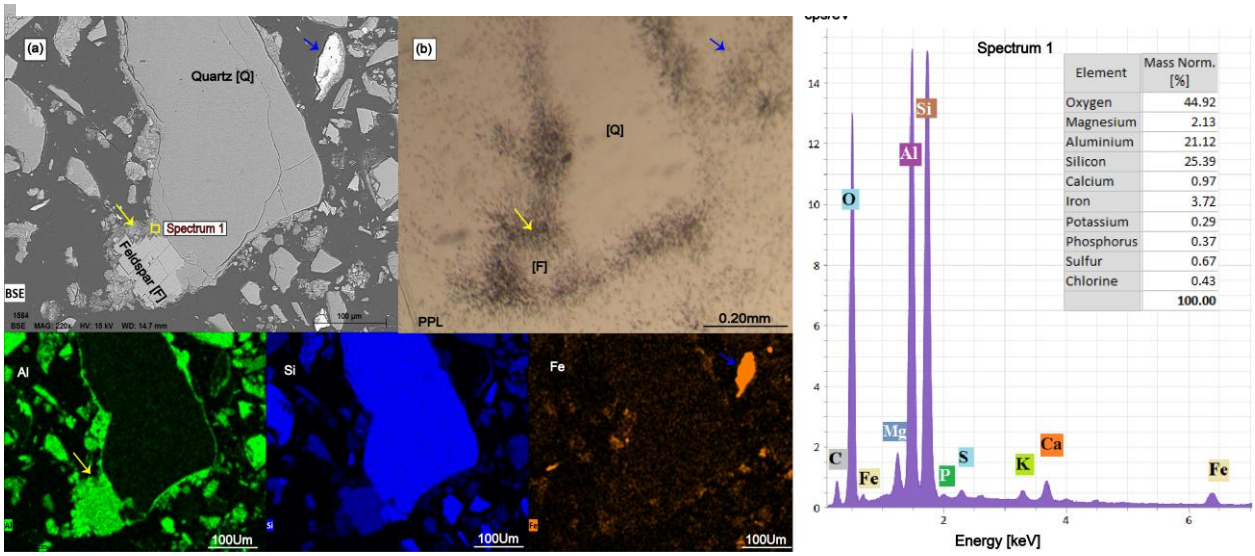

Fig. 2.5 Boring 859-2: a BSE image of Al-rich coating around feldspar (Spectrum 1) and quartz. b Fission-track radiography image of the same ROI in a shows uranium mostly occurring with aluminum hydroxide coating (yellow arrow) and less with iron oxide (blue arrow). The elemental maps (bottom) correspond to images a and b

In our sample, uranium was below the detection limits of the EDS technique; therefore, uranium could not be assessed using this analytical technique. However, uranium-enriched areas were identified by applying fission-track radiography where uranium fission tracks pinpointed uranium hotspots in the thin sections. Overlapping the fission-track maps with their corresponding BSE images and EDS elemental maps reveal the hosts of the trace uranium. The fission-track maps (Images [b] in Figs. 2.4 and 2.5) show that the signal of fission tracks is particularly strong along the Al-rich coatings that occur around feldspar and quartz (Images [a] in Figs. 2.4 and 2.5), which is also evidenced by high intensity of Al in the Al elemental maps and EDS spectra (Figs. 2.4 and 2.5). The strong signals of these Al-rich coatings overlapped with uranium fission tracks suggest that these coatings serve as preferential reservoirs for trace uranium.

Formation mechanism: A study by Luo et al. (2009) indicated that Al (oxyhydr)oxides precipitated at pH above 4.5 and formed an amorphous coating on sediment minerals. The formation of Al-(oxyhydr)oxide coatings was evidenced by a substantially increased Al signal in the EDS spectrum in their study. A previous study by White et al. (1984) in Riverton, Wyoming, suggested that significant amounts of Al and Fe hydroxides precipitated in Riverton due to the low- pH process waters, which caused the dissolution of calcite and the production of CO_2 upon contact with the underlying calcite-rich aquifer. The buffering of the mill tailing effluents in the groundwater caused the precipitation, indicated by the dramatic decrease of dissolved Al and Fe concentrations at near-neutral pH conditions in our study site. While our study does not strongly suggest that the Al-rich coatings found in boring 859 (source zone) are Al hydroxide/(oxyhydr)oxide precipitates, there is a possibility based on the findings of White et al. (1984). Luo et al. (2009) also demonstrated that at pH above 5 and a low carbonate concentration

in groundwater was found to effectively immobilize a large percentage of uranium by coprecipitation with the Al (oxyhydr)oxides that formed as amorphous coatings on minerals. Significant retardation of uranium by coprecipitation in Al/Si-rich gels was also reported by Allard et al. (1999). In our study, the location where Al-rich coating was found (boring 859) contains a low carbonate concentration (alkalinity total as CaCO3 is 314 mg/L) and a higher pH (> 5) in the aquifer. The co- occurrence of uranium with Al-rich coatings (Fig. 4 and Fig. 5) and the favorable site-specific conditions specified by Luo et al. (2009) suggests uranium coprecipitation with Al-rich coating in our study.

2.3.2.2 Fe-rich coating

Fe-rich coating as a uranium host: The aquifer sediments from boring 860 (Figs. 2.1 and 2.2), which is also located in the source zone, contain Fe-rich coating (Figs. 2.6 and 2.7), as described below. Figures 2.6 and 2.7 depict two different sample points (Online Resource-1 Fig. S21) from the same thin section prepared from boring 860 (source zone). The BSE images in Figs. 6 and 7 show that the feldspar grain around the edges is chemically weathered. The area around the feldspar in Fig. 2.6 shows a strong Fe signal in the Fe elemental map and has a significant mass percentage of Fe. Meanwhile, the weathered surface of the feldspar in Fig. 2.7 contains conspicuous small particles with bright signals in the BSE image, which correspond to Fe (Fe elemental map in Fig. 2.7) and have a significant mass percentage of Fe (Online Resource-1 Table. S8). A prominent Fe signal in the EDS elemental maps and the high mass percentage observed in the weathered feldspars provide evidence of Fe-rich coatings surrounding the feldspars. At least two morphologies of the Fe-rich coating are observed in the two sample points- purely amorphous (Fe elemental map in Fig. 2.6) and particulates (Fe elemental map in Fig. 2.7). The Fe-rich coatings are a few microns thick and appear around the edges of feldspar

(Image [a] and Fe elemental maps in Figs. 2.6 and 2.7). However, feldspars chemically weather into clays as explained by Banfield (1990). In the EDS spectra, significant amounts of Al, Si, and Mg—major clay com- ponents (Welton 1984)—with significantly high Fe peaks are observed (Figs. 2.6, 2.7, and Online Resource-1 Fig. S28). Therefore, it is possible that the Fe-rich coatings are inter- mixed with clay. According to Charlet et al. (2002), the surface coatings on clay particles frequently encountered in soil particles are likely a product of heterogeneous oxidative precipitation of iron by various natural electron acceptors. Jové Colón et al. (2006) also observed mixed layer clays and Fe-rich coatings as the main hosts for uranium at the Naturita site. Thus, the presence of significant amounts of clay components with enriched amounts of Fe in Figs. 2.6 and 2.7 supports the possibility of the Fe-rich coatings being inter- mixed with clay.

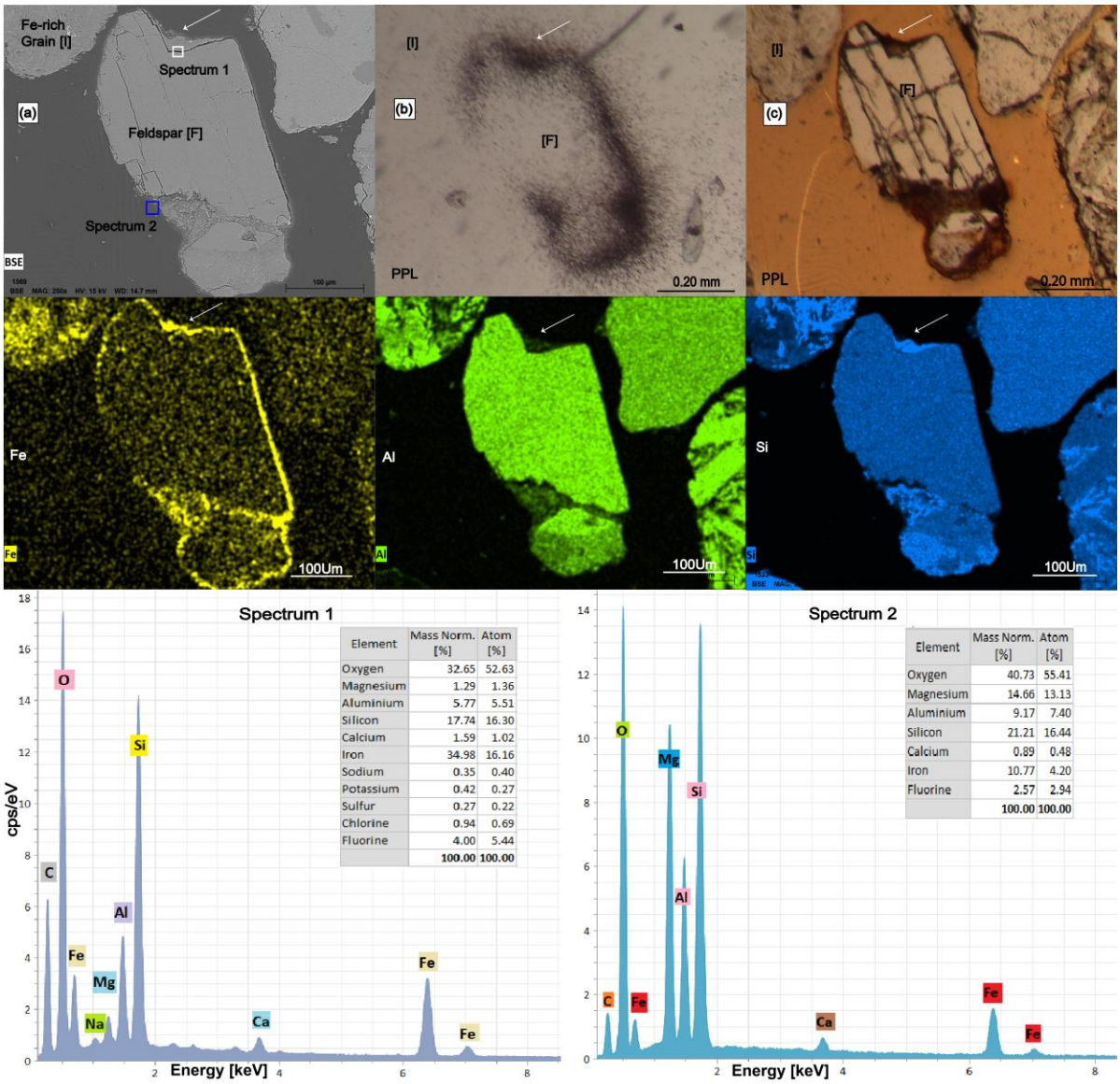

Fig. 2.6 Boring 860-1: a BSE of weathered feldspar with Fe-rich coating intermixed with clay (spectra 1 and 2). b The fission-track radiography image of the same ROI as a shows primary uranium occurrence at the coating. c Transmitted light microscopic image of the same ROI as a and b show a consistent color of clay (white and blue arrows). The elemental maps (bottom) correspond to images a, b, and c. Fe-rich and Al-Si-poor regions are shown by white arrows

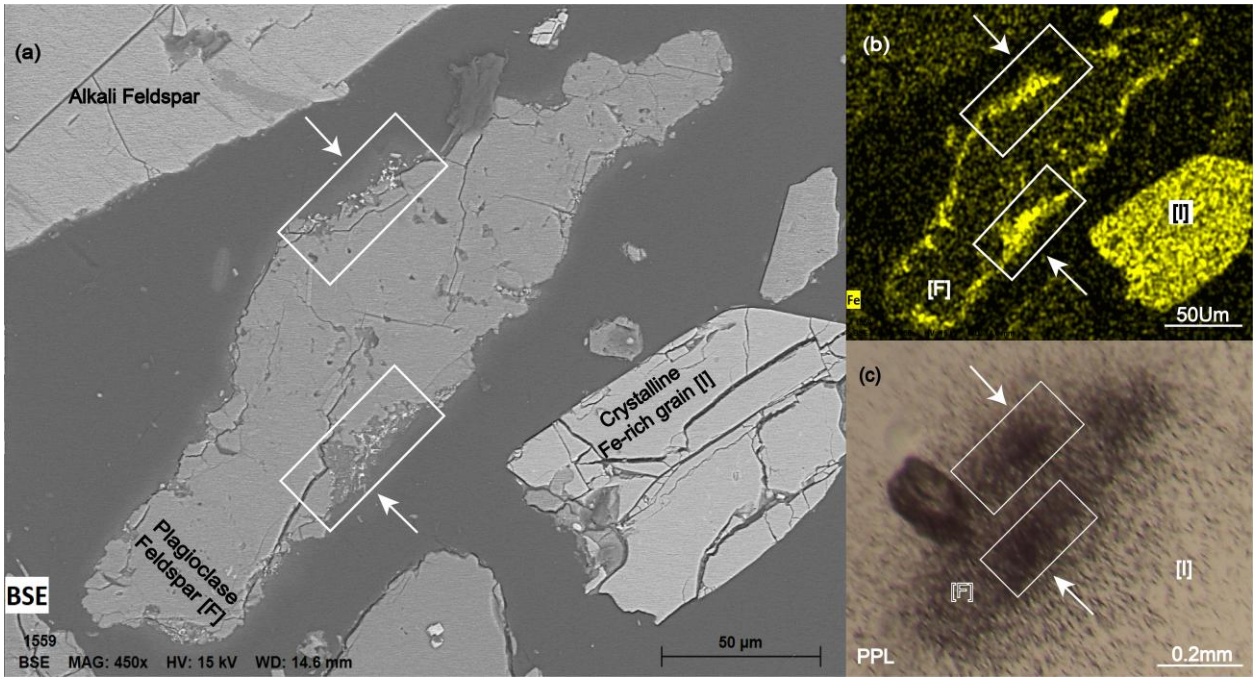

Fig. 2.7 Boring 860-2: a Fe-rich particulates (white rectangles and white arrows) with bright spots on weathered feldspar. b Iron particulate enriched area (white rectangles and white arrows) in weathered edge of feldspar. c Uranium fission tracks occur mostly where iron particulates are enriched (white rectangles and white arrows)

Uranium peak could not be observed using EDS, because the uranium in our sample was below the detection limit of this technique. However, the fission-track analysis (Images [b] in Figs. 2.6 and 2.7) identifies the occurrence of trace uranium in the sediment collected from boring 860 (Fig. 2.1). Corresponding to the fission-track maps (Images [b] in Figs. 2.6 and 2.7) with the BSE images (Images [a] in Figs. 2.6 and 2.7) shows a relatively high density of uranium fission tracks occurring with Fe-rich coatings around feldspar. Cor- responding images (a) and (c) in Fig. 2.7 show that uranium fission tracks are more concentrated where Fe-rich particles are apparent (Fig. 2.7). This occurrence is also suggested by the high intensity of Fe in the Fe elemental maps and EDS spectra with significant percent mass of Fe (Figs. 2.6 and 2.7). The above discussion of uranium fission tracks co-occurring with Fe-rich coating and particles (Figs.

2.6 and 2.7) suggests that Fe-rich coatings play a significant role as a uranium reservoir in a low-temperature environment.

Formation mechanism: A study by Goldberg (1989) showed the formation of Fe-rich coatings on clays. Their research suggested that iron oxides, carrying sufficient positive charge at low pH, precipitated on clay surfaces as amorphous Fe-rich coatings. They also proposed that the amorphous iron-oxide interactions with clays are pH dependent, and these coatings are stable at high pHs where they form oxide phases separate from clays. White et al. (1984) study in Riverton indicated the presence of low-pH process water in the source zone (Fig. 2.1), which might have favored the precipitation of Fe-oxide on clays. However, based on Goldberg's (1989) study, the Fe-rich coatings might be stable in the current near-neutral pH condition in the area (U.S. Department of Energy 2016). Moreover, Arias (1995) observed the formation of Fe hydroxides as discrete particles on the surface of clay. Our study also observed Fe-rich particulates forming on clay (Fig. 2.7). Although the exact phases of the Fe-rich coating could not be identified with the methods used in our study, based on the above discussion, it can be postulated that the Fe-rich coatings are ferric (oxyhydr)oxides in boring 860 (source zone).

The deposition of Fe-rich particles on clay (Figs. 2.6 and 2.7) would increase the surface area independently of the underlying material. Hence, a significant amount of uranium might get sorbed onto ferric (oxyhydr)oxide coating on feldspar (Arias 1995). The sorption onto the amorphous ferric (oxyhydr)oxide host phases can be irreversible if there is a long-term association of uranium with the ferric (oxyhydr)oxide phases that could result in coprecipitation (Noubactep et al. 2005; Duff et al. 2002). This coprecipitated uranium can only be released if the ferric (oxyhydr)oxide transforms through dissolution (Noubactep et al. 2005). Due to a lower

concentration of dissolved uranium in our study area, sorption and coprecipitation are most likely potential mechanisms for uranium retention as discussed by Duff et al. (2002) study.

2.4 Conclusion

This study demonstrates the advancement of combining fission-track radiography with scanning electron micros- copy and energy-dispersive X-ray spectrometry, providing valuable insights into potential reservoirs for residual solid-phase uranium from a former uranium milling operation. The application of fission-track radiography served as a preprocessing step and pinpointed low-concentration uranium in the aquifer sediments. The microscopic characterization of the uranium-contaminated aquifer sediments delineated residual solid-phase uranium co-associations with amorphous Al-rich coating around feldspar and quartz and Fe-rich coating interlayered with clay around feldspar. These coatings can affect the uranium sorption mechanism by significantly modifying the surface proper- ties of the associated minerals. Thus, the exact identification of uranium-bearing phases is crucial when developing site-wide models incorporating sorption and desorption processes in soils or weathered sediment environments. Due to the limited sample size in this study, it could not be concluded in a definite manner whether these observed coatings are major sources responsible for solid-phase uranium retention in the source zone. However, similar amorphous coatings have been observed on other former uranium mill tailings sites; Al–Si-rich coatings in Han- ford (Arai et al. 2007), and Grand Junction (Johnson et al. 2021); and Fe-rich coatings in Naturita (Jové Colón et al. 2006) that suggest a prevalent occurrence of such coatings in uranium mill tailings sites. Therefore, the amorphous Al-rich and Fe-rich coatings identified around the grains in this study could potentially serve as secondary sources for uranium released from the solid phase at the site. Nevertheless, additional data are required to confirm the impacts of these coatings on a broader

scale at the site. Overall, applying fission-track radiography as a preprocessing step to identify trace uranium locations, and combining it with available sophisticated spectroscopic and diffraction techniques, depending on the objectives of the study, can significantly enhance the characterization of trace-uranium- bearing phases in the uranium mill tailings sites.

Acknowledgements

Financial support was provided by the National Science Foundation (NSF) under award number 2229869, the 2022 Geological Society of America (GSA) Graduate Student Research Grant program under grant number 13597-22 and the U.S. Department of Energy Office of Legacy Management through contract number 89303020DLM000001, task order number 89303022FLM400039. The authors express their gratitude to Dr. Heather A. Owen, Director of Electron Microscope Laboratory at the Department of Bio- logical Sciences, University of Wisconsin-Milwaukee, for her guidance on operating the electron microscope. The authors also thank the anonymous reviewers and Editors-in-Chief Olaf Kolditz and Yan Zheng for their invaluable comments that improved the manuscript from its previous version.

References

Allard T, Ildefonse P, Beaucaire C, Calas G (1999) Structural chemistry of uranium associated with Si, Al, Fe gels in a granitic uranium mine. Chem Geol 158:81–103. https://doi.org/10.1016/S0009- 2541(99)00025-X

Arai Y, Marcus MA, Tamura N, Davis JA, Zachara JM (2007) Spectroscopic evidence for uranium bearing precipitates in vadose zone sediments at the Hanford 300-area site. Environ Sci Technol 41:4633–4639. https://doi.org/10.1021/es062196u

Arias M (1995) Effects of iron and aluminium oxides on the colloidal and surface properties of kaolin. Clays Clay Miner 43:406–416. https://doi.org/10.1346/CCMN.1995.0430403

Banfield JF (1990) Analytical transmission electron microscope studies of plagioclase, muscovite, and K-feldspar weathering. Clays Clay Miner 38:77–89. https://doi.org/10.1346/CCMN.1990.0380111

Bone SE, Dynes JJ, Cliff J, Bargar JR (2017) Uranium(IV) adsorption by natural organic matter in anoxic sediments. Proc Natl Acad Sci USA 114:711–716. https://doi.org/10.1073/pnas.1611918114

Campbell KM, Kukkadapu RK, Qafoku NP, Peacock AD, Lesher E, Williams KH, Bargar JR, Wilkins MJ, Figueroa L, Ranville J, Davis JA, Long PE (2012) Geochemical, mineralogical and micro- biological characteristics of sediment from a naturally reduced zone in a uranium-contaminated aquifer. Appl Geochem 27:1499– 1511. https://doi.org/10.1016/j.apgeochem.2012.04.013

Catalano JG, Heald SM, Zachara JM, Brown GE (2004) Spectroscopic and diffraction study of uranium speciation in contaminated vadose zone sediments from the Hanford site, Washington state. Environ Sci Technol 38:2822–2828. https://doi.org/10.1021/es049 963e

Charlet L, Bosbach D, Peretyashko T (2002) Natural attenuation of TCE, As, Hg linked to the heterogeneous oxidation of Fe(II): an AFM study. Chem Geol 190:303–319. https://doi.org/10.1016/ S0009-2541(02)00122-5

Dam WL, Campbell S, Johnson RH, Looney BB, Denham ME, Eddy-Dilek CA, Babits SJ (2015) Refining the site conceptual model at a former uranium mill site in Riverton, Wyoming, USA. Environ Earth Sci 74:7255–7265. https://doi.org/10.1007/ s12665-015-4706-y

Davis JA, Meece DE, Kohler M, Curtis GP (2004) Approaches to sur- face complexation modeling of uranium(VI) adsorption on aquifer sediments. Geochim Cosmochim Acta 68:3621–3641. https://doi. org/10.1016/j.gca.2004.03.003

Duff MC, Coughlin JU, Hunter DB (2002) Uranium co-precipitation with iron oxide minerals. Geochim Cosmochim Acta 66:3533– 3547. https://doi.org/10.1016/S0016-7037(02)00953-5

Dumitru TA, Stockli DF (1998) Technical note. In: van den Haute P, de Corte F (eds) Advances in fission-track geochronology. Springer, Dordrecht, pp 325–330. https://doi.org/10.1007/978-94-015-9133- 1_21

Esaka F, Lee C-G, Magara M, Kimura T (2012) Fission track–second- ary ion mass spectrometry as a tool for detecting the isotopic signature of individual uranium containing particles. Anal Chim Acta 721:122–128. https://doi.org/10.1016/j.aca.2012.01.045

Esaka F, Suzuki D, Magara M (2015) Identifying uranium particles using fission tracks and microsampling individual particles for analysis using thermal ionization mass spectrometry. Anal Chem 87:3107–3113. https://doi.org/10.1021/acs.analchem.5b00236

Fenton BR, Waite TD (1996) A kinetic study of cation release from a mixed mineral assemblage: implications for determination of uranium uptake. Radiochim Acta 74:251–256. https://doi.org/10. 1524/ract.1996.74.special-issue.251

Gallagher K, Brown R, Johnson C (1998) Fission track analysis and its applications to geological problems. Annu Rev Earth Planet Sci 26:519–572. https://doi.org/10.1146/annurev.earth.26.1.519

Goldberg S (1989) Interaction of aluminum and iron oxides and clay minerals and their effect on soil physical properties: a review. Commun Soil Sci Plant Anal 20:1181–1207. https://doi.org/10. 1080/00103629009368144

Herring JS (2013) Uranium and thorium resources. In: Tsoulfanidis N (ed) Nuclear energy. Springer, New York, pp 463–490. https://doi. org/10.1007/978-1-4614-5716-9_18

Hurford AJ, Carter A (1991) The role of fission track dating in dis- crimination of provenance,

57th edn. Springer, pp 67–78. https:// doi.org/10.1144/GSL.SP.1991.057.01.07

Johnson RH, Hall SM, Tigar AD (2021) Using fission-track radiography coupled with scanning electron microscopy for efficient identification of solid-phase uranium mineralogy at a former uranium pilot mill (grand junction, Colorado). Geosciences 11:294. https:// doi.org/10.3390/geosciences11070294

Johnson RH, Dam WL, Campbell S, Noël V, Bone SE, Bargar JR, Dayvault J (2016) Persistent secondary contaminant sources at a former uranium mill site, Riverton, Wyoming, USA. In: Proceedings IMWA 2016. Presented at the Mining Meets Water–Conflicts and Solutions, Freiberg/Germany, pp 398–404

Jové Colón CF, Sanpawanichakit C, Xu H, Cygan RT, Davis JA, Meece DM, Hervig RL (2006) A combined analytical study to character- ize uranium soil and sediment contamination: the case of the natu- rita UMTRA Site and the Role of Grain Coatings (No. NUREG/ CR-6898), Rockville, MD

Luo W, Kelly SD, Kemner KM, Watson D, Zhou J, Jardine PM, Gu B (2009) Sequestering uranium and technetium through co-precipi- tation with aluminum in a contaminated acidic environment. Envi- ron Sci Technol 43:7516–7522. https://doi.org/10.1021/es900731a

Merritt RC (1971) The extractive metallurgy of uranium. Colorado School of Mines Research Institute

Narasimhan TN, White AF, Tokunaga T (1986) Groundwater contami- nation from an inactive uranium mill tailings pile: 2. Application of a dynamic mixing model. Water Resour Res 22:1820–1834. https://doi.org/10.1029/WR022i013p01820

Noël V, Boye K, Kukkadapu RK, Bone S, Lezama Pacheco JS, Cardarelli E, Janot N, Fendorf S, Williams KH, Bargar JR (2017) Understanding controls on redox processes in floodplain

sedi- ments of the Upper Colorado River Basin. Sci Total Environ 603–604:663–675. https://doi.org/10.1016/j.scitotenv.2017.01.109

Noël V, Boye K, Kukkadapu RK, Li Q, Bargar JR (2019) Uranium storage mechanisms in wet-dry redox cycled sediments. Water

Res 152:251–263. https://doi.org/10.1016/j.watres.2018.12.040 Noubactep C, Schöner A, Dienemann H, Sauter M (2005) Release of

coprecipitated uranium from iron oxides. J Radioanal Nucl Chem 267:21–27. https://doi.org/10.1007/s10967-006-0004-1

Shin S-C, Park K-S (1989) Determination of low levels of uranium impurity by fission track registration using mica and polycar- bonate detectors. Int J Radiat Appl Instrum Part D 16:271–274. https://doi.org/10.1016/1359-0189(89)90026-5

Singer DM, Zachara JM, Brown GE Jr (2009) Uranium speciation as a function of depth in contaminated hanford sediments: a micro- XRF, micro-XRD, and micro- and bulk-XAFS study. Environ Sci Technol 43:630–636. https://doi.org/10.1021/es8021045

Stubbs JE, Veblen LA, Elbert DC, Zachara JM, Davis JA, Veblen DR (2009) Newly recognized hosts for uranium in the Hanford Site vadose zone. Geochim Cosmochim Acta 73:1563–1576. https:// doi.org/10.1016/j.gca.2008.12.004

U.S. Department of Energy (2016) 2015 Advanced site investigation and monitoring report Riverton, Wyoming, processing site september 2016 (No. S--14148, 1351628). US Department of Energy

U.S. Environmental Protection Agency (2014) Test methods for evalu- ating solid waste: physical/chemical methods, SW-846 update 5.

U.S. Environmental Protection Agency, Washington

US Department of Energy (2018) Plume persistence final project report (Doc. No. S15233). US Department of Energy

Welton JE (1984) SEM petrology atlas. Am Assoc Pet Geol. https:// doi.org/10.1306/Mth4442

White AF, Delany JM, Narasimhan TN, Smith A (1984) Groundwater contamination from an inactive uranium mill tailings pile:

1. Application of a chemical mixing model. Water Resour Res 20:1743–1752. https://doi.org/10.1029/WR020i011p01743

Wolf RA, Farley KA, Silver LT (1997) Assessment of (U-Th)/He thermochronometry: the low-temperature history of the San Jacinto mountains California. Geology 25:65. https://doi.org/10.1130/ 0091-7613(1997)025%3c0065:AOUTHT%3e2.3.CO;2

Wollenberg HA (1971) Fission-track radiography of uranium and thorium in radioactive minerals. In: Proceedings LBL-754 of the 4th International Symposium on Geochemical Exploration, pp 347–357

Zielinski RA, Budahn JR (1998) Radionuclides in fly ash and bottom ash: improved characterization based on radiography and low energy gamma-ray spectrometry. Fuel 77:259–267. https://doi. org/10.1016/S0016-2361(97)00194-4

CHAPTER 3 - Contaminant mobilization from the vadose zone to groundwater during experimental river flooding events

Abstract

Natural river flooding events can mobilize contaminants from the vadose zone and lead to increased concentrations in groundwater. Characterizing the mass and transport mechanisms of contaminants released from the vadose zone to groundwater during these recharge events is particularly challenging. Therefore, conducting highly-controlled in-situ experiments that simulate natural flooding events can help increase the knowledge of where contaminants can be stored and how they can move between hydrological compartments. This study specifically targets uranium pollution, which is accompanied by high sulfate levels in the vadose zone and groundwater. Two novel experimental river flooding events were conducted that utilized added non-reactive halides (bromide and iodide) and 2,6-difluorobenzoate tracers. In both experiments, about 8 m^3 of traced water from a nearby contaminant-poor river was flooded in a 3-m diameter basin and infiltrated through the vadose zone and into a contaminant-rich unconfined aquifer for an average of 10 days. The aquifer contained 13 temporary wells that were monitored for solute concentration for up to 40 days. The groundwater analysis was conducted for changes in contaminant mass using the Theissen polygon method and for transport mechanisms using temporal moments. The results indicated an increase in uranium (21 and 24%), and sulfate (24 and 25%) contaminant mass transport to groundwater from the vadose zone during both experiments. These findings confirmed that the vadose zone can store and release substantial amounts of contaminants to groundwater during flooding events. These results suggested that contaminant-rich pore water in the vadose zone was transported ahead of flood water and into the groundwater. During the first flooding event, elevated concentrations of contaminants were sustained, and that chloride behaved similarly. The findings implied that contaminant- and

chloride-rich evaporites in the vadose zone were dissolved during the first flooding event. For the second flooding event, the data suggested that the contaminant-rich evaporites continued to dissolve whereas chloride- rich evaporites were previously flushed. Overall, these findings indicated that contaminant-rich pore water and evaporites in the vadose zone can play a significant role in contaminant transport during flooding events.

3.1 Introduction

Flooding is a dynamic event with rapidly changing flows, chemical compositions, and sediment loads (Simpson et al., 2013). An extreme flooding event can result in a significant mobilization and redistribution of contaminants, leading to both socio-economic and environmental damage (Crawford et al., 2022; Ponting et al., 2021). When a soil floods, the mobility of contaminants can either increase or decrease based on soil mineralogy and texture, the properties that change spatially (Ponting et al., 2021). This phenomenon is particularly critical because when mobilized downward, contaminants can potentially persist for long time periods within the subsurface and become a continuing source of contamination to groundwater (Truex et al., 2009). As such, water quality is dependent on the interplay between river-groundwater-vadose zone system (Yabusaki et al., 2017).

The subsurface hydrogeological layers - the saturated zone (groundwater occurrence), unsaturated zone, and capillary fringe (Freeze and Cherry, 1979), play crucial roles in controlling water movement and quality in the river-groundwater-vadose zone system (Yabusaki et al., 2017). The saturated zone lies below the water table and comprises soil pores filled with water under positive pressure head. The capillary fringe, situated above the water table contains soil pores filled with water but has pressure heads less than atmospheric. The unsaturated zone is above the capillary fringe, with soil pores that are not fully saturated and have negative pressure

heads. Grouped together, in this study, the capillary fringe and unsaturated zone are referred to as the vadose zone that occurs above the water table and is under negative pressure head. The water table, defined as the surface where the fluid pressure is exactly atmospheric, separates the vadose zone from the saturated zone, where groundwater occurs. Understanding the dynamics between these layers is essential to identifying contaminant storage in the subsurface and comprehending the factors responsible for subsequent contaminant release during flooding events.

To understand the factors contributing to contaminant transport from the vadose zone to groundwater during a flooding event, continuous real-time physio-chemical data from the floodplain is required (Barber et al., 2017). Due to the unpredictability in the frequency and magnitude of occurrence of a flooding event, there is usually an absence of the baseline and continuous physio-chemical data during the event (Ponting et al., 2021). Occasionally, baseline data from pre- and post- natural events are established (U.S. Department of Energy, 2019) but it is usually difficult to use these data to assess the processes of events and their potential impacts (Ponting et al., 2021). Many of the findings on contaminant mobility during flooding events, therefore, are based on direct collection of time-series groundwater samples under normal flow and during inundations (Barber et al., 2017; U.S. Department of Energy, 2019; Yang et al., 2023). While these data can provide real-time physio- chemical data during a flooding event, controlled experiments can provide more robust understanding of the underlying processes of contaminant transport during the events by reducing uncertainties in evaluation of the recharge processes (Ofer Dahan et al., 2007; Ponting et al., 2021).

Some of the controlled experiments that are available on mobility of contaminants on floodplain soils are based on generating artificial flooding environments in the laboratory (Frohne et al., 2011; Izquierdo et al., 2017; Weber et al., 2009). Laboratory column experiment

has also been performed to analyze solute migration through the vadose zone and groundwater during flash floods (Amiaz et al., 2011). Although the laboratory-based studies can provide insights into the processes occurring during the course of the flooding events, these findings are difficult to extrapolate to field-scale interpretations (Hooda, 2010). In contrast, on-site experiments on the effect of flooding events on contaminant mobility in floodplain soils can better provide results on effects of flooding events on groundwater (Ponting et al., 2021). There are few studies that conducted field scale infiltration experiments to evaluate dynamics of flood water percolation and groundwater recharge via variation in the vadose zone water content profile (Benito et al., 2010; Dahan et al., 2008; Ofer Dahan et al., 2007). The dynamics of percolating flood water flow and subsequent contaminant transport through the vadose zone was first studied by multi-tracer field infiltration experiment in an alluvium underlying a stream channel (Dahan et al., 2009). These studies based on field infiltration experiments provided transient data on water percolation and contaminant migration during flooding events. However, river water was not utilized as the infiltration source in these field experiments, and the analysis did not specifically focus on reactive solute transport when examining contaminant trans- port during flooding events.

Contaminants such as uranium and sulfate, are highly reactive and are more mobile during oxic conditions such as a flooding event, than reducing conditions (Langmuir, 1977). Sulfate is also very soluble in groundwater and can travel a long distance in subsurface environments (Miao et al., 2012). Moreover, sulfate is a common anion in soluble-prone evaporite minerals and can potentially entrap uranium in dry conditions and subsequently release during groundwater recharge (Apaydın and Aktas¸, 2012; Carlisle et al., 1978). In addition, uranium is considered a primary contaminant in groundwater; primary contami- nants pose

significant health risks, for which the United States Envi- ronmental Protection Agency (EPA) sets enforceable Maximum Contaminant Levels (MCLs) under the Safe Drinking Water Act (National Primary Drinking Water Regulations, 2024). On the other hand, sulfate is considered a secondary contaminant in groundwater; secondary contaminants are not directly harmful to human health but can affect the aesthetic qualities of water, such as taste, odor, colour, and staining, with the EPA setting non-enforceable guidelines called Secondary Maximum Contaminant Levels (SMCLs) (Drinking Water Regulations and Contaminants, 2024). Given the complex geochemistry of contaminants like uranium and sulfate, especially their sensitivity to redox conditions and pH, it is crucial to understand their behavior during floods (Langmuir, 1977). To our knowledge, controlled in-situ flooding experiments have not been conducted to describe reactive contaminant transport behavior during the course of a flooding event.

In the present work, two in-situ experiments, the first of their kind, were performed to simulate flooding events at a contaminated field site to study contaminant behavior across hydrogeological compartments during the events. In the first flooding experiment non-reactive tracers (halides and fluorobenzoates) were utilized to contrast contaminant behavior with non-reactive tracers during floods. In the second flooding experiment, alkalinity was added along with a non-reactive tracer (halide) to suggest possible remediation of the contaminated site. The specific objectives of our study were to (1) identify the hydrogeological compartment(s) responsible for the contaminant transport, and (2) elucidate the dominant mobilization mechanisms of contaminants during floods. Significant past research (Johnson et al., 2016; Paradis et al., 2022a; U.S. Department of Energy, L.M, 2014) allowed us to hypothesize that contaminants mobilize from the vadose zone due to contaminant- rich evaporite dissolution during a flooding event. Overall, our study presents new results from the experimentally

simulated floods at a field scale and can inform the development of predictive models for groundwater management.

3.2 Materials and methods

3.2.1 Study Site

The study site is in central Wyoming (WY), 2 miles southwest of Riverton and on river alluvium between the Wind River and Little Wind River (Fig. S1). There are three aquifers at the site which are: (1) an unconfined aquifer, (2) a semiconfined aquifer, and (3) a confined aquifer (Fig. 3.1a). The unsaturated zone is composed of approximately 1.2–1.5 meters (m) of silt and clay. The shallow aquifer consists of approximately 4.5–6 m of sand and gravel, and the semiconfined and confined aquifers comprise the upper units of the Early Eocene Wind River Formation, which is over 150 m thick in the vicinity of the site (Dam et al., 2015). The predominant stratigraphic unit of Early Eocene Wind River Formation is composed of sandstone, conglomerate, silt- stone, and claystone (Keefer, 1970). The Wind River Formation was accumulated through the action of fluvial systems that transported debris to the Wind River Basin located to the north. Regionally, the deposition of the formation occurred on an erosional surface sloping towards the north, situated between the Granite Mountains to the south and the depression of the Wind River Basin to the north (Robert W. Gregory, 2019).

The Riverton Processing site, formerly a uranium mill tailings facility operating from 1958 to 1963 (U.S. Department of Energy, 2016) is currently among 107 sites managed by the United States (U.S.) Department of Energy across the U.S., aimed at restoring sites contaminated due to nuclear production activities (Dwivedi et al., 2022). The primary source of contamination to the surface and shallow groundwater beneath and downgradient of the site was the tailings slurry from the former mill (Fig. 3.1a). Surface remediation was completed

in 1989 by removing the tailings to radioactivity standards for radium (Narasimhan et al., 1986; White et al., 1984). Despite these measures, substantial concentrations of solid-phase contaminants are present in both the vadose zone and aquifer sediments at our study area (Paradis et al., 2022a; U.S. Department of Energy, 2016). Due to the presence of shale layers (Fig. 3.1a), confined aquifer remains uncontaminated and mill-related contaminants are not detected in the semiconfined aquifer. However, the surficial unconfined aquifer is contaminated with uranium (~1.7 milligrams/liters [mg/L]), and sulfate (~6300 mg/L) concentrations (U.S. Department of Energy, 2016) exceeding regulatory limits. Uranium has a maximum concentration limit (MCL) of 0.03 mg/L (National Primary Drinking Water Regulations, 2024) and sulfate has a secondary MCL of 250 mg/L (Drinking Water Regulations and Contaminants, 2024) in groundwater. The major dissolved uranium species, as determined using the PHREEQC 3.7.3 with the LLNL database (Input file. S1), in the groundwater of the site are UO_2SO_4, $UO_2(SO_4)_2^{2-}$, $UO_2(CO_3)_3^{4-}$, $UO_2(CO_3)_2^{2-}$, UO_2CO_3, and $UO_2(OH)_2$. For sulfur, the main dissolved species is SO_4^{2-}, with no significant precipitation of sulfate- bearing minerals, as indicated by the saturation indices (SI) of anhydrite (—0.41), gypsum (—0.15), bloedite (—6.32), and epsomite (—2.56) in the aquifer sediments. The groundwater plume was estimated to be attenuated below MCLs through natural flushing within the past 100 years from 1997, according to the Riverton Groundwater Analysis and Network Design Tool (GANDT) model simulated by Sandia National Laboratories (Knowlton Jr et al., 1997; U.S. Department of Energy, 1998). The GANDT code incorporated groundwater flow and transport uncertainty through Monte Carlo simulations, accounting for concentration data and spatial variability using geostatistical methods while employing a single sorption partitioning coefficient (K_d) approach. However, the annual monitoring indicated persistence of the plume, including an increase in

uranium concentration following a flooding event in 2010 (Fig. 3.1b). The discrepancy between the model predictions and observational data caused concern for the longevity of the contaminant plume and exhibited lapses in the knowledge of the processes governing contaminant storage and release (Dam et al., 2015).

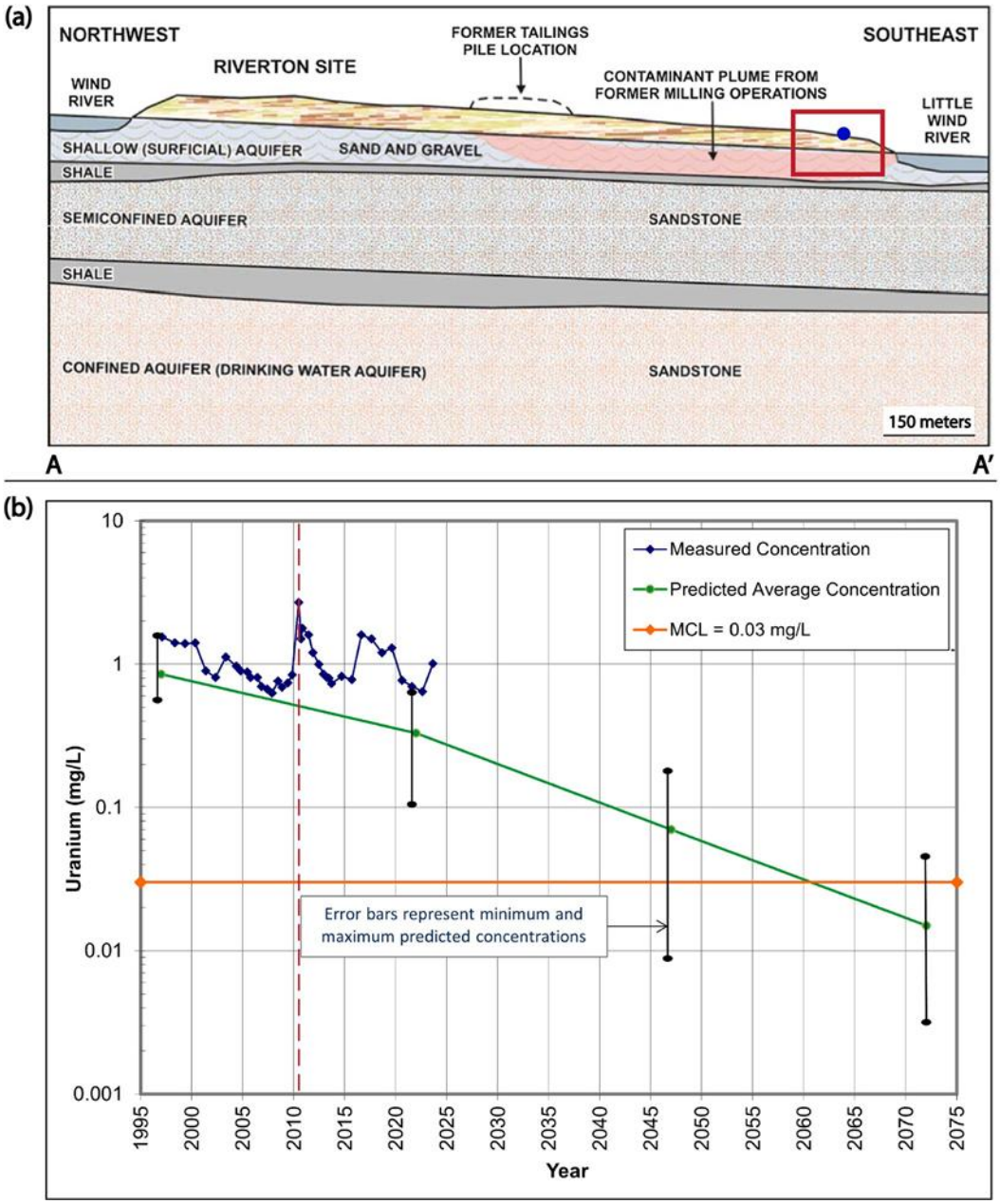

Fig. 3.1 (a) Cross-sectional area, AA' of the study area (Fig. S1) (Dam et al., 2015). The red rectangle shows the downgradient location where the two field experiments were performed. The blue dot shows the approximate location of the flood basin (Fig. 2). (b) Comparisons between the GANDT model predictions and actual groundwater concentrations at Riverton, WY, in 1998. Uranium concentration spike in groundwater during flooding in 2010 is indicated by red dotted line. (For interpretation of the references to colour in this figure legend, the reader is referred to the web version of this article.)

Given the arid climate and dry summer in Riverton, evaporite deposits are prevalent especially in the upper vadose zone due to high evapotranspiration, particularly along south-facing riverbanks on the north side of the Little Wind River (Looney et al., 2014; U.S.

Department of Energy, L.M, 2014). These deposits, primarily consisting of halite (NaCl), blo¨dite ($Na_2Mg(SO_4)_2{\cdot}4(H_2O)$), and thenardite ($Na_2SO_4$) are widespread in the vadose zone (Management, 2016). The sulfate- bearing evaporites collected along the river in 2014 (Fig. S2) indicated uranium (0.0014 to 0.066 g/kg), and sulfate (5.4 to 2200 g/kg) from following strong acid digestion of the evaporite samples (Management, 2016; U.S. Department of Energy, L.M, 2014). Based on the data, previous researchers suggested that these evaporite minerals pre- sent in the vadose zone could serve as a secondary source of persistent contaminant plumes (Dam et al., 2015; Johnson et al., 2016).

Prior to conducting our flooding experiments in 2020 (August 3–October 4) and 2021 (August 1–September 10), an in-situ tracer injection experiment directly to the aquifer was performed in 2020 (July 17–July 31) within the same area of interest as our study (Fig. 3.2). The goal of the injection experiment was to investigate contaminant (uranium) behavior solely in the aquifer during a flood (Paradis et al., 2022a). The injection experiment was initiated by directly injecting traced river water into the groundwater through well 1001 (Fig. 3.2b). The injection phase was followed by sampling and analysis of the tracers in the 13 monitoring wells (Fig. 3.2b) under natural-gradient conditions for 18 days.

In the present study, contaminant mobility is investigated through two tracer flooding experiments with river water (flood water) percolating through the vadose zone and downward into the groundwater.

3.2.2 Experimental flooding events

Two tracer field experiments (Table 3.1), each simulating a flooding event, were conducted near the banks of Little Wind River, Riverton, WY (Fig. 3.1). A series of 13 temporary monitoring wells (Fig. 3.2) were installed by direct push and screened across the

water Table A 3 m (m) diameter basin was placed upgradient of the wells. About 8 m^3 of river water (flood water) was filled in an infiltration tank (Fig. 3.1). Specific field and laboratory measurements with corresponding instruments and the relevant information of added tracers and alkalinity are listed in Table S1 and Table S2. The hydrochemistry of the river water (flood water) was different in composition than that of groundwater (Table S3). The typical depth of the water table was between 2 and 2.5 m below ground surface (bgs) during the experiments. The wells were installed as three transects oriented perpendicular to groundwater flow, i.e., southwest to northeast. The target screen interval for the temporary gallery wells was between 2 and 3.5 m bgs. The total distance between the first and last transects was 3 m with uniform spacing in between wells to allow for the transport of the tracer to be completed within a reasonable timeframe. Borehole dilution, slug testing, and groundwater pumping tests were completed before any tracer testing to get ground- water hydraulic conductivity estimates (U.S. Department of Energy, 2023). The average linear groundwater velocity was estimated at 0.2 to 0.3 m/day from a field tracer test performed prior to the injection experiment and our flooding experiments to investigate physical properties (groundwater velocity and matrix diffusion) of the uranium-contaminated aquifer (Paradis et al., 2022b). Matrix diffusion affects the migration of contaminants from the mobile zone to adjacent immobile zones of the porous matrix and vice versa, thereby impacting contaminant travel times by spreading contaminants over a larger vol-ume of the subsurface (Paradis et al., 2020).

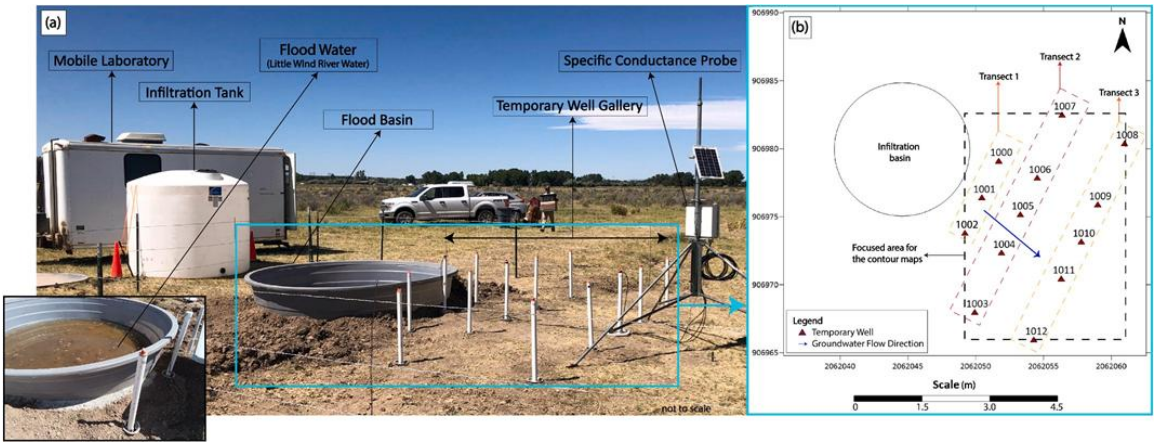

Fig. 3.2 13 monitoring wells and a flood basin at the experimental location and, (b) experimental set-up for two consecutive floodings at the site. The inset at the left bottom corner shows the flood basin with traced river water after initiating the experiment.

Table 3.1 Summary of two tracer field experiments conducted in 2020 (Flood-1) and 2021 (Flood-2).

Experiment	Water	Rate	Flooded	Tracers	Alkalinity	Sampled
(#)	Source (m^3)	(m^3/h)	(days)	Type (g)	Type (g)	(months)
Flood-1	Little Wind River (~8)	0.041	~8	Bromide (948) DFB (979)	None Added	≈2
Flood-2		0.027	~12	Iodide -2117	$NaHCO_3$ (20,000)	≈1

In Flood-1, two non-reactive solute tracers, lithium bromide (LiBr) and sodium 2,6 difluorobenzoate (NaDFB), each with different aqueous diffusion coefficients, were introduced into the flood water in the infiltration tank (Fig. 3.2a). The water from the tank was then pumped into the flood basin (Fig. 3.2a) using a peristaltic pump over a period of approximately 8 days. This process allowed the tracers to travel through the vadose zone and into the contaminant-rich unconfined aquifer. Difluorobenzoate has a much lower aqueous diffusion coefficient (7.2 × 10—

^{10} m^2/s) (Bowman and Gibbens, 1992) than bromide (21×10^{-10} m^2/s) (Callahan et al., 2000). The presence of matrix diffusion would result in a relatively lower peak concentration and longer mean arrival time of bromide than difluorobenzoate. Thus, the difference between the diffusion coefficient was used to characterize any mass transport of solutes from mobile to immobile zones due to molecular diffusion, i.e., matrix diffusion, in the groundwater (Paradis et al., 2020). However, the non-reactive tracers, bromide, and difluorobenzoate, employed in Flood-1 demonstrated similar behavior (Fig. S3), suggesting negligible matrix diffusion in our study. Since there was no discernible difference between the transport behavior of two tracers, bromide was selected for discussions pertaining to Flood-1. Following the completion of Flood-1 in summer 2020, Flood-2 was performed in summer 2021 at the same location. Flood-2 was done with added alkalinity, sodium bicarbonate ($NaHCO_3$), to investigate its influence on uranium mobility. A different artificial non-reactive solute tracer, sodium iodide (NaI) was used in Flood-2 to differentiate between Flood-1 and Flood-2 when analyzing the traced groundwater. NaI and $NaHCO_3$ were added to flood water similarly as Flood-1 and flooded into the basin for about 12 days. Notably, before both flooding experiments, an injection experiment was performed directly into the same aquifer as this study (Paradis et al., 2022a; U.S. Department of Energy, 2023). This injection experiment applied NaI and potassium pentafluorobenzoate (KPFB) to study contaminant release solely from the aquifer. The experiment did not observe any difference in the behavior of iodide and pentafluorobenzoate (Fig. S4), suggesting that iodide behaved conservatively during the injection experiment. Daily static water levels were measured, and samples were collected via peristaltic pumps under low- volume and low-flow conditions at 100 mL/min. Samples were measured immediately for temperature, specific conductance, pH, dissolved oxygen (DO), ferrous iron, alkalinity, and oxidation-reduction potential. Laboratory

analyses for uranium and other metals was completed at the U.S. Department of Energy Office of Legacy Management Environmental Sciences Laboratory, Los Alamos National Laboratory and University of Wisconsin-Milwaukee. More detailed information on the field methods is available in the relevant documentation for the study (U.S. Department of Energy, 2023).

3.2.3 Data analyses

3.2.3.1 Temporal Analyses

Breakthrough curves of potentially reactive solutes, chloride (Cl), uranium (U), sulfate (SO_4), sodium (Na), magnesium (Mg), potassium (K), calcium (Ca), manganese (Mn), and molybdenum (Mo), were con- structed and plotted for concentrations in groundwater (pre flooding), observed (during and post flooding), expected, and flood water (infiltrated river water). Breakthrough curves for Fe^{2+} were not considered due to being below the detection limit (0.03 mg/L). Similarly, the total Fe (Fe^{2+}+Fe^{3+}) data was disregarded due to its noisy signals. The breakthrough curves of non-reactive added tracers, bromide (Br) in Flood-1 and iodide (I) in Flood-2 were not constructed explicitly since their concentrations were used to calculate the expected concentrations of the reactive solutes (Paradis et al., 2019). Moreover, in Flood-1, bromide and difluorobenzoate behaved similarly so only bromide concentrations were used to analyze expected concentration in Flood-1. In the context of our experimental design, where flood water with low solute concentration (Table S2) was mixed with groundwater with high solute concentration, the potential reactive solutes would be expected to be diluted, if no reaction occurred (Paradis et al., 2020). Thus, the breakthrough curves of a solute are bound by the flood water in the lower concentrations and groundwater in the upper concentrations; with the expected concentrations being between the two boundaries. The expected concentrations are based on the behavior of added non- reactive tracers, namely bromide for Flood-1 and iodide for Flood-2.

The expected concentration assumes that the solutes in groundwater would behave as added non-reactive tracers and thus only be dominated by advection and dispersion during floodings (Paradis et al., 2019). When plotted on the same graph, any difference between observed and expected breakthrough curve will indicate reactivity of the solute. For an evaluation of solutes being added or removed from the groundwater, an observed concentration greater than the expected concentration indicates constituent addition, and vice versa (Paradis et al., 2020). The expected concentrations were determined using Eq. (11) from Paradis et al. (2019). The equation generates the expected concentration of a potentially reactive solute due to dilution occurred upon mixture of low concentration flood water and high concentration aquifer fluids. More detailed derivation and parameters of the expected concentration equation and its assumptions can be found in Paradis et al. (2019).

While the above-mentioned approach is a qualitative measure of reactivity, a quantitative measurement of reactivity and subsequent mechanisms was done using relative temporal moment analysis (TMA) (Paradis and Sultana, 2024). The principle of relative TMA is to evaluate the behavior of solutes in a system by analyzing their temporal distribution; all without the need to solve the advection-dispersion-reaction equation or modify true concentrations. This relative approach involved calculating the ratio of observed to expected zeroth temporal moments, the ratio of observed to expected normalized first temporal moments, and the ratio of observed to expected normalized second temporal moments via Eqs. (21), (22), and (23), in Paradis and Sultana, 2024. The zeroth moment measures the area underneath the break- through curve. The normalized first moment is the first moment divided by the zeroth moment and indicates the center of mass in time [T]. Likewise, the normalized second moment is the second moment divided by the zeroth moment and represents the spread in time squared [T^2]. Finally,

the ratio calculations resulted in unitless and dimensionless temporal moments, which are relative zeroth moment (M_o), relative first moment (M_1) and relative second moment (M_2). More detailed derivation and parameters of the relative moment equations can be found in Paradis and Sultana (2024).

M_o,M_1, and M_2 were applied to calculate the mass, advection and dispersion, respectively for all potential reactive solutes and added tracers. $M_o > 1$ indicates a net addition of solute mass to the aqueous phase, whereas $M_o < 1$ indicates a net removal; $M_o = 1$ indicates no net addition or removal. Similarly, $M_1 \neq 1$ indicates a change in solute advection and $M_2 \neq 1$ indicates a change in solute dispersion. The overall reactivity of a reactive solute, reactivity index (RI), can be quantified by calculating the weighted residual sum of squares for each of the three relative moments from Eq. (24) in Paradis and Sultana, 2024. In theory, RI = 0 indicates no reactivity whereas RI > 0 indicates reactivity; negative RI values of RI is not viable. Equal moment weights for mass, advection, and dispersion ($\omega_0 = \omega_1 = \omega_2 = 1$), and a multiplication factor (f) of 1000 were applied. The weights (ωi) and multiplication factor (f) in Eq. (24) are chosen by the user. The weights (ωi) can vary depending on how much weight to put on reactions that affect mass (M_o), advection (M1), and dispersion (M2). The multiplication factor (f) can typically be some factor of 10, e.g., 10, 100, 1000, etc., to avoid decimals and ensure whole numbers which are easier to comprehend, making negative values of the multiplication factor not viable. However, it is important to consider the relative reactivity among k^{th} solutes while approximate these numerical approaches.

3.2.3.2 Mass Calculation

Transect-wise mass calculation was completed for reactive solutes (U, Cl, SO_4, Na, Mg, K, Ca, Mn, Mo) and tracers (Br and I). Due to being below the detection limits (0.03 mg/L),

transect-wise mass for Fe^{2+} could not be calculated. The total Fe (Fe^{2+}+Fe^{3+}) data was also not considered due to its noisy signals. Thus, considering Fe^{2+} or total Fe data for the mass calculation was of limited usefulness. For other reactive solutes, both observed and expected mass going through a transect was calculated. Among the three transects (Fig. 3.2), Transect-2 had the maximum number of wells with substantial signals from the tracers during our study. Thus, in this study, the mass calculation will be dis- cussed for transect-2. It is to be noted that, well no. 1007 was excluded while calculating transect wise mass since it did not have any detectable tracer signal. The mass of solutes going through transect-2 was deter- mined in two steps. First, the Theissen Polygon Method (TPM) (Mackay et al., 2012) was used to calculate the mass discharge of the solutes going through transect-2. The density (1.08 points/m^2) and the distance between the wells (average 0.08 m) in transect-2 were in agreement (Mackay et al., 2012) to ensure TPM calculation accuracy. In the TPM calculation at our site, while the concentration varied in each scenario, the hydraulic conductivity (1.8 m/day) and hydraulic gradient (0.03) were assumed constant. The hydraulic conductivity was calculated based on groundwater velocity (0.18 m/day) at the site (Paradis et al., 2022b), hydraulic gradient (0.03) and porosity (0.3) of the sandy groundwater. Finally, the mass of each solute was determined by calculating the area under the breakthrough curve of the calculated mass discharge of the respective solutes. The time duration (40 days) was kept constant, and the mass discharge was kept similar for each solute in both the experiments. An analytical error of 10% was applied to all the calculated values. The percentage was selected as it aligns with standard practices in similar studies (Paradis et al., 2022a), where a 10% margin is commonly accepted as reasonable.

3.2.3.3 Spatial Analysis

The contoured maps for both observed and expected solute concentrations were constructed using the anisotropic kriging interpolation method in Surfer version 24 (Surfer® from Golden Software, LLC, www. goldensoftware.com). Due to the skewed distribution of tracer and chloride concentration data, the concentrations were log transformed prior to creating the grid file in Surfer (Ricker, 2008) and then inverse log transformed before plotting. The center mass of the tracer plumes was calculated (Ricker, 2008) and plotted after filtering data to include concentrations greater than approximately 10% of the initial concentration added with flood water.

All the data processing and analyses were performed using Microsoft Excel 2016 and Python (version 3.11.3).

3.3 Results and discussions

The experimental results and their interpretations are presented in the following sections that start with (1) plume distribution maps of added tracers, uranium and chloride in the experimental location (Section 3.1.1), (2) observed and expected breakthrough curves of chloride (Section 3.1.2), and uranium and sulfate (Section 3.1.3), along with transect-wise mass calculation of non-reactive added tracers and potentially reactive solutes (U, Cl, SO_4, Na, Mg, K, Ca, Mn, and Mo) (Section 3.1.3), (3) identifying hydrogeological compartment that is responsible for mobilization of solutes (Section 3.2), (4) mobilization mechanisms with moment analyses, M (zeroth moments, relative first and relative second moments) with reactivity indices (RI) (Section 3.3 with results from the two flooding experiments summarized in Table 2), and (5) evaluating the impact of added alkalinity as a remediation effort (Section 3.4). Finally, our experimental data were combined with previous solid-phase data on evaporites (U.S. Department

of Energy, L.M, 2014), and direct injection experimental data (Paradis et al., 2022a) to support possible contaminant mobilizing and mechanistic insights.

3.3.1 Mass mobilization of solutes

3.3.1.1 Plume distribution maps of added tracers, uranium, and chloride

During Flood-1, the flood water contained bromide as an added tracer and infiltrated for about 8 days (Table 3.1) through the flood basin (Fig. 3.2). The center of mass of the resulting plume moved in a south-east (SE) direction, with notable concentrations detected in monitoring wells 1001, 1005, and 1011 post flooding (Fig. 3.3a). Tracer mass calculations revealed that about 23% (218 g) of the total bromide mass (949 g) passed (Fig. S5) across transect-2 (Fig. 3.2) during the flooding, with higher masses observed in wells 1001, 1005, and 1011 (Fig. S6). Bromide isocontours illustrated a relatively consistent distribution of the flood water which is evident in both spatial (Fig. 3.3a) and temporal (Fig. S3) patterns. The spatial and temporal extent with elevated signals across the three transects of the well gallery (Fig. 3.3a) implied that a significant volume of flood water traversed the experimental site during the experiment.

Before Flood-1, uranium exhibited a uniform distribution, with concentrations ranging from 0.88 to 1.12 mg/L in the groundwater (Fig. 3.3b). However, following the flooding, uranium concentrations increased, ranging from 0.89 to 1.51 mg/L on day 15 (Fig. 3.3c). The flood water had a negligible uranium concentration (0.01 mg/L) than the groundwater uranium concentration (mean = 0.97 mg/L). Consequently, the observed uranium concentration would be expected to be diluted, ranging from 0.41 to 1.09 mg/L (Fig. 3.3d). Instead of being diluted as expected, higher uranium concentrations were detected along the path of the flood water, suggesting significant uranium mobilization during the flooding, eventually entering the groundwater (Fig. 3.3e). The distribution and direction of the added uranium in the groundwater corresponded to that of bromide, indicating uranium addition during the flooding. Additionally,

chloride exhibited a similar pattern to uranium, further suggesting mobilization of potentially reactive solutes during the flooding event (Fig. 3.3f).

During Flood-2, the flood water contained iodide as an added tracer and infiltrated for

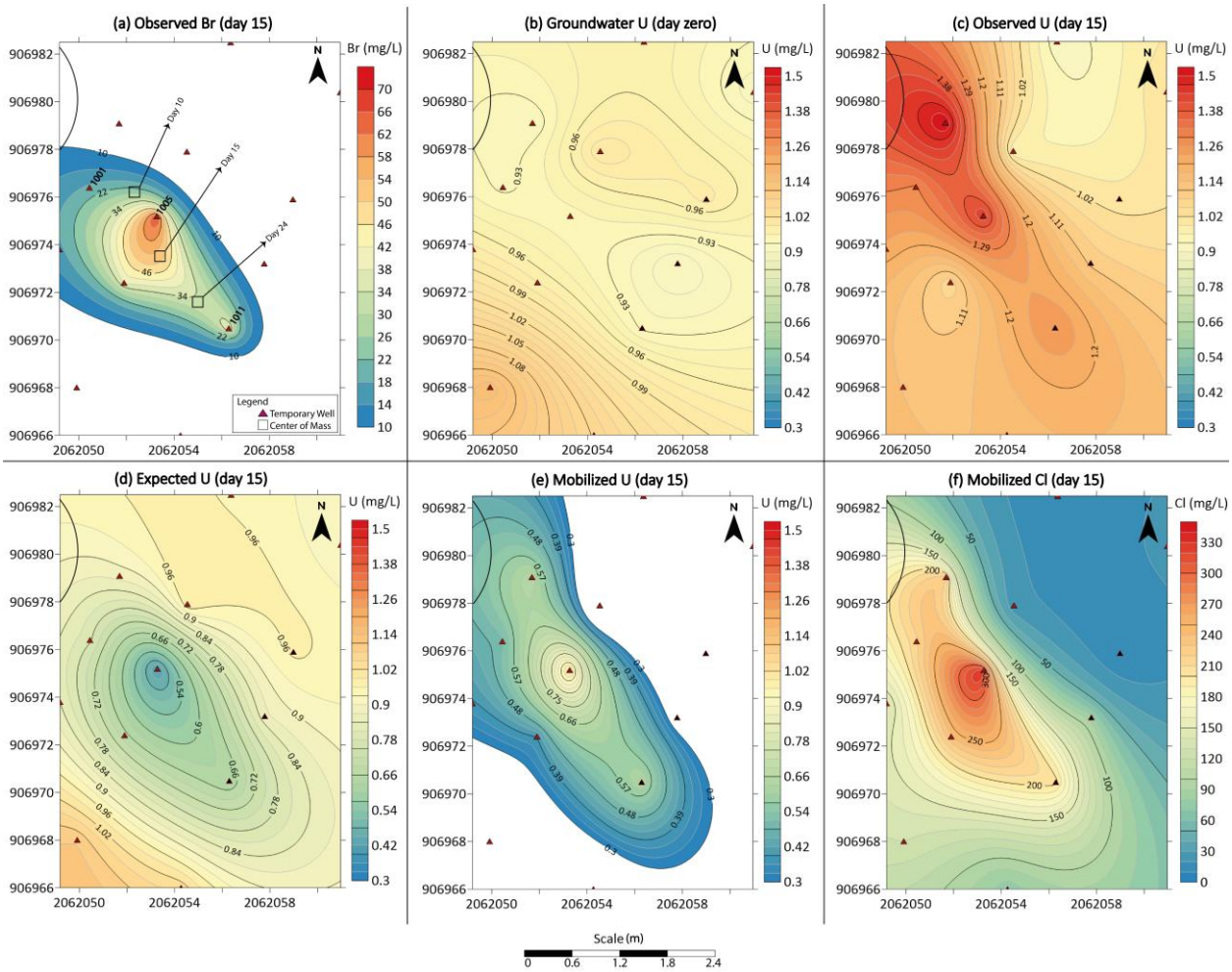

Fig. 3.3 (a) Homogenous bromide (Br) isocontours after flooding, (b) homogeneous uranium (U) distribution before flooding, (c) elevated observed uranium concentration after flooding, (d) diluted expected uranium (U) after flooding, (e) mobilized uranium (U) during flooding, (f) mobilized chloride (Cl) during flooding. It is noteworthy that uranium (0.01 mg/L) and chloride (14 mg/L) concentrations were very low in flood water compared to that of groundwater (uranium = 0.97 mg/L and chloride = 422 mg/L). The semi-circle at the upper left of each figure indicates the location of the flood basin. The plume maps are skewed to SE direction, in line with groundwater flow direction.

about 12 days (Table 3.1) through the flood basin (Fig. 3.2). The center of mass of the resulting plume followed a southeast direction, with elevated iodide signals detected in monitoring wells 1000, 1005, and 1010 post flooding (Fig. 3.4a). Tracer mass calculations revealed that about

28.3% (600 g) of the total infiltrated iodide mass (2118 g) passed across transect-2 (Fig. 3.2) during Flood-2 (Fig. S5), with higher masses observed in wells 1000, 1005, and 1010 (Fig. S6). Unlike bromide in Flood-1, iodide isocontours illustrated a heterogeneous behavior across the site in Flood-2 (Fig. 3.4a). The heterogeneity was also evident in the breakthrough curve patterns with double hump pattern in the breakthrough curves (Fig. S3). Despite the heterogeneity observed during Flood-2, the spatial (Fig. 3.4a) and temporal (Fig. S3) extent of iodide with elevated signals across the three transects of the well gallery suggested that a significant volume of flood water passed through the experimental site.

Before Flood-2, uranium concentration in groundwater ranged from 0.84 to 1.08 mg/L with a homogenous distribution in the groundwater (Fig. 3.4b). The data indicated that aqueous uranium concentration reached a similar range as the first flooding (Flood-1) before initiation of Flood-2. Following the initiation of Flood-2, the aqueous uranium con- centration increased, ranging from 0.85 to 1.41 mg/L with higher values being concentrated along the flood water path (Fig. 3.4c). Similar to Flood-1, flood water during Flood-2 had a lower uranium concentration (0.01 mg/L) than that of groundwater (mean = 0.94 mg/L). Consequently, the uranium concentration in the groundwater after the experiment would be expected to be diluted, ranging from 0.34 to 1.06 mg/L (Fig. 3.4d). However, the observed uranium concentration did not behave as expected, indicating a substantial amount of uranium was mobilized and added (Fig. 3.4e) to the groundwater during the experiment. The plume pattern and direction of the mobilized uranium in the groundwater corresponded to that of iodide, indicating uranium was mobilized and added during the flooding. Furthermore, chloride was also observed to be mobilized in a similar pattern to uranium (Fig. 3.4f). While much lower chloride mobilized during Flood-2 compared to Flood-1, the area of higher concentration of the chloride plume

corresponded to that of iodide and uranium, indicating that the chloride was mobilized during Flood-2. These results reinforced the concept of contaminant mobilization during flooding events.

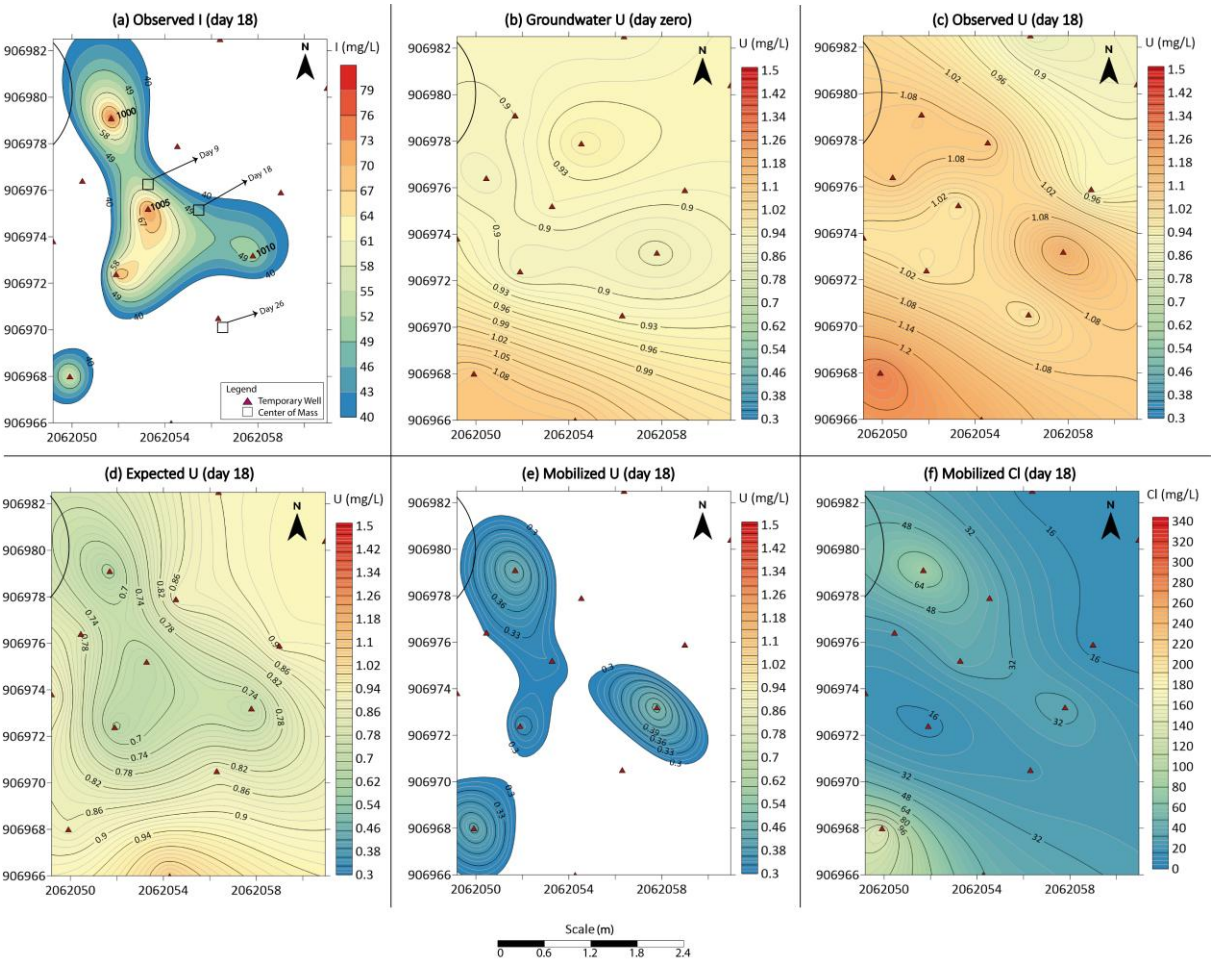

Fig. 3.4 (a) Heterogenous iodide (I) isocontours after flooding, (b) homogeneous uranium (U) distribution before flooding, (c) elevated observed uranium concentration after flooding, (d) diluted expected uranium (U) after flooding, (e) mobilized uranium (U) during flooding, (f) mobilized chloride (Cl) during flooding. It is noteworthy that uranium (0.01 mg/L) and chloride (66 mg/L) concentrations were very low in flood water compared to that of groundwater (uranium = 0.94 mg/L and chloride = 328 mg/L). The semi-circle at the upper left of each Fig. indicates the location of the flood basin. The plume maps are skewed to SE direction, in line with groundwater flow direction.

3.3.1.1 Chloride breakthrough curves

During Flood-1, the signal of the observed breakthrough curve was notably stronger at well 1001, gradually decreasing in wells 1005 and 1011. However, the observed and expected breakthrough curves of chloride differed across the transects during Flood-1 (Fig. 3.5). These results suggested that mass transport characteristic of chloride was different than that of added tracer (bromide) and chloride mobilization was controlled by mechanisms other than advection and dispersion during the flooding (Paradis et al., 2019). Furthermore, observed chloride concentrations exceeded expected concentrations in all three wells (Fig. 3.5). The results indicated a net addition of chloride in the ground- water during the flooding event (Paradis et al., 2019) that resulted in approximately 29% chloride mass increase in groundwater (Fig. 3.8).

During Flood-2, the signal of the observed breakthrough curve was relatively stronger at well 1000, gradually decreasing in wells 1005 and 1010. Similar to Flood-1, the observed and expected breakthrough curves of chloride were not identical throughout the transects during Flood-2 (Fig. 3.5). Consistent to results obtained in Flood-1, these observations indicated that mobility of chloride differed from than that of added tracer (iodide) and the mobility was controlled by mechanisms other than advection and dispersion during the flooding (Paradis et al., 2019). Additionally, Fig. 3.5 indicated that after approximately 5 days, the observed breakthrough curves of chloride aligned closely with expectations, suggesting dilution occurred after this period during Flood-2. Moreover, the observed chloride concentrations did not substantially exceed the expected concentrations, as seen in Flood-1 in all three wells (Fig. 3.5). The results indicated that despite a net addition of chloride resulting in about 10% chloride mass

increase in groundwater (Fig. 3.7), there was a considerable decline in chloride mass during Flood-2 compared to Flood-1.

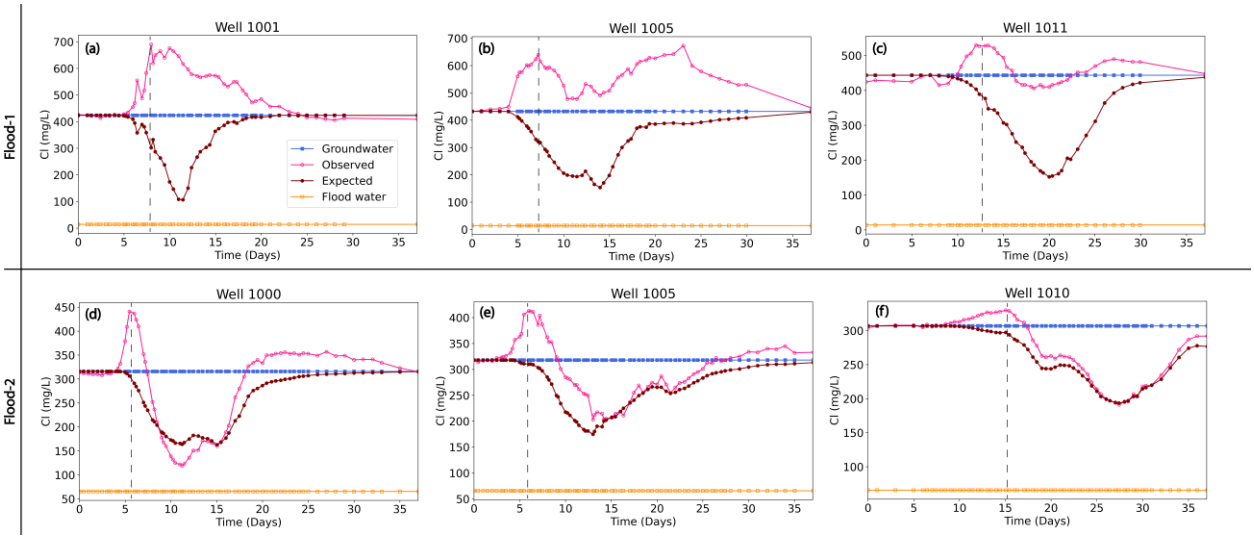

Fig. 3.5 Chloride breakthrough curves in (a) well 1001 (transect-1), (b) well 1005 (transect-2), and (c) well 1011 (transect-3) during Flood-1; (d) well 1000 (transect- 1), (e) well 1005 (transect-2), and (f) well 1010 (transect-3) during Flood-2. The dashed line shows the arrival times of the maximum concentrations of the 'observed' breakthrough curves.

3.3.1.3 Uranium and sulfate breakthrough curves

The signal of the observed breakthrough curve was relatively stronger at well 1001, gradually decreasing in wells 1005 and 1011 for both contaminant species (uranium and sulfate) (Fig. 3.6 and Fig. 3.7). The observed and expected breakthrough curves of the contaminants were not identical throughout the transects during Flood-1 (Fig. 3.6 and Fig. 3.7). These results suggested that the mobility of the contaminants during Flood-1 was dissimilar to that of the added tracer (bromide), indicating that other mechanisms beyond advection and dispersion controlled their mobility during the flooding event (Paradis et al., 2019). Moreover, the breakthrough curves of observed uranium and sulfate concentrations exceeded the expected curves during the event (Fig. 3.6 and Fig. 3.7), indicating a net addition of the contaminants (Paradis et al., 2019). The net addition resulted in approximately 21% of uranium and 24% of sulfate mass increase in groundwater (Fig. 3.8).

Similar to Flood-1, the observed and expected breakthrough curves of the contaminants (uranium and sulfate) differed from each other in all three wells during Flood-2 (Fig. 3.6 and Fig. 3.7). These results indicated that the mobilization of uranium and sulfate was different than that of added tracer (iodide), and the mobility was controlled by mechanisms other than advection and dispersion during the flooding (Paradis et al., 2019). Similar to Flood-1, the observed uranium concentration exceeded significantly than expected concentrations during Flood-2. The results indicated a net addition of contaminants which caused about 24% of uranium and 25% of sulfate mass increase (Fig. 3.8) in groundwater during Flood-2.

Similar to chloride, uranium, and sulfate, the mobilization of other potentially reactive solutes (Na, Mg, K, Ca, Mo) differed from that of the added tracers during flooding events, indicating a net addition to the groundwater (Fig. 3.8). However, a substantial reduction in manganese mass was observed during both flooding events (Fig. 3.8). Other redox sensitive ion, iron (Fe^{2+}) revealed a notably low concentration of 0.42 mg/L in well 1001 (Fig. 3.2), which gradually decreased below detection limit of 0.03 mg/L along the transects during both flooding experiments. It is possible that the flooding of oxygenated river water (ORP = 103 mV in Flood-1 and ORP = 207 mV in Flood-2) caused manganese and iron (Fe^{2+}) to eventually precipitate or get adsorbed within sediments (Aiken and Ying, 2023; Singh et al., 2014).

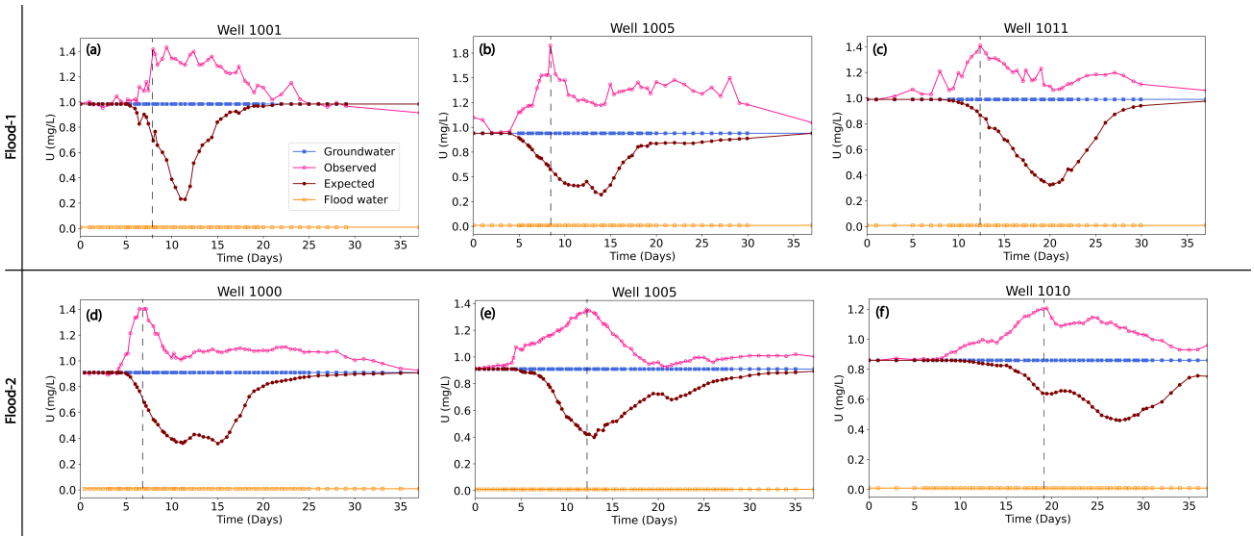

Fig. 3.6 Uranium breakthrough curves in (a) well 1001 (transect-1), (b) well 1005 (transect-2), and (c) well 1011 (transect-3) during Flood-1; (d) well 1000 (transect- 1), (e) well 1005 (transect-2), and (f) well 1010 (transect-3) during Flood-2. The dashed line shows the arrival times of the maximum concentrations of the 'observed' breakthrough curves.

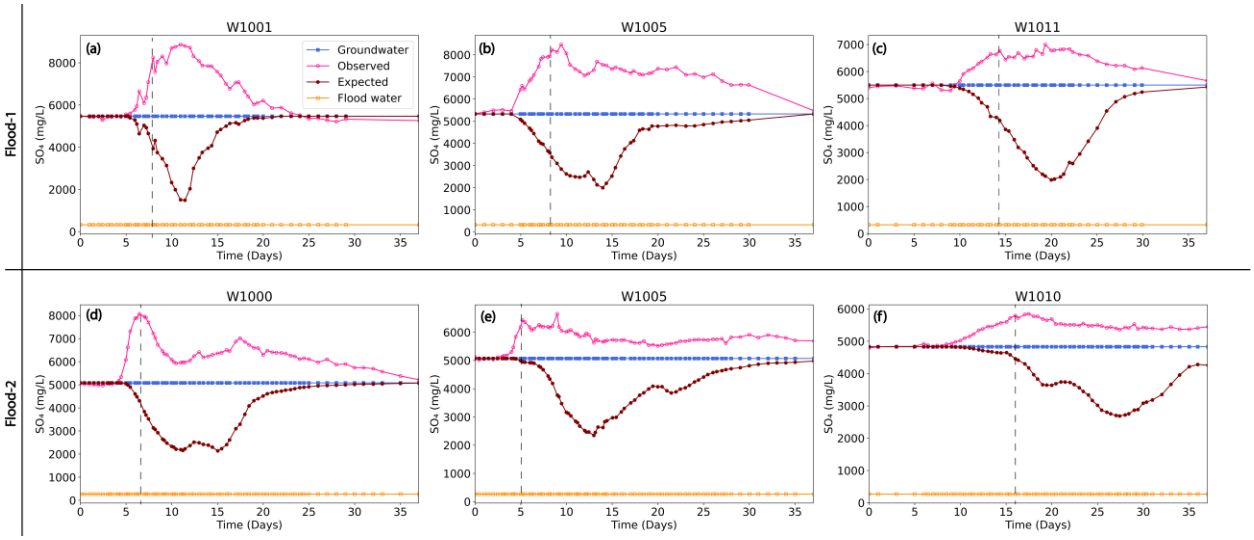

Fig. 3.7 Sulfate breakthrough curves in (a) well 1001 (transect-1), (b) well 1005 (transect-2), and (c) well 1011 (transect-3) during Flood-1; (d) well 1000 (transect-1), (e) well 1005 (transect-2), and (f) well 1010 (transect-3) during Flood-2. The dashed line shows the arrival times of the maximum concentrations of the 'observed' breakthrough curves.

3.3.2 Mobilizing hydrogeological compartment

Our study area is characterized by two compartments (Fig. 3.9) which are an overlying vadose zone and an underlying groundwater (Dam et al., 2015). The injection experiment (mentioned in Section 3.2.1), conducted directly into the aquifer prior to our flooding experiments, found that the potentially reactive solutes (chloride, uranium, sulfate, sodium, magnesium, potassium, calcium, and molybdenum) behaved conservatively as expected, except for manganese and iron in the aquifer (Paradis et al., 2022a). The study concluded that these reactive solutes (except for manganese and iron) in the aquifer sediments were non- reactive and did not get mobilized upon direct injection to the ground- water. In contrast, during our flooding experiments, where the flood water travelled through the vadose zone (Fig. 3.9) before entering the groundwater, mobilization of reactive solutes and the addition of the solute mass to the groundwater were observed (Fig. 3.8). The results from our study suggested that while manganese and iron decreased their mobility during the floodings, all other potentially reactive solutes, exhibited reactivity and increased mobilization, resulting in a substantial release of these solutes into the groundwater during the flooding experiments (Fig. 3.8). The contrast between the findings of the previous study (Paradis et al., 2022a) and our analyses indicated that mass mobilization during the flooding experiments occurred primarily from the vadose zone and not from the aquifer. The results are in line with the three-year multilevel groundwater monitoring data report at our study site, Riverton (U.S. Department of Energy, 2019). The report showed that the concentration of the reactive solutes in shallow groundwater increased during large flooding events in 2010, 2016 and 2017, near the Little Wind River (Fig. S1). However, the groundwater quality remained unchanged during monitoring in 2018 when no flooding or extreme recharge events occurred. The results from our study and well monitoring indicated that vadose zone is the key hydrogeological compartment that served as a storage for contaminants

before the flooding events and that the contaminants were substantially mobilized from the vadose zone during the events.

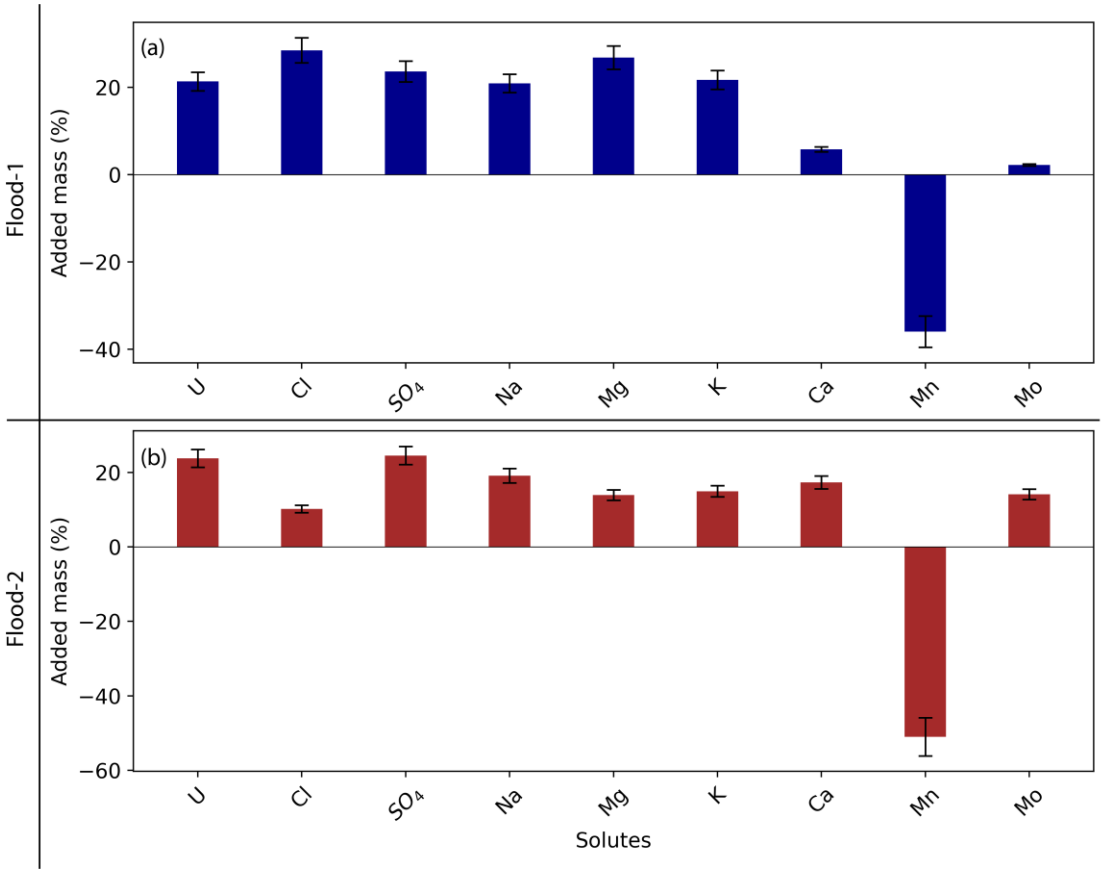

Fig. 3.8 Added (U, Cl, SO4, Na, Mg, K, Ca, Mo) and removed (Mn) of potentially reactive solutes during (a) Flood-1 and (b) Flood-2 in transect-2.

3.3.3 Mobilizing mechanisms

3.3.3.1 Physical Mechanism

During Flood-1, the observed breakthrough curves of the contaminants (uranium, and sulfate) along with chloride exhibited a gradual arrival of a peak throughout the transects (Fig. 3.5, Fig. 3.6, and Fig. 3.7). The arrival of the peak of observed chloride, uranium and sulfate break- through curves was approximately 4 days earlier in well 1001, and about 3 days earlier in well 1005 and about 7 days earlier in well 1011 than that of expected (Fig. 3.5, Fig. 3.6, and Fig.

3.7). These data suggested that chloride, sulfate, and uranium arrived earlier than the tracer-induced flood water during Flood-1.

During Flood-2, the observed breakthrough curves of contaminants (uranium, and sulfate) along with chloride exhibited a rapid arrival of a peak in well 1000. The peak concentration became gradually less pronounced in wells 1005, and 1010 (Fig. 3.5, Fig. 3.6, and Fig. 3.7). The peak of observed chloride concentrations arrived about 6 days earlier in well 1000, 7 days earlier in well 1005, and 3 days earlier in well 1010 than that of expected (Fig. 3.5). The peak of observed uranium concentrations arrived about 4 days earlier in well 1000, about 1 day earlier in well 1005 than that of expected, and almost at the same time as the expected in well 1010 (Fig. 3.6). The peak of observed sulfate concentrations arrived about 4 days earlier in well 1000, 7 days earlier in well 1005, and 2 days earlier in well 1010 than that of expected (Fig. 3.7). These data suggested that chloride, uranium, and sulfate arrived earlier than the tracer-induced flood water during Flood-2.

The early arrival of the peak concentrations during both floods can be explained by the action of a compression wave that propagate through saturating density-driven fluid (Gross et al., 2003). During a flooding event, the arrival of flood water at the surface causes an abrupt pressure change, that subsequently generates the compression wave. Such abrupt pressure changes often occur at the wetting fronts of floodings (Amiaz et al., 2011; Dahan et al., 2008). In our flooding ex- periments, the wetting fronts were indicated by the arrival of the non- reactive tracers in the expected breakthrough curves (Fig. 3.5, Fig. 3.6, and Fig. 3.7). The compression wave, in turn, enhances the advection of solute and can cause abrupt solute-displacement in the groundwater (Amiaz et al., 2011). The mechanisms are also suggested by mathematical models developed for compressible fluid (Sorek and Bear, 1990) and compressible fluid with a solute in saturated

porous media, following the onset of an abrupt pressure change (Sorek, 1996). These mechanisms can be attributed to wave-driven transport, regardless of saturated or unsaturated conditions (Amiaz et al., 2011). Moreover, Warrick et al., 1971 theoretically and experimentally showed solute displacement in the vadose zone with percolating water where the displacement is highly dependent on the moisture content at the soil surface during infiltration.

In view of the previous studies, the results from our study suggested that contaminant-rich pore water in the vadose zone (Fig. 3.9) could be impacted by the propagating wave, thereby generating the peak ahead of the tracer-induced flood water. In addition, the pore water can accumulate a significant amount of contaminants that become more concentrated in the variably saturated zone and gradually dilutes closer to the water table (Du Laing et al., 2007; Nativ et al., 1995). Therefore, in our flooding experiments, it is plausible that the tracer-induced flood water generated the compression wave upon arrival the surface and subsequently propelled solute-concentrated pore water above the water table (Fig. 3.9) and then into the groundwater, leading to the earlier arrival of the solute pool.

3.3.3.2 Chemical mobilization

During Flood-1, the breakthrough curves of chloride, uranium, and sulfate (Fig. 3.5, Fig. 3.6, and Fig. 3.7) showed a sustained elevated concentration for the duration of the flooding. The data suggested that an additional mobilization mechanism was prominent for all three solutes during the flooding event. The reactive mobilization was further quantified via relative temporal moment analysis (Paradis and Sultana, 2024) of the solute breakthrough curves. These relative moments (M) characterize mass (M_o), advection (M_1), and dispersion (M_2) of a solute with numeric values. The numerical values indicate the dominant mobilization mechanism of a solute and measure its reactivity with reactivity index (RI). In addition, such values identify solutes

with similar transport mechanisms to further understand their potential mechanisms of reactive transport.

Analysis of the relative moments for bromide, a non-reactive tracer, yielded expected results, with its relative moments (M) equal to one and a reactivity index (RI) of zero, indicating no reactivity throughout the transects (Table. S4). However, for the reactive solutes, M_o were significantly greater than 1, with M_1 and M_2 moments were closer to 1 and RI greater than zero (Table. 3.2). The RI values suggested reactivity of the solutes that is attributed to their reactive mass mobilization based on M_o values, during Flood-1. These findings align with breakthrough curve observations and the added mass of the solutes (Fig. 3.8). In addition, the values of M_o, M_1 and M_2 of chloride, uranium, and sulfate were almost similar throughout the transects with reactivity indices closer in values in well 1001 than others (Table. 3.2). The data suggested that the additional mass mobilization mechanism for chloride and the contaminants (uranium and sulfate) were similar to each other during the flooding event.

During Flood-2, the breakthrough curves of uranium and sulfate (Fig. 3.6 and Fig. 3.7) consistently exhibited elevated concentrations throughout the flooding period. In contrast, the sustained elevated concentration of chloride was negligible after its initial peak arrival (Fig. 3.5). The difference suggested that while an additional mobilization mechanism was prominent for uranium and sulfate during Flood-2, it was not significant for chloride. The reactive mobilization was further quantified via moment calculation (Paradis and Sultana, 2024) of the solute breakthrough curves. Iodide, a non-reactive tracer, exhibited relative moments (M) equal to one and a reactivity index (RI) of zero in all three wells, as expected (Table S3). In contrast, for uranium and sulfate, the relative moments M_o was significantly greater than 1, while the relative M_1 and M_2 moments were closer to 1 with reactivity indices significantly greater than zero

(Table. 3.2). The results of RI indicated reactivity of the contaminants (uranium and sulfate) that could be attributed to their reactive mass mobilization based on the M_o values, during Flood-2. These results are consistent with the breakthrough curve observations and the added mass of the solutes (Fig. 3.8). In contrast, chloride exhibited relative moments, M_o that was not significantly greater than 1, and M_1 and M_2 closer to 1 with RI significantly closer to zero (Table. 3.2). The results of RI indicated that, unlike Flood-1, chloride was not significantly reactive during Flood-2, which was also evident in the breakthrough curves of chloride (Fig. 4). In addition, the values of M_o, M_1, M_2 and RI for the contaminants were almost similar throughout the transects, whereas these values for chloride was significantly different from that of contaminants. The results suggested that, while the additional mass mobilization mechanism for contaminants was similar during Flood-2, chloride behaved differently.

The additional mass mobilization mechanism during Flood-1 for chloride, uranium, and sulfate, and during Flood-2 for uranium and sulfate, can be explained by the generation of wetting fronts by flood water propagating downward through the vadose zone to the water table (Fig. 3.9) during flooding events (Dahan et al., 2008). During the dry seasons the sediments in the vadose zone accumulate high concentration evaporite salts (Fig. 3.9) due to evaporation of sediment pore water to a low water content (Amiaz et al., 2011). As recharge proceeds during the flooding events, percolating flood water through the vadose zone interacts with soluble salts and the flood water wetting front leaches out salts (Fig. 3.9) from the vadose zone (Amiaz et al., 2011). The evaporite salts, notably bearing chloride and sulfate, are highly soluble when in contact with water (Drever, 1982). Surface and subsurface evaporites with concentrated uranium were also observed in our study area (Johnson et al., 2016). The majority of these evaporites were sulfate- and chloride-bearing evaporites (U.S. Department of Energy, 2019) where sulfate

was present at an average of 85 g/kg with uranium concentrated at an average of 0.014 g/kg (U.S. Department of Energy, 2014). Therefore, it is possible that as the wetting front of the flood water was propagating during our flooding experiments through the vadose zone, it dissolved the precipitated sulfate- and chloride-bearing evaporites with concentrated uranium and subsequently released then into groundwater. The relative moments analysis and solid-phase data suggested that the additional mass mobilization was prominently via uranium-rich sulfate evaporite dissolution likely forming uranium-bearing evaporite couple such as $U(SO_4)_2$, UO_2SO_4, $UO_2(SO_4)_2^{2-}$, as identified from PHREEQC simulations, during both flooding events. Contaminant release from the evaporite dissolution was further supported by the release of other evaporite-related constituents (sodium, calcium, magnesium, and potassium) from the vadose zone during both flooding events (Fig. 3.8), which were likely in sulfate-bearing evaporite forms ($NaSO_4^-$, $CaSO_4$, $MgSO_4$, and KSO_4^-). The release of the evaporite-related constituents with uranium were also observed during larger flooding events occurred in 2016 and 2017 in Riverton (U.S. Department of Energy, 2019). In addition, the relative moments and reactivity indices of these evaporitic constituents were close to that of uranium, and sulfate during both floodings and with chloride during Flood-1 (Table. S4). These results further indicated uranium-rich sulfate evaporite dissolution as the predominant contaminant release from the vadose zone during both floodings, with chloride evaporites contributing primarily during Flood-1.

While both chloride- and sulfate-rich evaporite salts are soluble upon contact with water, chloride salts dissolve faster than sulfate salts during the re-solution stage (Drever, 1982). In contrast, chloride salts precipitate slower than sulfate salts during the dry stage (Armellini et al., 1994). Thus, it is possible that the chloride evaporite salts that were present in the vadose zone prior to our flooding experiments, dissolved away faster than sulfate evaporites during Flood-1.

There was a one-year interval between the two flooding experiments which might not be enough for chloride evaporite salts to fully precipitate in the vadose zone before Flood-2. Consequently, less chloride release was observed during Flood-2.

Table 3.2 Temporal moment analysis (M) of chloride (Cl), uranium (U), and sulfate (SO4) showing relative zeroth, relative first (M1) and relative second moment, about the mean (M2) with Reactivity Indices (RI)

		Well 1001			**Well 1005**			**Well 1011**		
	M	Cl	U	SO_4	Cl	U	SO_4	Cl	U	SO_4
Flood-1	M_o	1.26	1.25	1.26	1.52	1.66	1.54	1.25	1.40	1.34
	M_1	0.91	0.92	0.91	0.96	0.96	0.95	1.03	1.03	1.04
	M_2	0.87	0.87	0.87	0.82	0.81	0.82	0.84	0.80	0.80
	RI	9.13	8.23	9.39	29.9	47.81	32.87	8.86	20.10	15.47
	M	**Well 1000**			**Well 1005**			**Well 1010**		
		Cl	U	SO_4	Cl	U	SO_4	Cl	U	SO_4
Flood-2	M_o	1.09	1.42	1.45	1.11	1.40	1.35	1.04	1.39	1.31
	M_1	1.00	0.93	0.93	0.99	0.96	0.98	1.00	1.12	1.11
	M_2	0.97	0.86	0.85	0.99	0.86	0.88	0.98	0.91	0.95
	RI	1.02	20.09	23.19	1.16	18.21	13.96	0.17	18.13	10.89

3.3.4 Impact of added alkalinity

Since the primary contaminant at our study site is uranium (Dam et al., 2015), alkalinity was added during Flood-2 to determine whether this addition could remediate the contaminated site by accelerating uranium flushing from the vadose zone. Moreover, the accumulated secondary uranium mass that persists in the vadose zone, mostly in association with evaporites, can maintain a dissolved contaminant plume for numerous millennia at uranium-contaminated

sites. This persistence occurs even after approximately 99% of the primary uranium mass has been removed from the surface (Kent et al., 2024), as observed at the Riverton site (Dam et al., 2015). In addition, the groundwater downgradient of the Riverton site remains contaminated despite large flooding and recharge events in 2010, 2016, and 2017 (U.S. Department of Energy, 2019). This observation further supports the persistence of uranium-associated evaporites in the vadose zone and the continuous contamination of groundwater from the vadose zone. Thus, during Flood-2, an additional 1553 mg/L NaHCO3 was mixed with the flood water for remediation purpose (Table. 3.1). The added alkalinity was 1.8 times higher than that of pre-flooding groundwater which was 550 mg/L as CaCO3 (Table. S2). High bicarbonate concentration was previously found to increase uranium desorption rate due to formation of aqueous U-CO3 species (Alam and Cheng, 2014; Liu et al., 2017). U(VI) is far more mobile than U(IV) and the mobility of U(VI) is enhanced by the relatively high carbonate concentrations characteristic of many alkaline systems (Dong and Brooks, 2006; Qafoku and Icenhower, 2008).

During Flood-2, the mobilized uranium mass from the vadose zone was slightly higher (24%) than it was in Flood-1 (21%) (Fig. 3.8). The results suggested the added alkalinity might have an impact on increased uranium mobility during Flood-2. However, the pattern and concentration of alkalinity was observed to be almost identical to that of expected during the flooding event (Fig. S7) with pH in range of about 7-7.4. The results indicated that, despite the added alkalinity, the net addition of uranium to the groundwater during Flood-2 was not significantly higher, albeit solid-phase uranium concentrations before Flood-2 were unknown. Thus, the effectiveness of added alkalinity on uranium mobilization could not be determined with confidence. It is noteworthy that an excess alkalinity injection could cause more uranium retardation than desorption via uranium coprecipitation with calcite (Chen et al., 2016;

Dangelmayr et al., 2023). Thus, the possibility of a certain amount of uranium retardation during Flood-2 with added alkalinity cannot be disregarded. The above results suggested that added alkalinity might not be an effective remediation technique for a uranium-contaminated site with uranium in the vadose zone.

3.4 Conclusion

This study experimentally simulated two flooding events at a field scale, to characterize contaminant mobility during natural flooding events. It was hypothesized that the contaminant mobilization from the vadose zone was due to contaminant-rich evaporite dissolution during a flooding event. The current study clearly established that the vadose zone serves as a long-term source for contaminant release during flooding events. Additionally, the study identified two primary mobilization mechanisms of contaminants from the vadose zone - (1) physical mobilization attributing to the release of contaminant-rich pore water from the vadose zone, and (2) chemical mobilization attributing to the dissolution of contaminant-rich evaporite minerals that accumulated in the vadose zone sediments. The study was inconclusive with regard to effectiveness added alkalinity as a remediation measure in a field setting, particularly for uranium, and was unable not determine whether contaminant-rich pore water originated from the unsaturated zone or the capillary fringe layer. Nonetheless, our findings have important implications for plume monitoring as they contribute to identifying secondary source locations and understanding the processes governing the release of contaminants during flooding events. Our study documented the release of contaminants from the vadose zone, with findings from our flooding experiments potentially transferable to other unconfined granular porous media. The findings from this study will better inform reactive transport models by pinpointing the primary mechanisms responsible for contaminant mobilization from the vadose zone during flooding

events. This refined understanding will, in return, improve the predictive capabilities of future reactive transport models.

Acknowledgements

The authors express their sincere gratitude for the financial support from the National Science Foundation (NSF) under award number: 2229869 and the 2022 Geological Society of America (GSA) Graduate Student Research Grant: 13597-22. The authors would also like to thank the U.S. Department of Energy Office of Legacy Management for their invaluable support with site access, personnel, and funding to conduct field experiments, and overall technical assistance, provided through contract #DE-LM0000421 with Navarro Research and Engineering, Inc. (through March 30, 2021) and contract #89303020DLM000001 with RSI EnTech, LLC (after April 1, 2021).

References

Aiken, M.L., Ying, S.C., 2023. Small Community Water Systems Have the Highest Prevalence of Mn in Drinking Water in California, USA. ACS EST Water 3, 2168–2178. https://doi.org/10.1021/acsestwater.3c00007

Alam, Md.S., Cheng, T., 2014. Uranium release from sediment to groundwater: Influence of water chemistry and insights into release mechanisms. Journal of Contaminant Hydrology 164, 72–87. https://doi.org/10.1016/j.jconhyd.2014.06.001

Amiaz, Y., Sorek, S., Enzel, Y., Dahan, O., 2011. Solute transport in the vadose zone and groundwater during flash floods. Water Resources Research 47, 2011WR010747. https://doi.org/10.1029/2011WR010747

Apaydın, A., Aktaş, S.D., 2012. Assessment of groundwater quality of the Tatlicay aquifer and relation to the adjacent evaporitic formations (Cankiri, Turkey). Environ Monit Assess 184, 2337–2357. https://doi.org/10.1007/s10661-011-2121-8

Armellini, F.J., Tester, J.W., Hong, G.T., 1994. Precipitation of sodium chloride and sodium sulfate in water from sub- to supercritical conditions: 150 to 550 °C, 100 to 300 bar. The Journal of Supercritical Fluids 7, 147–158. https://doi.org/10.1016/0896-8446(94)90019-1

Barber, L.B., Paschke, S.S., Battaglin, W.A., Douville, C., Fitzgerald, K.C., Keefe, S.H., Roth, D.A., Vajda, A.M., 2017. Effects of an Extreme Flood on Trace Elements in River Water—From Urban Stream to Major River Basin. Environ. Sci. Technol. 51, 10344–10356. https://doi.org/10.1021/acs.est.7b01767

Benito, G., Rohde, R., Seely, M., Külls, C., Dahan, O., Enzel, Y., Todd, S., Botero, B., Morin, E., Grodek, T., Roberts, C., 2010. Management of Alluvial Aquifers in Two Southern African Ephemeral Rivers: Implications for IWRM. Water Resour Manage 24, 641–667. https://doi.org/10.1007/s11269-009-9463-9

Bowman, R.S., Gibbens, J.F., 1992. Difluorobenzoates as Nonreactive Tracers in Soil and Ground Water. Ground Water 30, 8–14. https://doi.org/10.1111/j.1745-6584.1992.tb00805.x

Callahan, T.J., Reimus, P.W., Bowman, R.S., Haga, M.J., 2000. Using multiple experimental methods to deter-mine fracture/matrix interactions and dispersion of non-reactive solutes in saturated volcanic tuff. WaterResour. Res. 36 (12), 3547 – 3558

Carlisle, D., Merifield, P.M., Orme, A.R., Kohl, M.S., Kolker, O., Lunt, O.R., 1978. Distribution of calcretes and gypcretes in southwestern United States and their uranium favorability,

based on a study of deposits in Western Australia and South West Africa (Namibia) (No. GJBX-29(78), 5049447). https://doi.org/10.2172/5049447

Chen, X., Romaniello, S.J., Herrmann, A.D., Wasylenki, L.E., Anbar, A.D., 2016. Uranium isotope fractionation during coprecipitation with aragonite and calcite. Geochimica et Cosmochimica Acta 188, 189–207. https://doi.org/10.1016/j.gca.2016.05.022

Crawford, S.E., Brinkmann, M., Ouellet, J.D., Lehmkuhl, F., Reicherter, K., Schwarzbauer, J., Bellanova, P., Letmathe, P., Blank, L.M., Weber, R., Brack, W., Van Dongen, J.T., Menzel, L., Hecker, M., Schüttrumpf, H., Hollert, H., 2022. Remobilization of pollutants during extreme flood events poses severe risks to human and environmental health. Journal of Hazardous Materials 421, 126691. https://doi.org/10.1016/j.jhazmat.2021.126691

Dahan, O., Talby, R., Yechieli, Y., Adar, E., Lazarovitch, N., Enzel, Y., 2009. In Situ Monitoring of Water Percolation and Solute Transport Using a Vadose Zone Monitoring System. Vadose Zone Journal 8, 916–925. https://doi.org/10.2136/vzj2008.0134

Dahan, O., Tatarsky, B., Enzel, Y., Kulls, C., Seely, M., Benito, G., 2008. Dynamics of Flood Water Infiltration and Ground Water Recharge in Hyperarid Desert. Groundwater 46, 450–461. https://doi.org/10.1111/j.1745-6584.2007.00414.x

Dam, W.L., Campbell, S., Johnson, R.H., Looney, B.B., Denham, M.E., Eddy-Dilek, C.A., Babits, S.J., 2015. Refining the site conceptual model at a former uranium mill site in Riverton, Wyoming, USA. Environ Earth Sci 74, 7255–7265. https://doi.org/10.1007/s12665-015-4706-y

Dangelmayr, M., Meurer, C., Tigar, A., Johnson, R.H., Paradis, C., 2023. Desorption and Co-Dissolution of Uranium-Bearing Solids During Alkalinity-Enhanced Flushing of

Contaminated Sediments. Groundwater Monitoring Rem gwmr.12573. https://doi.org/10.1111/gwmr.12573

Dong, W., Brooks, S.C., 2006. Determination of the Formation Constants of Ternary Complexes of Uranyl and Carbonate with Alkaline Earth Metals (Mg^{2+}, Ca^{2+}, Sr^{2+}, and Ba^{2+}) Using Anion Exchange Method. Environ. Sci. Technol. 40, 4689–4695. https://doi.org/10.1021/es0606327

Drever, J.I., 1982. The geochemistry of natural waters. Prentice-Hall, Englewood Cliffs, N.J.

"Drinking Water Regulations and Contaminants" EPA.gov. Last modified on February 14, 2024. https://www.epa.gov/sdwa/drinking-water-regulations-and-contaminants

Du Laing, G., Vanthuyne, D.R.J., Vandecasteele, B., Tack, F.M.G., Verloo, M.G., 2007. Influence of hydrological regime on pore water metal concentrations in a contaminated sediment-derived soil. Environmental Pollution 147, 615–625. https://doi.org/10.1016/j.envpol.2006.10.004

Dwivedi, D., Steefel, C.I., Arora, B., Banfield, J., Bargar, J., Boyanov, M.I., Brooks, S.C., Chen, X., Hubbard, S.S., Kaplan, D., Kemner, K.M., Nico, P.S., O'Loughlin, E.J., Pierce, E.M., Painter, S.L., Scheibe, T.D., Wainwright, H.M., Williams, K.H., Zavarin, M., 2022. From legacy contamination to watershed systems science: a review of scientific insights and technologies developed through DOE-supported research in water and energy security. Environ. Res. Lett. 17, 043004. https://doi.org/10.1088/1748-9326/ac59a9

Freeze, R.A., Cherry, J.A., 1979. Physical Properties and Principles, in: Groundwater. Prentice-Hall, Englewood Cliffs, N.J., pp. 38-40.

Frohne, T., Rinklebe, J., Diaz-Bone, R.A., Du Laing, G., 2011. Controlled variation of redox conditions in a floodplain soil: Impact on metal mobilization and biomethylation of

arsenic and antimony. Geoderma 160, 414–424. https://doi.org/10.1016/j.geoderma.2010.10.012

Gregory, R.W., 2019, Uranium geology and resources of the Gas Hills district, Wind River Basin, central Wyoming: Wyoming State Geological Survey Public Information Circular 47, 31 p.

Gross, A., Besov, A., Diaz Reck, D., Sorek, S., Ben-Dor, G., Britan, A., Palchikov, E., 2003. Application of Waves for Remediation of Contaminated Aquifers. Environ. Sci. Technol. 37, 4481–4486. https://doi.org/10.1021/es026297d

Harkness, J.S., Darrah, T.H., Moore, M.T., Whyte, C.J., Mathewson, P.D., Cook, T., Vengosh, A., 2017. Naturally Occurring versus Anthropogenic Sources of Elevated Molybdenum in Groundwater: Evidence for Geogenic Contamination from Southeast Wisconsin, United States. Environ. Sci. Technol. 51, 12190–12199. https://doi.org/10.1021/acs.est.7b03716

Hooda, P.S. (Ed.), 2010. Trace Elements in Soils, 1st ed. Wiley. https://doi.org/10.1002/9781444319477

Izquierdo, M., Tye, A.M., Chenery, S.R., 2017. Using isotope dilution assays to understand speciation changes in Cd, Zn, Pb and Fe in a soil model system under simulated flooding conditions. Geoderma 295, 41–52. https://doi.org/10.1016/j.geoderma.2017.02.006

Johnson, R.H., Dam, W.L., Campbell, S., Noël, V., Bone, S.E., Bargar, J.R., Dayvault, J., 2016. Persistent Secondary Contaminant Sources at a Former Uranium Mill Site, Riverton, Wyoming, USA, in: Proceedings IMWA 2016. Presented at the Mining Meets Water – Conflicts and Solutions, Freiberg/Germany, pp. 398–404.

Keefer, W. R., 1970. Structural Geology of the Wind River Basin, Wyoming (No. 495- D). Prepared in cooperation with the Geological Survey of Wyoming and the Department of

Geology of the University of Wyoming as part of a program of the Department of the Interior for development of the Missouri River basin.

Kent, R.D., Johnson, R.H., Laase, A.D., Nyman, J.L., 2024. Modeling evaluation of the impact of residual source material on remedial time frame at a former uranium mill site. Journal of Contaminant Hydrology 261, 104298. https://doi.org/10.1016/j.jconhyd.2024.104298

Knowlton RG Jr, Peterson DM, Zhang H (1997) Analysis of natural attenuation as the preferred ground water alternative at the DOE UMTRA site near Riverton. Sandia National Laboratories, WY

Langmuir, D., 1977. Uranium solution-mineral equilibria at low temperatures with applications to sedimentary ore deposits (No. GJO-1659-3, GJBX-54(78), 6774931). https://doi.org/10.2172/6774931

Liu, B., Peng, T., Sun, H., Yue, H., 2017. Release behavior of uranium in uranium mill tailings under environmental conditions. Journal of Environmental Radioactivity 171, 160–168. https://doi.org/10.1016/j.jenvrad.2017.02.016

Looney, B.B., Denham, M.E., Eddy-Dilek, C.A., 2014. Independent technical evaluation and recommendations for contaminated groundwater at the department of energy office of legacy management Riverton processing site (No. SRNL-STI--2014-00163, 1130785). https://doi.org/10.2172/1130785

Mackay, D.M., Einarson, M.D., Kaiser, P.M., Nozawa-Inoue, M., Goyal, S., Chakraborty, I., Rasa, E., Scow, K.M., 2012. Mass Discharge in a Tracer Plume: Evaluation of the Theissen Polygon Method. Groundwater 50, 895–907. https://doi.org/10.1111/j.1745-6584.2012.00912.x

Management DL, 2016. Uranium-Bearing Evaporite Mineralization Influencing Plume Persistence: Literature Review and DOE-LM Site Surveys. LMS/S13437; ESL-RPT-2015-05.

Miao, Z., Brusseau, M.L., Carroll, K.C., Carreón-Diazconti, C., Johnson, B., 2012. Sulfate reduction in groundwater: characterization and applications for remediation. Environ Geochem Health 34, 539–550. https://doi.org/10.1007/s10653-011-9423-1

Narasimhan, T.N., White, A.F., Tokunaga, T., 1986. Groundwater contamination from an inactive uranium mill tailings pile: 2. Application of a dynamic mixing model. Water Resour. Res. 22, 1820–1834. https://doi.org/10.1029/WR022i013p01820

"National Primary Drinking Water Regulations" EPA.gov. Last modified on January 2, 2024. epa.gov/ground-water-and-drinking-water/national-primary-drinking-water-regulations

Nativ, R., Adar, E., Dahan, O., Geyh, M., 1995. Water Recharge and Solute Transport Through the Vadose Zone of Fractured Chalk Under Desert Conditions. Water Resources Research 31, 253–261. https://doi.org/10.1029/94WR02536

Ofer Dahan, Dahan, O., Yuval Shani, Shani, Y., Yehouda Enzel, Enzel, Y., Yoseph Yechieli, Yechieli, Y., A. Yakirevich, Yakirevich, A., 2007. Direct measurements of floodwater infiltration into shallow alluvial aquifers. Journal of Hydrology 344, 157–170. https://doi.org/10.1016/j.jhydrol.2007.06.033

Paradis, C., Sultana, R., 2024. Tracer-based Separation of Advection and Dispersion from Breakthrough Curves. Geosciences Faculty Articles, 28.

Paradis, C., Van Ee, N., Hoss, K., Meurer, C., Tigar, A., Reimus, P., Johnson, R., 2022. Single-Well Injection-Drift Test to Estimate Groundwater Velocity. Groundwater 60, 565–570. https://doi.org/10.1111/gwat.13184

Paradis, C.J., Dixon, E.R., Lui, L.M., Arkin, A.P., Parker, J.C., Istok, J.D., Perfect, E., McKay, L.D., Hazen, T.C., 2019. Improved Method for Estimating Reaction Rates During Push-Pull Tests. Groundwater 57, 292–302. https://doi.org/10.1111/gwat.12770

Paradis, C.J., Hoss, K.N., Meurer, C.E., Hatami, J.L., Dangelmayr, M.A., Tigar, A.D., Johnson, R.H., 2022. Elucidating mobilization mechanisms of uranium during recharge of river water to contaminated groundwater. Journal of Contaminant Hydrology 251, 104076. https://doi.org/10.1016/j.jconhyd.2022.104076

Paradis, C.J., Johnson, R.H., Tigar, A.D., Sauer, K.B., Marina, O.C., Reimus, P.W., 2020. Field experiments of surface water to groundwater recharge to characterize the mobility of uranium and vanadium at a former mill tailing site. Journal of Contaminant Hydrology 229, 103581. https://doi.org/10.1016/j.jconhyd.2019.103581

Ponting, J., Kelly, T.J., Verhoef, A., Watts, M.J., Sizmur, T., 2021. The impact of increased flooding occurrence on the mobility of potentially toxic elements in floodplain soil – A review. Science of The Total Environment 754, 142040. https://doi.org/10.1016/j.scitotenv.2020.142040

Qafoku, N.P., Icenhower, J.P., 2008. Interactions of aqueous U(VI) with soil minerals in slightly alkaline natural systems. Rev Environ Sci Biotechnol 7, 355–380. https://doi.org/10.1007/s11157-008-9137-8

Ricker, J.A., 2008. A Practical Method to Evaluate Ground Water Contaminant Plume Stability. Ground Water Monitoring & Remediation 28, 85–94. https://doi.org/10.1111/j.1745-6592.2008.00215.x

Simpson, S.C., Meixner, T., Hogan, J.F., 2013. The role of flood size and duration on streamflow and riparian groundwater composition in a semi-arid basin. Journal of Hydrology 488, 126–135. https://doi.org/10.1016/j.jhydrol.2013.02.049

Singh, G., Şengör, S.S., Bhalla, A., Kumar, S., De, J., Stewart, B., Spycher, N., Ginn, T.M., Peyton, B.M., Sani, R.K., 2014. Reoxidation of Biogenic Reduced Uranium: A Challenge Toward Bioremediation. Critical Reviews in Environmental Science and Technology 44, 391–415. https://doi.org/10.1080/10643389.2012.728522

Sorek, S., 1996. A model for solute transport following an abrupt pressure impact in saturated porous media. Transp Porous Med 22, 271–285. https://doi.org/10.1007/BF00161627

Sorek, S., Bear, J., 1990. Evolution of governing mass and momentum balances following an abrupt pressure impact in a porous medium. Transp Porous Med 5, 169–185. https://doi.org/10.1007/BF00144602

Truex, M.J., Oostrom, M., Brusseau, M.L., 2009. Estimating Persistent Mass Flux of Volatile Contaminants from the Vadose Zone to Ground Water. Groundwater Monitoring Rem 29, 63–72. https://doi.org/10.1111/j.1745-6592.2009.01236.x

U.S. Department of Energy, 2023. Applied Studies and Technology Persistent Secondary Contaminant Sources Data Release from Field Tracer Testing Studies at the Riverton, Wyoming, Processing Site (No. LMS/ESL/43015), AS&T- Persistent Secondary Contaminant Sources Data Release, Field Tracer Testing Studies at Riverton Site.

U.S. Department of Energy, 2019. Three Years of Multilevel Monitoring Data at the Riverton, Wyoming, Processing Site That Show Contaminant Increases After River Flooding Events and a Large Recharge Event (No. LMS/RVT/S26137). Office of Legacy Management.

U.S. Department of Energy, 2016. 2015 Advanced Site Investigation and Monitoring Report Riverton, Wyoming, Processing Site September 2016 (No. S--14148, 1351628). https://doi.org/10.2172/1351628

U.S. Department of Energy, L.M., 2014. Evaluation of Mineral Deposits Along the Little Wind River, Riverton, Wyoming, Processing Site.

U.S. Department of Energy, 1998. Final Site Observational Work Plan for the UMTRA Project Site at Riverton, Wyoming, Report No. U0013801.

Warrick, A.W., Biggar, J.W., Nielsen, D.R., 1971. Simultaneous Solute and Water Transfer for an Unsaturated Soil. Water Resources Research 7, 1216–1225. https://doi.org/10.1029/WR007i005p01216

Weber, F.-A., Voegelin, A., Kretzschmar, R., 2009. Multi-metal contaminant dynamics in temporarily flooded soil under sulfate limitation. Geochimica et Cosmochimica Acta 73, 5513–5527. https://doi.org/10.1016/j.gca.2009.06.011

White, A.F., Delany, J.M., Narasimhan, T.N., Smith, A., 1984. Groundwater contamination from an inactive uranium mill tailings pile: 1. Application of a chemical mixing model. Water Resour. Res. 20, 1743–1752. https://doi.org/10.1029/WR020i011p01743

Yabusaki, S.B., Wilkins, M.J., Fang, Y., Williams, K.H., Arora, B., Bargar, J., Beller, H.R., Bouskill, N.J., Brodie, E.L., Christensen, J.N., Conrad, M.E., Danczak, R.E., King, E., Soltanian, M.R., Spycher, N.F., Steefel, C.I., Tokunaga, T.K., Versteeg, R., Waichler, S.R., Wainwright, H.M., 2017. Water Table Dynamics and Biogeochemical Cycling in a Shallow, Variably-Saturated Floodplain. Environ. Sci. Technol. 51, 3307–3317. https://doi.org/10.1021/acs.est.6b04873

Yang, F., Yue, S., Wu, X., Zhang, C., Li, D., Zhu, R., 2023. Effects of flood inundation on biogeochemical processes in groundwater during riverbank filtration. Journal of Hydrology 617, 129101. https://doi.org/10.1016/j.jhydrol.2023.129101

CHAPTER 4 - Mechanisms for Contaminant Transport in the Vadose Zone During Infiltration Events

Abstract

Infiltration events, such as natural river flooding or managed aquifer recharge, can mobilize contaminants, such as chloride and uranium stored in the vadose zone. Quantifying contaminant transport during these events is challenging due to the changing nature of flow and solute movement in the vadose zone. Field tracer experiments, one direct injection into the saturated zone and two surface infiltration experiments through the vadose zone, identified two primary contaminant mobilization mechanisms: (1) non-reactive transport of contaminant-rich pore water ahead of the wetting front and (2) dissolution of contaminant-rich evaporites by infiltrating water. In this study, a one-dimensional mathematical model was applied to inversely simulate the field data and quantify the relative contributions of these mechanisms. The injection test showed that advection and dispersion dominated uranium and chloride transport in the saturated zone, indicating it was not a substantial source of contaminant mobilization. In the first infiltration test, both uranium and chloride were initially mobilized by advection and dispersion of contaminant-rich pore water, followed by dissolution of contaminant-rich evaporites, with uranium desorption, in the vadose zone. In the second infiltration test, chloride transport was primarily driven by advection and dispersion of chloride-rich pore water, while uranium transport occurred via initial advection and dispersion followed by dissolution of uranium-bearing evaporites with uranium desorption. The results confirmed the hypothesized mobilization mechanisms and demonstrated that the vadose zone is the primary source of contaminant release during infiltration events. These insights into transport mechanisms are crucial for evaluating contaminant behavior and designing effective remediation strategies.

4.1 Introduction

Infiltration processes, both natural, such as flooding, and anthropogenic, such as managed aquifer recharge, significantly influence the movement of contaminants through the vadose zone which encompasses the unsaturated zone and capillary fringe layers above the water table (Freeze and Cherry, 1979). The vadose zone acts as a key reservoir for contaminants, including heavy metals, radionuclides and salts, hence is known for its critical role in controlling groundwater quality (Dahan et al., 2020, Sultana et al., 2024b). Infiltration events, coupled with the inherent heterogeneity of the vadose zone and the resulting development of preferential flow paths, facilitate the mobilization of contaminants into underlying aquifers, thereby posing considerable risks to groundwater resources (Siirila et al., 2015; Šimůnek and van Genuchten, 2017; Perzan et al., 2023).

These contaminants are primarily transported by advection - the bulk movement of solutes with infiltrating water, and hydrodynamic dispersion, caused by variations in pore water velocity and including both mechanical mixing and molecular diffusion (Bear, 1979; Bidwell, 2000; Freeze and Cherry, 1979). Controlled laboratories (Amiaz et al., 2011; Frohne et al., 2011) and field-scale infiltration studies (Dahan et al., 2008; Sultana et al., 2024b) have demonstrated that these processes significantly increase contaminant mobility through the vadose zone to groundwater during flooding events.

While the laboratory and field studies provided empirical evidence linking flood events to contaminant spikes in groundwater, these studies did not provide relative quantitative contributions of advection, hydrodynamic dispersion, and geochemically driven release under dynamic, non-steady-state conditions. In this scenario, mathematical models can act as critical components for interpreting site-specific flow and transport processes and quantifying the behavior of solutes in the subsurface (Šimůnek and van Genuchten, 2017).

A wide variety of computer models, employing both analytical and numerical approaches to flow and solute transport equations, are now available to support diverse research and management applications in natural subsurface systems (Šimůnek, 2005). Numerical models, such as HYDRUS (Šimůnek et al., 2008) and MODFLOW 6 (Langevin et al., 2017, 2022), offer comprehensive simulations of saturated and vadose zone processes. However, these models are computationally intensive, require extensive parameterization, that might reduce their generalizability (Šimůnek & Bradford, 2008; Skaggs et al., 2007).

In contrast, analytical models provide a computationally efficient and theoretically robust alternative for isolating and quantifying individual transport mechanisms under controlled conditions (van Genuchten & Alves, 1982; Ogata & Banks, 1961). These models, however, rely on simplifying assumptions, such as homogeneity of the subsurface or linearization of nonlinear reactions that can limit their applicability. Nevertheless, in some cases, these simplifications may not be overly restrictive (Liu et al., 2000); for example, short-term boundary fluctuations from precipitation can be averaged, allowing an analytical model with time-averaged boundary conditions and transport properties to closely approximate a more complex model (e.g., Destouni, 1991).

Among analytical solute transport models, abundant literature exists on the classical advection–dispersion equation (ADE).While analytical solutions to the ADE are widely available, most analytical solutions to the ADE (e.g., van Genuchten & Alves, 1982; Skaggs & Leij, 2002) are limited to steady-state conditions and do not account for time-varying analyte changes during infiltration scenarios, such as flooding. As a result, the application of analytical models to simulate flood-induced contaminant transport in the vadose zone, especially under controlled field infiltration experiments (e.g., Sultana et al., 2024b) remains underexplored.

To address this knowledge gap, this study employed the one-dimensional mathematical (analytical) model developed by Wexler (1992) to simulate variably saturated flow and solute transport during infiltration events. The model allowed incorporation of time-dependent boundary conditions and facilitated quantitative assessment of advective transport, hydrodynamic dispersion, and vadose zone processes. The model was applied to three field scenarios - a direct saturated zone tracer injection (Paradis et al., 2022) and two surface infiltration experiments conducted through the vadose zone at one-year intervals (Sultana et al., 2024b). Through systematic inverse simulation and parametric evaluation, the study aimed to test two mechanistic hypotheses derived from the two infiltration experimental data (Sultana et al., 2024b) - (1) the rapid displacement of contaminant-rich pore water ahead of the flood wetting front, and (2) the dissolution of contaminant-rich evaporite minerals with infiltrating water. The model is further applied to isolate the respective roles of advection, hydrodynamic dispersion, and impact of vadose zone to the mobilization of uranium and chloride during floods.

The modeling approach bridges empirical field observations with theoretical transport frameworks, providing a more mechanistic understanding of flood-induced contaminant dynamics and addressing critical knowledge gaps in the quantitative assessment of vadose zone processes.

4.2 Methods and Materials

4.2.1 Study Site

The study site, located ~2 miles southwest of Riverton, Wyoming, lies on river alluvium between the Wind River and Little Wind River; detailed hydrogeology, history and activities of the site was provided by Dam et al. (2015). In brief, it comprises an unsaturated zone (1.2–1.5 m of silt and clay) overlying three aquifers: an unconfined sand and gravel aquifer (4.5–6 m), a semiconfined aquifer, and a confined aquifer within the Wind River Formation (over 150 m

thick), composed of sandstone, conglomerate, siltstone, and claystone (Keefer, 1970, Robert W. Gregory, 2019).

Historically, the site operated as a uranium milling facility between 1958 and 1963, resulting in contamination of the shallow, unconfined sand and gravel aquifer due to uranium tailings. Although the U.S. Department of Energy (DOE) removed these tailings by 1989 to meet radium radioactivity standards, uranium levels in the unconfined aquifer remain high up to 1.7 mg/L vs. the 0.03 mg/L MCL (National Primary Drinking Water Regulations, 2024). In contrast, the confined aquifer remains uncontaminated due to protective shale layers. The Riverton Groundwater Analysis and Network Design Tool (GANDT) model, simulated by Sandia National Laboratories, estimated that natural flushing would attenuate the groundwater plume below MCLs within 100 years from 1997 (Knowlton Jr et al., 1997; U.S. Department of Energy, 1998). However, annual monitoring revealed the persistence of the plume, with uranium concentrations increasing after a 2010 flooding event (Dam et al., 2015).

The arid climate and dry summers of Riverton result in widespread chloride and sulfate-rich evaporite deposits (halite, blödite, and thenardite) in the upper vadose zone, particularly along south-facing riverbanks (DOE, 2016). These deposits, enriched in uranium (0.0014–0.066 g/kg) and sulfate (5.4–2200 g/kg), may act as secondary contamination sources (Dam et al., 2015; Johnson et al., 2016). This hydroclimatic setting is typical of arid and semi-arid regions; while Riverton is characterized by uranium contamination, the underlying processes are broadly applicable to other contaminants and similarly impacted areas (DOE, 2018).

The area near the Little Wind River, characterized by a silty clay vadose zone and a sandy gravel saturated zone, is a critical site for studying uranium mobility during river water infiltration into groundwater (Dam et al., 2015). Groundwater and river water differ markedly in redox state,

uranium concentration, pH (~7 vs. ~8.5), and alkalinity (~500 vs. ~200 mg/L as $CaCO_3$; DOE 2016). Tracer injection studies (Paradis et al., 2022) and flooding experiments (Sultana et al., 2024b) conducted between 2020 and 2021 have further investigated uranium dynamics under varying hydrologic conditions.

4.2.2 Conceptual Model

Figure 4.1 presents three conceptual scenarios illustrating the impact of contaminant-poor river water (RW) infiltration during a flood on the contaminant-rich groundwater (saturated zone - SZ), based on field tracer experiments conducted to evaluate contaminant mobility in the vadose zone (VZ). These scenarios model varying contamination distributions and their effects on breakthrough curves observed at downgradient monitoring wells (MW). Section 2.2 refers RW, VZ, and SZ as distinct hydrogeological compartments.

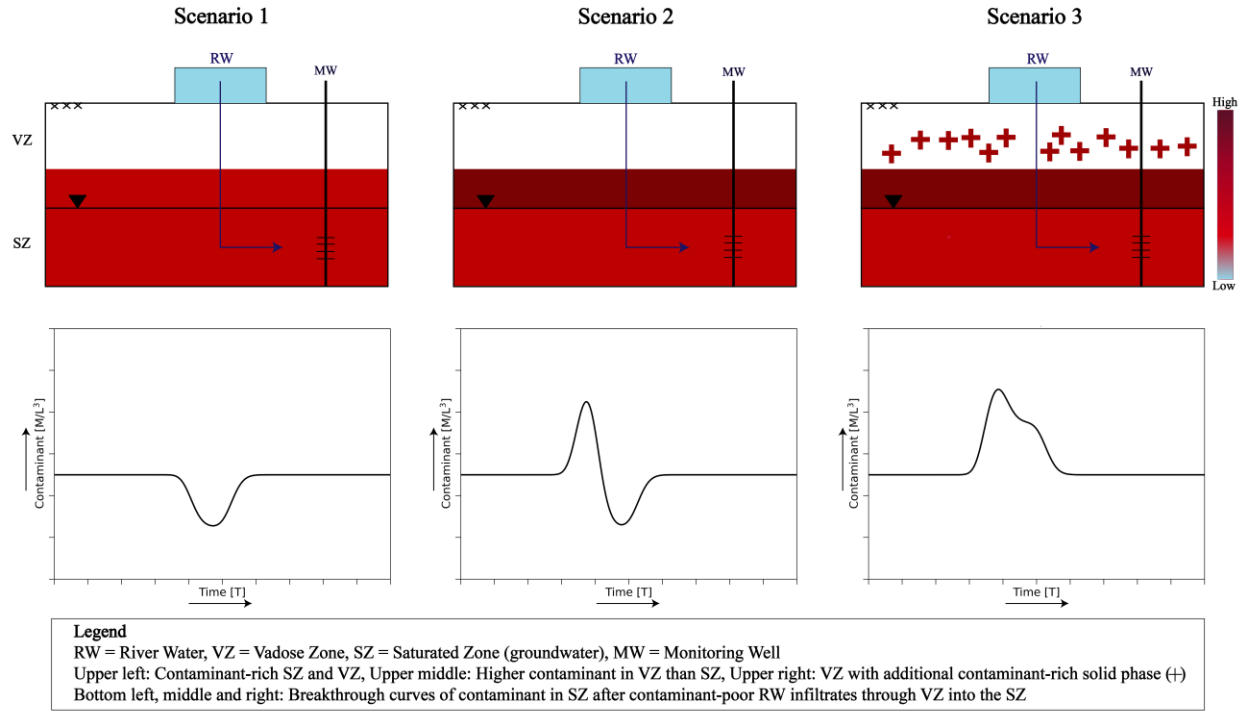

Fig. 4.1 Conceptual model of the contaminant-rich (red) and contaminant-poor (blue) hydrogeological compartments (upper insets) and breakthrough curve response of the contaminants in response to river water infiltration into groundwater (lower insets).

Scenario 1 (left panel) represents an infiltration test where contaminant-poor RW infiltrates into a system where both the VZ pore water and the SZ show similar levels of contamination. The breakthrough curve results in a dip, reflecting dilution of contaminant concentration in groundwater.

Scenario 2 (middle panel) represents an infiltration test where contaminant-poor RW infiltrates through a VZ with pore water contamination higher than that in the underlying SZ. The breakthrough curve results in an initial hump, followed by a dip in groundwater.

Scenario 3 (right panel) represents an infiltration test where contaminant-poor RW infiltrates through a VZ with both contaminated pore water and solid phase; with higher contamination in the pore water than the solid phase (e.g., evaporites). As RW infiltrates through the VZ, it produces a double-hump breakthrough curve.

4.2.3 Field Tests Design

Three field tests were conducted to evaluate contaminant transport in the subsurface: a river water injection test directly into the SZ in summer 2020, followed by two river water infiltration tests through the VZ in summers 2020 and 2021 at the same study site. Detailed descriptions of these experiments are provided in Paradis et al. (2022) and Sultana et al. (2024b). Brief descriptions of each experiment are outlined in the subsections below.

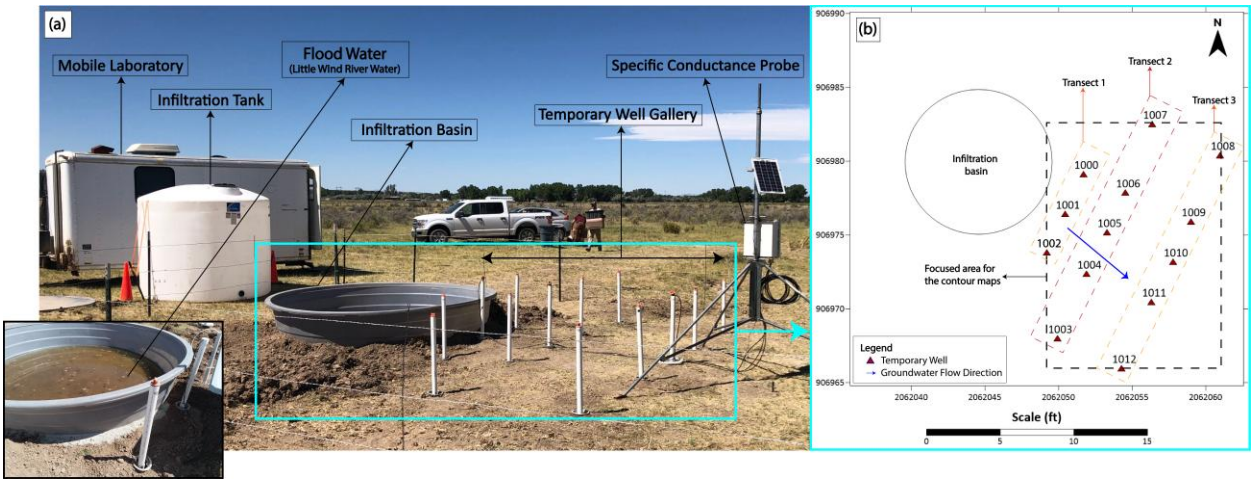

Figure 4.2 (a) Field site showing 13 monitoring wells, including an injection well (designated as well 1000 in Fig. 2b) used for a direct river water injection test. These 13 monitoring wells and an adjacent flood basin (shown in inset) were subsequently used in the infiltration tests at the same location. (b) Plan view map showing the experimental set-up for both the direct injection and infiltration tests (Sultana et. al., 2024b).

4.2.3.1 River Water Injection Test

The direct injection test, as detailed by Paradis et al. (2022), involved 13 monitoring wells (Fig. 4.2) installed by direct push in uranium-contaminated sand and gravel sediments. The wells were arranged in three transects perpendicular to groundwater flow, with a maximum distance of 10 ft (3 m) between upper and lower transects to facilitate tracer transport within 30 days. Two solute tracers, iodide and pentafluoro benzoate (PFB), were mixed into a 100-gallon (379-liter) volume of river water to achieve a target concentration of 500 mg/L and were injected into upgradient well 1001 using a peristaltic pump under forced-gradient conditions for 8 hours. Vertical tracer distribution was ensured through fluid recirculation during injection. Samples were collected over 18 days from the wells under natural-gradient conditions (Experimental data given in Table S1 and S2).

4.2.3.2 River Water Infiltration Test: Flood-1 (Year-1)

The first infiltration test, as described by Sultana et al. (2024b), included a 9-ft (3-m) diameter basin positioned upgradient of the monitoring wells. An infiltration tank containing 2000 gallons (7571 liters) of river water was mixed with two non-reactive tracers, lithium bromide (LiBr) and sodium 2,6-difluorobenzoate (NaDFB), each with distinct diffusion coefficients. The tracer-mixed river water was pumped into the basin over approximately 8 days via a peristaltic pump, facilitating the tracer transport through the vadose zone into a contaminant-rich groundwater (Experimental data given in Table S3, S4, and S5).

4.2.3.3 River Water Infiltration Test: Flood-2 (Year-2)

The second infiltration test, one year after the first infiltration test, used a similar setup at the same location (Sultana et al., 2024b). Sodium iodide (NaI) served as the non-reactive tracer, with sodium bicarbonate (NaHCO3) added to the infiltration water. The tracer- and alkalinity-added river water was flooded into the 9-ft (3-m) diameter basin over approximately 12 days, followed by 40 days of monitoring (Experimental data given in Table S6, S7, and S8).

More detailed information on the field methods and groundwater sampling and analysis is available in the relevant documentation for the study (U.S. Department of Energy, 2023).

4.2.4 Data Analysis

Breakthrough curves of non-reactive added tracers (I, PFB, Br, DFB) and potentially reactive solutes, chloride (Cl), and uranium (U), were constructed and plotted for concentrations in groundwater for both types of tests. The temporal moment method (Yu et al., 1999) were applied to calculate a reasonable estimate of the parameters (time difference between solute change, and observation distance) required for further analytical model simulation. The zeroth moment measures the area underneath the breakthrough curve $\left[\frac{\mathrm{M}}{\mathrm{L}^3}\mathrm{T}\right]$ using trapezoidal rule (Yu

et al., 1999 [Eqn. 1]). The normalized first moment (Yu et al., 1999 [Eqn. 2]) is the first moment divided by the zeroth moment and indicates the center of mass in time [T]. Likewise, the normalized second moment is the second moment divided by the zeroth moment and represents the spread in time squared [T^2]. The zeroth moment when divided by the injected or infiltrated concentration $[\frac{M}{L^3}]$ of the solute provided the estimate for duration Δ[T] between changes of solutes (river water to background groundwater). The normalized first moment when multiplied by velocity [L^2/T] provided the estimate for observation distance of the solutes.

4.2.5 Analytical Model

An analytical solution from Wexler (1992) for the one-dimensional (1D) advective-dispersive solute transport equation (Eqn. 1) was used to inversely model solute transport from the vadose zone to groundwater. Although applicable to 2D or 3D systems, this study adopted a 1D framework to isolate key transport processes, assuming constant groundwater velocity along the x-axis. To adapt Wexler (1992) 1D model for application to river water injection (single-layer) and infiltration tests (two-layer vertical), the vertical transport domain was conceptually reoriented into a horizontal 1D domain (Fig. 4.3), simplifying the 3D system while preserving the dominant solute transport mechanisms. In section 2.5, RW (river water), VZW (vadose zone water), GW_o (initial groundwater) and GW_b (background groundwater) are referred to distinct influents with solutes in their respective hydrogeological compartments. These compartments are represented schematically as cylinders in Figure 3, with valve symbols (no-fill green triangle) indicating the times [T] at which influent switches (Fig. 4.3).

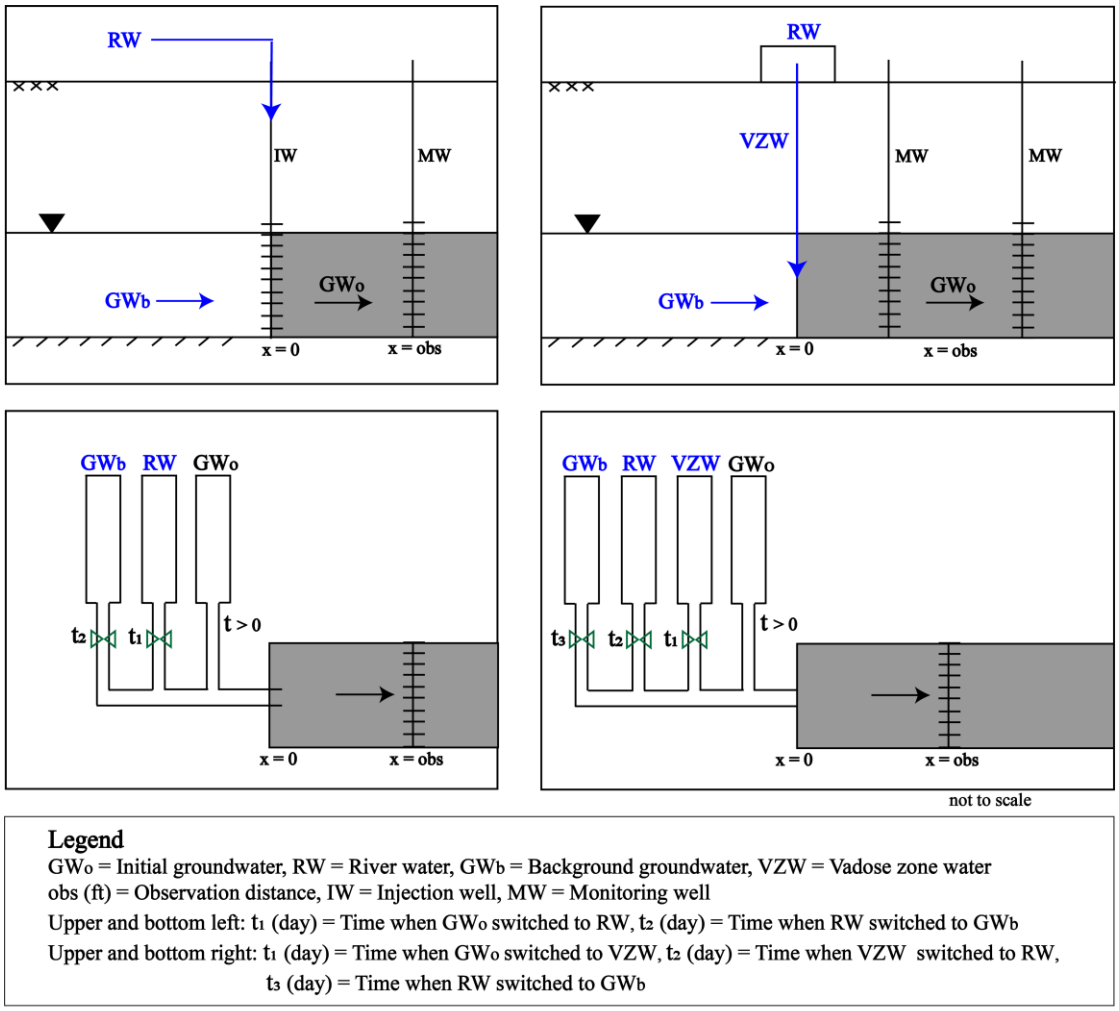

Figure 4.3 The conceptual schematics and 1D model representations of two field experiments: a river water injection test (left panels) and a river water infiltration test (right panels). The concentration of GW_b is similar to GW_o. The black inverted triangle indicate the water table. Bottom left and right are adapted from Wexler, 1992.

The upper left panel (Fig. 4.3) shows river water injection test schematic with three influents: initial groundwater (GW_o) in the model domain (grey area) with solute concentrations [M/L^3] equal to background groundwater (GW_b), river water (RW) with added non-reactive tracers [M/L^3] and background groundwater (GW_b) with non-added solutes [M/L^3]. The background groundwater is denoted as GW_o during the initial condition and as GW_b after the injection is turned off. RW is injected directly into the aquifer via an injection well (IW) and

monitored at a distance x = obs by a monitoring well (MW). The x = obs (ft) is estimated from moments [Section 2.3].

The bottom left panel (Fig. 4.3) illustrates the corresponding 1D model schematic for the injection test and consequent influent changes (Table 4.1). As the injection starts, the GW_o(=GW_b) switches to RW at time t_1 and enters through the inlet (x = 0) of the model domain; t_1 is a long enough time to reach steady-state GW_o. After the injection is tuned off, at time t_2, the RW switches back to GW_b. The injection time in the model is defined as $t_2 - t_1$, estimated from moments [Section 2.3]. All the influents are observed at a MW located at a distance x=obs [L].

The upper right panel (Fig. 4.3) shows the river water infiltration test schematic with four influents: initial groundwater (GW_o), vadose zone water (VZW) with non-added solutes [M/L^3], RW with added non-reactive tracers [M/L^3], and GW_b with non-added solutes [M/L^3], in their respective compartments. As in the injection test, GW_o represents initial background groundwater and is referred to as GW_b post infiltration. RW infiltrates through the vadose zone and then into the groundwater; observed by a MW at x = obs distance.

The bottom right panel (Fig. 4.3) illustrates the 1D model schematic for the river water infiltration test and consequent influent changes (Table 4.2). At the start of infiltration, the GW_o(=GW_b) switches to VZW at time t_1, after reaching steady-state background conditions (GW_o). As infiltration continues, VZW advected by the RW, enters through the inlet (x = 0) of the model domain. At time t_2 days VZW switches to RW. After the infiltration is tuned off at time t_3, the RW switches back to GW_b. The infiltration time in the model is defined as $t_3 - t_2$, estimated from moments [Section 2.3], representing the period during which RW enters the system. All the influents are observed from a monitoring well at a distance x=obs [L].

Notably, concentrations of VZW, GW_b and RW influents are represented as C_{vzw}, C_{gw}, and C_{rw}, respectively in subsequent sections.

The transport of the one-dimensional advective and dispersive solute in the different compartments are governed by:

$$\frac{\partial C(x,t)}{\partial t} = D\frac{\partial^2 C(x,t)}{\partial x^2} - v\frac{\partial C(x,t)}{\partial x} \quad (1)$$

where: C(x,t) = solute concentration [M/L^3], x = distance [L], t = time [T], D = dispersion co-efficient [L^2/T], and v = velocity [L/T]. Equation (1) can be solved analytically under the following initial and boundary conditions that allow for changes of the influent solute concentration.

Initial condition:

For the analytical solutions applied in this work, the initial conditions are specified such that all initial concentrations are equal to zero as shown by,

$$C(x, t = 0) = 0 \quad (2)$$

Boundary condition at inlet:

The boundary at the model inlet (x=0) is represented by specified concentration (Dirichlet conditions):

$$C(x = 0, t_{n-1} \leq t < t_n) = C_{n-1} \quad (3)$$

where: C_{n-1} = solute concentration of $(n-1)^{th}$ influent [M/L^3], t_{n-1} = time [T] when a previous influent is switched to $(n-1)^{th}$ influent, and L = length of domain [L].

Boundary condition at outlet:

The boundary at the model outlet (x=L) is represented by specified flux (Neumann conditions) with no concentration gradient across the boundary:

$$\frac{\partial C(x = L, t > 0)}{\partial x} = \ 0 \tag{4}$$

A solution to Equation (1) under the initial and boundary conditions in Equations (2) through (4) was provided by Wexler (1992) as:

$$C^k(x,t) = C_0^k A(x,t) + \left(C_1^k - C_0^k\right)A(x, t - t_1) + \cdots + \left(C_n^k - C_{n-1}^k\right)A(x, t - t_n) \tag{5}$$

where: C_n = solute concentration of nth influent [M/L^3], t_n = time to change to the nth influent [T], and L = length of domain [L]. It is important to note that the time to change to the first influent (t_0) is zero and the concentration of first influent is denoted as C_0.

$$A(x,t) = \frac{1}{2}\left[erfc\left(\frac{x - v^k t}{2\sqrt{D^k t}}\right) + exp\left(\frac{v^k x}{D^k}\right) erfc\left(\frac{x + v^k t}{2\sqrt{D^k t}}\right)\right] \tag{6}$$

where: A(x,t) is a dimensionless function that is defined using the complimentary error function, erfc [dimensionless] and accounts for the effects of advection and dispersion of the solute.

Equation (5) can be written for any number of changes in the influents. For example, from groundwater to river water to groundwater or from groundwater to vadose zone water to river water to groundwater.

Table 4.1 Influent changes for river water injection test

Influent	Concentration Term	Coefficient Term
Groundwater	C_{gw}	A(x,t)
River water	$C_{rw} - C_{gw}$	$A(x,t - t_1)$
Groundwater	$C_{gw} - C_{rw}$	$A(x,t - t_2)$

$$C^k(x,t) = C^k_{gw}A(x,t) + \left(C^k_{rw} - C^k_{gw}\right)A(x,t-t_1) + \left(C^k_{gw} - C^k_{rw}\right)A(x,t-t_2) \quad (7)$$

Table 4.2 Influent changes for river water infiltration tests

Influent	Concentration Term	Coefficient Term
Groundwater	C_{gw}	A(x,t)
Vadose zone water	$C_{vzw} - C_{gw}$	$A(x,t - t_1)$
River water	$C_{rw} - C_{vzw}$	$A(x,t - t_2)$
Groundwater	$C_{gw} - C_{rw}$	$A(x,t - t_3)$

$$C^k(x,t) = C^k_{gw}A(x,t) + \left(C^k_{vzw} - C^k_{gw}\right)A(x,t-t_1) + (C^k_{rw} - C^k_{vzw})A(x,t-t_2) + \left(C^k_{gw} - C^k_{rw}\right)A(x,t-t_3) \quad (8)$$

Breakthrough curves for the added halide were fitted using three parameters: 1) observation distance (x) for mean arrival time, time to change influent (t_n) for area under the curve, and dispersion (D) for spread.

For added tracers in river water injection and infiltration tests, the concentration in river water (C_{rw}) was set to measured values, while concentrations in vadose zone water (C_{vzw}) and groundwater (C_{gw}) were set to the lower detection limit. For non-added chloride and uranium, C_{gw} was set to measured groundwater concentrations in all three tests. In injection test simulations, C_{rw} for chloride and uranium was set as measured river water concentrations. In infiltration test simulations, C_{vzw} and C_{rw} were used as fitting parameters, informed by pore water data from Roycroft (2017). The time t_1, representing the duration required to reach steady-state background groundwater conditions, was set to 100 days and subtracted to adjust the initial phase of the breakthrough curve. The implementation of the analytical model, and the fitting of breakthrough curves, are available at GitHub.

4.3 Results and Discussions

The simulated results, along with the corresponding observed data, are presented in the following sections to analyze the behavior of added tracers, chloride, and uranium during one

injection test and two infiltration tests. These results and their interpretations are as follows: (1) River Water Injection Test (Section 3.1), (2) River Water Infiltration Test: Flood-1 (Year-1) (Section 3.2), (3) River Water Infiltration Test: Flood-2 (Year-2) (Section 3.3), (4) Summary of the mechanistic insights interpreted from the data and calibrated model (Section 3.4)

4.3.1 River Water Injection Test

4.3.1.1 Added Tracers (Halide and Benzoate)

Model simulations were conducted for the two highest signal wells, W1005 and W1011, to evaluate solute transport behavior in the saturated zone. For W1005, the model effectively captured the leading edge, rise to peak concentration, and trailing decline of the observed iodide tracer data within ±10% uncertainty bounds (Fig. 4.4). Similarly, for W1011, the model reproduced the shape of the leading and trailing concentration fronts of the iodide data. However, for both wells, the model did not capture the observed double-hump pattern. Subsurface characterization from nearby Backhoe Trench (BHT-1 and BHT-2) profiles indicated that the saturated zone consisted of poorly sorted gravel interbedded with finer sandy materials (DOE, 2016), suggesting centimeter- to decimeter-scale macropores (Hendrickx et al., 1993). These heterogeneities might create multiple flow paths with distinct velocities, leading to temporally separated solute arrivals and the observed double-hump breakthrough behavior (Siirila-Woodburn et al., 2015).

The parameters used to fit the halide tracer data included observation distance (x), time (t_2) when the river water (C_{rw}) switched to background groundwater (C_{gw}), and dispersion coefficient (D) (Table 4.3). For W1005, the fitted values were x = 4.8 ft, t_2 = 102.7 days, and D = 2.9 ft²/day. In comparison, W1011 had x = 10.48 ft, t_2 = 100.72 days, and D = 0.9 ft²/day. The higher dispersion coefficient in W1005 suggested greater subsurface heterogeneity and more complex flow

pathways compared to W1011, indicating increased mixing and spreading of the tracer, likely due to tortuous preferential flow paths (Gelhar et al., 1992). In contrast, the lower dispersion coefficient in W1011 suggested less pronounced heterogeneity than W1005, resulting in reduced tracer spreading (Bear, 1979).

The parameter values used for halide transport (Table 4.3) were subsequently applied to simulate benzoate transport. The model captured the leading edge of the benzoate breakthrough curves at both wells, although it underpredicted the extent of tailing at W1011. The pronounced tailing observed in both wells was consistent with strong velocity contrasts and solute channeling along preferential flow paths (Bianchi and Pedretti, 2017). The ability of the model to reasonably fit both tracers using a consistent parameter set suggested that the transport behavior of these non-reactive solutes was similar and primarily controlled by advection and hydrodynamic dispersion within the saturated zone. This outcome was consistent with findings reported by Paradis et al. (2022).

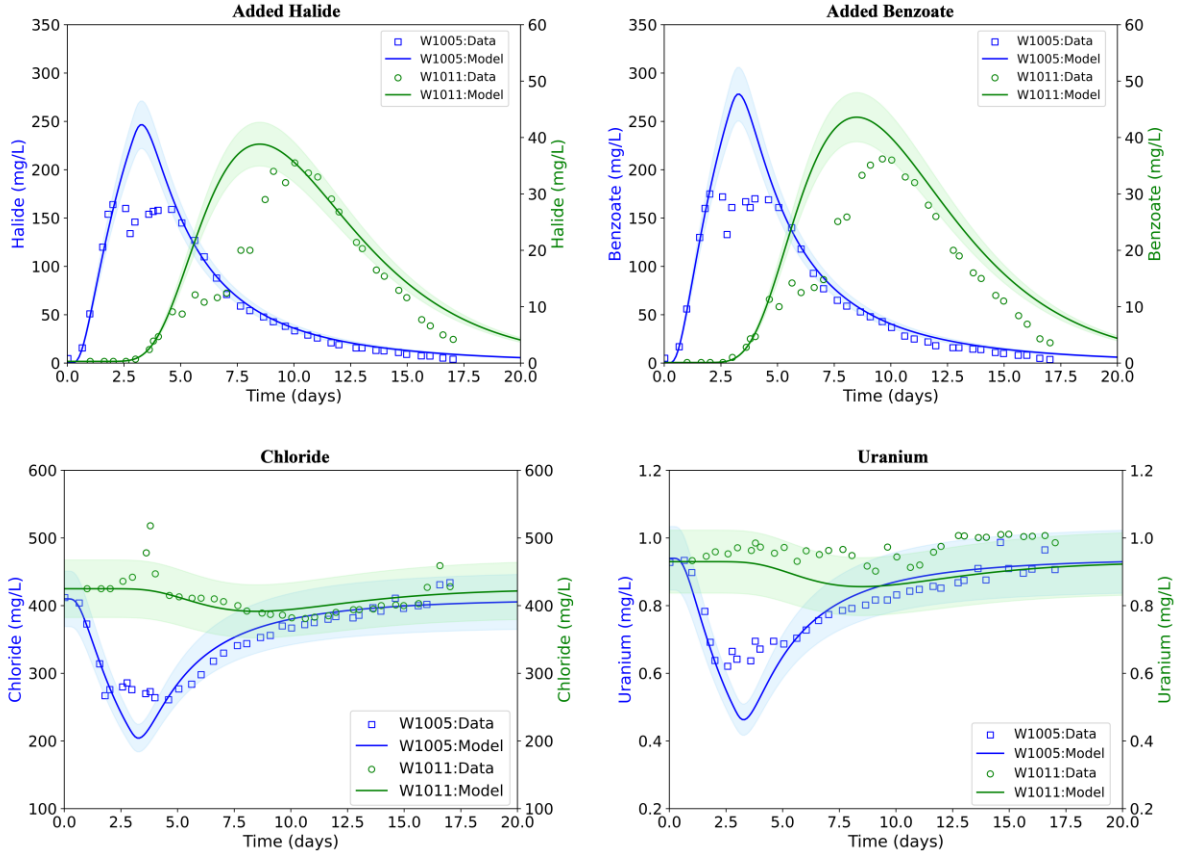

Figure 4.4 Breakthrough curves of solutes during direct river water injection. Measured concentrations are shown as open squares (W1005) and open circles (W1011); model simulations are shown as solid lines (blue for W1005, green for W1011) with ±10% uncertainty bands (shaded region). Top panels show added tracers (halide and benzoate), and bottom panels show background solutes (chloride and uranium).

Table 4.3 Fitted parameters and moments in direct river water injection test

TW1005 Analyte→ Parameters↓	Halide	Benzoate	Chloride	Uranium
C_{gw} (mg/L)	0.3	0.1	410	0.940
C_{rw} (mg/L)	482	544	7.6	0.007
t_1 (days)	100	100	100	100
t_2 (days)	102.7	102.7	102.7	102.7
v (ft/day)	1	1	1	1
x (ft)	4.8 (M=5.32)	4.8	4.8	4.8
D (ft^2/day)	2.9	2.9	2.9	2.9
TW1011 Analyte→ Parameters↓	Halide	Benzoate	Chloride	Uranium
C_{gw} (mg/L)	0.3	0.1	425.0	0.930

C_{rw} (mg/L)	482.0	544.0	7.6	0.007
t_1 (days)	100	100	100	100
t_2 (days)	100.72	100.72	100.72	100.72
v (ft/day)	1	1	1	1
x (ft)	10.48 (M=10.31)	10.48	10.48	10.48
D (ft^2/day)	0.9	0.9	0.9	0.9

4.3.1.2 Non-added Solutes (Chloride and Uranium)

Model simulations were conducted for the two high-signal wells, W1005 and W1011, to evaluate chloride and uranium transport (Fig. 4.4) in the saturated zone, using the previously calibrated parameter set with the added halide tracer.

For chloride in W1005, the model accurately captured the observed trend of an initial decline followed by a gradual recovery within ±10% uncertainty bounds. This pattern reflected the dilution of chloride-rich background groundwater (~410 mg/L) by the injected low-chloride river water (~7.6 mg/L), followed by a rebound toward background levels. The model reproduced the general timing and shape of both the dilution and rebound phases; however, it did not replicate the double-dip feature evident in the data. In contrast, the model for chloride in W1011 showed a smaller degree of dilution, which was consistent with the observed data. This suggested a more limited influence of the injected river water at W1011, likely due to its greater distance (x=10.48 ft versus 4.8 ft) from the injection point.

For uranium, the model for W1005 also captured the general trend, an initial decline due to dilution by low-uranium river water (~0.007 mg/L), followed by a gradual rebound toward background levels (~0.940 mg/L). Most observed values fell within the ±10% uncertainty range, indicating a reasonable fit despite some variability. At W1011, uranium concentrations remained relatively stable throughout the monitoring period, and the model closely matched this trend, further suggesting minimal impact from the injected water at that location.

Importantly, the single parameter set (Table 4.3) calibrated using halide data yielded consistent fits for both the added (halide) and background (chloride and uranium) solutes. This consistency suggested that advection and hydrodynamic dispersion governed the transport behavior of all solutes in the saturated zone during the direct river water injection test, aligning with the behavior in Scenario 1 (Fig 4.1) and findings of Paradis et al. (2022).

4.3.2 River Water Infiltration Test: Flood-1 (Year-1)

4.3.2.1 Added Solutes (halide and benzoate)

Model simulations were conducted for wells W1001, W1005, and W1011, which exhibited the highest signal responses, to assess solute transport behavior in the vadose zone. The model effectively reproduced the leading edges and trailing concentrations of the observed breakthrough curves of halide for all three wells (Fig. 4.5). However, consistent with results from the injection experiment, the model did not capture the double-hump observed in W1005. Subsurface characterization from nearby Backhoe Trench profiles (BHT-1 and BHT-2; DOE, 2016) indicated a vadose zone composed of silt and clay, and a saturated zone consisting of poorly sorted gravel interbedded with finer sandy materials. These sedimentary structures suggested centimeter- to decimeter-scale macropores and layered heterogeneities extending across both zones, likely generating multiple flow paths with distinct velocities (Hendrickx et al., 1993). Such conditions potentially explained the double-hump breakthrough curve observed in W1005, which was not captured by the model.

The model was fitted using four key parameters (Table 4.4): observation distance (x), time (t_2) when the vadose zone water (C_{vzw}) switched to river water (C_{rw}), time (t_3) when the river water switched back to background groundwater (C_{gw}), and dispersion coefficient (D). The fitted values for these parameters varied among wells, reflecting differences in solute transport conditions

across the site. For W1001, the best-fit values were x = 8.7 ft, t_2 = 101.03 days, t_3 = 105.5 days, and D = 0.25 ft²/day. For W1005, the fitted values were x = 11.1 ft, t_2 = 100.5 days, t_3 = 108.8 days, and D = 1.5 ft²/day. W1011 was characterized by x = 17 ft, t_2 = 100.5 days, t_3 = 107.9 days, and D = 0.55 ft²/day.

Dispersion coefficients varied notably across the wells, consistent with differences in flow path complexity and subsurface heterogeneity. The lowest dispersion in W1001 (D = 0.25 ft²/day) indicates relatively homogeneous pathways, while the highest in W1005 (D = 1.5 ft²/day) suggested complex preferential flow. The intermediate value in W1011 (D = 0.55 ft²/day) reflected moderate solute spreading over a longer distance, consistent with increased dispersion due to velocity variations in heterogeneous media (Gelhar et al., 1992).

The same parameter sets (Table 4.4) used to simulate halide transport were also applied to benzoate. The model reproduced the timing and overall shape of benzoate breakthrough curves in all three wells (Fig. 4.5), capturing leading fronts and peak concentrations in W1001 and W1011 and closely following the general trend in W1005. The consistent performance across halide and benzoate tracers indicated that both were transported conservatively, primarily governed by advection and hydrodynamic dispersion under the test conditions, consistent with previous findings (Sultana et al., 2024b).

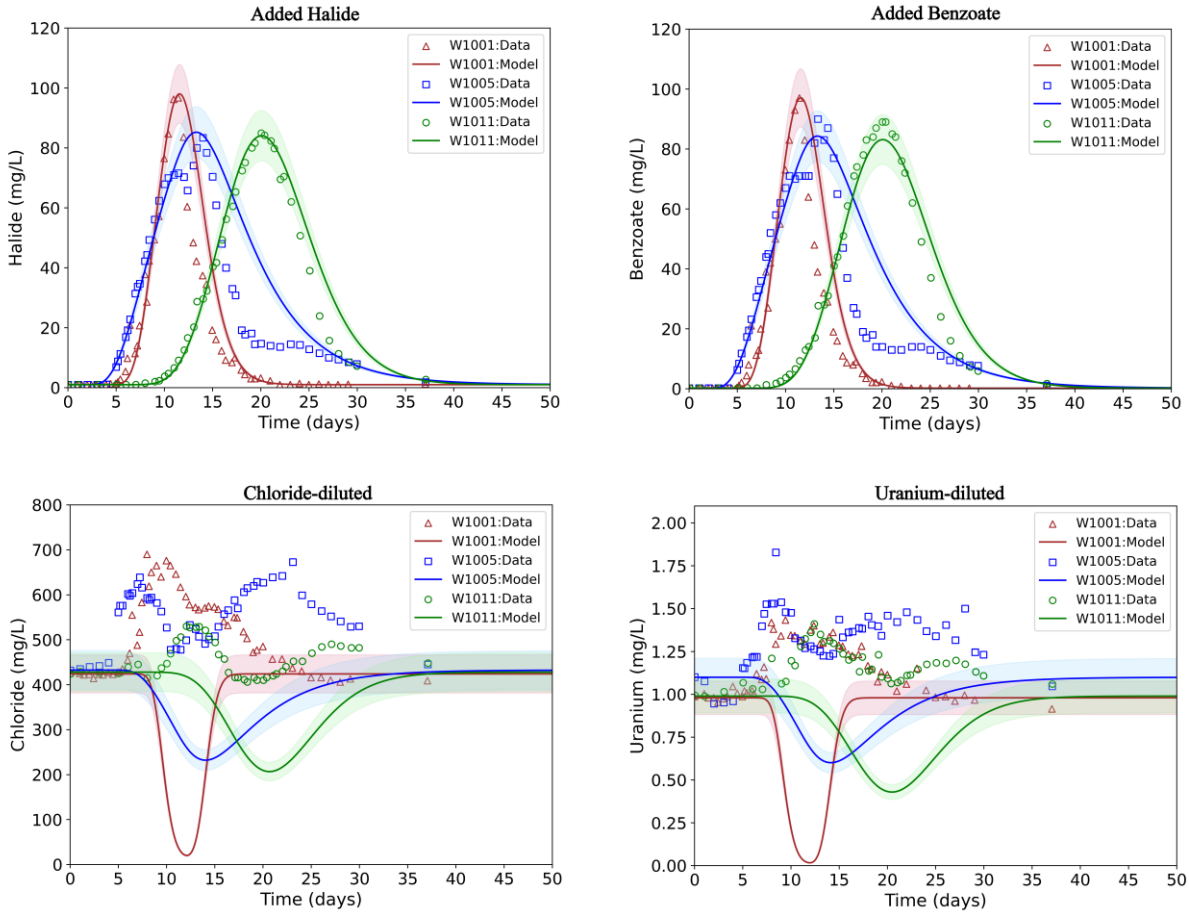

Figure 4.5 Breakthrough curves of solutes during river infiltration test-01. Measured concentrations are shown as open triangles (W1001), open squares (W1005) and open circles (W1011); model simulations are shown as solid lines with ±10% uncertainty bands (red for W1001, blue for W1005, green for W1011). Top panels show added tracers (halide and benzoate), and bottom panels show non-added solutes (chloride and uranium).

Table 4.4 Fitted parameters and moments in river infiltration test – 01 (Flood-1)

TW1001 Analyte→ Parameters↓	Halide	Benzoate	Chloride	Uranium
C_{gw} (mg/L)	1.0	0.2	424	0.98
C_{vzw} (mg/L)	1.0	0.2	890 (C_{gw}*2.1)	2 (C_{gw}*2.1)
C_{rw} (mg/L)	131	130	560 (C_{gw}*1.3)	1.3 (C_{gw}*1.3)
t_1 (days)	100	100	100	100
t_2 (days)	101.03	101.03	101	100.6
t_3 (days)	105.5	105.5	105.5	105.5
v (ft/day)	1	1	1	1
x (ft)	8.7 (M=11.92)	8.7	8.7	8.7

D (ft^2/day)	0.25	0.25	0.05	0.05
TW1005 Analyte→ Parameters↓	Halide	Benzoate	Chloride	Uranium
C_{gw} (mg/L)	1.0	0.2	432.5	1.1
C_{vzw} (mg/L)	1.0	0.2	1514 (C_{gw}*3.5)	2.4 (C_{gw}*2.2)
C_{rw} (mg/L)	131	130	1211 (C_{gw}*2.8)	2.2 (C_{gw}*2)
t_1 (days)	100	100	100	100
t_2 (days)	100.5	100.5	103.2	103.5
t_3 (days)	108.8	108.8	108.8	108.8
v (ft/day)	1	1	1	1
x (ft)	11.1 (M=14.69)	11.1	11.1	11.1
D (ft^2/day)	1.5	1.5	1.5	1.5
TW1011 Analyte→ Parameters↓	Halide	Benzoate	Chloride	Uranium
C_{gw} (mg/L)	1.0	0.2	428	0.99
C_{vzw} (mg/L)	1.0	0.2	1284 (C_{gw}*3)	4.9 (C_{gw}*5)
C_{rw} (mg/L)	131	131	642 (C_{gw}*1.5)	1.5 (C_{gw}*1.5)
t_1 (days)	100	100	100	100
t_2 (days)	100.5	100.5	102	101.5
t_3 (days)	107.9	107.9	107.9	107.9
v (ft/day)	1	1	1	1
x (ft)	17 (M=20.21)	17	17	17
D (ft^2/day)	0.55	0.55	0.55	0.55

4.3.2.2 Non-Added Solutes (Chloride and Uranium)

Model simulations were conducted for the wells W1001, W1005, and W1011, to evaluate chloride and uranium transport in the vadose zone, using parameter sets previously calibrated with iodide tracer data (Table 4.4). In these simulations, the concentrations were defined with $C_{vzw} = C_{gw}$, consistent with the tracer concentration pattern, with $C_{rw} < C_{gw}$. Under these conditions, however, the model did not reproduce the timing or overall shape of the observed breakthrough curves for either chloride or uranium in any of the wells. While the measured data consistently exhibited a distinct concentration peak (or hump) for these reactive solutes, the model instead showed a systematic concentration dip during the same period. This behavior aligned with the conceptual framework of Scenario 1 in Figure 4.1, where instantaneous mixing

of low-concentration C_{rw} with higher concentrations of C_{vzw} and C_{gw} produced a dilution response in the saturated zone.

This discrepancy highlighted the contrast in transport behavior between non-reactive tracers and reactive solutes during infiltration through the vadose zone. While the transport of halide and benzoate could be effectively captured by advection and hydrodynamic dispersion alone, the breakthrough patterns of chloride and uranium evidently involved additional mechanisms. The inability of the halide-calibrated parameter sets to capture the breakthrough features of chloride and uranium reinforced the conclusion that their mobilization during infiltration was governed by more complex processes in addition to the advection and dispersion.

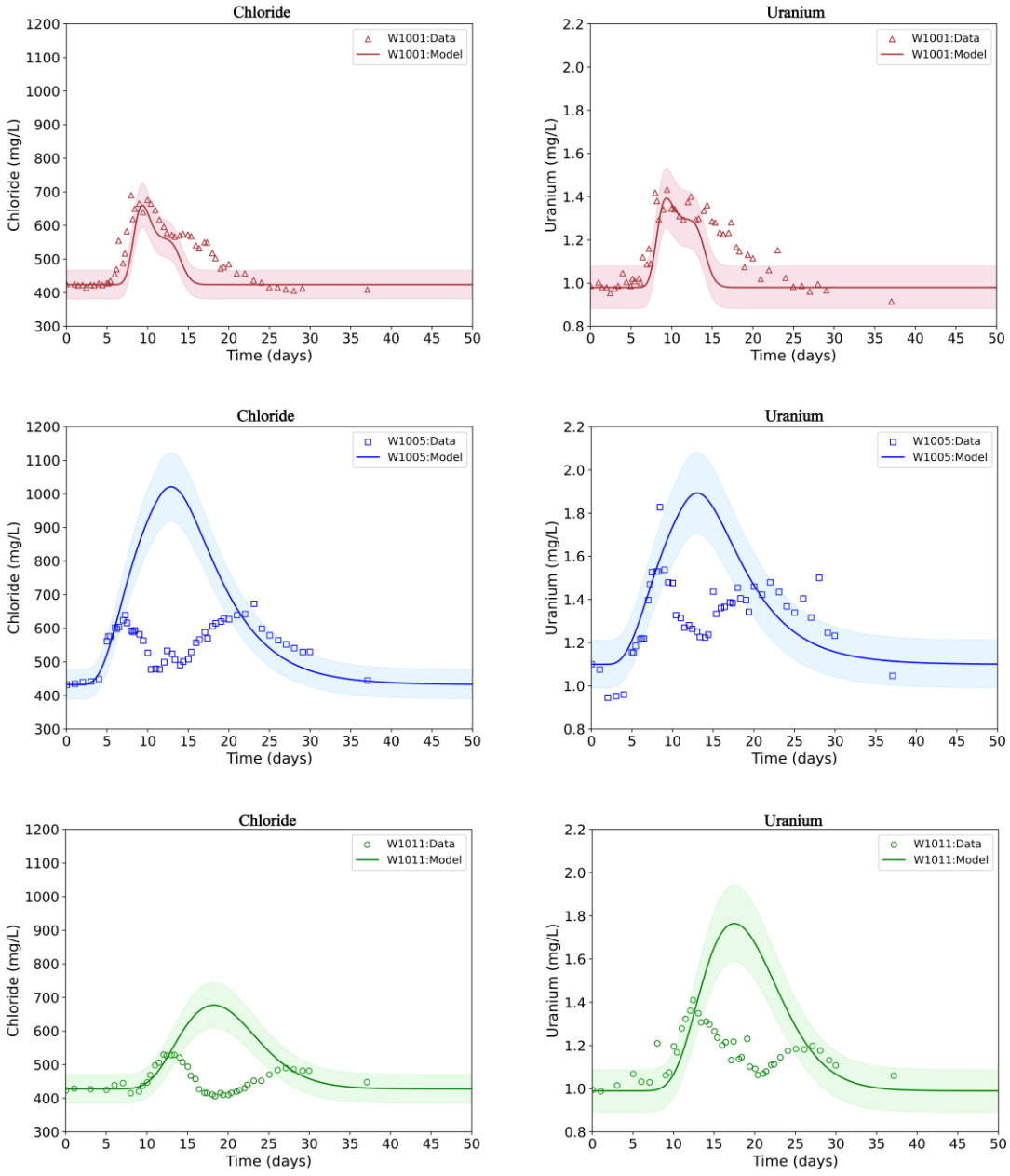

Figure 4.6 Breakthrough curves of solutes during river infiltration test-01. Measured concentrations are shown as open triangles (W1001) open squares (W1005) and open circles (W1011); model simulations (red for W1001, blue for W1005, green for W1011) are shown as solid lines with ±10% uncertainty bands (shaded region). The left panels show chloride, and right panels show uranium.

Figure 4.6 presents model simulations for chloride and uranium transport in the vadose zone at wells W1001, W1005, and W1011, under conditions where river water (C_{rw}) and vadose zone water (C_{vzw}) concentrations were elevated relative to background groundwater (C_{gw}).

Breakthrough curves for chloride (left panels) and uranium (right panels) are shown for W1001 (top), W1005 (middle), and W1011 (bottom). Compared to earlier simulations that used parameter sets derived from non-reactive tracer behavior (Fig. 4.5), the simulations in Figure 4.6 more accurately captured both the timing and shape of the observed breakthrough curves for chloride and uranium across all three wells. In each case, the data exhibited an early hump followed by an extended tail, characteristic of dual-source solute transport.

In W1001, the model effectively reproduced the sharp initial rise and peak concentrations for both solutes, followed by a gradual decline to background levels, indicating strong alignment with observed trends. Similarly, in W1005, the model closely matched the timing and shape of the observed peaks, while in W1011, it captured the key breakthrough features, including peak magnitude and arrival time.

Model calibration (Table 4.4) involved adjusting t_2, the dispersion coefficient (D), and source concentrations for C_{rw} and C_{vzw}, while holding the observation distance (x) and t_3 fixed at values used in the non-reactive tracer simulations. Influent concentrations varied across wells to reflect field observations, where a consistent relationship of $C_{gw} < C_{rw} < C_{vzw}$ was observed for both solutes. While dispersion coefficients (0.25 ft^2/day) from the halide fits performed well in W1005 and W1011, a lower value (0.05 ft^2/day versus 0.25 ft^2/day) was needed in W1001 to replicate the observed sharp peaks. This suggested that in W1001, reactive solutes were transported through more uniform flow paths with fewer macropores or lithologic heterogeneities compared to the more complex and dispersive conditions in W1005 and W1011. These observations were consistent with prior findings that link increased dispersion to greater subsurface heterogeneity (Gelhar et al., 1992; Tajima et al., 2024).

Model performance improved considerably when elevated C_{vzw} and C_{rw} values were incorporated, consistent with field observations during Flood-1 (Sultana et al., 2024b). The initial peak, elevated C_{vzw} values likely resulted from the flushing of contaminant-rich porewater via a compression wave mechanism, which accelerated downward porewater displacement and led to early breakthrough and sharp concentration peaks (Gross et al., 2003; Amiaz et al., 2011; Sorek and Bear, 1990). This wave displaced concentrated porewater ahead of the floodwater front, leading to dilution during transport to the saturated zone (Du Laing et al., 2007; Nativ et al., 1995; Warrick et al., 1971). Elevated C_{rw} values were attributed to mobilization of evaporite salts enriched in chloride and uranium during infiltration. These salts, formed during antecedent dry periods, were dissolved by incoming floodwater, releasing both solutes into the system (Dahan et al., 2008; Johnson et al., 2016). Site reports (DOE, 2016) and fieldwork for this study documented the presence of evaporite crusts in both the surface soil and vadose zone, supporting this mechanism. These evaporites in the vadose zone contain oxidized U(VI)-containing phases (Looney et al., 2014; Tolar et al., 2020). Additionally, the vadose zone is composed of silty clay layers containing clay minerals (e.g., smectite) and ferrihydrite, which are known sorbents for U(VI) (Abdelouas et al., 2006; Waite et al., 1994; Sultana et al., 2024a). Upon infiltration, sorbed U(VI) might have been partially desorbed (Qafoku et al., 2005), contributing further to the observed uranium breakthrough in combination with dissolution of uranium-rich evaporites (Johnson et al., 2016).

Incorporating elevated source concentrations for C_{rw} and C_{vzw} concentrations significantly improved model agreement with observed chloride and uranium breakthrough behavior. This outcome is consistent with Scenario 3 (Figure 4.1), where the vadose zone contains both contaminant-rich porewater and solid-phase sources (e.g., evaporites). In this scenario, infiltrating

river water mobilizes both sources, producing a double-hump breakthrough curve characterized by an initial peak from porewater flushing, followed by a prolonged release from evaporite dissolution and uranium desorption. However, the assumption of uniform porewater flushing may oversimplify the process since vadose zone heterogeneity strongly impacts infiltration (Perzan et al., 2023). Spatial variability in microtopography, soil texture, or antecedent moisture could result in non-uniform flushing efficiency, potentially affecting both the timing and magnitude of the initial breakthrough peak (Warrick et al., 1971).

4.3.3 River Water Infiltration Test: Flood-2 (Year-2)

4.3.3.1 Added Solutes (Halide)

Model simulations were conducted to evaluate halide transport behavior in the vadose zone for wells W1000, W1005, and W1010, which exhibited the highest signal responses (Fig. 4.7). Notably, while W1005 was monitored during both infiltration events, the other two wells exhibiting high signals during Flood-2 (W1000 and W1010) differed from those in the first event. Unlike Flood-1, where only W1005 displayed a distinct double-hump breakthrough curve, all three wells showed this characteristic pattern during Flood-2. This shift suggested altered flow dynamics between the two events, potentially due to local-scale heterogeneity in the newly selected wells contributing to the observed double-hump responses across the site (Siirila-Woodburn et al., 2015). Despite these complexities, the model effectively captured the leading edges and tailing behavior of the breakthrough curves for W1000 (red triangles), W1005 (blue squares), and W1010 (green circles).

Model calibration (Table 4.5) involved fitting the observation distance (x), the transition time from vadose zone water to river water (t_2), the return time to background groundwater conditions (t_3), and the dispersion coefficient (D). The fitted parameter values varied across wells,

reflecting differences in transport conditions. For W1000, the best-fit values were x = 7 ft, t_2 = 103 days, t_3 = 111 days, and D = 0.45 ft²/day. For W1005, the fitted values were x = 8 ft, t_2 = 105.5 days, t_3 = 113.8 days, and D = 1.8 ft²/day. W1010 was characterized by x = 19 ft, t_2 = 107 days, t_3 = 115 days, and D = 1.15 ft²/day. These variations in dispersion coefficients reinforced the interpretation that solute spreading was shaped by localized heterogeneity and differences in hydraulic connectivity among wells (Gelhar et al., 1992).

The consistent performance of the model for the tracer data suggested that solute transport was primarily governed by advection and hydrodynamic dispersion during floods, aligning with findings from previous studies (Sultana et al., 2024b).

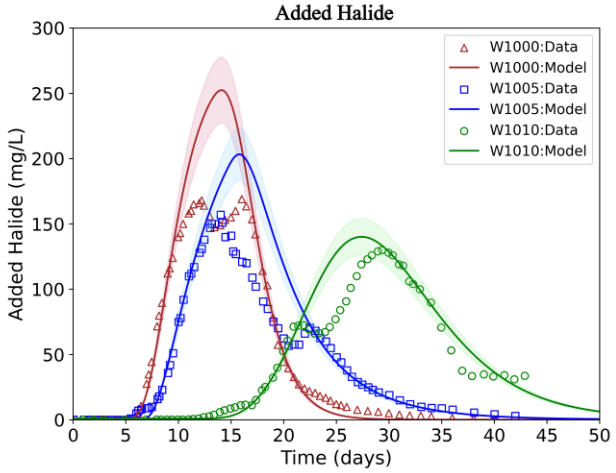

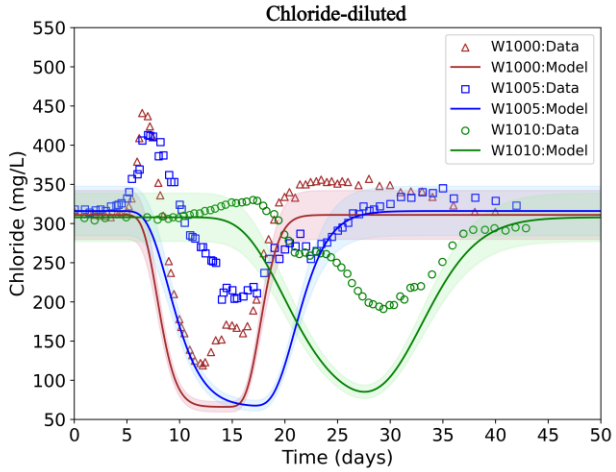

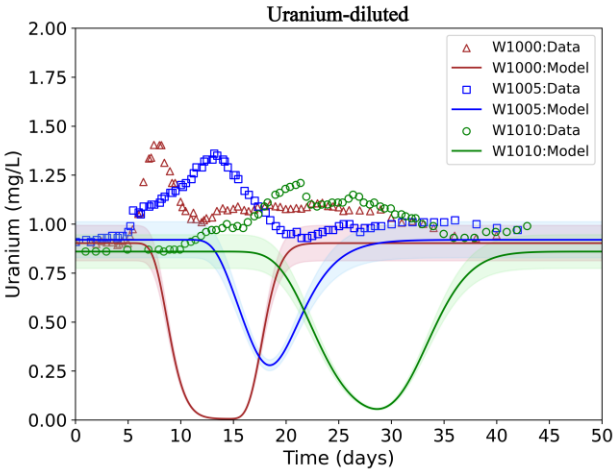

Figure 4.7 Breakthrough curves of solutes during river infiltration test-01. Measured concentrations are shown as open triangles (W1001) open squares (W1005) and open circles (W1011); model simulations (red for W1001, blue for W1005, green for W1011) are shown as solid lines with ±10% uncertainty bands (shaded region). The left panels show chloride, and right panels show uranium.

Table 4.5 Fitted parameters and moments in river infiltration test – 02 (Flood-2)

TW1000 Analyte→ Parameters↓	Halide	Chloride	Uranium
C_{gw} (mg/L)	0.2	311	0.903
C_{vzw} (mg/L)	0.2	777.5 (C_{gw}*2.5)	1.8 (C_{gw}*2)
C_{rw} (mg/L)	275	118 (C_{gw}*0.4)	1 (C_{gw}*1.1)
t_1 (days)	100	100	100
t_2 (days)	103	101.2	102
t_3 (days)	111	111	111
v (ft/day)	1	1	1
x (ft)	7 (M=13.13)	7	7
D (ft^2/day)	0.45	0.11	0.11
TW1005 Analyte→ Parameters↓	Halide	Chloride	Uranium
C_{gw} (mg/L)	0.2	316	0.92
C_{vzw} (mg/L)	0.2	695 (C_{gw}*2.2)	1.42 (C_{gw}*1.5)
C_{rw} (mg/L)	275	190 (C_{gw}*0.6)	0.87 (C_{gw}*0.95)
t_1 (days)	100	100	100
t_2 (days)	105.5	101.8	108.7
t_3 (days)	113.8	113.8	113.8
v (ft/day)	1	1	1
x (ft)	8 (M=16.56)	8	8
D (ft^2/day)	1.8	0.3	0.5
TW1010 Analyte→ Parameters↓	Halide	Chloride	Uranium
C_{gw} (mg/L)	0.2	308	0.86
C_{vzw} (mg/L)	0.2	539 (C_{gw}*1.7)	1.5 (C_{gw}*1.8)
C_{rw} (mg/L)	275	154 (C_{gw}*0.5)	1.04 (C_{gw}*1.2)
t_1 (days)	100	100	100
t_2 (days)	107	102	104
t_3 (days)	115	115	115
v (ft/day)	1	1	1
x (ft)	19 (M=26.28)	19	19
D (ft^2/day)	1.15	0.38	0.6

4.3.3.2 Non-Added Solutes (Chloride and Uranium)

In Flood-2, the parameter sets (Table 4.5) previously developed for halide transport were applied to simulate the breakthrough behavior of chloride and uranium (Fig. 4.5), using concentration assumptions of $C_{vzw} = C_{gw}$ and $C_{rw} < C_{gw}$. As observed in Flood-1, these

conditions resulted in poor agreement between model predictions and observed breakthrough curves for the reactive solutes. The model could not reproduce the double-peak patterns observed in all three wells, instead predicting a concentration dip during the same period indicative of dilution from the mixing of low-concentration river water with higher concentrations already present in the groundwater, response conceptually aligned with Scenario 1 in Figure 4.1.

These discrepancies highlighted the limitations of using parameter sets derived from non-reactive tracers to simulate the transport of reactive solutes during infiltration. While chloride displayed a sharp initial peak followed by a gradual decline, suggesting semi-conservative behavior after the initial spike, uranium exhibited a more sustained elevation in concentration, indicative of ongoing mobilization. The limited ability of the halide-calibrated parameter sets to reproduce the breakthrough features of both chloride and uranium suggests that their transport during infiltration is influenced by additional mechanisms beyond advection and dispersion.

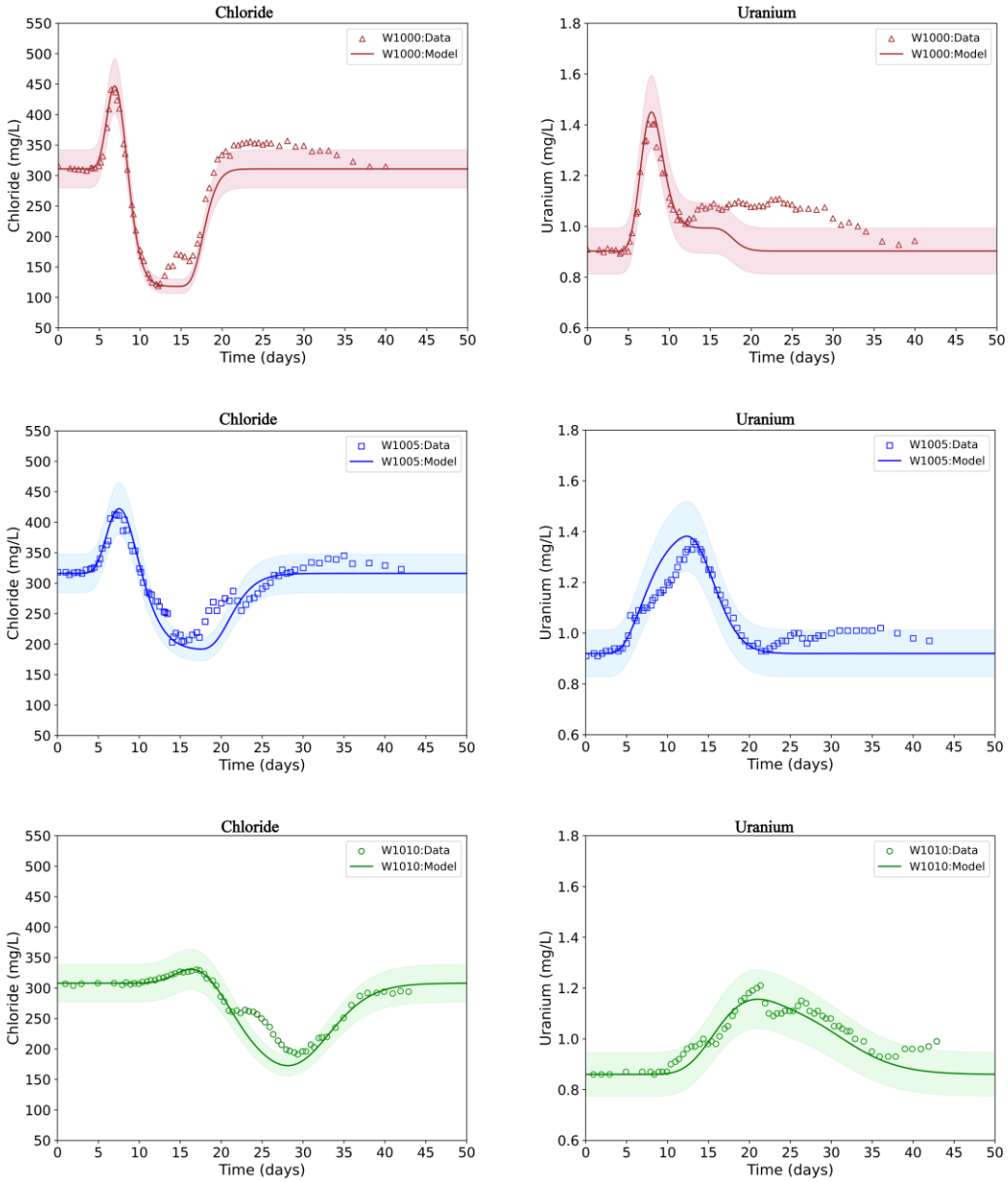

Fig. 4.8 Breakthrough curves of solutes during river infiltration test-01. Measured concentrations are shown as open triangles (W1000) open squares (W1005) and open circles (W1010); model simulations are shown as solid lines with ±10% uncertainty bands (red for W1000, blue for W1005, green for W1010). The left panels show chloride, and right panels show uranium.

Figure 4.8 presents breakthrough curves for chloride (left panels) and uranium (right panels) in wells W1000 (top), W1005 (middle), and W1010 (bottom) during Flood-2, under conditions where both vadose zone water (C_{vzw}) and river water (C_{rw}) were elevated relative to background groundwater (C_{gw}). Compared to earlier simulations using parameter sets derived from

non-reactive tracer behavior (Fig. 4.7), the model fits in Figure 4.8 more accurately reproduced the timing and general shape of the observed breakthrough curves for both chloride and uranium across all three wells. While chloride data exhibited an initial peak followed by a dip, uranium consistently showed an extended hump following the initial peak, similar to patterns observed during Flood-1.

In W1000, the model captured the sharp initial rise, peak concentrations, and gradual return to background levels for both solutes. In W1005, the model closely matched the timing and magnitude of the observed peaks, with minor deviations for chloride, likely due to local-scale heterogeneity not fully represented in the model. In W1010, the model reproduced the key breakthrough features, including peak magnitude and arrival time, for both chloride and uranium.

Model calibration (Table 4.5) involved adjusting the time (t_2) when vadose zone water switched to river water, dispersion coefficient (D), C_{vzw} and C_{rw}, while keeping observation distance (x), and time (t_3) when river water switched to background groundwater constant at halide simulation values.

Dispersion coefficients (D) for chloride and uranium were lower than those for halide. In W1000, D was 0.11 ft²/day for both solutes (versus 0.45 ft²/day for iodide); in W1005, D was 0.3 ft²/day for chloride and 0.5 ft²/day for uranium (versus 1.8 ft²/day); and in W1010, D was 0.4 ft²/day for chloride and 0.6 ft²/day for uranium (versus 1.15 ft²/day). These lower values reflected shorter transport distances for chloride and uranium mobilized from the vadose zone compared to surface-applied added halide, aligning with the direct relationship between travel distance and dispersion (Gelhar et al., 1992). This finding suggested that using non-reactive tracer-calibrated dispersion values for reactive solutes could overestimate subsurface spreading, potentially leading to conservative remedial design strategies.

Compared to Flood-1, the C_{vzw} values during Flood-2 were consistently much higher relative to C_{rw}, particularly for chloride, underscoring the continued dominance of vadose zone porewater mobilization as the primary transport mechanism. Here, influent concentrations varied across wells based on site-specific observations, where in all wells $C_{gw} < C_{rw} << C_{vzw}$ was consistently observed for chloride; and $C_{gw} < C_{rw} < C_{vzw}$ for uranium. The one-year interval between floods likely limited chloride precipitation due to its high solubility (Drever, 1982), while uranium precipitation remained possible only under specific geochemical conditions such as redox changes or the presence of complexing ligands (Langmuir, 1997). Moreover, due to silt and clay in the vadose zone, the vadose zone pore water can extend to a considerable amount (Johnson et al., 2016).

While vadose zone pore water contributions (C_{vzw}) remained prominent, especially for chloride; uranium transport during Flood-2 was influenced by additional processes. Notably, the river water in this event was amended with 1553 mg/L $NaHCO_3$, raising alkalinity to about 1.8× the background level (550 mg/L as $CaCO_3$). This addition was intended to enhance uranium desorption from vadose zone solids, forming aqueous U–CO_3 complexes (Qafoku et al., 2005) and thereby increasing U(VI) solubility and mobility. However, uranium mobilization increased only modestly, from 21% in Flood-1 to 24% in Flood-2 (Sultana et al., 2024b). This limited increase might be attributed to Flood-1 depleting much of the labile uranium from easily accessible binding sites on vadose zone solids, leaving fewer sites available for Flood-2. Additionally, competing processes such as precipitation or adsorption of U–CO_3 complexes onto aquifer solids could have further restricted uranium release (Zachara et al., 2013; Qafoku et al., 2005).

Overall, the results demonstrated that elevated C_{vzw} and C_{rw} relative to C_{gw}, enabled the model to effectively capture reactive solute behavior, which was evident in the data. During Flood-

2, chloride transport was still dominated by high C_{vzw} concentrations, producing sharp early peaks driven by compression wave-induced porewater flushing, consistent with Scenario 2 in Figure 1, where the vadose zone contained high contaminant-rich porewater. In contrast, uranium exhibited sustained transport, consistent with a dual-source mechanism involving both porewater displacement and solid-phase release (e.g., evaporite dissolution and sorbed uranium desorption). This pattern aligned with Scenario 3 in Figure 4.1 and reinforced conclusions drawn from Flood-1 (Sultana et al., 2024b) that chloride acted as a semi-conservative solute mobilized primarily by physical mechanisms, while uranium transport was governed by both physical and geochemical processes not accounted for by advection-dispersion alone.

4.3.4 Mechanistic Insights and Implications

The conceptual diagram (Fig. 4.9) illustrates contaminant (e.g., U and Cl) behavior in the subsurface during pre-injection, pre-infiltration, and post-test events. In semi-arid to arid regions, the partially saturated vadose zone (VZ) forms conservative (e.g., Cl rich) and non-conservative (e.g., U rich) evaporites during dry seasons. These evaporites, combined with shallow contaminated groundwater, become enriched with contaminants as evaporation and evapotranspiration occur. Additionally, metals [e.g., U(VI)] in evaporites sorb onto soil grains (e.g., clay and ferrihydrite [Fh]) under oxidized conditions in the VZ. Fluctuating water tables (e.g., due to river stages or wet-dry cycles) enrich the vadose zone pore water with contaminants from groundwater below.

During infiltration, the flood water wetting front mobilizes the pore water into groundwater via advection and dispersion, causing an initial concentration peak. Subsequently, evaporite dissolution releases contaminants, while metal ions desorb from soil grains, producing a breakthrough curve with a spike and extended hump post-infiltration. In contrast, if infiltration

only occurred in the saturated zone (e.g., through direct injection into groundwater), contaminant mobility would be governed only by advection and dispersion, with no additional mechanisms.

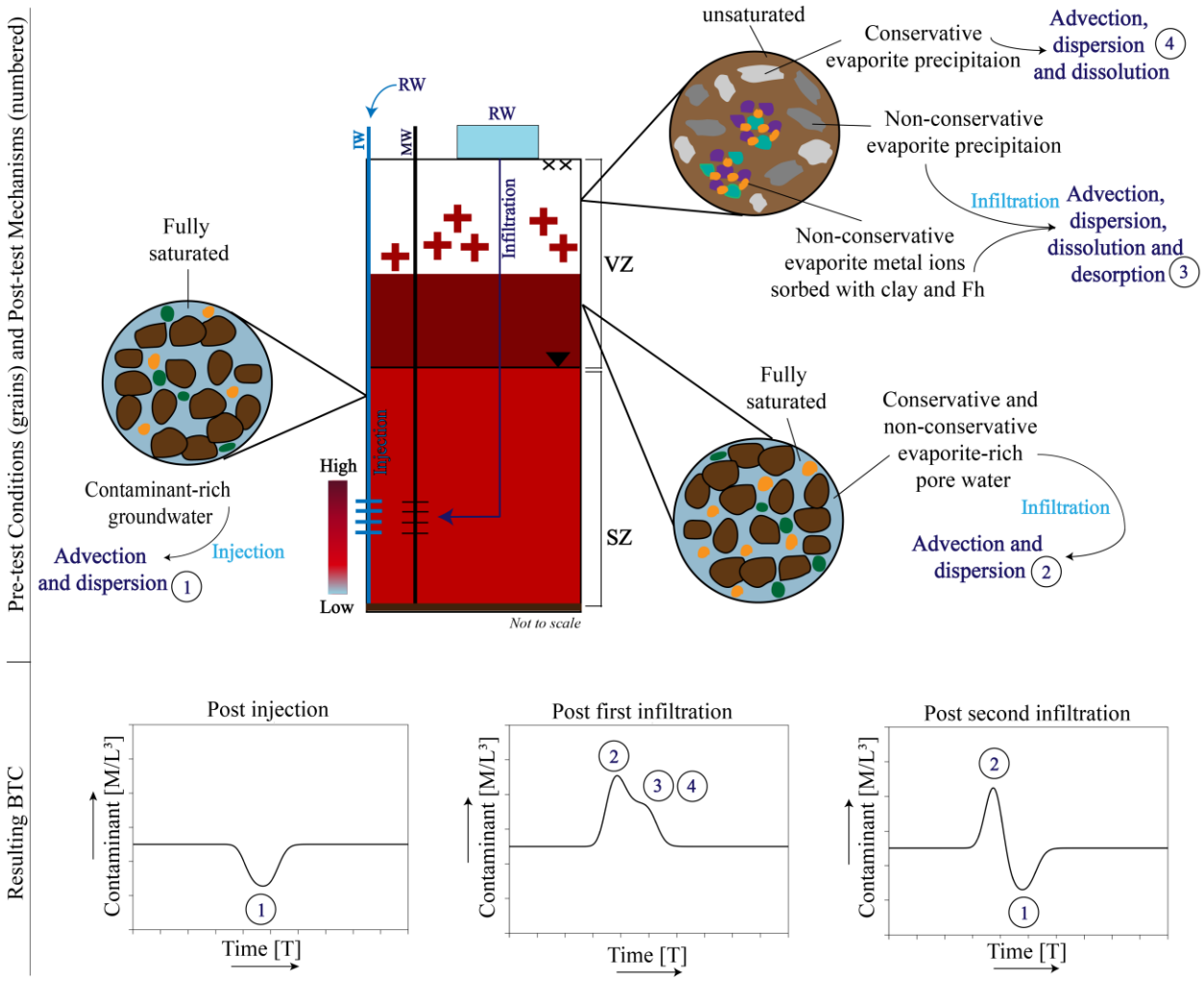

Fig. 4.9 Schematic of contaminant (e.g., U and Cl) mobilization mechanisms during flood tests (injection and infiltration), showing direct river water (RW) injection into the saturated zone (SZ) and RW infiltration through the vadose zone (VZ). Pre-test conditions are depicted with grains in each domain, with curved arrows indicating post-test mechanisms and the resulting breakthrough curves shown below. The legend shows contaminant levels.

The following table outlines the mobilization mechanisms of conservative and non-conservative evaporites across various test stages in a semi-arid to arid environment with shallow groundwater and evaporite deposits. These stages: pre-test, injection, infiltration, elapsed time, and post-test, illustrated the processes of advection, dispersion, precipitation-dissolution, and sorption-desorption that govern contaminant behavior in the vadose and saturated zones.

Table 4.6 Summary of contaminant release mechanisms during floods; the numbers as superscripts correspond to the mechanism numbers in the conceptual figure (Fig. 4.9)

Test stages	Mobilization Mechanisms	
	Conservative (e.g., Cl rich) evaporites and contaminants (e.g., Cl)	Non-conservative (e.g., U rich) evaporites and contaminants (e.g., U)
Pre test (Initial Conditions)	Evaporites precipitated and contaminants concentrated in vadose zone pore water (e.g., Scenario 3 in Fig. 4.1)	Evaporites precipitated, metal ions sorbed onto clay minerals (e.g., smectite) and ferrihydrite, and concentrated in vadose zone pore water (e.g., Scenario 3 in Fig. 4.1)
Injection (saturated zone)	Advection and dispersion[1]	Advection and dispersion[1]
Infiltration (vadose zone)	Advection and dispersion of contaminant-rich pore water[2], followed by advection, dispersion, and dissolution of evaporites[4]	Advection and dispersion of contaminant-rich pore water followed by dissolution of evaporites and metal ion desorption from clay minerals (e.g., smectite) and ferrihydrite[3]
Elapsed Time (1 year)	Contaminants dominantly concentrate in pore water over time (Scenario 2 in Fig. 4.1)	Contaminants concentrate in pore water over time, with reduced precipitation and sorption (Scenario 3 in Fig. 4.1)
Infiltration (vadose zone)	Advection and dispersion of contaminant-rich pore water[2] (e.g., Scenario 2 in Fig. 4.1)	Advection and dispersion of contaminant-rich pore water[2] followed by less dissolution of evaporites and desorption from clay minerals (e.g., smectite) and ferrihydrite[4]
Post Test	Contaminants reaccumulate in pore water due to river stage changes, with precipitation in evaporites	Contaminants reaccumulate in pore water due to river stage changes, with sorption onto soil and precipitation in evaporites

Mechanisms of mobilization during flood from the vadose zone are applicable to similar semi-arid to arid sites with shallow groundwater and evaporite deposits (DOE, 2018), including sites with Managed Aquifer Recharge applications (Interstate Technology & Regulatory Council, 2024). Vadose zone pore water might act as source (low river stage) and sink (high river stage) for

groundwater contaminants, contributing to plume persistence in the long term; with the pore water sustaining the contaminants.

4.4 Conclusions

The study employed a one-dimensional analytical model to inversely calibrate data from a series of field experiments, including a direct river water injection test and two infiltration tests, to characterize chloride and uranium mobilization mechanisms during flooding events. The results confirmed the hypothesis that the vadose zone significantly influences contaminant mobilization through contaminant-rich porewater flushing and contaminant-rich evaporite dissolution.

Modeling and experimental data from the river water injection test indicated that, within the saturated zone, chloride and uranium transport was governed primarily by advection and dispersion. In contrast, model and data from the river water infiltration experiments revealed that, in the vadose zone, transport mechanisms included not only advection and dispersion of contaminant-rich pore water ahead of the advancing river water front, but also the dissolution of contaminant-rich evaporites (chloride and uranium) and desorption (uranium), which contributed additional solute mass to the system. When river water with elevated alkalinity was used, the model and data showed that uranium mobilization in the vadose zone was further enhanced by desorption and evaporite dissolution, while chloride transport continued to be dominated by advective-dispersive movement of pore water.

A key finding of the study was that advection and dispersion of contaminant-rich vadose zone pore water would serve as the primary mobilization mechanism for contaminants during floods.

A limitation of the study is that the applied one dimensional model, with boundary conditions defined at the saturated zone, was used to represent processes occurring in variably saturated, three-dimensional system where lateral heterogeneity, macropore flow, and vertical stratification likely played significant roles. These dynamics were simplified in our 1D model, but the agreement with data suggested that the governing first-order processes were still captured.

These findings provided valuable insights for management and predictive modeling of contaminant mobilization during floods, helping to identify and quantify the primary processes that govern solute transport under dynamic hydrologic conditions. Specifically, the results underscored the need for incorporating not only physical transport mechanisms but also geochemically variable processes in the vadose zone, particularly during extreme infiltration events.

Funding

The authors express their sincere gratitude for the financial support from the National Science Foundation (NSF) under award number: 2229869 and the 2022 Geological Society of America (GSA) Graduate Student Research Grant: 13597-22.

Acknowledgements

The authors would like to thank the U.S. Department of Energy Office of Legacy Management for their invaluable support with site access, personnel, and funding to conduct field experiments, and overall technical assistance, provided through contract #DE-LM0000421 with Navarro Research and Engineering, Inc. (through March 30, 2021) and contract #89303020DLM000001 with RSI EnTech, LLC (after April 1, 2021).

References

Abdelouas, A., 2006. Uranium Mill Tailings: Geochemistry, Mineralogy, and Environmental Impact. Elements 2, 335–341. https://doi.org/10.2113/gselements.2.6.335

Amiaz, Y., Sorek, S., Enzel, Y., Dahan, O., 2011. Solute transport in the vadose zone and groundwater during flash floods. Water Resour. Res. 47 https://doi.org/10.1029/2011WR010747, 2011WR010747.

Alam, Md.S., Cheng, T., 2014. Uranium release from sediment to groundwater: influence of water chemistry and insights into release mechanisms. J. Contam. Hydrol. 164, 72–87. https://doi.org/10.1016/j.jconhyd.2014.06.001.

Bear, J., 1979. Hydraulics of groundwater, McGraw-Hill series in water resources and environmental engineering. McGraw-Hill International Book Co, London ; New York.

Bianchi, M., and Pedretti, D. (2017). Geological entropy and solute transport in heterogeneous porous media. Water Resour. Res. 53.

Bidwell, V.J., 2000. A formula for predicting advection-dispersion in the vadose zone at uneven drainage intervals. Water Resources Research 36, 3077–3080. https://doi.org/10.1029/2000WR900192

Chen, X., Romaniello, S.J., Herrmann, A.D., Wasylenki, L.E., Anbar, A.D., 2016. Uranium isotope fractionation during coprecipitation with aragonite and calcite. Geochim. Cosmochim. Acta 188, 189–207. https://doi.org/10.1016/j.gca.2016.05.022.

Dahan, O., Tatarsky, B., Enzel, Y., Kulls, C., Seely, M., Benito, G., 2008. Dynamics of flood water infiltration and ground water recharge in Hyperarid Desert. Groundwater 46, 450–461. https://doi.org/10.1111/j.1745-6584.2007.00414.x.

Dahan, O., 2020. Vadose Zone Monitoring as a Key to Groundwater Protection. Front. Water 2, 599569. https://doi.org/10.3389/frwa.2020.599569

Dam, W.L., Campbell, S., Johnson, R.H., Looney, B.B., Denham, M.E., Eddy-Dilek, C.A., Babits, S.J., 2015. Refining the site conceptual model at a former uranium mill site in Riverton, Wyoming, USA. Environ. Earth Sci. 74, 7255–7265. https://doi.org/ 10.1007/s12665-015-4706-y.

Destouni, G. 1991. Applicability of the steady state flow assumption for solute advection in fi eld soils. Water Resour. Res. 27:2129–2140.

Drever, J.I., 1982. The Geochemistry of Natural Waters. Prentice-Hall, Englewood Cliffs, N.J.

DOE, 1998. Final Site Observational Work Plan for the UMTRA Project Site at Riverton, Wyoming, Report No. U0013801.

DOE, 2016. 2015 Advanced Site Investigation and Monitoring Report Riverton, Wyoming, Processing Site, S14148 edn. United States Department of Energy Office of Legacy Management.

DOE, 2018. Plume Persistence Final Project Report.

DOE, 2021. Environmental Sciences Laboratory Procedures Manual: LMS/PRO/S04343- 4.1 (continuously updated). United States Department of Energy Office of Legacy Management, Grand Junction, CO, USA.

DOE, 2023. Applied Studies and Technology Persistent Secondary Contaminant Sources Data Release from Field Tracer Testing Studies at the Riverton, Wyoming, Processing Site (No. LMS/ESL/43015), AS&T- Persistent Secondary Contaminant Sources Data Release, Field Tracer Testing Studies at Riverton Site.

Dong, W., Brooks, S.C., 2006. Determination of the Formation Constants of Ternary Complexes of Uranyl and Carbonate with Alkaline Earth Metals (Mg 2+, Ca 2+, Sr 2+, and Ba 2+) Using Anion Exchange Method. Environ. Sci. Technol. 40, 4689–4695. https://doi.org/10.1021/es0606327.

Du Laing, G., Vanthuyne, D.R.J., Vandecasteele, B., Tack, F.M.G., Verloo, M.G., 2007. Influence of hydrological regime on pore water metal concentrations in a contaminated sediment-derived soil. Environ. Pollut. 147, 615–625. https://doi.org/ 10.1016/j.envpol.2006.10.004.

Freeze, R.A., Cherry, J.A., 1979. Physical properties and principles. In: Groundwater. Prentice-Hall, Englewood Cliffs, N.J, pp. 38–40.

Frohne, T., Rinklebe, J., Diaz-Bone, R.A., Du Laing, G., 2011. Controlled variation of redox conditions in a floodplain soil: impact on metal mobilization and biomethylation of arsenic and antimony. Geoderma 160, 414–424. https://doi.org/ 10.1016/j.geoderma.2010.10.012.

Gelhar, L.W., Welty, C., Rehfeldt, K.R., 1992. A critical review of data on field-scale dispersion in aquifers. Water Resources Research 28, 1955–1974. https://doi.org/10.1029/92WR00607

Gregory, R.W., 2019. Uranium Geology and Resources of the Gas Hills District, Wind River Basin. In: Central Wyoming: Wyoming State Geological Survey Public Information Circular, vol. 47, p. 31.

Gross, A., Besov, A., Diaz Reck, D., Sorek, S., Ben-Dor, G., Britan, A., Palchikov, E., 2003. Application of waves for remediation of contaminated aquifers. Environ. Sci. Technol. 37, 4481–4486. https://doi.org/10.1021/es026297d.

Hendrickx, J.M.H. and Flury, M., Uniform and preferential flow, Mechanisms in the vadose zone. In Conceptual Models of Flow and Transport in the Fractured Vadose zone. National Research Council, National Academy Press,Washington, D.C., pp. 149–187, 2001.

Johnson, R.H., Dam, W.L., Campbell, S., No¨el, V., Bone, S.E., Bargar, J.R., Dayvault, J., 2016. Persistent secondary contaminant sources at a former uranium mill site, Riverton, Wyoming, USA. In: Proceedings IMWA 2016. Presented at the Mining Meets Water – Conflicts and Solutions, Freiberg/Germany, pp. 398–404.

Hoss, Kendyl N. "Mass Transport of Uranium During Recharge of Surface Water to Contaminated Groundwater." Master's thesis, The University of Wisconsin-Milwaukee, 2022.

Interstate Technology & Regulatory Council (ITRC), 2024. Managed Aquifer Recharge: Case Studies. Available at: https://mar-1.itrcweb.org/case-studies/ (Accessed 24 June 2025)

Keefer, W.R., 1970. Structural Geology of the Wind River Basin, Wyoming (No. 495- D). Prepared in Cooperation with The Geological SURVEY of Wyoming and the Department of Geology of the University of Wyoming as Part of a Program of the Department of the Interior for development of the Missouri River basin.

Kent, R.D., Johnson, R.H., Laase, A.D., Nyman, J.L., 2024. Modeling evaluation of the impact of residual source material on remedial time frame at a former uranium mill site. J. Contam. Hydrol. 261, 104298 https://doi.org/10.1016/j. jconhyd.2024.104298

Knowlton Jr., R.G., Peterson, D.M., Zhang, H., 1997. Analysis of Natural Attenuation as the Preferred Ground Water Alternative at the DOE UMTRA Site near Riverton. Sandia National Laboratories, WY.

Langevin, C.D., Hughes, J.D., Banta, E.R., Niswonger, R.G., Panday, Sorab, and Provost, A.M., 2017, Documentation for the MODFLOW 6 Groundwater Flow Model: U.S. Geological

Survey Techniques and Methods, book 6, chap. A55, 197 p., https://doi.org/10.3133/tm6A55.

Langevin, C.D., Provost, A.M., Panday, Sorab, and Hughes, J.D., 2022, Documentation for the MODFLOW 6 Groundwater Transport Model: U.S. Geological Survey Techniques and Methods, book 6, chap. A61, 56 p., https://doi.org/10.3133/tm6A61.

Langmuir, D., 1997. Aqueous environmental geochemistry. Prentice Hall, Upper Saddle River, NJ.

Liu, C., Szecsody, J.E., Zachara, J.M., Ball, W.P., 2000. Use of the generalized integral transform method for solving equations of solute transport in porous media. Advances in Water Resources 23, 483–492. https://doi.org/10.1016/S0309-1708(99)00048-2

Looney, B. B., Denham, M. E., and Eddy-Dilek, C. A. (2014). *Independent Technical Evaluation and Recommendation for Contaminated Groundwater at the Department of Energy Office of Legacy Management Riverton Processing Site. Report No. STI-2014-00163* (Jackson, SC: Savannah River National Laboratory).

National Primary Drinking Water Regulations, 2024. EPA.gov. Last Modified on January 2 epa.gov/ground-water-and-drinking-water/national-primary-drinking-water-regulations.

Nativ, R., Adar, E., Dahan, O., Geyh, M., 1995. Water recharge and solute transport through the vadose zone of fractured chalk under desert conditions. Water Resour. Res. 31, 253–261. https://doi.org/10.1029/94WR02536.

Ogata, A., Banks, R.B., 1961. A solution of the differential equation of longitudinal dispersion in porous media (Professional Paper), Professional Paper.

Paradis, C.J., Hoss, K.N., Meurer, C.E., Hatami, J.L., Dangelmayr, M.A., Tigar, A.D., Johnson, R.H., 2022. Elucidating mobilization mechanisms of uranium during recharge of river

water to contaminated groundwater. J. Contam. Hydrol. 251, 104076 https://doi.org/10.1016/j.jconhyd.2022.104076.

Perzan, Z., Osterman, G., Maher, K., 2023. Controls on flood managed aquifer recharge through a heterogeneous vadose zone: hydrologic modeling at a site characterized with surface geophysics. Hydrol. Earth Syst. Sci. 27, 969–990. https://doi.org/10.5194/hess-27-969-2023

Qafoku NP, Arey BW, Kukkadapu RK, Williams KH, Davis JA, Zachara JM. The effect of bicarbonate, calcium, and phosphate on the leachability of uranium from contaminated sediments. Environ Sci Technol 2005;39(21):8439-45

Roycroft, Scott. "Influences of Evaporite Minerals on the Vertical Distribution, Storage, and Mobility of Uranium in response to Hydrologic Conditions." Master's thesis, Stanford Digital Repository, 2017.

Siirila-Woodburn, E.R., Sanchez-Vila, X., Fernàndez-Garcia, D., 2015. On the formation of multiple local peaks in breakthrough curves. Water Resources Research 51, 2128–2152. https://doi.org/10.1002/2014WR015840

Šimůnek, J., 2005. Models of Water Flow and Solute Transport in the Unsaturated Zone, in: Anderson, M.G., McDonnell, J.J. (Eds.), Encyclopedia of Hydrological Sciences. Wiley. https://doi.org/10.1002/0470848944.hsa080

Šimůnek, J., Bradford, S.A., 2008. Vadose Zone Modeling: Introduction and Importance. Vadose Zone Journal 7, 581–586. https://doi.org/10.2136/vzj2008.0012

Šimůnek, J., Van Genuchten, M.Th., Šejna, M., 2008. Development and Applications of the HYDRUS and STANMOD Software Packages and Related Codes. Vadose Zone Journal 7, 587–600. https://doi.org/10.2136/vzj2007.0077

Šimůnek, J., van Genuchten, M.Th., 2017. , in: Contaminant Transport in the Unsaturated Zone: Theory and Modeling. CRC Press, Taylor & Francis Group, Boca Raton London New York. https://doi.org/10.1201/9781315371801

Skaggs, T.H., Leij, F.J., 2018. 6.3 Solute Transport: Theoretical Background, in: Dane, J.H., Clarke Topp, G. (Eds.), SSSA Book Series. Soil Science Society of America, Madison, WI, USA, pp. 1353–1380. https://doi.org/10.2136/sssabookser5.4.c56

Skaggs, T.H., Jarvis, N.J., Pontedeiro, E.M., Van Genuchten, M.Th., Cotta, R.M., 2007. Analytical Advection–Dispersion Model for Transport and Plant Uptake of Contaminants in the Root Zone. Vadose Zone Journal 6, 890–898. https://doi.org/10.2136/vzj2007.0124

Sorek, S., 1996. A model for solute transport following an abrupt pressure impact in saturated porous media. Transp. Porous Media 22, 271–285. https://doi.org/ 10.1007/BF00161627.

Sultana, R., Dangelmayr, M.A., Paradis, C.J., Johnson, R.H., 2024a. Combining fission-track radiography and scanning electron microscopy to identify uranium host phases. Environ Earth Sci 83, 56. https://doi.org/10.1007/s12665-023-11373-5

Sultana, R., Johnson, R.H., Tigar, A.D., Wahl, T.J., Meurer, C.E., Hoss, K.N., Xu, S., Paradis, C.J., 2024b. Contaminant mobilization from the vadose zone to groundwater during experimental river flooding events. Journal of Contaminant Hydrology 265, 104391. https://doi.org/10.1016/j.jconhyd.2024.104391.

Tolar, B.B., Boye, K., Bobb, C., Maher, K., Bargar, J.R., Francis, C.A., 2020. Stability of Floodplain Subsurface Microbial Communities Through Seasonal Hydrological and Geochemical Cycles. Front. Earth Sci. 8, 338. https://doi.org/10.3389/feart.2020.00338

van Genuchten, M.Th. and Alves, W.J. (1982) Analytical Solutions of the One-Dimensional Convective-Dispersive Solute Transport Equation. Technical Bulletin 1661, US Department of Agriculture, Washington DC.

Waite, T.D., Davis, J.A., Payne, T.E., Waychunas, G.A., Xu, N., 1994. Uranium(VI) adsorption to ferrihydrite: Application of a surface complexation model. Geochimica et Cosmochimica Acta 58, 5465–5478. https://doi.org/10.1016/0016-7037(94)90243-7

Warrick, A.W., Biggar, J.W., Nielsen, D.R., 1971. Simultaneous solute and water transfer for an unsaturated soil. Water Resour. Res. 7, 1216–1225. https://doi.org/10.1029/WR007i005p01216.

Wexler, Eliezer J. Analytical solutions for one-, two-, and three-dimensional solute transport in ground-water systems with uniform flow. US Government Printing Office, 1992.

Yu, C., Warrick, A.W., Conklin, M.H., 1999. A moment method for analyzing breakthrough curves of step inputs. Water Resources Research 35, 3567–3572. https://doi.org/10.1029/1999WR900225

Zachara JM, Long PE, Bargar J, Davis JA, Fox P, Fredrickson JK, et al. Persistence of uranium groundwater plumes: Contrasting mechanisms at two DOE sites in the groundwater–vadose zone–transition region. J Contam Hydrol 2013;147:45-72

CHAPTER 5 - Conclusion

This dissertation advances the understanding of contaminant behavior in variably saturated compartments by integrating high-resolution mineralogical characterization, field-scale flooding experiments, and analytical modeling. Collectively, the three studies presented herein underscore the critical role of the vadose zone as a long-term secondary source of uranium and other co-contaminants, particularly during transient hydrologic events such as flooding.

In the first study, a combination of fission-track radiography, scanning electron microscopy (SEM), and energy-dispersive X-ray spectrometry (EDS) was applied to characterize low-concentration uranium in aquifer sediments. This multimodal approach revealed that uranium is retained in association with amorphous Al-rich and Fe-rich coatings around feldspar and quartz grains. These coatings significantly modify the surface properties of minerals and may influence uranium sorption and desorption behavior. Although the sample size was limited, the observation of similar coatings at other former uranium milling sites supports the broader relevance of these findings and highlights the potential of such coatings to act as long-term secondary sources of uranium.

The second study involved controlled field-scale flooding experiments designed to simulate natural infiltration events and assess contaminant mobilization mechanisms from the vadose zone. Results confirmed that the vadose zone functions as a persistent contaminant reservoir, with two primary mobilization mechanisms identified: (1) physical mobilization via the release of contaminant-rich pore water, and (2) chemical mobilization via the dissolution of evaporite minerals. These insights contribute to improved conceptual models of plume evolution and emphasize the importance of identifying vadose zone hotspots in site monitoring and remediation efforts. While the field evaluation of alkalinity enhancement as a remediation strategy

yielded inconclusive results, the study underscored the utility of simulating real-world hydrologic conditions to evaluate contaminant dynamics.

The third study used a one-dimensional analytical transport model to inversely calibrate data from infiltration and injection experiments, refining mechanistic understanding of solute transport during flooding events. Modeling results corroborated experimental findings, demonstrating that uranium and chloride mobilization is governed by both advective-dispersive pore water transport and geochemical processes such as desorption and evaporite dissolution. When river water with elevated alkalinity was introduced, uranium mobilization was further enhanced by desorption, while chloride transport remained dominated by physical processes. Although the model simplified a complex, variably saturated system, its strong agreement with data confirmed the dominance of first-order processes in governing solute movement.

Taken together, these studies provide an integrated framework for identifying, characterizing, and modeling contaminant release mechanisms in dynamic vadose zone systems. The findings have significant implications for the development of reactive transport models, particularly in environments influenced by episodic hydrologic events. They highlight the importance of incorporating both physical transport and geochemical processes into site assessment and remediation planning.

Broader Impacts and Future Work

This research provides critical insights into contaminant mobilization processes in variably saturated environments, with implications for flood-prone semi-arid to arid area. By highlighting the significance of both physical and geochemical processes in the vadose zone, this work supports the development of more accurate, mechanistic models for contaminant transport. The findings

encourage more comprehensive consideration of vadose zone dynamics in regulatory assessments, long-term monitoring strategies, and remediation planning.

Future work should prioritize more advanced modeling approaches to better capture system complexity and improve predictive capabilities. Key modeling-focused directions include:

1. Development of multidimensional, variably saturated flow and transport models that incorporate spatial heterogeneity, vertical stratification, and preferential flow to better represent real-world conditions beyond the limitations of 1D models.
2. Coupling of hydrologic and geochemical models to simulate the interplay between physical transport processes (e.g., advection, dispersion) and geochemical reactions (e.g., sorption, desorption, dissolution, redox), especially under transient hydrologic conditions.
3. Integration of time-varying boundary conditions into reactive transport models to assess the effects of long-term hydrologic variability on contaminant mobilization.
4. Inverse modeling and parameter estimation frameworks to constrain model uncertainty, improve calibration, and identify key controls on contaminant fate.

Advancing these modeling efforts will enable more robust decision-making for contaminated site management, allowing stakeholders to better predict contaminant behavior, assess risks, and design effective interventions under dynamic environmental conditions.

Page intentionally left blank

Appendix A: Supplementary of Chapter 2

Source zone: borings 859 and 860

Boring 859: (below water table)

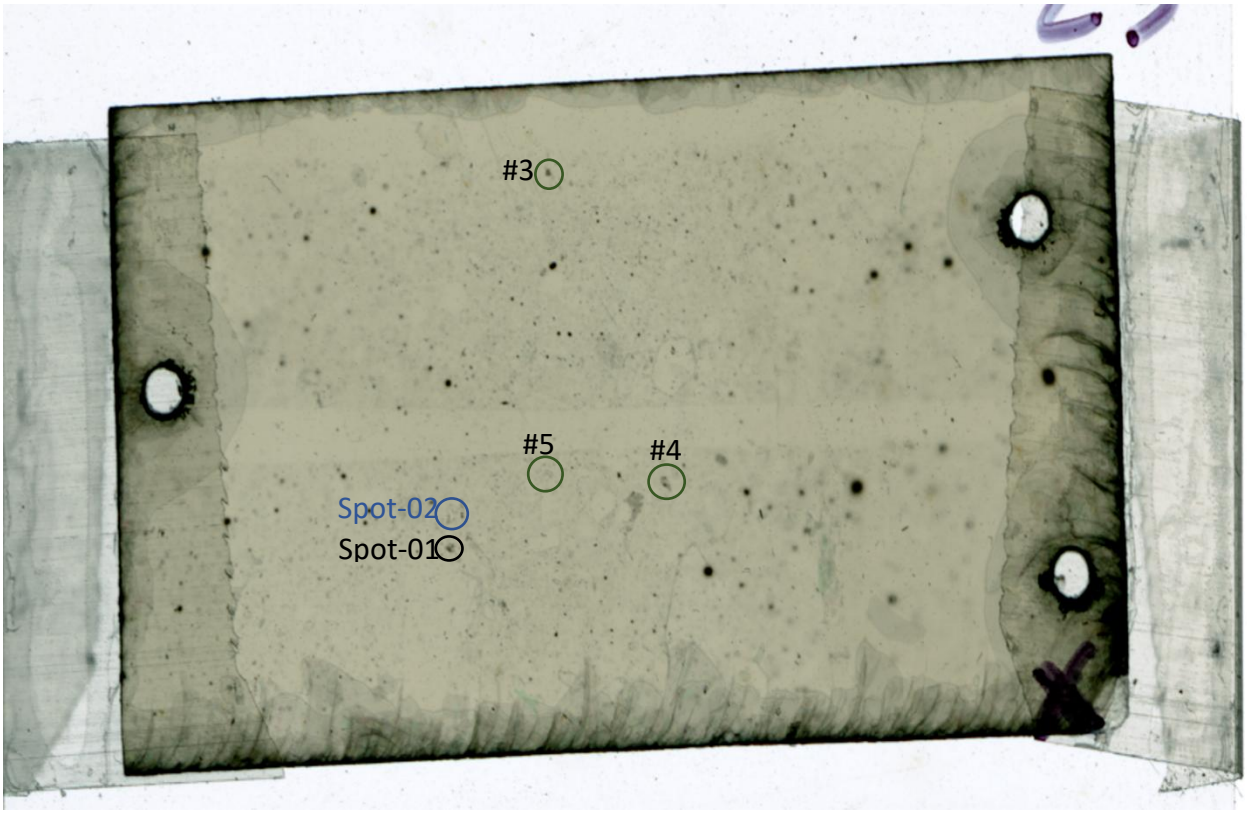

Fig. S1 Fission tracks on thin section of boring 859 (8.5 ft below ground surface)

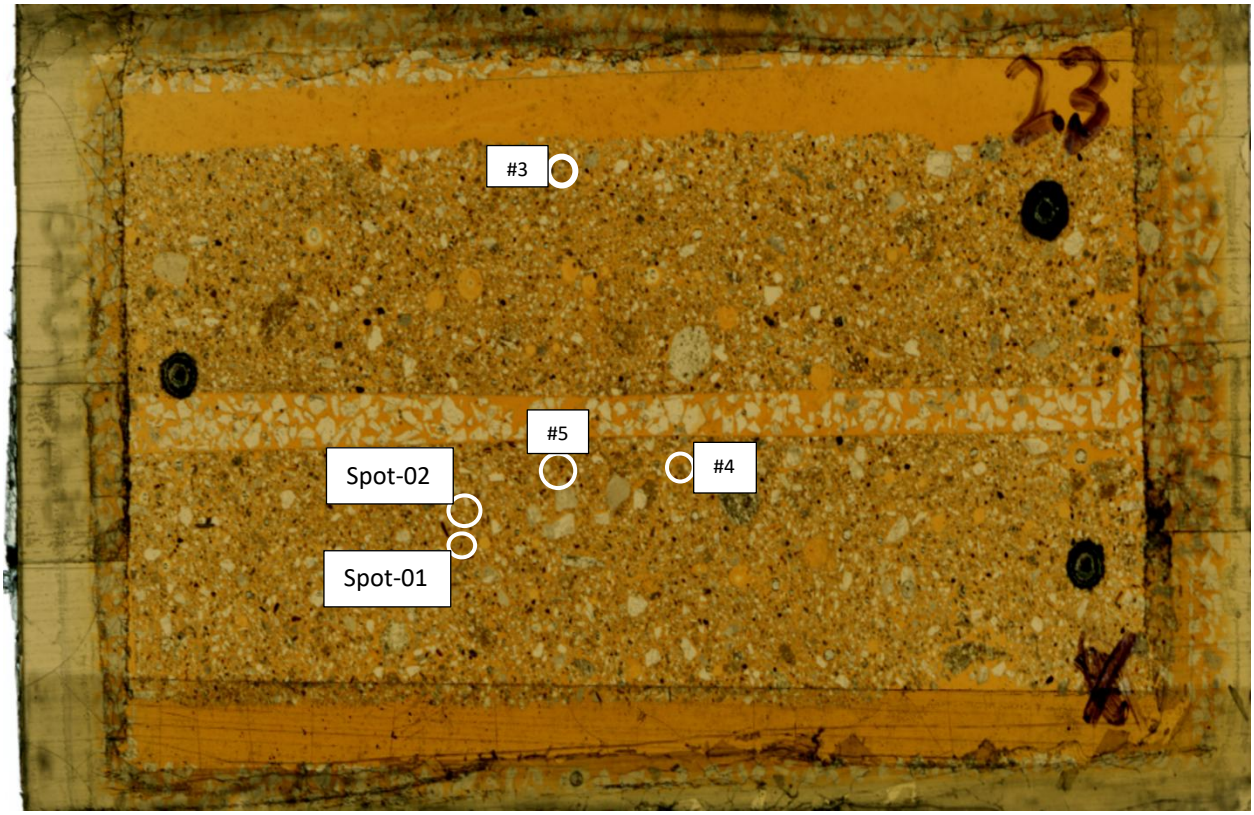

Fig. S2 Transmitted light image of thin section of boring 859 (8.5 ft below ground surface)

Boring 859 (below water table): spot-01

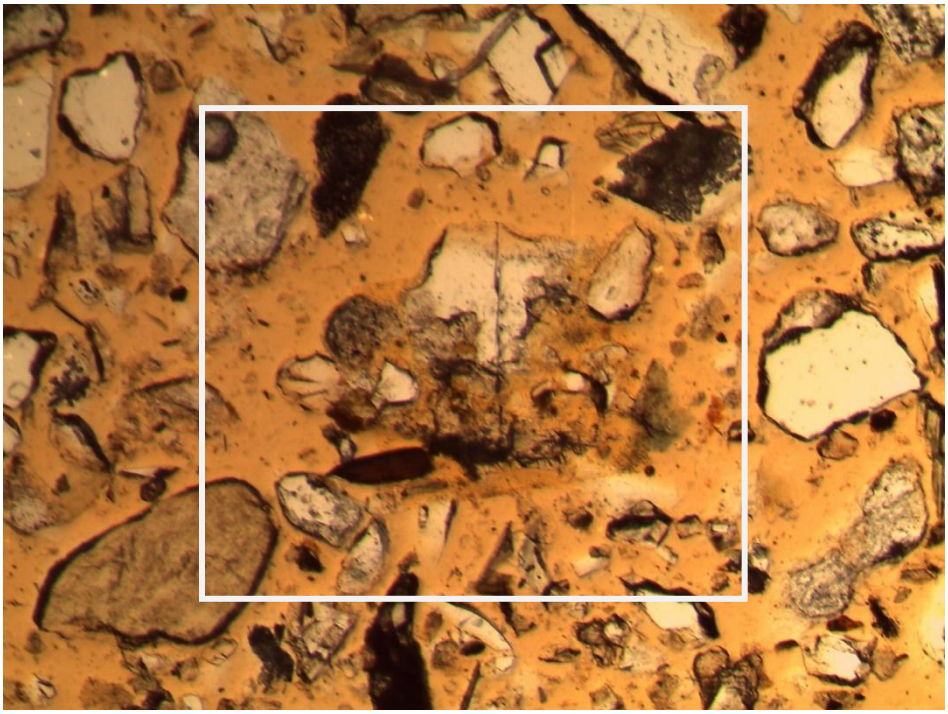

Fig. S3 Transmitted light image of spot 01

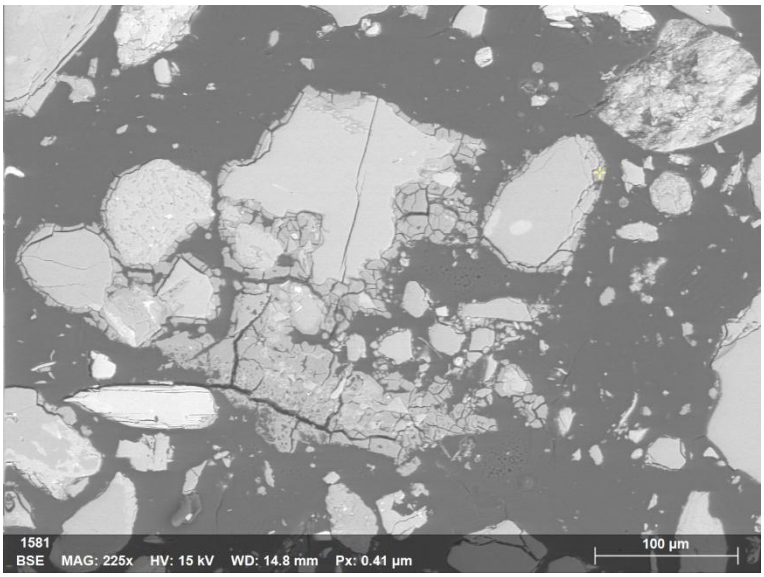

Fig. S4 Point map-01 (yellow point showing location)

Element	At. No.	Netto	Mass [%]	Mass Norm. [%]	Atom [%]	abs. error [%] (1 sigma)	rel. error [%] (1 sigma)
Oxygen	8	115426	34.03	52.11	65.18	3.83	11.25
Magnesium	12	1676	0.18	0.28	0.23	0.04	20.15
Aluminium	13	161839	15.67	24.00	17.80	0.75	4.80
Silicon	14	100709	11.44	17.52	12.48	0.50	4.39
Calcium	20	7213	0.83	1.27	0.63	0.05	6.30
Sodium	11	575	0.08	0.13	0.11	0.03	38.34
Potassium	19	1178	0.15	0.22	0.11	0.03	21.63
Phosphorus	15	2684	0.34	0.53	0.34	0.04	11.83
Sulfur	16	7842	0.98	1.50	0.94	0.06	6.36
Chlorine	17	3864	0.53	0.81	0.46	0.05	8.60
Fluorine	9	2140	1.06	1.62	1.71	0.22	21.01
		Sum	**65.31**	**100.00**	**100.00**		

Table S1 Quantitative analysis of point map-01 (Fig. S4)

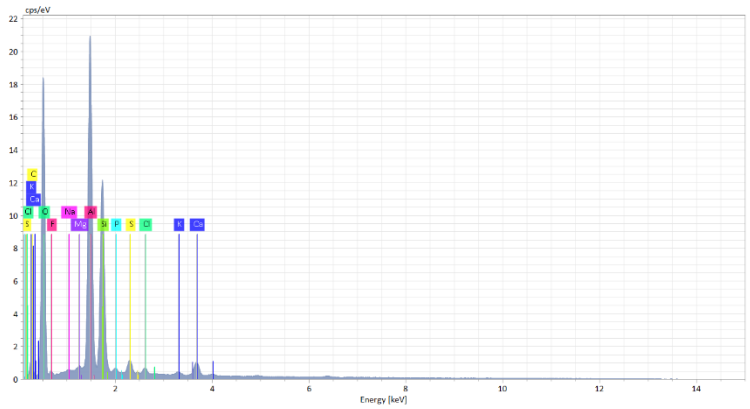

Fig. S5 Spectrum of point map-01 showing a high Al peak (Fig. S4)

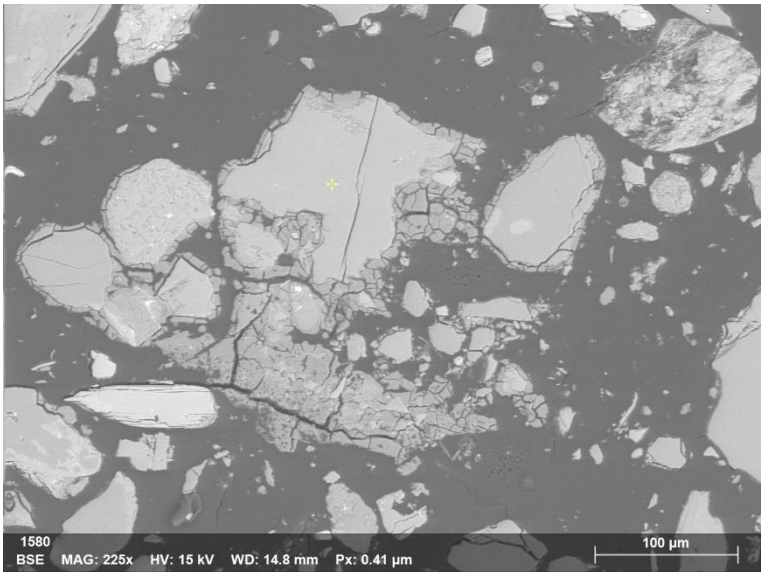

Fig. S6 Point map-02

Element	At. No.	Netto	Mass [%]	Mass Norm. [%]	Atom [%]	abs. error [%] (1 sigma)	rel. error [%] (1 sigma)
Oxygen	8	107840	22.01	42.72	56.26	2.49	11.33
Aluminium	13	131374	7.63	14.81	11.57	0.38	4.97
Silicon	14	268028	17.82	34.59	25.95	0.77	4.29
Calcium	20	20014	1.31	2.54	1.34	0.07	5.00
Sodium	11	36293	2.75	5.33	4.88	0.20	7.16
		Sum	**51.52**	**100.00**	**100.00**		

Table S2 Quantitative analysis of point map-02 (Fig. S6)

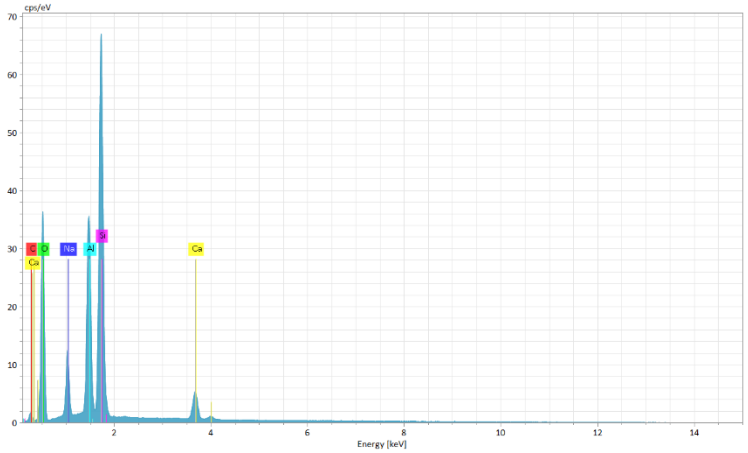

Fig. S7 Spectrum of point map-02 showing feldspar (Fig. S6)

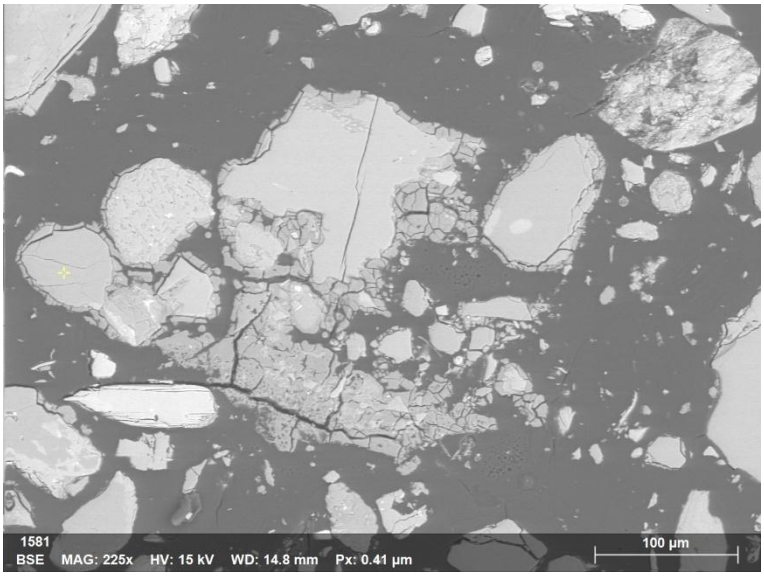

Fig. S8 Point map-03

Element	At. No.	Netto	Mass [%]	Mass Norm. [%]	Atom [%]	abs. error [%] (1 sigma)	rel. error [%] (1 sigma)
Oxygen	8	153615	36.11	46.52	60.43	4.00	11.09
Silicon	14	628645	41.51	53.48	39.57	1.75	4.21
		Sum	**77.62**	**100.00**	**100.00**		

Table S3 Quantitative analysis of point map-03 (Fig. S8)

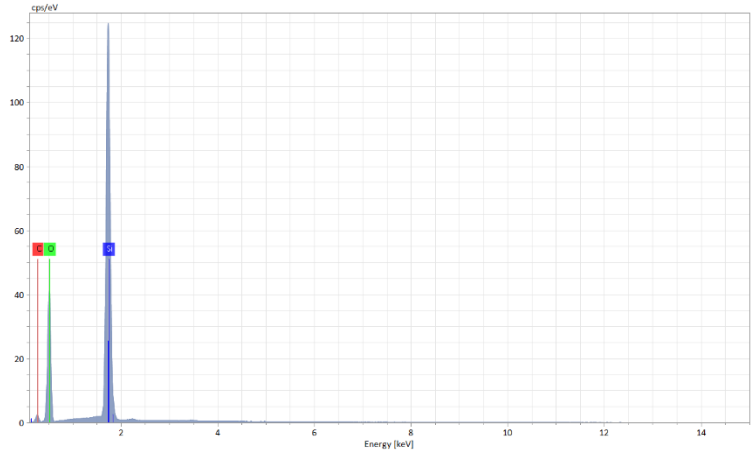

Fig. S9 Spectrum of point map-03 showing quartz (Fig. S8)

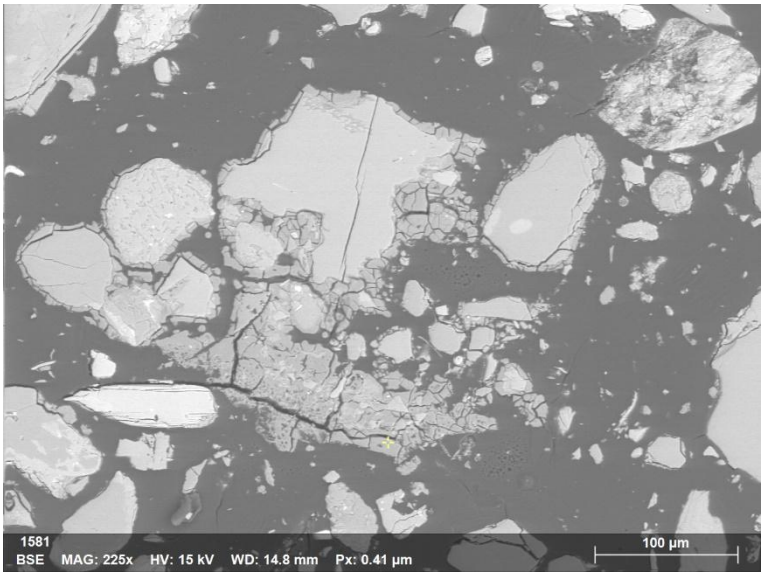

Fig. S10 Point map-04

Element	At. No.	Netto	Mass [%]	Mass Norm. [%]	Atom [%]	abs. error [%] (1 sigma)	rel. error [%] (1 sigma)
Oxygen	8	487834	35.54	52.04	65.43	3.78	10.64
Aluminium	13	754460	17.98	26.33	19.63	0.86	4.76
Silicon	14	436035	12.25	17.94	12.85	0.53	4.35
Calcium	20	30328	0.84	1.23	0.62	0.05	6.03
Iron	26	1567	0.17	0.25	0.09	0.03	18.80
Phosphorus	15	11340	0.35	0.52	0.34	0.04	11.05
Sulfur	16	31257	0.94	1.37	0.86	0.06	6.27
Chlorine	17	6832	0.22	0.32	0.18	0.03	15.01
		Sum	**68.30**	**100.00**	**100.00**		

Table S4 Quantitative analysis of point map-04 (Fig. S10)

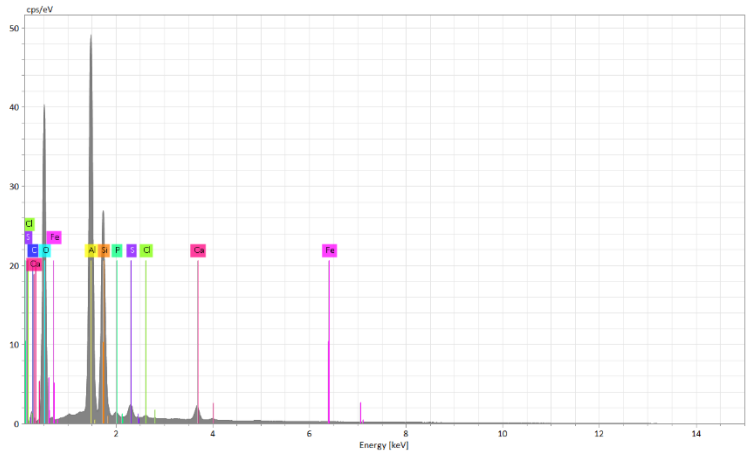

Fig. S11 Spectrum of point map-04 showing Al-rich precipitate (Fig. S10)

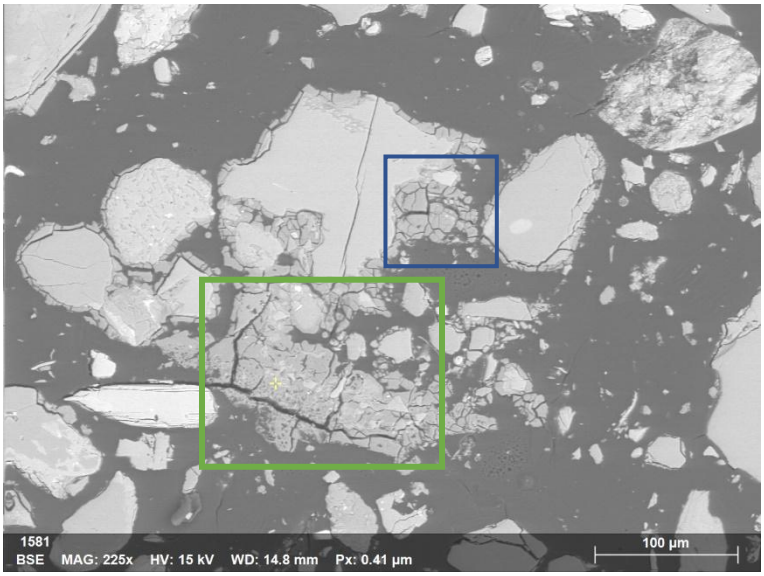

Fig. S12 Point map-05

Element	At. No.	Netto	Mass [%]	Mass Norm. [%]	Atom [%]	abs. error [%] (1 sigma)	rel. error [%] (1 sigma)
Oxygen	8	216817	34.30	46.19	59.60	3.75	10.93
Magnesium	12	5336	0.30	0.41	0.35	0.04	13.94
Aluminium	13	391647	19.24	25.91	19.82	0.92	4.76
Silicon	14	309974	17.44	23.48	17.26	0.75	4.30
Calcium	20	17556	0.83	1.12	0.57	0.05	6.12
Sodium	11	4636	0.37	0.49	0.44	0.05	13.50
Phosphorus	15	5618	0.35	0.48	0.32	0.04	11.26
Sulfur	16	13024	0.76	1.02	0.65	0.05	7.02
Fluorine	9	2867	0.67	0.90	0.98	0.14	21.21
		Sum	**74.25**	**100.00**	**100.00**		

Table S5 Quantitative analysis of point map-05 (Fig. S12)

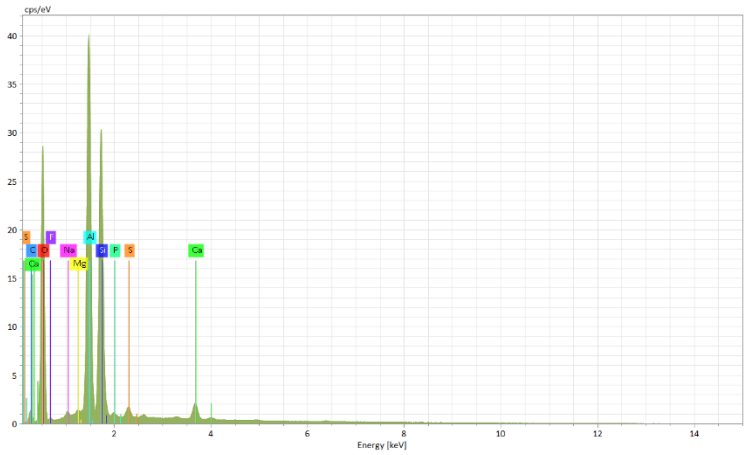

Fig. S13 Spectrum of point map-05 showing Al-rich precipitate (Fig. S12)

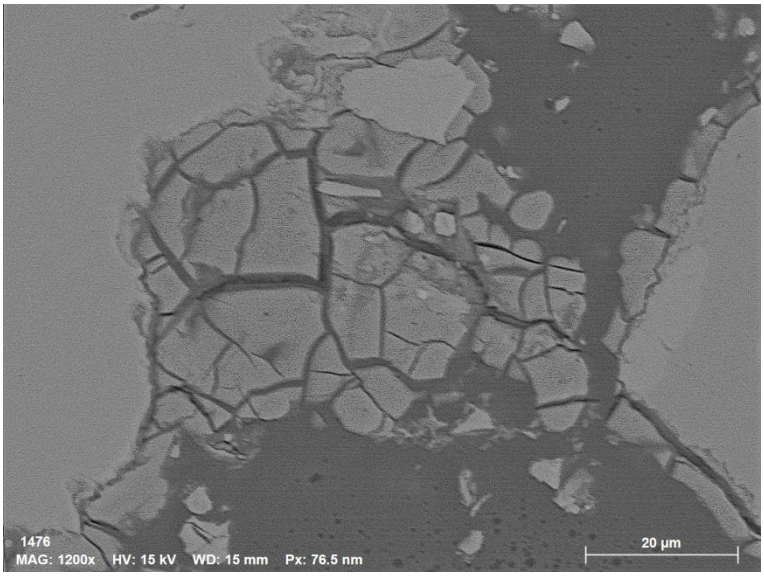

Fig. S14 Zoomed area shown in Fig S12 (blue rectangle)

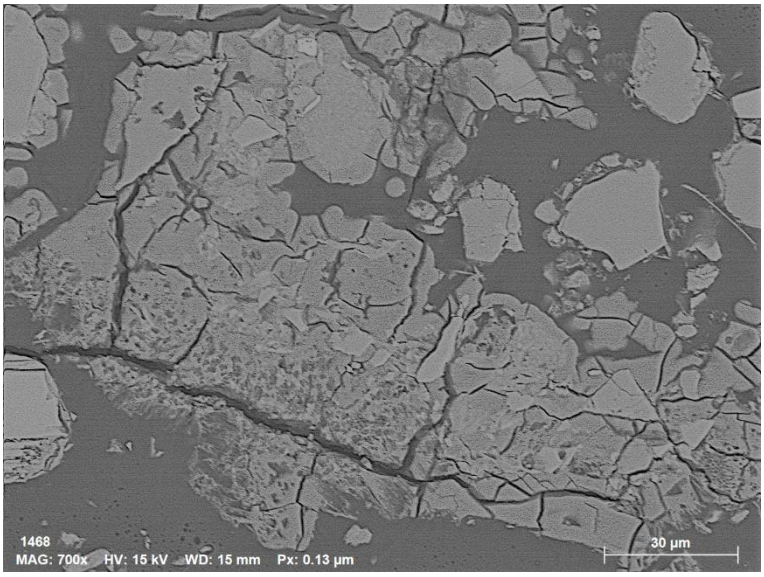

Fig. S15 Zoomed area shown in Fig S12 (green rectangle)

Boring 859 (below water table): spot-02

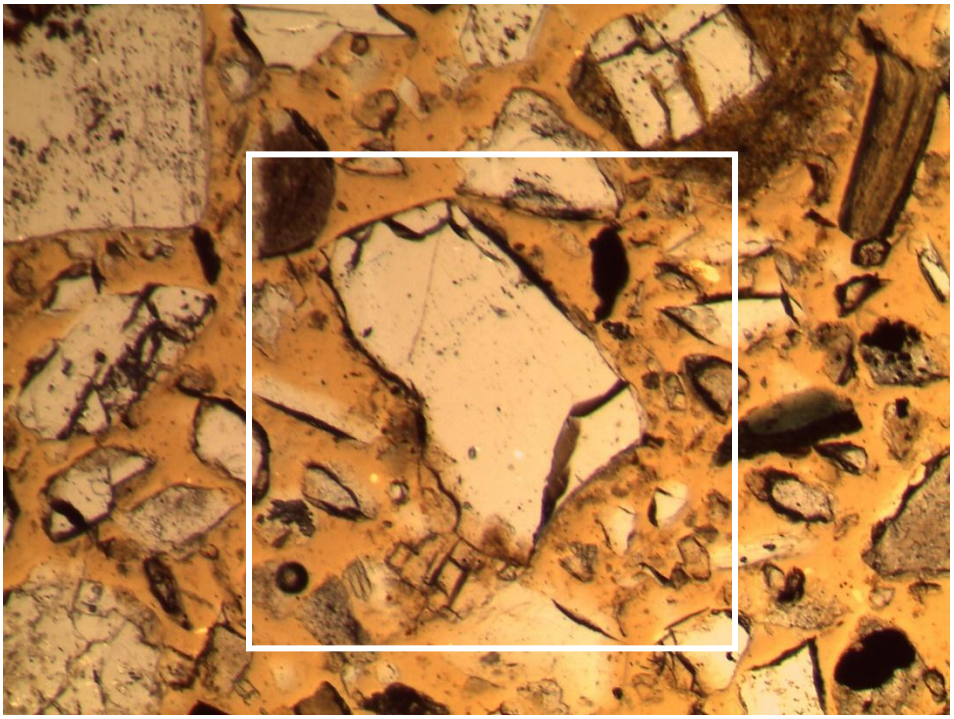

Fig. S16 Transmitted light image of spot 02

Fig. S17 Point map-01

Element	At. No.	Netto	Mass [%]	Mass Norm. [%]	Atom [%]	abs. error [%] (1 sigma)	rel. error [%] (1 sigma)
Oxygen	8	58186	28.40	37.38	51.36	3.34	11.75
Magnesium	12	6086	0.97	1.27	1.15	0.08	8.23
Aluminium	13	126706	17.73	23.33	19.01	0.85	4.78
Silicon	14	152710	24.17	31.81	24.90	1.03	4.26
Calcium	20	5956	0.76	1.00	0.55	0.05	6.63
Iron	26	3774	1.74	2.30	0.90	0.09	4.93
Sodium	11	2674	0.58	0.76	0.73	0.07	11.29
Potassium	19	2876	0.30	0.40	0.22	0.04	12.11
Phosphorus	15	1827	0.35	0.45	0.32	0.04	12.11
Sulfur	16	3066	0.53	0.70	0.48	0.05	8.91
Chlorine	17	2530	0.45	0.60	0.37	0.04	9.66
		Sum	**75.97**	**100.00**	**100.00**		

Table S6 Quantitative analysis of point map-05 (Fig. S15)

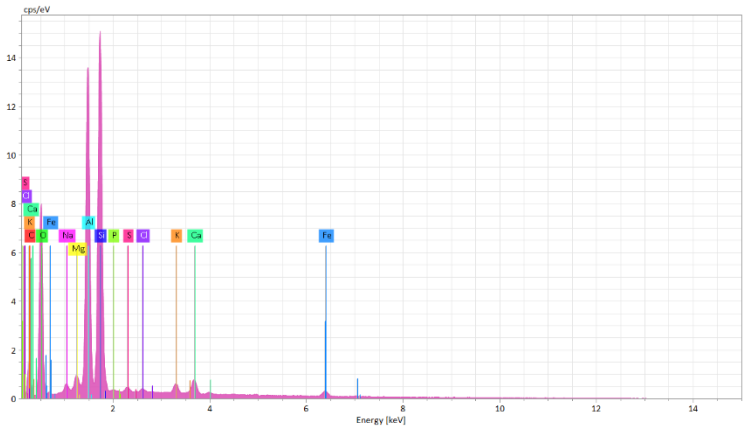

Fig. S18 Spectrum of point map-05 showing Al-rich precipitate (Fig. S15)

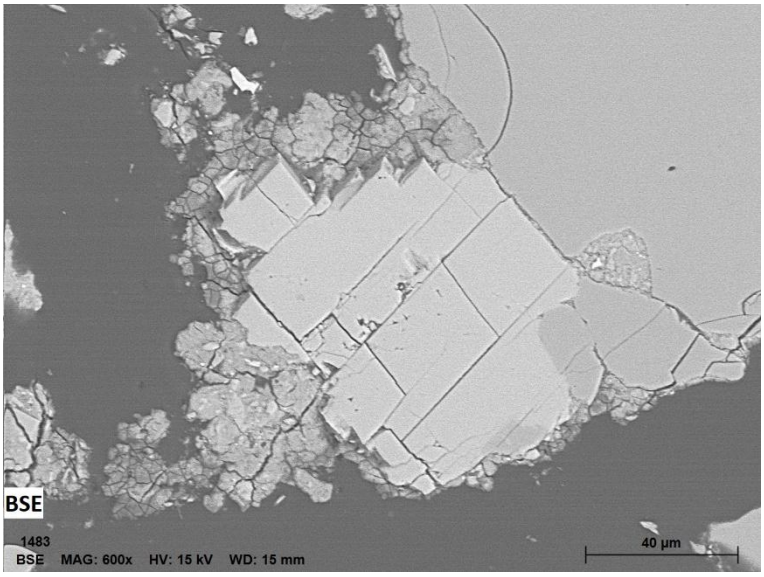

Fig. S19 Zoomed area shown in Fig S17 (blue rectangle)

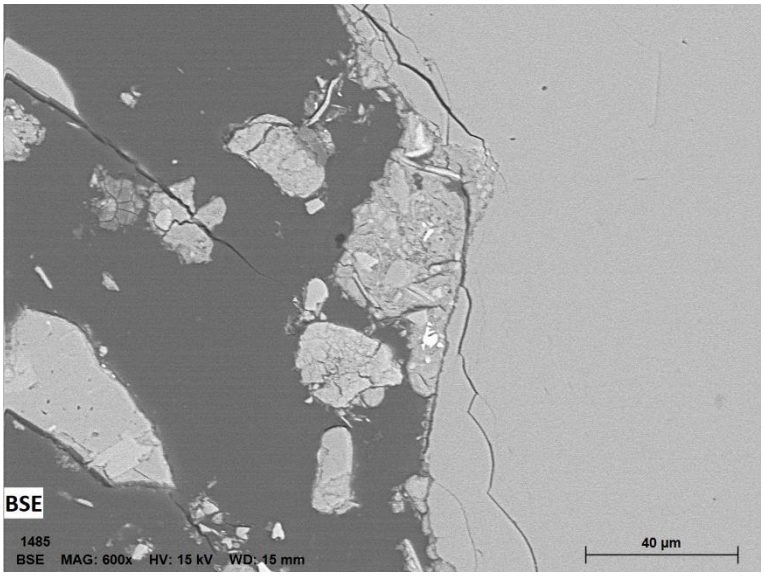

Fig. S20 Zoomed area shown in Fig S17 (green rectangle)

Boring 860: (below water table)

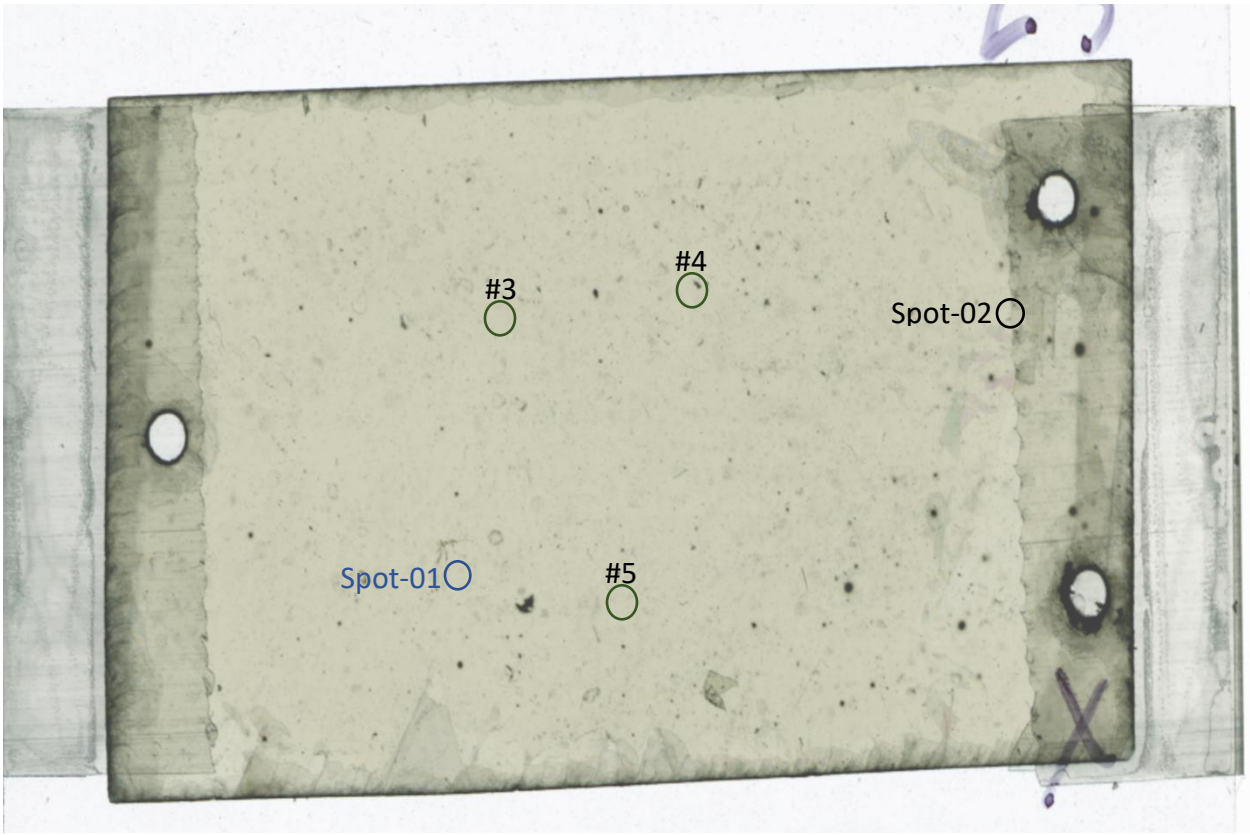

Fig. S21 Fission tracks on thin section of boring 860 (15.5 ft below ground surface)

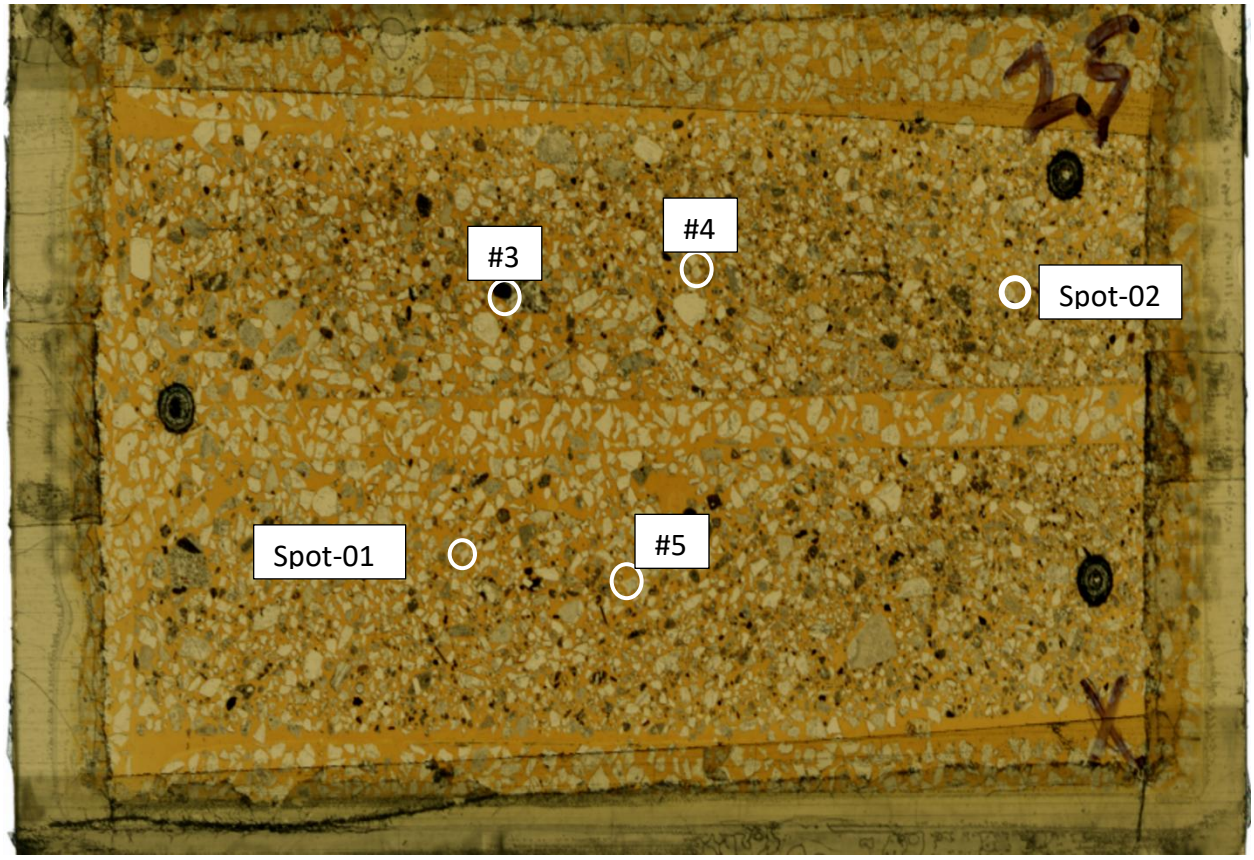

Fig. S22 Plain light image of thin section of boring 860 (15.5 ft below ground surface)

Boring 860 (below water table): spot-01

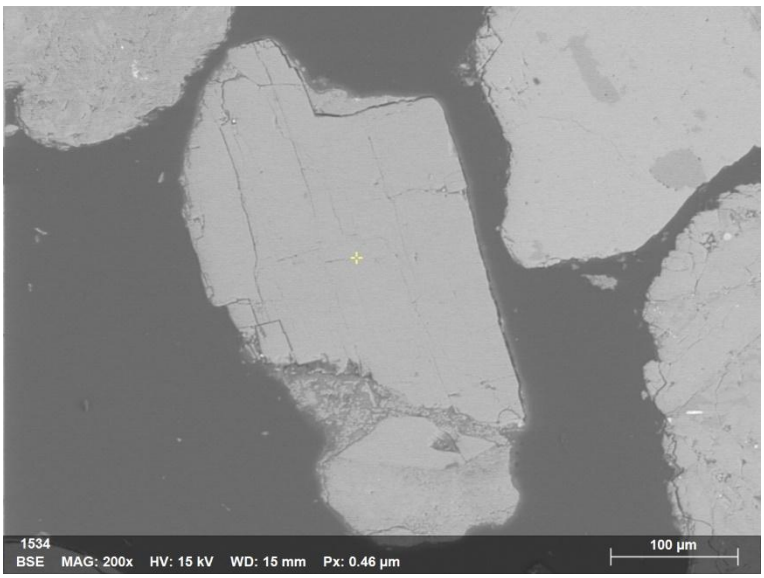

Fig. S23 Point map-01

Element	At. No.	Netto	Mass [%]	Mass Norm. [%]	Atom [%]	abs. error [%] (1 sigma)	rel. error [%] (1 sigma)
Oxygen	8	61027	22.95	43.05	56.63	2.69	11.73
Aluminium	13	73795	7.85	14.72	11.48	0.39	4.97
Silicon	14	149496	18.39	34.49	25.85	0.79	4.30
Calcium	20	11490	1.34	2.52	1.32	0.07	5.03
Sodium	11	19680	2.69	5.05	4.62	0.19	7.23
Potassium	19	554	0.09	0.18	0.10	0.03	32.09
		Sum	**53.32**	**100.00**	**100.00**		

Table S7 Quantitative analysis of point map-01 (Fig. S15)

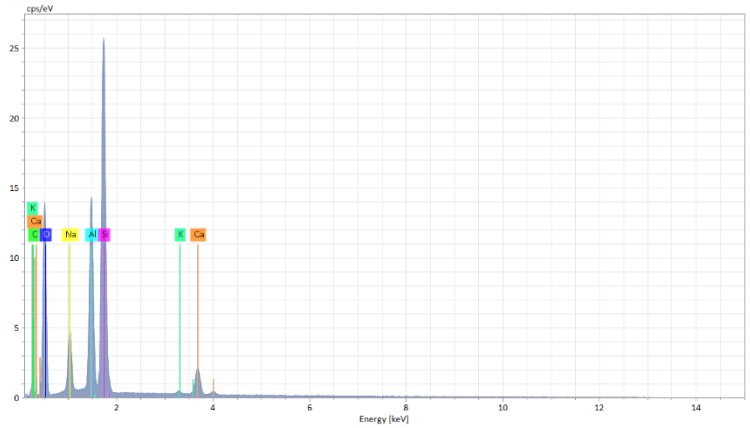

Fig. S24 Spectrum of point map-01 showing feldspar (Fig. S15)

Boring 860 (below water table): spot-02

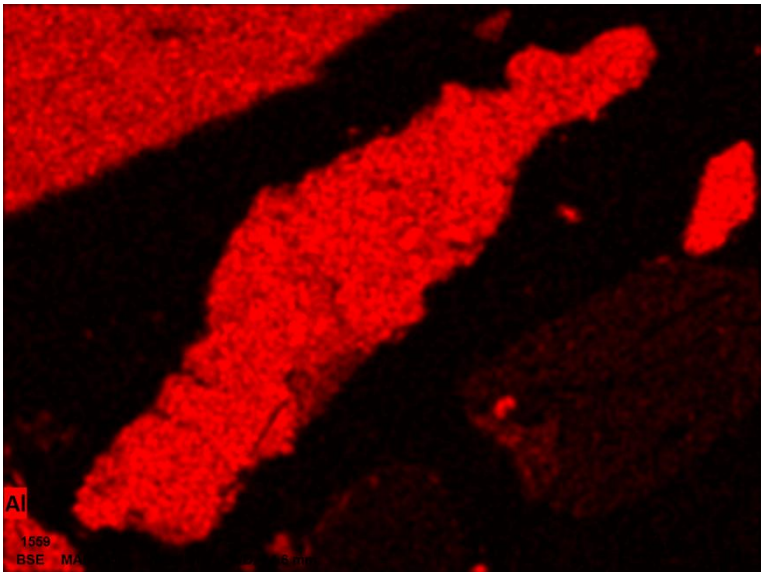

Fig. S25 Al elemental map

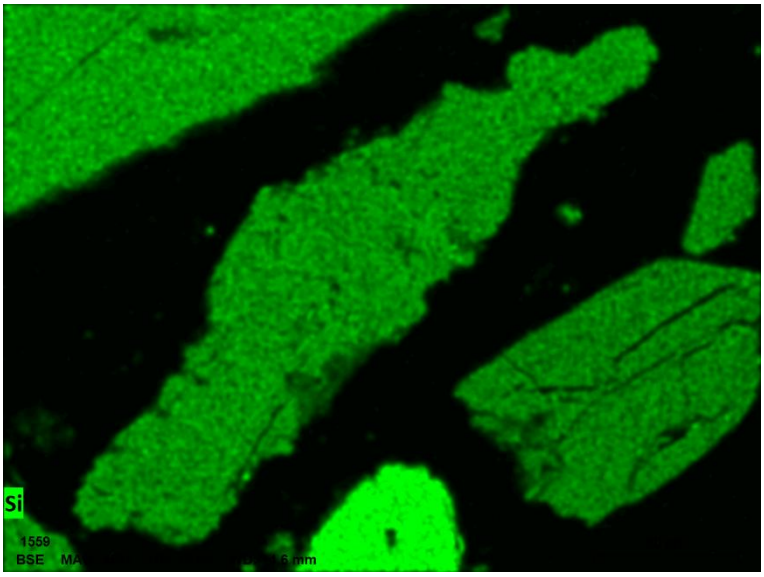

Fig. S26 Si elemental map

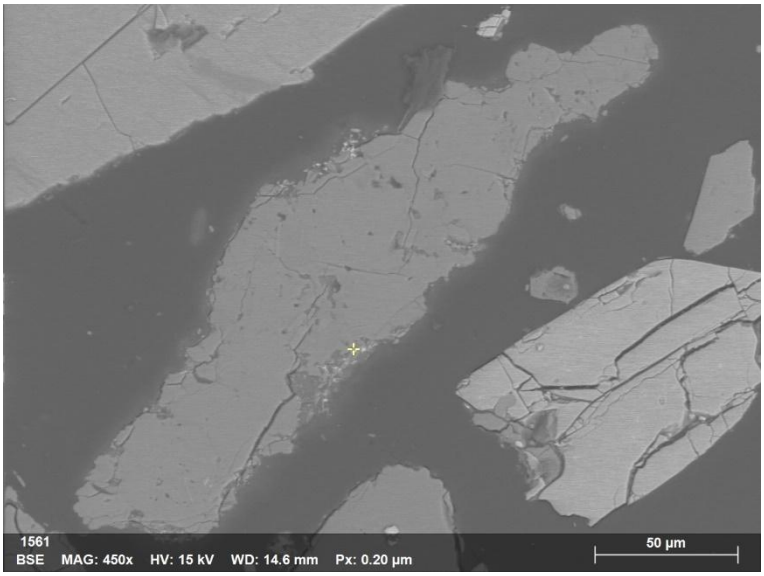

Fig. S27 Point map-03

Element	At. No.	Netto	Mass [%]	Mass Norm. [%]	Atom [%]	abs. error [%] (1 sigma)	rel. error [%] (1 sigma)
Oxygen	8	596791	16.56	27.77	43.83	1.77	10.67
Magnesium	12	53403	0.79	1.32	1.37	0.07	8.49
Aluminium	13	657135	8.59	14.41	13.48	0.42	4.92
Silicon	14	1188522	16.55	27.76	24.96	0.71	4.30
Calcium	20	28655	0.43	0.72	0.45	0.04	8.90
Iron	26	451115	13.08	21.94	9.92	0.41	3.11
Sodium	11	41293	0.82	1.38	1.51	0.08	9.28
Potassium	19	49868	0.46	0.77	0.50	0.04	8.54
Titanium	22	18312	0.39	0.65	0.34	0.04	9.43
Fluorine	9	42225	1.25	2.10	2.79	0.17	13.95
Chlorine	17	37047	0.70	1.18	0.84	0.05	6.94
		Sum	**59.62**	**100.00**	**100.00**		

Table S8 Quantitative analysis of point map-03 (Fig. S19)

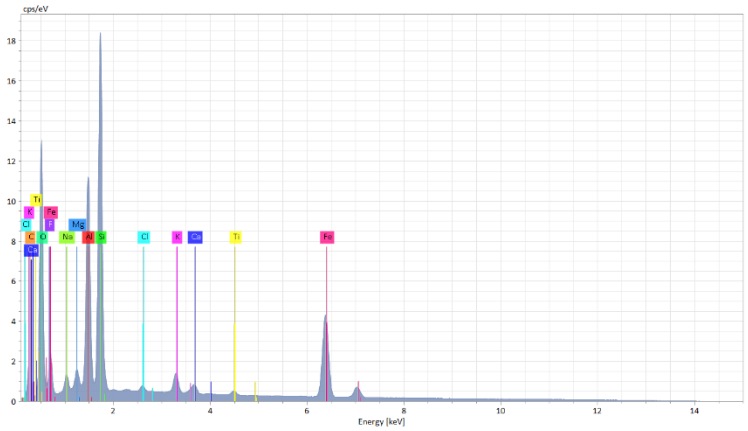

Fig. S28 Spectrum of point map-03 Fe particles (Fig. S19)

Appendix B: Supplementary of Chapter 3

Table. S1. Physical and chemical measurements for experimental flooding events

A. Field Measurements	**Instruments[A]**	**B. Laboratory Measurements**	**Instruments[B]**
Infiltration rate Depth to groundwater Bromide and Iodide Temperature Specific conductance pH Oxidation-reduction potential Dissolved oxygen Ferrous ion and Alkalinity	Peristaltic pump[1] Heron Skinny Dipper water level meter[2] Bromide ISE, Iodide ISE[3] YSI 556MPS (Yellow Springs, OH)[3,4,5,6] AccuVac ampules and a DR890 handheld colorimeter, Hach[8] DR890, Hach 8146[9] Titration w/1.6N sulfuric acid, and Bromocresol Green-Methyl Red indicator, Hach[10]	Uranium Tracers (a. Bromide, b. Iodide, c. DFB) Dissolved Organic Carbon Major cations (filtered, acidified) Major anions (filtered, unacidified)	Kinetic phosphorescence analyzer[1] Ion chromatography[2a,5] High Performance Liquid Chromatography [2b, 2c] Combustion-oxidation[3] Atomic adsorption spectrometry[4]

Table. S2. Information of tracers and alkalinity used in field experiments

Added Tracer/Alkalinity	**Experiment**	**Certified American Chemical Society (ACS) grade purity**	**Supplier Name**	**Chemical Abstracts Service (CAS) number**
Potassium penta-fluoro benzoate	Injection (7/18/20-8/6/20) (Paradis et al., 2022)	95%	Synquest Laboratories	58521-27-0
Sodium Bromide	Flood-1 (8/6/20-10/4/2020)	99%	Fisher Scientific	7550-35-8
Sodium 2,6-difluorobenzoate	Flood-1 (8/6/20-10/4/2020)	96%	Synquest Laboratories	6185-28-0
Sodium Iodide	Flood-2 (8/2/2021-9/10/2021)	>95%	Fisher Scientific	7681-82-5
Sodium bi carbonate	Flood-2 (8/2/2021-9/10/2021)	>95%	Fisher Scientific	144-55-8

Table. S3. Pre-experimental hydro-chemical data of groundwater and flood water

Experiments	Media		U (mg/L)	Cl (mg/L)	pH	Alkalinity (mg/L as $CaCO_3$)	ORP (mV)
Flood-1	Groundwater	Well 1001	0.98	424	7.1	520	4.9
		Well 1005	0.94	432.5	7.2	524	136.2
		Well 1011	0.99	443.5	7.2	523	97
	Flood water		0.009	14	8.5	221	136.3
Flood-2 (added alkalinity)	Groundwater	Well 1000	0.91	316	7.1	432	217
		Well 1005	0.91	318	7.2	472	193.3
		Well 1010	0.86	307	7.2	446	192.2
	Flood water		0.006	66	7.9	1556	174.6

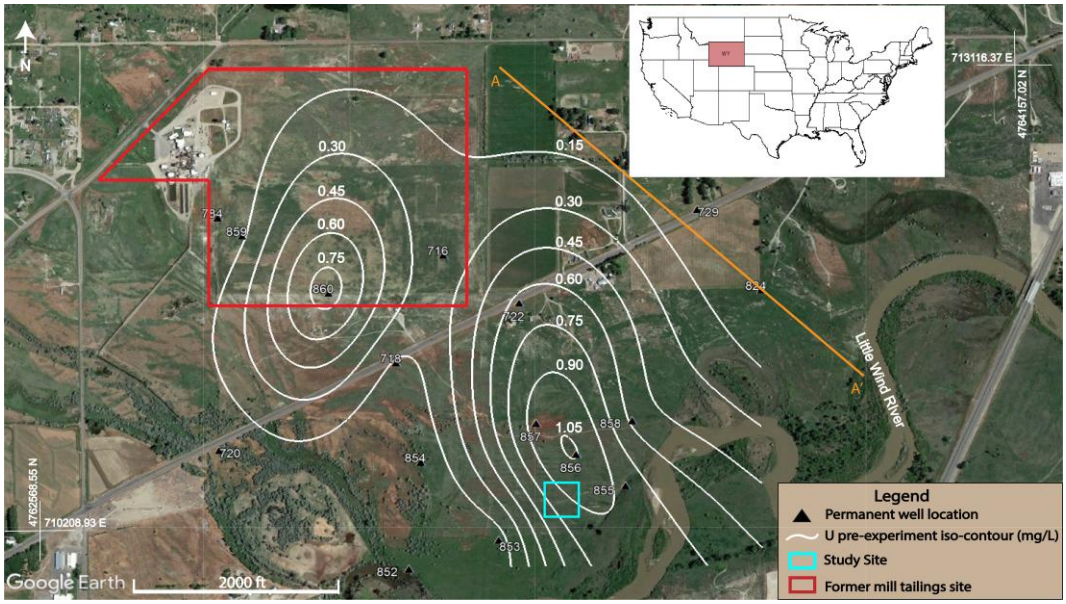

Fig. S1. Uranium plume distribution in Riverton, Wyoming. The pastel color box indicates the downgradient experimental location of this study (Fig. 2).

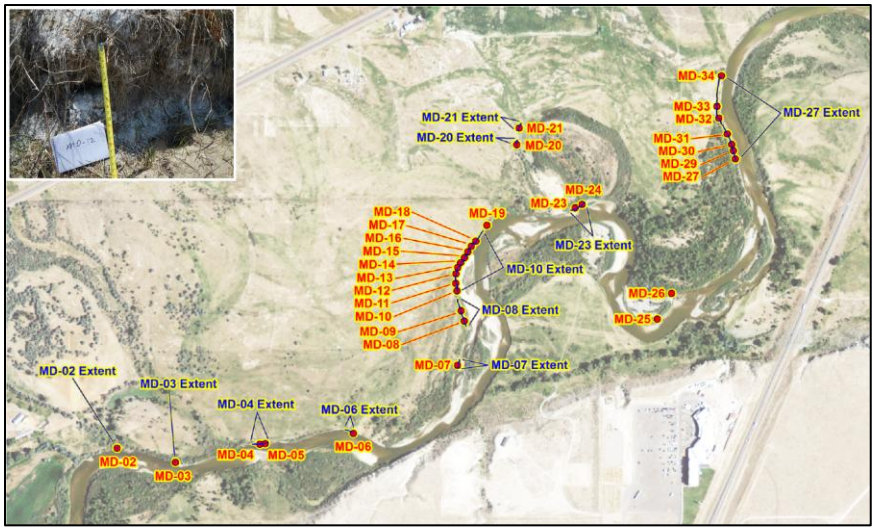

Fig. S2. Evaporite sampling location and the inset shows close-up view of an evaporite sample (U.S. Department of Energy, 2014).

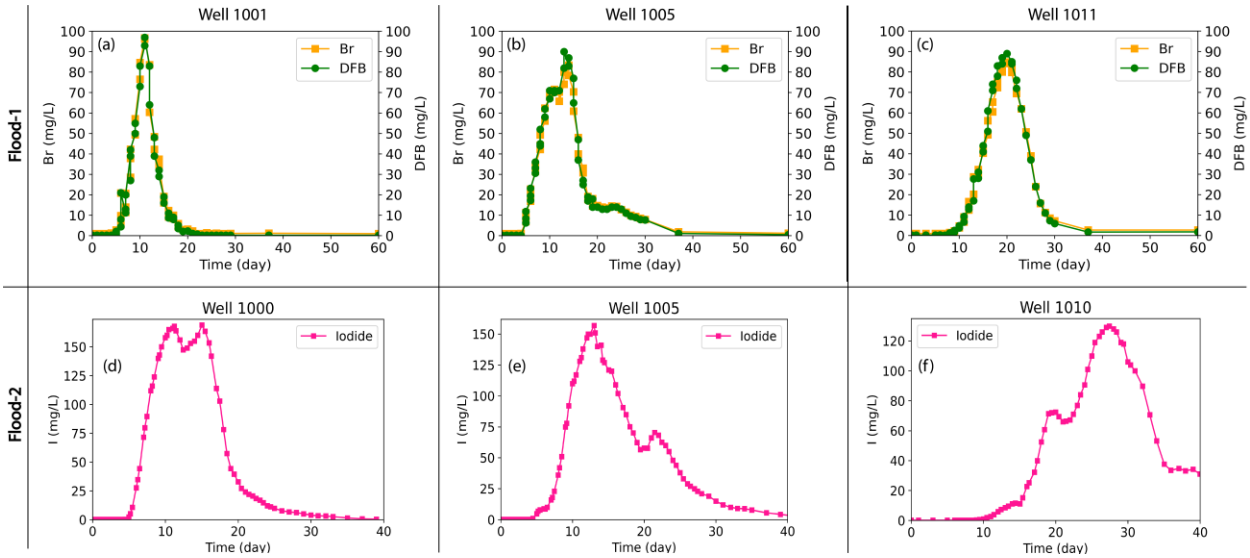

Fig. S3. Breakthrough curves of bromide (Br) and difluoro benzoate (DFB) during Flood-1 [(a), (b), (c)] and iodide (I) during Flood-2 [(d), (e), (f)].

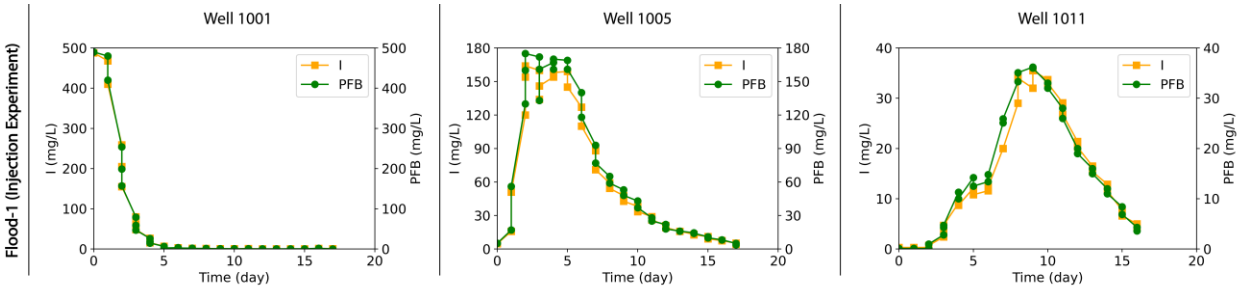

Fig. S4. Breakthrough curves of iodide (I) and pentafluorobenzoate (PFB) during injection experiment (Paradis et al., 2022) that was performed prior to the flooding experiments.

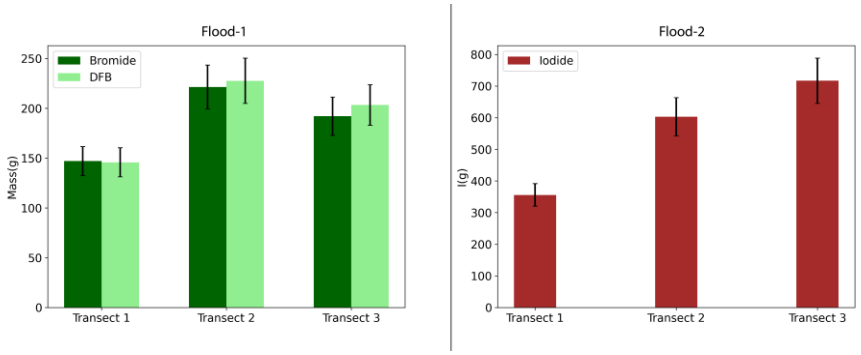

Fig. S5. Transect-wise mass for bromide and DFB during Flood-1 and iodide during Flood-2

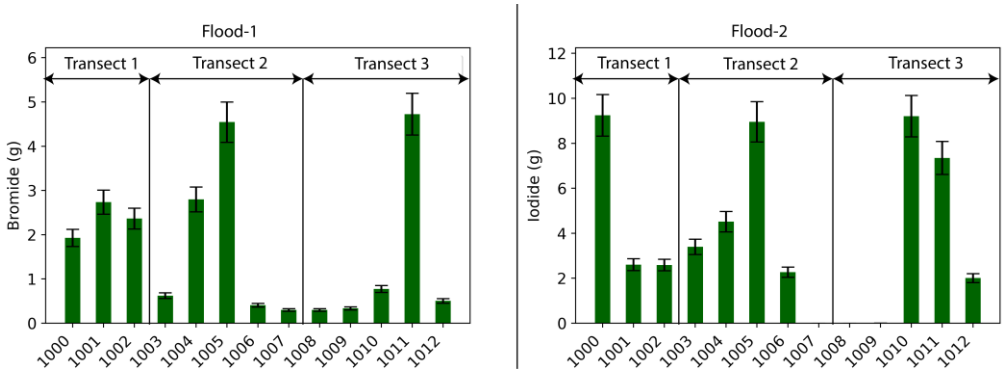

Fig. S6. Well-wise mass for bromide and iodide during Flood-1 and Flood-2, respectively

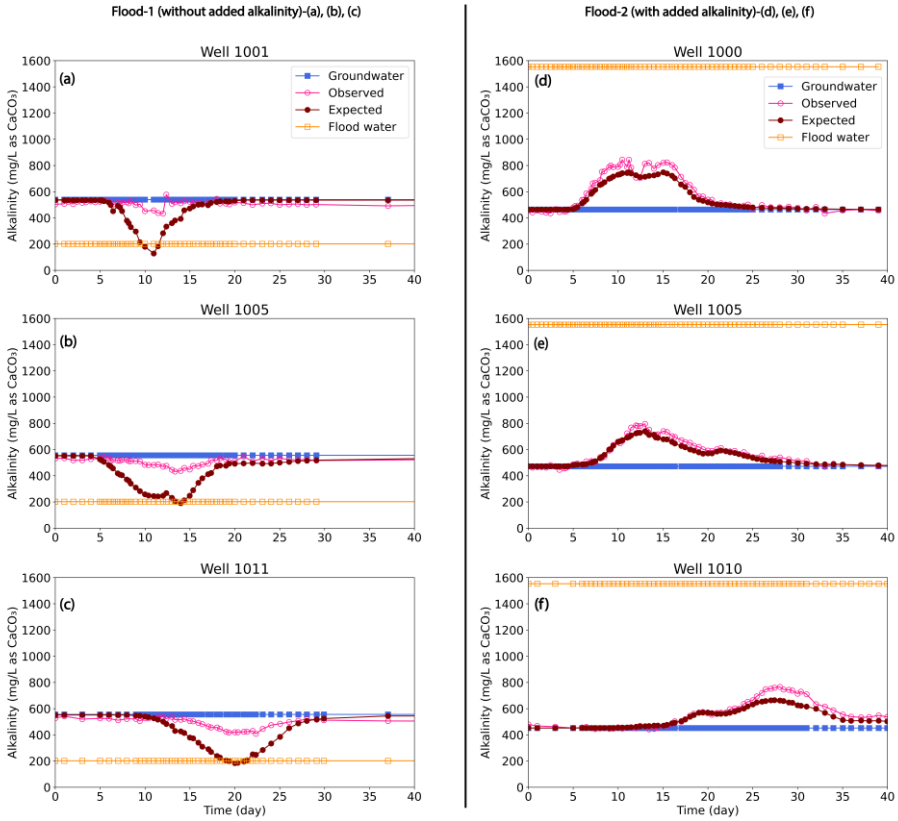

Fig. S7. Breakthrough curves of alkalinity as $CaCO_3$ (mg/L) at downgradient wells during Flood-1 and Flood-2

Table. S4. Relative moments and reactivity indices for reactive analytes

		Well 1001							Well 1005							Well 1011						
	M	Br	Na	Mg	K	Ca	Mn	Mo	Br	Na	Mg	K	Ca	Mn	Mo	Br	Na	Mg	K	Ca	Mn	Mo
Flood-1	M_o	1	1.27	1.32	1.07	1.07	0.43	1.06	1	1.54	1.59	1.49	1.25	0.36	1.23	1	1.44	1.35	1.39	1.27	0.68	1.28
	M_1	1	0.92	0.91	0.88	0.92	0.54	0.96	1	0.96	0.94	1.04	0.91	0.59	0.94	1	1.05	1.02	1.04	0.98	0.69	1
	M_2	1	0.86	0.84	0.89	0.98	0.83	0.95	1	0.83	0.84	0.99	0.85	1.07	0.89	1	0.81	0.80	0.84	0.79	0.57	0.83
	RI	0	10.06	13.5	3.30	1.11	57.22	0.79	0	32.07	38.35	23.77	9.61	58.7	6.79	0	22.75	16.17	18.11	11.3	38.37	10.66
		Well 1000							**Well 1005**							**Well 1010**						
	M	I	Na	Mg	K	Ca	Mn	Mo	I	Na	Mg	K	Ca	Mn	Mo	I	Na	Mg	K	Ca	Mn	Mo
Flood-2	M_o	1	1.44	1.48	1.36	1.23	0.24	1.36	1	1.32	1.40	1.31	1.31	0.38	1.25	1	1.14	1.33	1.20	1.36	0.89	1.27
	M_1	1	0.97	0.95	0.96	0.90	0.59	0.91	1	1.00	0.98	1	0.97	0.7	0.96	1	1.08	1.11	1.08	1.08	0.69	1.13
	M_2	1	0.87	0.87	0.88	0.91	1.09	0.86	1	0.92	0.89	0.91	0.89	0.89	0.84	1	0.99	0.93	0.97	0.91	0.52	0.97
	RI	0	20.08	25.26	14.49	7.24	75.18	15.85	0	10.73	17.47	10.44	10.59	48.45	8.97	0	2.59	12.48	4.75	14.29	34.07	9.28

References:

Paradis, C.J., Hoss, K.N., Meurer, C.E., Hatami, J.L., Dangelmayr, M.A., Tigar, A.D., Johnson, R.H., 2022. Elucidating mobilization mechanisms of uranium during recharge of river water to contaminated groundwater. Journal of Contaminant Hydrology 251, 104076. https://doi.org/10.1016/j.jconhyd.2022.104076

Appendix C: Supplementary for Chapter 4

Table S1 Data for river water injection test in temporary well 1005 from Hoss (2022)

TW1005 Time (days)	Halide Conc. (mg/L)	Benzoate Conc. (mg/L)	Chloride Conc. (mg/L)	Uranium Conc. (mg/L)
Injection	482.0	544.0	7.6	0.007
Background	0.3	0.1	410.0	0.940
0.02	4.7	5.1	412.0	0.928
0.66	15.8	17.0	404.0	0.934
0.99	51.0	56.0	373.0	0.898
1.56	120.0	130.0	314.0	0.783
1.80	154.0	160.0	267.0	0.692
2.01	164.0	175.0	276.0	0.638
2.57	160.0	172.0	280.0	0.621
2.77	134.0	133.0	286.0	0.665
2.98	146.0	161.0	276.0	0.642
3.59	154.0	167.0	270.0	0.637
3.79	157.0	161.0	273.0	0.695
4.00	158.0	170.0	264.0	0.672
4.60	159.0	169.0	261.0	0.695
5.05	145.0	161.0	277.0	0.687
5.62	127.0	140.0	284.0	0.704
6.04	110.0	118.0	298.0	0.728
6.58	88.0	92.9	318.0	0.756
7.03	71.0	77.0	330.0	0.774
7.64	59.1	65.0	341.0	0.786
8.05	54.3	59.0	344.0	0.792
8.66	47.8	53.0	353.0	0.802
9.09	42.8	48.0	356.0	0.817
9.62	38.2	43.0	370.0	0.817
10.03	33.5	37.0	367.0	0.832
10.61	29.0	28.0	372.0	0.843
11.03	26.0	25.0	375.0	0.848
11.64	21.1	22.0	380.0	0.857
11.98	19.1	18.0	384.0	0.852
12.74	15.8	16.0	382.0	0.868
13.00	15.8	16.0	386.0	0.875
13.62	13.2	14.5	397.0	0.910
13.97	12.7	14.0	392.0	0.876
14.61	11.1	11.0	411.0	0.987
14.97	9.1	10.0	396.0	0.910

15.62	7.5	8.2	400.0	0.896
16.00	7.4	8.2	402.0	0.908
16.57	5.3	5.0	431.0	0.965
17.02	4.1	3.8	434.0	0.907

Table S2 Data for river water injection test in temporary well 1011 from Hoss (2022)

TW1011 Time (days)	Halide Conc. (mg/L)	Benzoate Conc. (mg/L)	Chloride Conc. (mg/L)	Uranium Conc. (mg/L)
Injection	482.0	544.0	7.6	0.007
Background	0.3	0.1	425.0	0.930
1.01	0.3	0.1	425.0	0.933
1.63	0.3	0.1	425.0	0.946
2.03	0.3	0.1	425.0	0.959
2.59	0.3	0.1	436.0	0.953
3.01	0.7	1.0	442.0	0.971
3.62	2.4	2.8	478.0	0.963
3.80	3.9	4.3	518.0	0.985
4.02	4.7	4.7	447.0	0.973
4.64	9.1	11.3	415.0	0.955
5.07	8.7	10.0	413.0	0.972
5.64	12.1	14.2	411.0	0.931
6.04	10.8	12.5	411.0	0.962
6.62	11.6	13.4	410.0	0.951
7.03	12.4	14.8	406.0	0.963
7.66	20.0	25.1	400.0	0.966
8.06	20.0	25.9	392.0	0.948
8.73	29.0	33.3	389.0	0.917
9.10	34.0	35.1	387.0	0.902
9.63	32.0	36.2	386.0	0.973
10.04	35.5	36.0	382.0	0.944
10.64	33.7	33.0	381.0	0.913
11.05	33.0	32.0	383.0	0.920
11.66	29.1	28.0	385.0	0.958
11.99	26.8	26.0	390.0	0.975
12.76	21.4	20.0	394.0	1.007
13.02	20.3	19.0	394.0	1.006
13.64	16.5	16.0	395.0	1.001
13.99	15.4	15.0	400.0	1.002
14.63	12.9	12.0	401.0	1.010
14.98	11.6	11.0	400.0	1.011
15.64	7.7	8.4	403.0	1.004
16.02	6.6	6.9	427.0	1.005
16.58	5.0	4.3	459.0	1.007
17.03	4.2	3.6	428.0	0.986

Table S3 Data for river water infiltration test-01 in temporary well 1001 from Sultana et al., (2024)

TW1001 Time (days)	Halide Conc. (mg/L)	Benzoate Conc. (mg/L)	Chloride Conc. (mg/L)	Uranium Conc. (mg/L)
Inj.	131.0	130.0	14.2	0.009
Bkg.	1.0	0.2	424.0	0.980
0.00	1.0	0.2	426.0	0.987
1.00	1.0	0.2	425.0	1.003
1.43	1.0	0.2	422.0	0.980
1.99	1.0	0.2	423.0	0.980
2.43	1.0	0.2	414.0	0.954
2.99	1.0	0.2	423.0	0.975
3.41	1.0	0.2	422.0	0.987
3.97	1.0	0.2	427.0	1.046
4.43	1.3	0.2	423.0	1.005
4.96	1.4	0.4	428.0	0.987
5.17	1.9	1.1	428.0	1.020
5.43	2.8	2.1	435.0	1.009
5.97	5.4	4.4	455.0	1.022
6.17	9.8	8.0	470.0	1.002
6.43	20.9	21.0	555.0	1.120
6.96	11.4	11.2	488.0	1.087
7.20	14.0	12.9	517.0	1.159
7.43	20.7	20.0	583.0	1.091
7.97	37.8	39.0	690.0	1.418
8.18	28.6	27.0	619.0	1.380
8.42	42.3	42.0	650.0	1.293
8.96	49.4	50.0	665.0	1.341
9.43	57.2	55.0	640.0	1.433
9.98	76.5	73.0	676.0	1.345
10.39	84.7	83.0	665.0	1.342
10.96	96.2	93.0	646.0	1.310
11.44	96.7	97.0	617.0	1.293
12.00	83.6	83.0	596.0	1.375
12.37	60.4	64.0	578.0	1.400
12.99	48.4	48.0	572.0	1.293
13.32	42.2	39.0	567.0	1.299
13.97	37.4	32.0	571.0	1.335
14.36	34.5	29.0	575.0	1.361
14.96	19.2	19.0	573.0	1.286
15.35	16.1	16.0	568.0	1.280
15.93	12.3	11.0	541.0	1.235
16.35	9.2	8.7	532.0	1.226
17.01	8.4	8.0	550.0	1.233

17.32	10.0	9.0	549.0	1.281
17.97	5.9	5.1	518.0	1.167
18.34	4.4	3.5	503.0	1.147
18.98	3.0	2.1	472.0	1.074
19.37	3.0	2.1	477.0	1.131
19.99	3.2	2.3	485.0	1.115
20.97	2.3	1.1	457.0	1.019
21.97	1.0	0.8	457.0	1.060
23.05	1.0	0.2	437.0	1.152
24.01	1.4	0.2	430.0	1.024
24.98	1.0	0.2	416.0	0.983
26.02	1.2	0.2	416.0	0.987
27.00	1.0	0.2	410.0	0.961
28.00	1.0	0.2	406.0	0.995
29.05	1.1	0.2	413.0	0.967
37.05	1.2	0.2	409.0	0.915
60.18	1.0	0.2	394.0	0.900

Table S4 Data for river water infiltration test-01 in temporary well 1005 from Sultana et al., (2024)

TW1005 Time (days)	Halide Conc. (mg/L)	Benzoate Conc. (mg/L)	Chloride Conc. (mg/L)	Uranium Conc. (mg/L)
Inj.	131.0	130.0	14.2	0.009
Bkg.	1.0	0.2	432.5	1.220
0.02	1.0	0.2	432.0	1.101
1.03	1.0	0.2	435.0	1.076
2.02	1.0	0.2	440.0	0.946
3.03	1.0	0.2	442.0	0.953
3.99	1.1	0.2	449.0	0.960
4.99	6.9	6.3	561.0	1.155
5.18	8.8	8.4	576.0	1.153
5.44	11.3	11.8	576.0	1.185
5.99	16.9	17.3	602.0	1.216
6.19	19.2	19.5	598.0	1.220
6.45	22.8	23.2	604.0	1.219
6.98	31.4	30.6	624.0	1.397
7.23	33.7	33.1	639.0	1.470
7.45	34.7	36.0	616.0	1.526
7.98	42.2	44.0	593.0	1.529
8.20	44.3	45.0	589.0	1.529
8.43	49.3	52.0	594.0	1.828
8.99	56.1	58.0	582.0	1.537
9.45	62.4	62.0	563.0	1.479
10.01	67.9	67.0	527.0	1.476
10.41	70.0	71.0	478.0	1.327
10.99	71.0	70.0	480.0	1.314
11.46	71.6	71.0	478.0	1.270
12.03	70.3	71.0	499.0	1.281
12.40	65.8	71.0	533.0	1.264
13.01	74.1	82.0	524.0	1.251
13.36	80.0	90.0	507.0	1.226
13.99	83.4	83.0	491.0	1.224
14.38	78.4	87.0	501.0	1.237
15.00	70.4	77.0	508.0	1.436
15.37	60.9	65.0	529.0	1.333
15.96	48.0	47.0	557.0	1.361
16.39	40.0	37.0	566.0	1.366
17.05	33.0	27.0	588.0	1.387
17.38	30.8	25.0	570.0	1.383
18.02	19.2	19.0	606.0	1.454
18.37	17.7	17.0	615.0	1.405
19.03	18.1	18.0	620.0	1.397

19.38	14.5	14.0	629.0	1.342
20.02	14.7	14.0	627.0	1.459
21.00	14.0	13.0	639.0	1.422
22.00	13.6	13.0	642.0	1.479
23.10	14.5	14.0	673.0	1.434
24.05	14.3	14.0	599.0	1.368
25.02	12.8	13.0	579.0	1.339
26.07	11.5	11.0	564.0	1.404
27.05	10.0	9.5	552.0	1.316
28.05	9.4	8.9	541.0	1.500
29.10	8.5	7.9	529.0	1.246
29.96	7.9	7.7	530.0	1.232
37.08	1.9	1.1	445.0	1.047
60.20	1.2	0.5	418.0	0.940

Table S5 Data for river water infiltration test-01 in temporary well 1011 from Sultana et al., (2024)

TW1011 Time (days)	Halide Conc. (mg/L)	Benzoate Conc. (mg/L)	Chloride Conc. (mg/L)	Uranium Conc. (mg/L)
Inj.	131.0	130.0	14.2	0.009
Bkg.	1.0	0.2	443.5	0.990
0.05	1.0	0.2	424.0	0.994
1.05	1.0	0.2	429.0	0.988
3.06	1.0	0.2	427.0	1.015
5.04	1.0	0.2	425.0	1.068
6.03	1.0	0.3	439.0	1.032
7.05	1.0	0.2	445.0	1.029
8.01	1.5	1.3	415.0	1.210
9.03	2.0	1.8	420.0	1.062
9.47	2.3	2.5	437.0	1.075
10.04	3.8	3.7	447.0	1.196
10.42	4.7	4.8	469.0	1.168
11.02	6.6	6.6	498.0	1.279
11.48	9.1	9.3	506.0	1.323
12.07	12.5	12.9	530.0	1.361
12.42	16.6	14.0	527.0	1.410
13.06	20.2	17.0	528.0	1.349
13.39	28.7	27.7	529.0	1.307
14.03	29.6	28.0	521.0	1.311
14.41	32.3	31.0	507.0	1.297
15.04	40.3	41.0	494.0	1.266
15.40	41.7	44.0	467.0	1.236
16.00	49.3	51.0	457.0	1.201
16.43	56.2	61.0	427.0	1.215
17.11	60.5	71.0	416.0	1.132
17.40	65.3	74.0	416.0	1.218
18.07	72.4	78.0	411.0	1.137
18.38	75.1	83.0	406.0	1.146
19.08	80.0	84.0	416.0	1.231
19.39	81.6	87.0	410.0	1.102
20.05	84.9	89.0	410.0	1.092
20.39	84.2	89.0	416.0	1.063
21.06	82.3	85.0	420.0	1.069
21.40	79.8	84.0	424.0	1.080
22.04	69.5	76.0	430.0	1.110
22.39	70.4	72.0	440.0	1.113
23.16	62.0	62.0	452.0	1.145
24.09	50.7	49.0	452.0	1.175
25.08	39.0	37.0	470.0	1.184

26.10	23.9	24.0	484.0	1.181
27.11	15.7	16.0	490.0	1.198
28.07	11.3	11.0	486.0	1.176
29.17	8.5	7.3	482.0	1.131
29.97	7.2	5.9	482.0	1.108
37.11	2.7	1.7	448.0	1.060
60.24	2.7	1.8	447.0	1.064

Table S6 Data for river water infiltration test-02 in temporary well 1000 from Sultana et al., (2024)

TW1000 Time (days)	Halide Conc. (mg/L)	Chloride Conc. (mg/L)	Uranium Conc. (mg/L)
0.00	275	66	0.006
0.00	0.2	311	0.903
0.00	0.2	316	0.909
1.44	0.2	312	0.908
1.98	0.2	311	0.899
2.47	0.2	310	0.913
2.97	0.2	310	0.906
3.46	0.2	308	0.907
3.98	0.2	313	0.893
4.17	0.2	312	0.900
4.46	0.2	312	0.913
4.98	0.2	316	0.902
5.18	0.2	322	0.941
5.44	0.403	332	0.974
5.97	2.3	379	1.052
6.17	5.21	409	1.058
6.45	10.7	441	1.215
6.98	27.6	437	1.335
7.18	34.8	424	1.339
7.45	44.4	410	1.404
7.98	71.6	352	1.403
8.16	79.8	336	1.403
8.44	89.6	310	1.313
8.97	112	252	1.270
9.17	116	237	1.210
9.46	124	210	1.210
9.98	140	178	1.114
10.16	143	168	1.087
10.45	150	160	1.067
10.97	158	139	1.026
11.20	160	132	1.058
11.45	165	125	1.025
11.98	166	122	1.010
12.20	168	119	1.020
12.43	164	123	1.030
12.98	156	136	1.034
13.43	147.5	151	1.067
13.98	149	152	1.081
14.43	153	171	1.071
14.98	155	170	1.078

15.42	160	167	1.090
16.02	169	160	1.072
16.44	163.5	169	1.066
16.99	153.5	189	1.076
17.30	142	203	1.087
17.99	114	262	1.091
18.45	103	280	1.099
18.98	78.3	305	1.091
19.44	57.4	327	1.088
19.97	44.4	334	1.077
20.43	39.5	340	1.078
20.97	32.8	333	1.082
21.43	27.2	350	1.079
21.97	24.1	350	1.087
22.44	22	353	1.105
22.98	20.6	354	1.106
23.44	18.4	356	1.109
23.98	16.9	353	1.092
24.44	14.7	354	1.090
24.99	12.1	351	1.086
25.44	11.2	354	1.067
25.98	9.9	353	1.071
26.99	7.7	349	1.070
27.98	6.8	357	1.066
28.98	6.2	348	1.075
29.98	5.1	349	1.032
30.98	4	340	1.007
31.96	3.4	341	1.016
33.02	3.2	341	1.001
34.01	2.7	334	0.980
36.00	1.5	323	0.941
38.03	0.75	315	0.928
39.98	0.48	315	0.943

Table S7 Data for river water infiltration test-02 in temporary well 1005 from Sultana et al., (2024)

TW1005 Time (days)	Halide Conc. (mg/L)	Chloride Conc. (mg/L)	Uranium Conc. (mg/L)
0.00	275	66	0.006
0.00	0.2	316	0.92
0.03	0.2	318	0.91
1.01	0.2	318	0.92
1.46	0.2	314	0.91
2.01	0.2	317	0.92
2.48	0.2	318	0.93
2.99	0.2	316	0.93
3.48	0	322	0.94
4.00	0	323	0.93
4.19	0	324	0.94
4.48	0	326	0.94
5.01	0	332	0.96
5.20	0	340	0.99
5.47	1	357	1.07
6.00	5	363	1.06
6.19	7	369	1.05
6.46	8	406	1.09
7.00	9	413	1.09
7.20	9	412	1.10
7.47	10	411	1.10
8.01	16	386	1.11
8.18	18	404	1.13
8.46	23	387	1.14
9.00	36	362	1.16
9.19	42	353	1.16
9.49	51	353	1.17
10.01	75	324	1.20
10.19	78	318	1.19
10.48	92	301	1.21
11.00	110	285	1.23
11.22	112	283	1.26
11.48	117	281	1.29
12.01	128	270	1.29
12.22	131	270	1.32
12.46	138	262	1.33
13.01	147	253	1.33
13.17	150	252	1.36
13.45	150	250	1.35
14.01	157	203	1.33

14.17	151	212	1.32
14.46	140	218	1.29
15.01	141	215	1.25
15.20	129	204	1.25
15.45	127	205	1.23
16.05	121	207	1.17
16.46	120	215	1.15
17.02	109	219	1.12
17.34	102	211	1.09
18.05	90.7	237	1.06
18.48	85	255	1.02
19.02	75.2	269	0.99
19.47	70.2	255	0.97
20.00	62.3	267	0.95
20.46	56.7	275	0.95
21.00	57.8	271	0.96
21.46	57.7	287	0.93
22.00	66.1	271	0.93
22.47	70.5	255	0.94
23.01	68.2	265	0.95
23.46	62.6	274	0.96
24.00	60	276	0.97
24.46	55	283	0.97
25.02	48	291	0.99
25.46	44	295	1.00
26.01	38	301	1.00
26.47	33	313	0.98
27.03	29	312	0.96
27.46	27	322	0.98
28.02	25	316	0.98
28.45	23	318	0.99
29.02	21	322	0.99
30.02	19	325	1.00
31.02	15	334	1.01
32.00	12	333	1.01
33.06	10	340	1.01
34.04	9.1	339	1.01
35.00	8.9	345	1.01
36.03	7.8	332	1.02
38.07	5.6	333	1.00
40.01	4.3	329	0.98
41.98	2.96	323	0.97

Table S8 Data for river water infiltration test-02 in temporary well 1010 from Sultana et al., (2024)

TW1010 Time (days)	Halide Conc. (mg/L)	Chloride Conc. (mg/L)	Uranium Conc. (mg/L)
0.00	275	66	0.006
0.00	0.20	308	0.86
0.96	0.20	307	0.86
1.93	0.20	304	0.86
2.93	0.20	307	0.86
4.93	0.20	308	0.87
6.92	0.20	308	0.87
7.92	0.20	305	0.87
8.38	0.20	309	0.86
8.93	0.20	306	0.87
9.38	0.20	308	0.87
9.92	0.20	307	0.87
10.40	0.20	310	0.90
10.96	0.33	311	0.91
11.39	0.63	313	0.92
11.92	1.00	313	0.94
12.40	2.01	316	0.96
12.93	2.72	317	0.97
13.37	3.92	319	0.97
13.94	5.94	322	0.98
14.37	7.30	324	1.00
14.94	8.62	327	0.98
15.37	9.59	326	0.99
15.92	11.20	327	0.98
16.36	11.60	328	1.01
16.98	11.20	330	1.04
17.37	15.20	329	1.05
17.94	22.70	322.7	1.09
18.24	25.20	316	1.11
18.98	32.30	312	1.15
19.39	39.90	304	1.16
19.94	52.50	286	1.18
20.37	60.70	278	1.19
20.93	71.40	263	1.20
21.37	72.10	261	1.21
21.92	72.40	263	1.14
22.37	69.50	259	1.10
22.93	66.10	264	1.09
23.37	66.40	262	1.10

23.92	67.20	261	1.10
24.37	71.10	257	1.11
24.92	77.00	250	1.11
25.36	84.00	244	1.11
25.93	90.70	236	1.13
26.36	101.00	224	1.15
26.93	110.00	214	1.14
27.37	119.00	207	1.11
27.95	123.00	199	1.10
28.36	126.00	197	1.11
28.95	129.00	194	1.09
29.35	130.00	191	1.08
29.94	128.00	196	1.08
30.35	126.00	196	1.05
30.95	119.00	207	1.05
31.34	118.00	203	1.04
31.92	106.00	218	1.03
32.29	104.00	219	1.03
32.92	100.00	220	1.00
33.97	89.80	235	0.99
34.96	70.70	251	0.95
35.91	53.20	272	0.93
36.95	37.60	287	0.93
37.88	33.50	292	0.93
39.00	34.80	292	0.96
39.90	33.20	294	0.96
40.95	34.20	291	0.96
41.90	31.00	295	0.97
42.89	33.70	294	0.99

Appendix D: Supplementary Solid Phase (Spectroscopy)

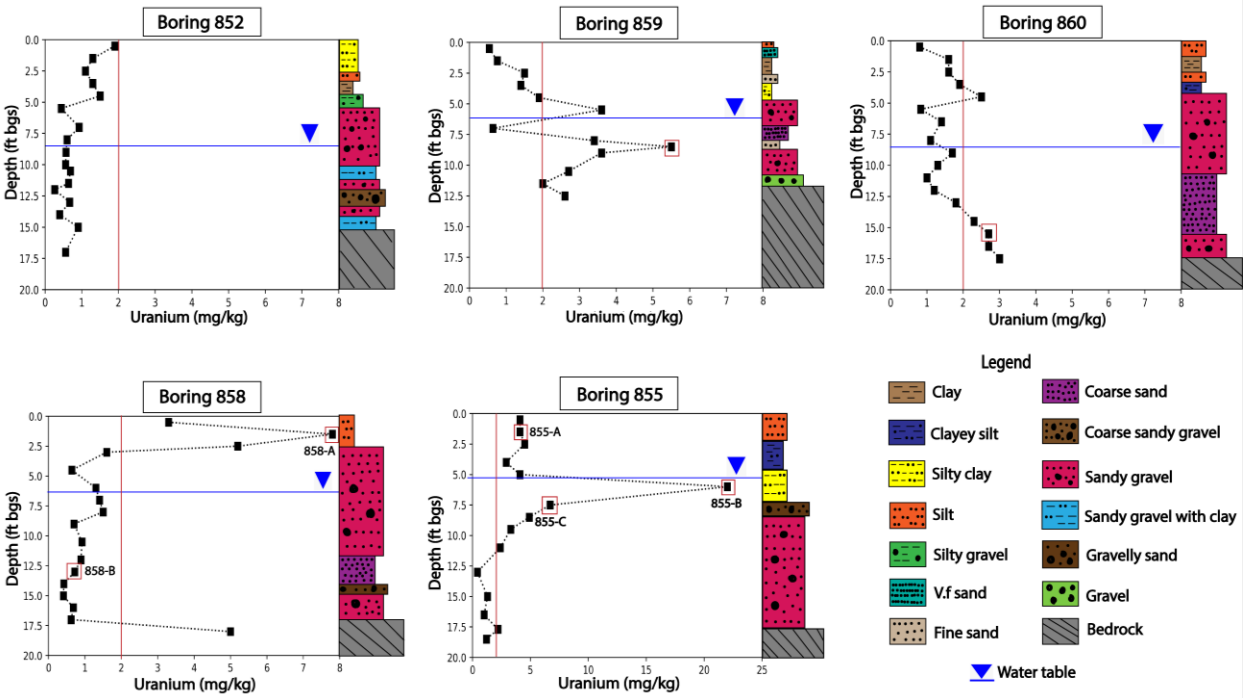

Fig. S1. Boring and Sample Locations for Fission Track (FT) on Mica Plate under Plain Light Microscope, Thin Section Slides under Plain Light Microscope, Backscattered Electron Image (BSE) under Scanning Electron Microscope (SEM), Elemental Map (EM) from Energy Dispersive X-ray Spectroscope (EDS), and Point Map from Energy Dispersive X-ray Spectroscope (EDS)

Note: 'Site' in the following images refer to different locations in a single slide.

Boring 859: 9.5 ft depth (Site 3)

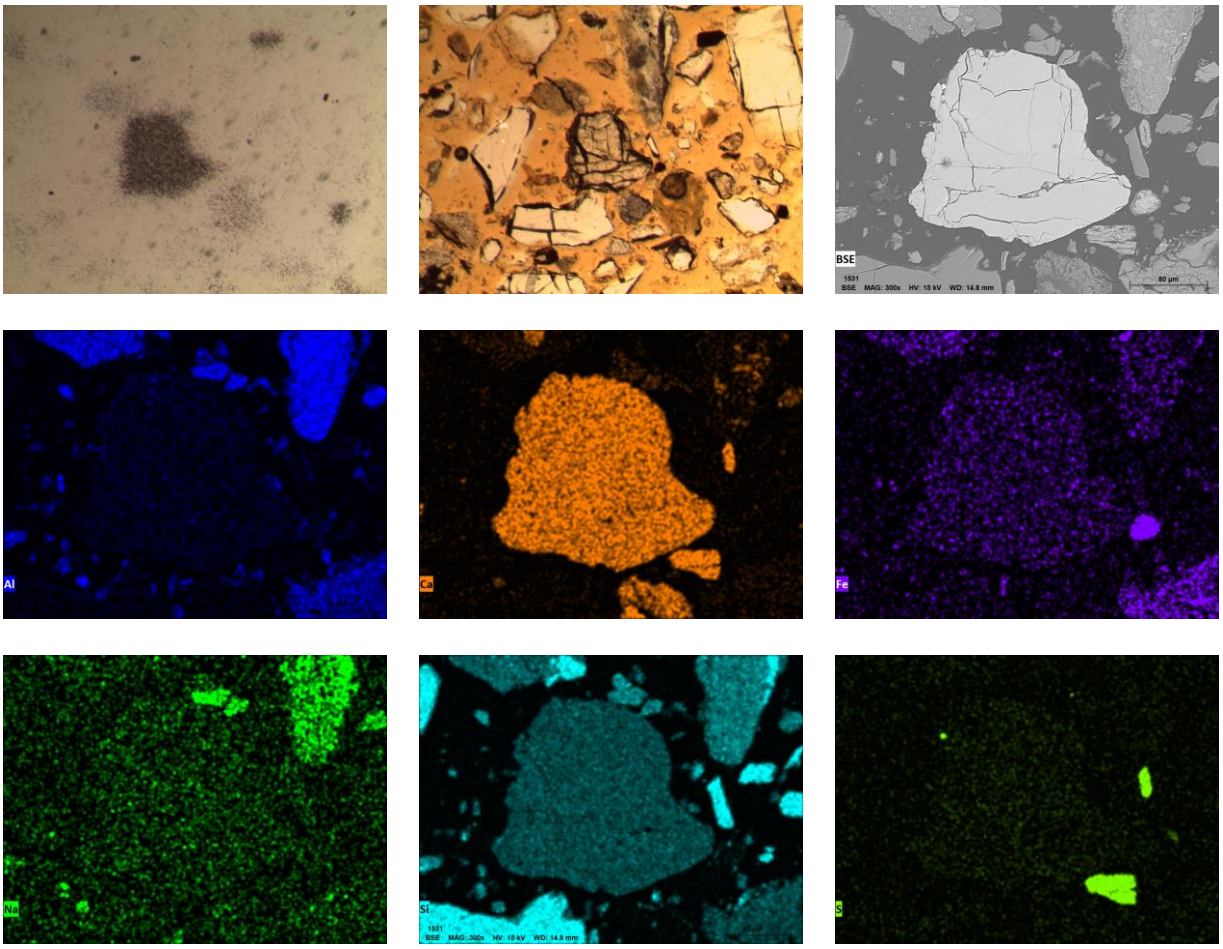

Fig. S2. Row 1: FT, Thin Section, BSE; Row 2 and Row 3: EM

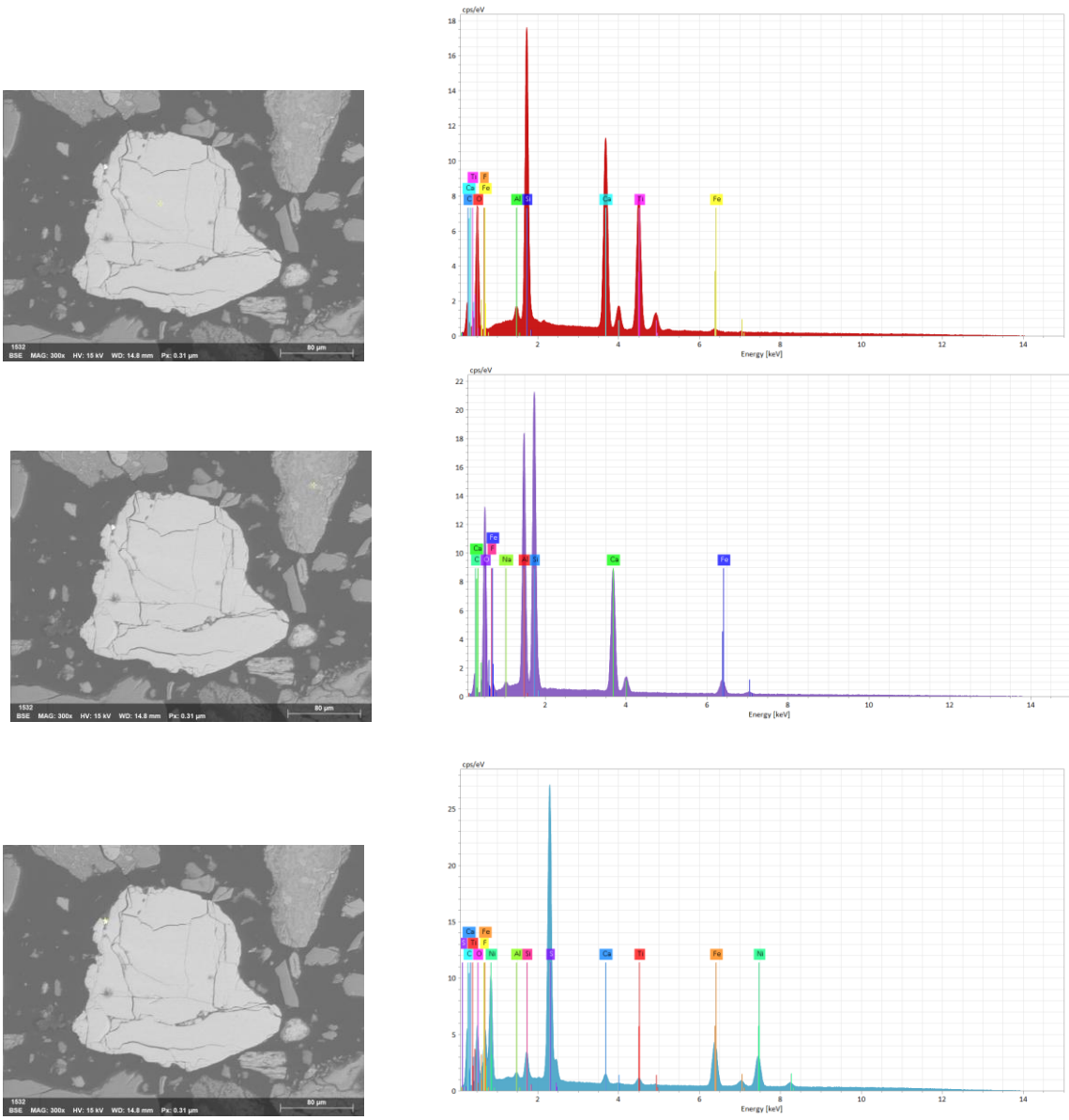

Fig. S3. Column 1: EDS locations; Column 2: Corresponding EDS

Boring 859: 9.5 ft depth (Site 4)

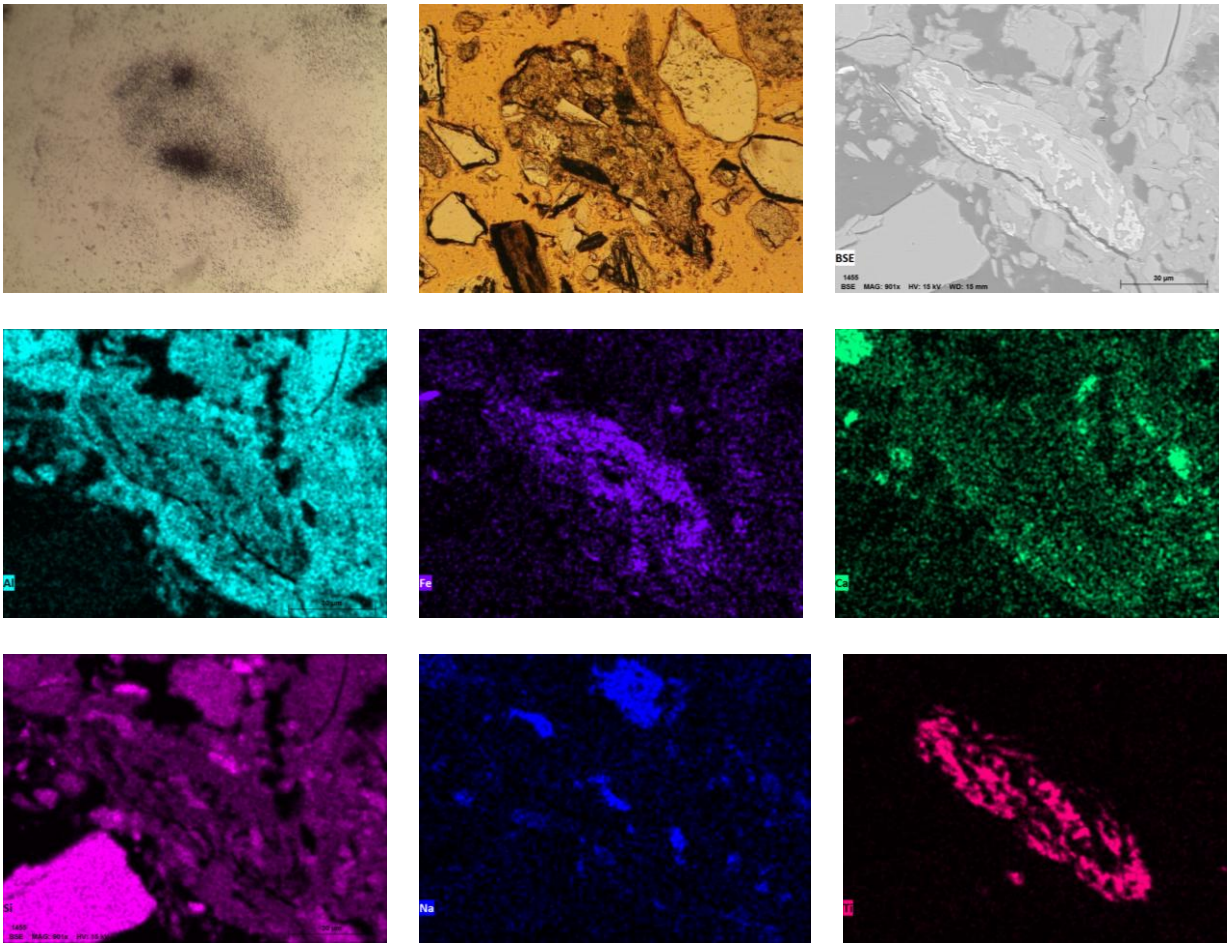

Fig. S4. Row 1: FT, Thin Section, BSE; Row 2 and Row 3: EM

Boring 859: 9.5 ft depth (Site 5)

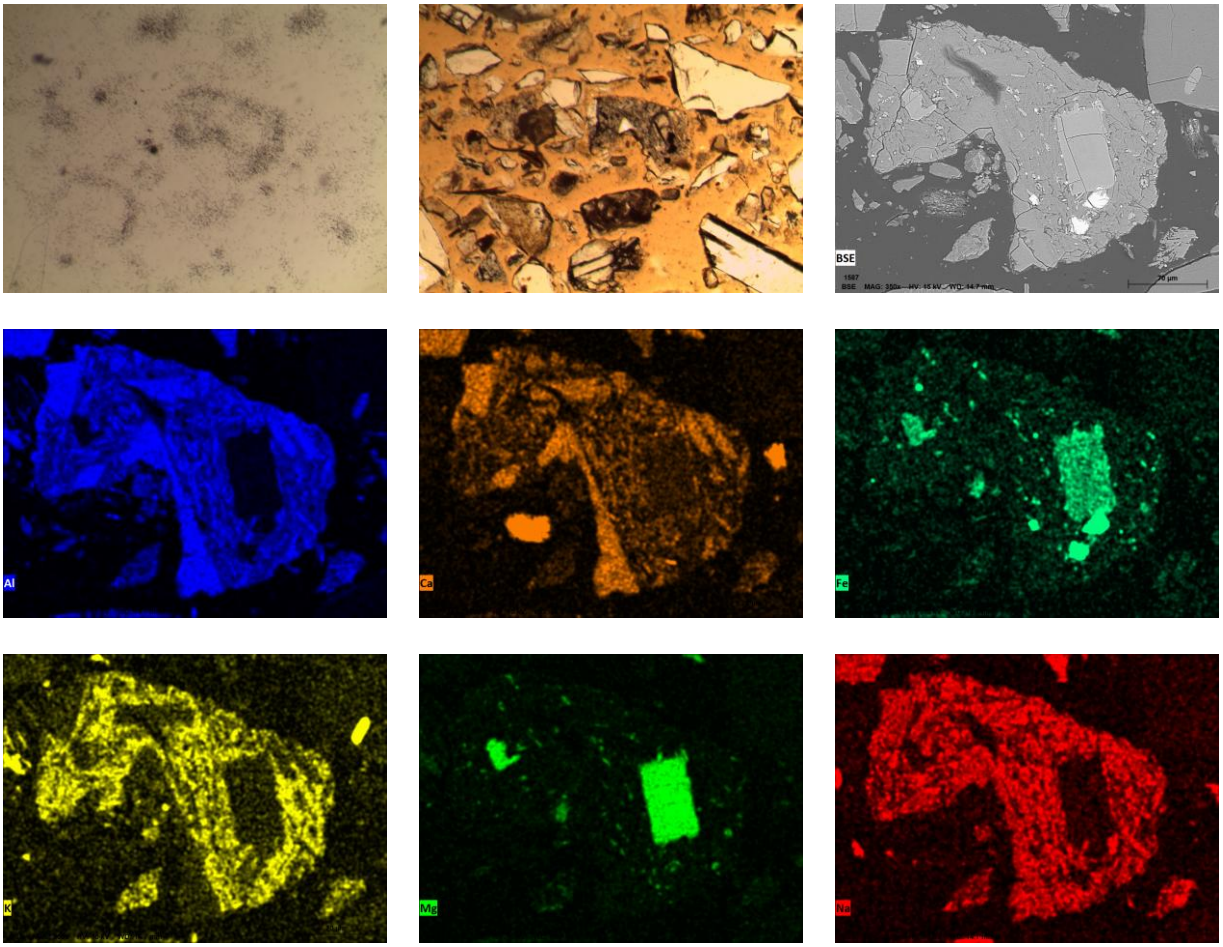

Fig. S5. Row 1: FT, Thin Section, BSE; Row 2 and Row 3: EM

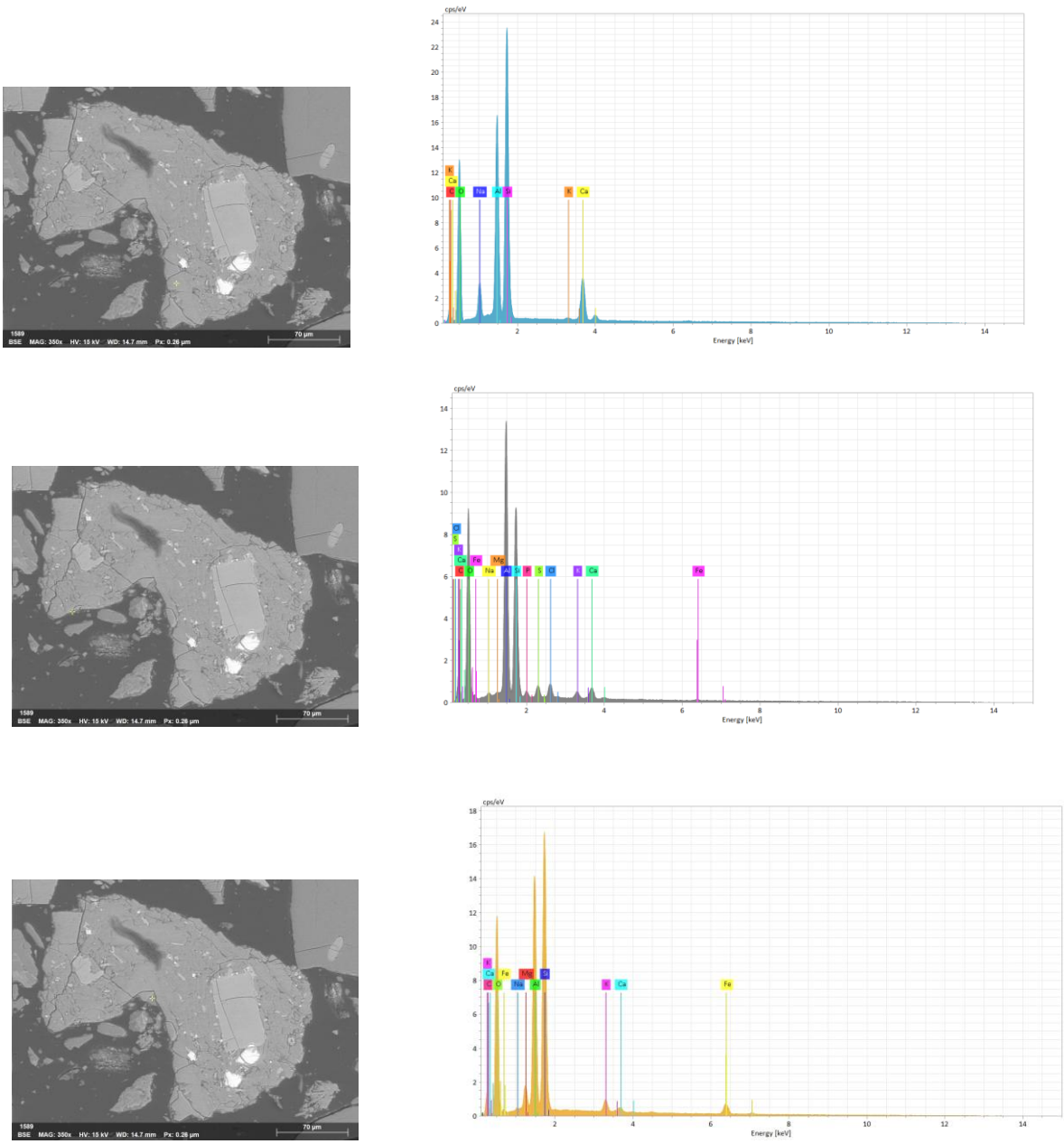

Fig. S6. Column 1: EDS locations; Column 2: Corresponding EDS

Boring 860: 15.5 ft depth (Site 3)

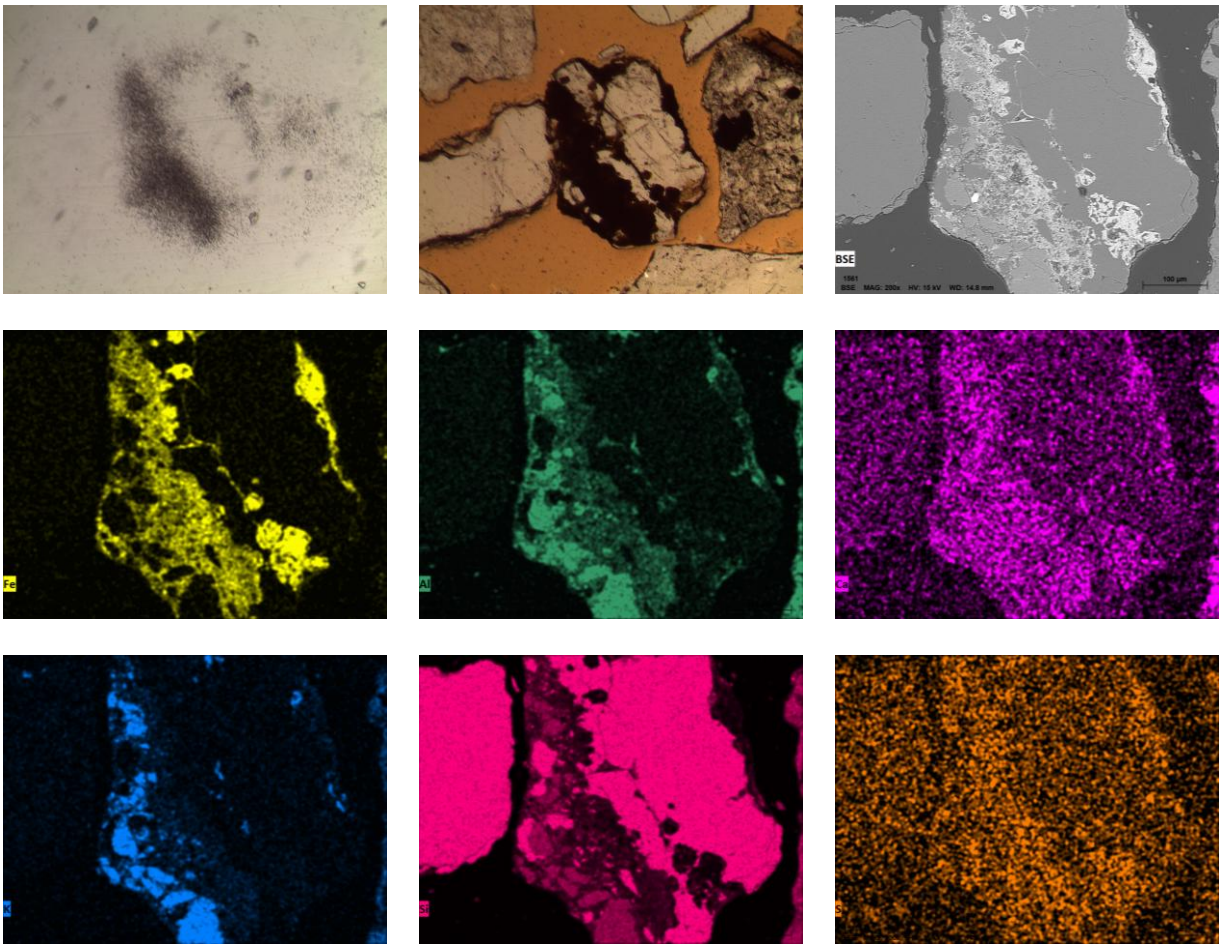

Fig. S7. Row 1: FT, Thin Section, BSE; Row 2 and Row 3: EM

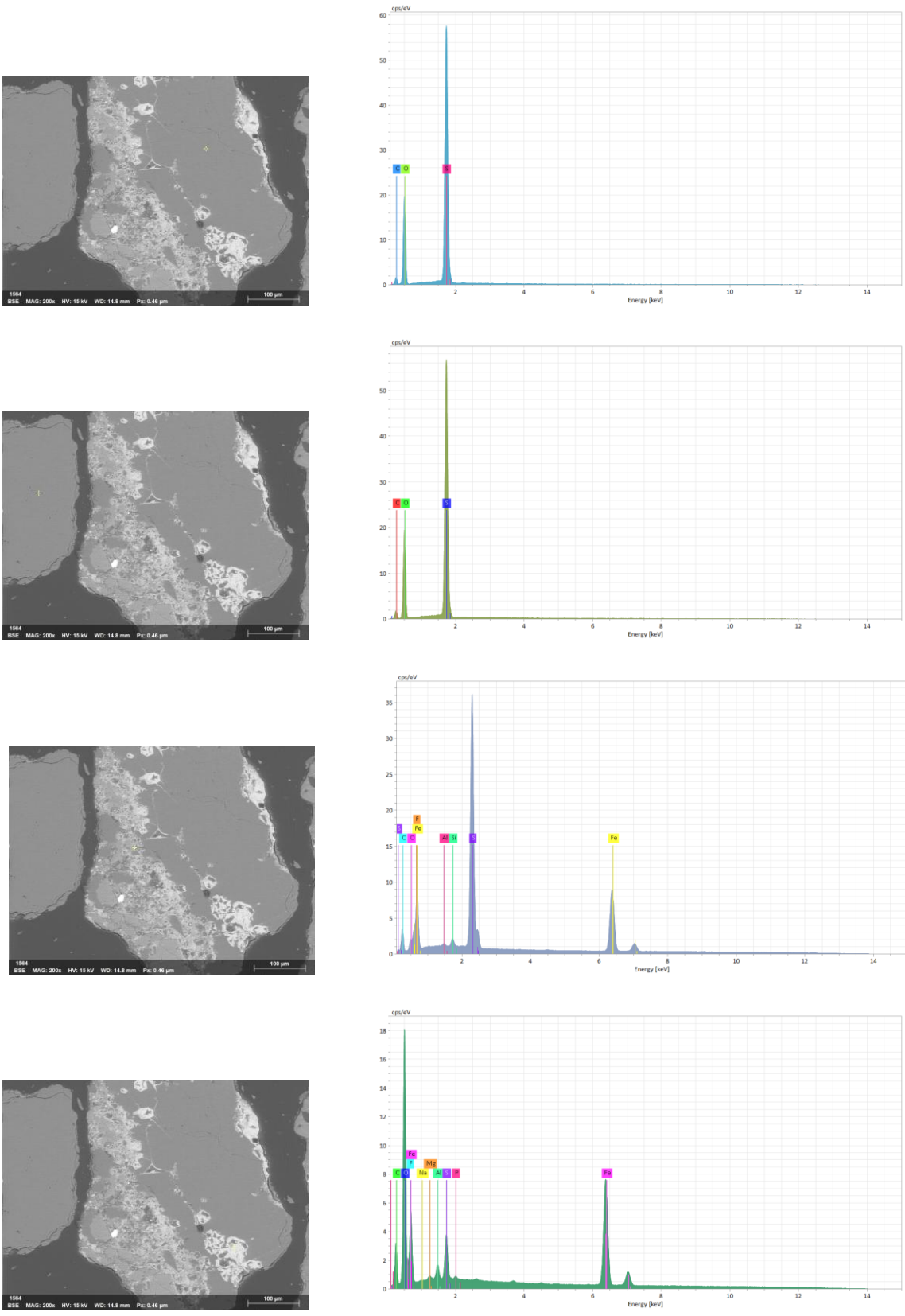

Fig. S8. Column 1: EDS locations; Column 2: Corresponding EDS

Boring 860: 15.5 ft depth (Site 3 - FeS)

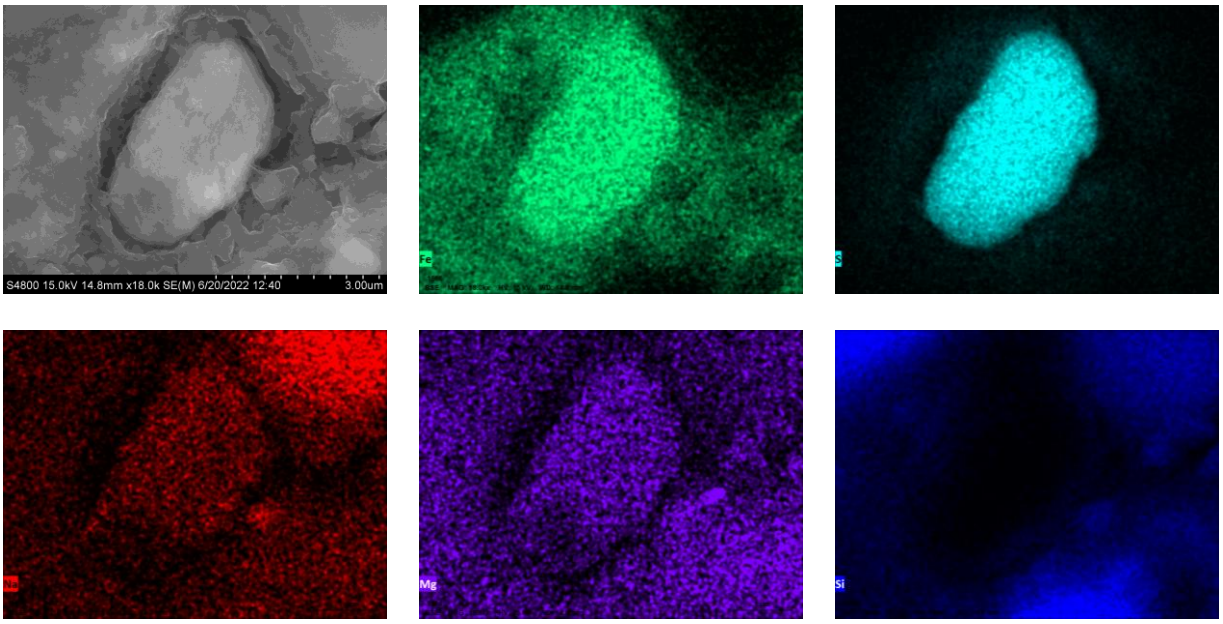

Fig. S9. Row 1: BSE, EM (Fe and S); Row 2: EM (Na, Mg, Si)

Boring 860: 15.5 ft depth (Site 4)

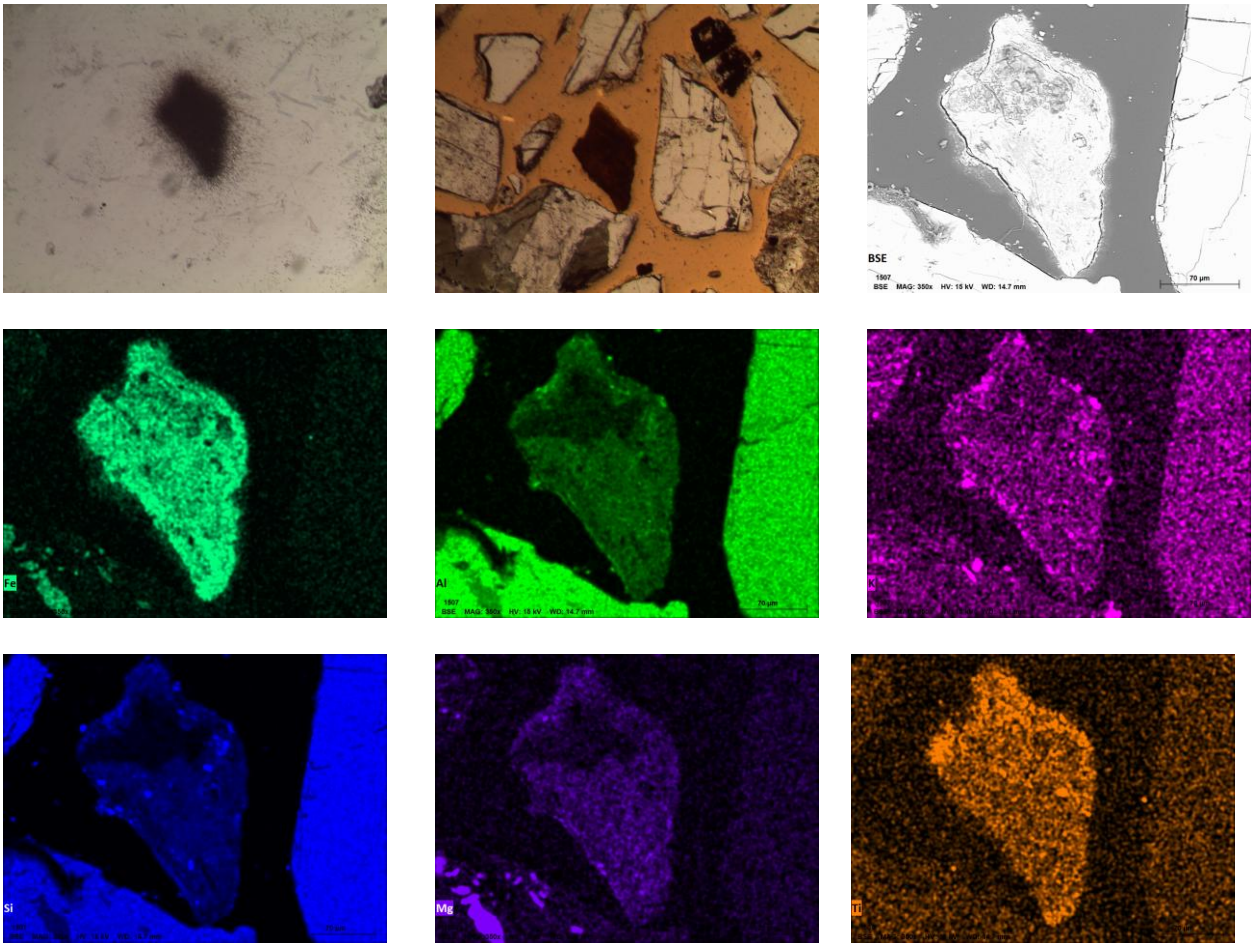

Fig. S10. Row 1: FT, Thin Section, BSE; Row 2 and Row 3: EM

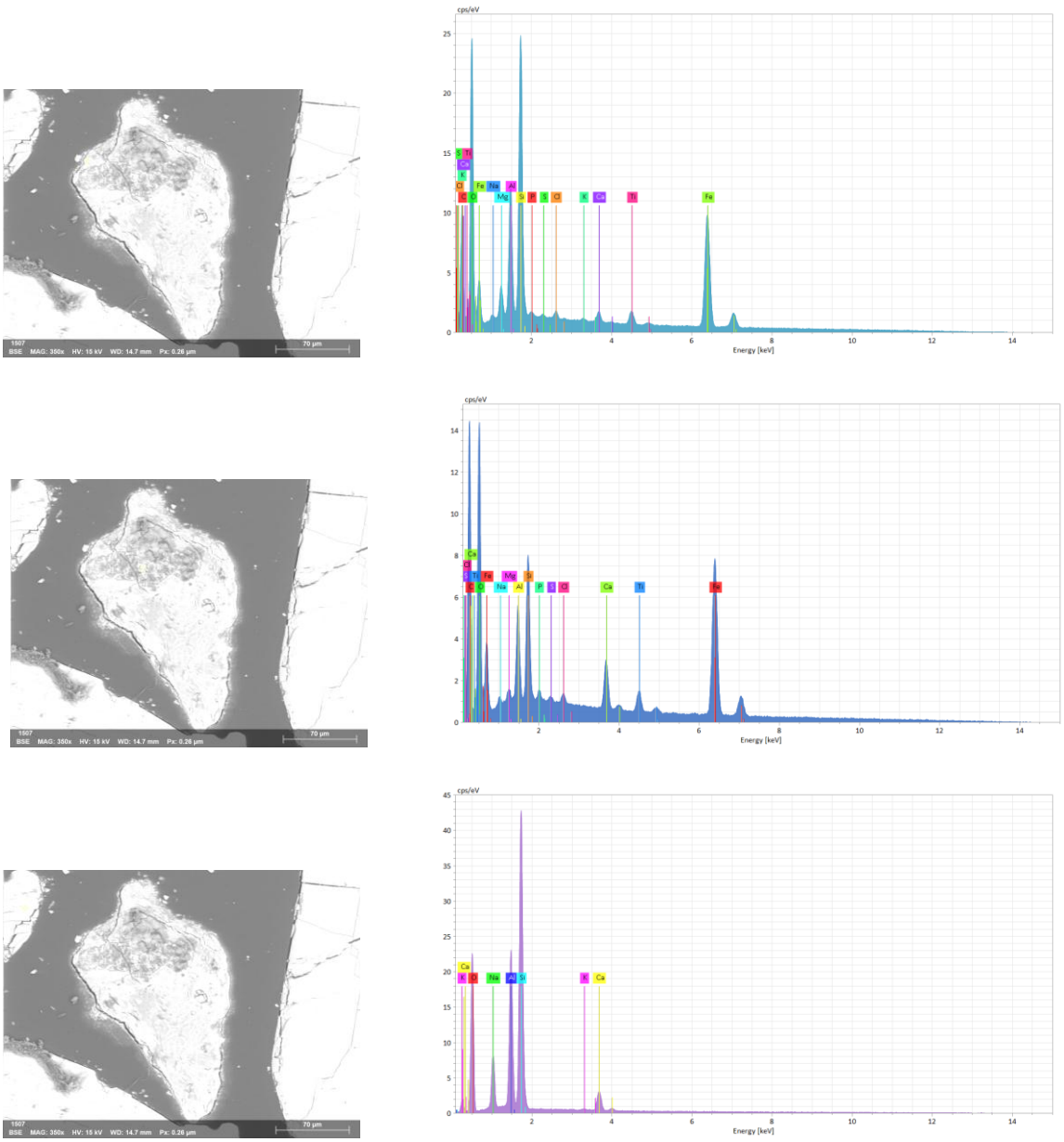

Fig. S11. Column 1: EDS locations; Column 2: Corresponding EDS

Boring 860: 15.5 ft depth (Site 5)

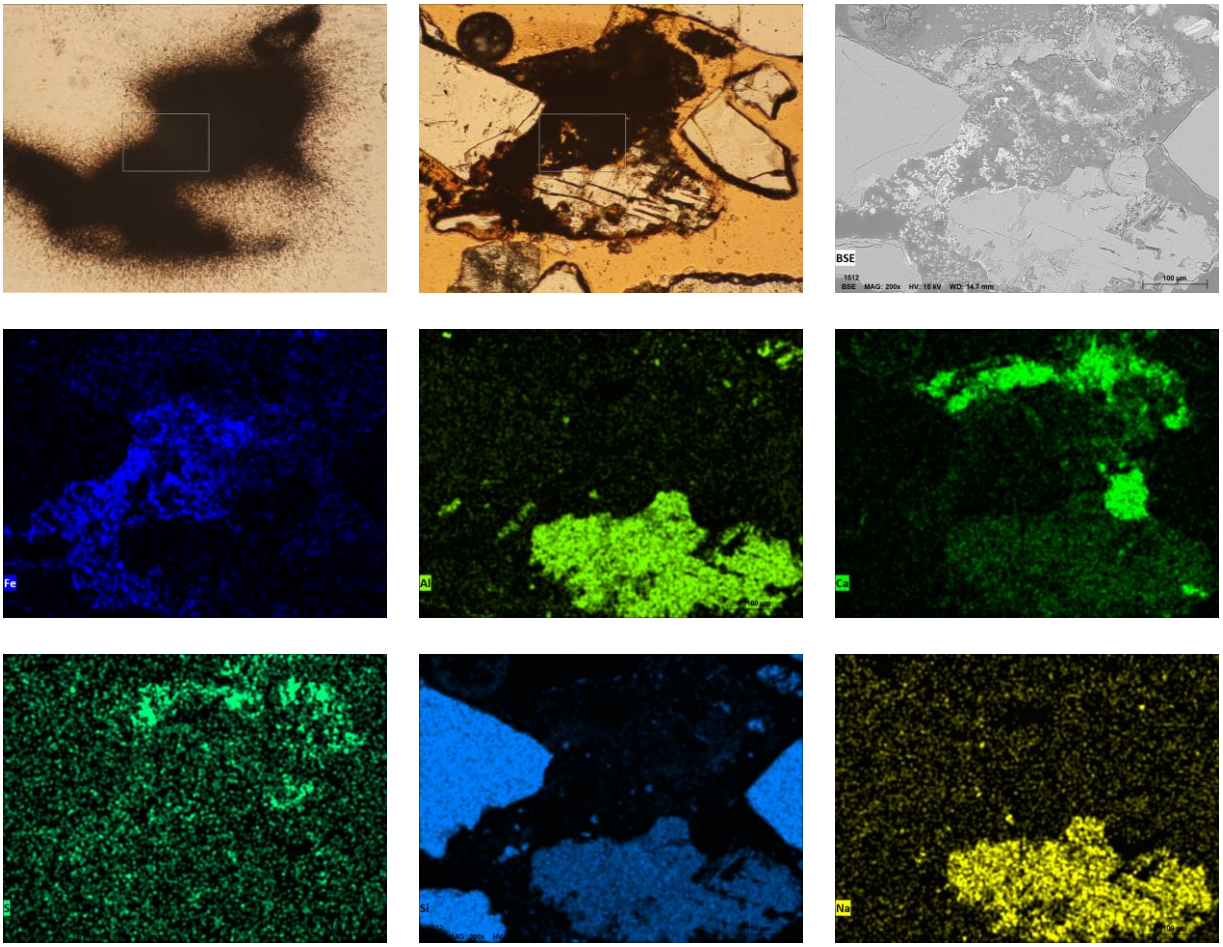

Fig. S12. Row 1: FT, Thin Section, BSE; Row 2 and Row 3: EM

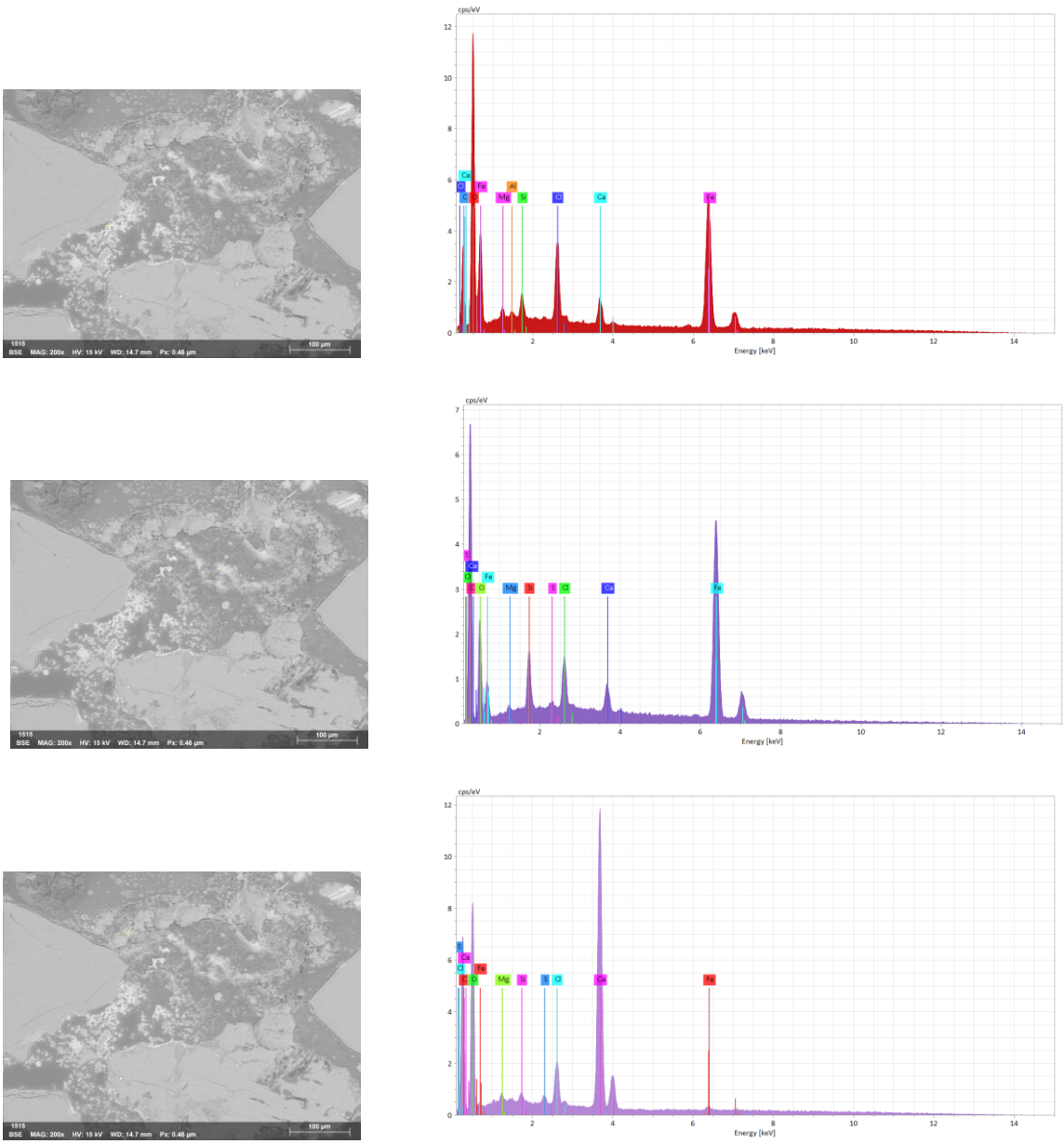

Fig. S13. Column 1: EDS locations; Column 2: Corresponding EDS

Boring 858: 2.5 ft depth (Site 1-part 1)

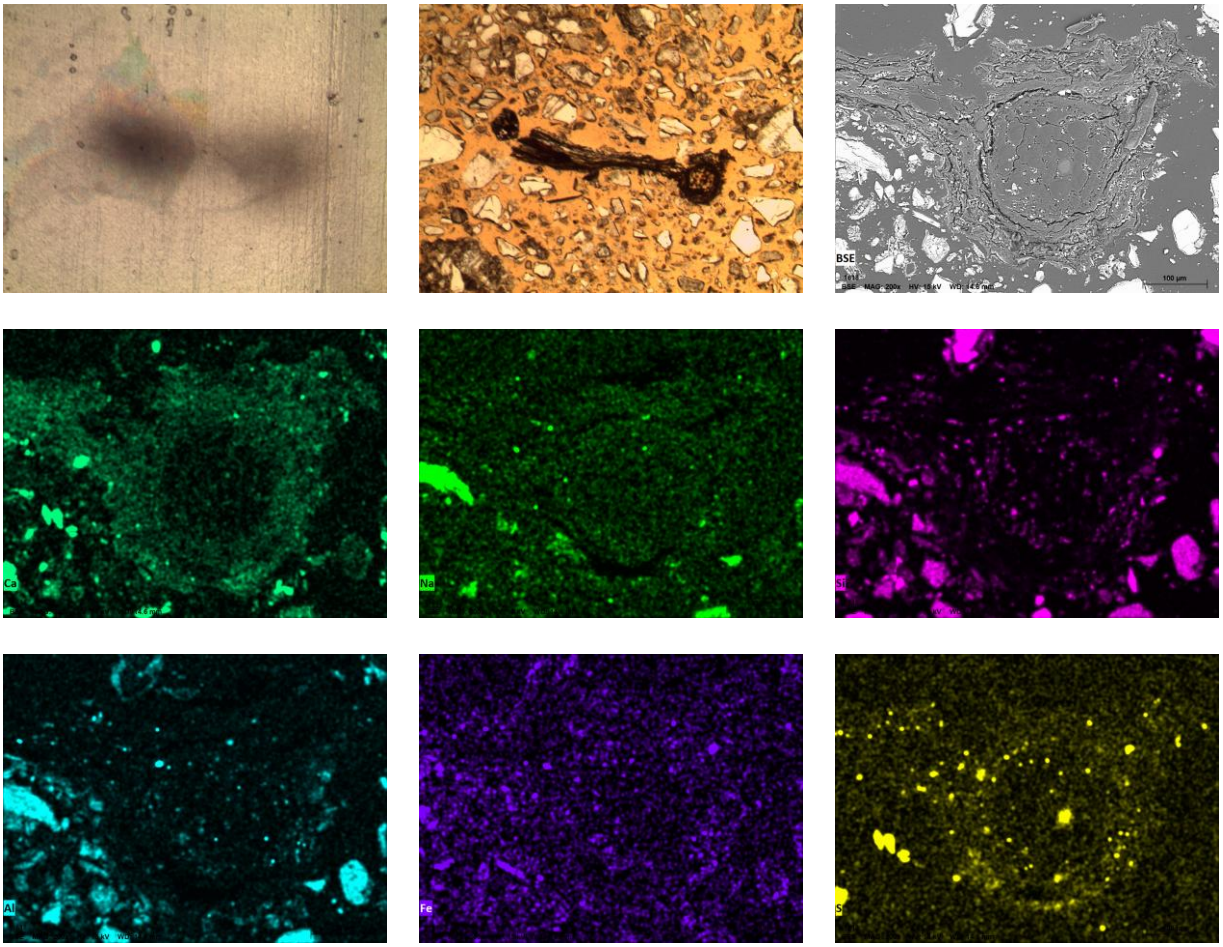

Fig. S14. Row 1: FT, Thin Section, BSE; Row 2 and Row 3: EM

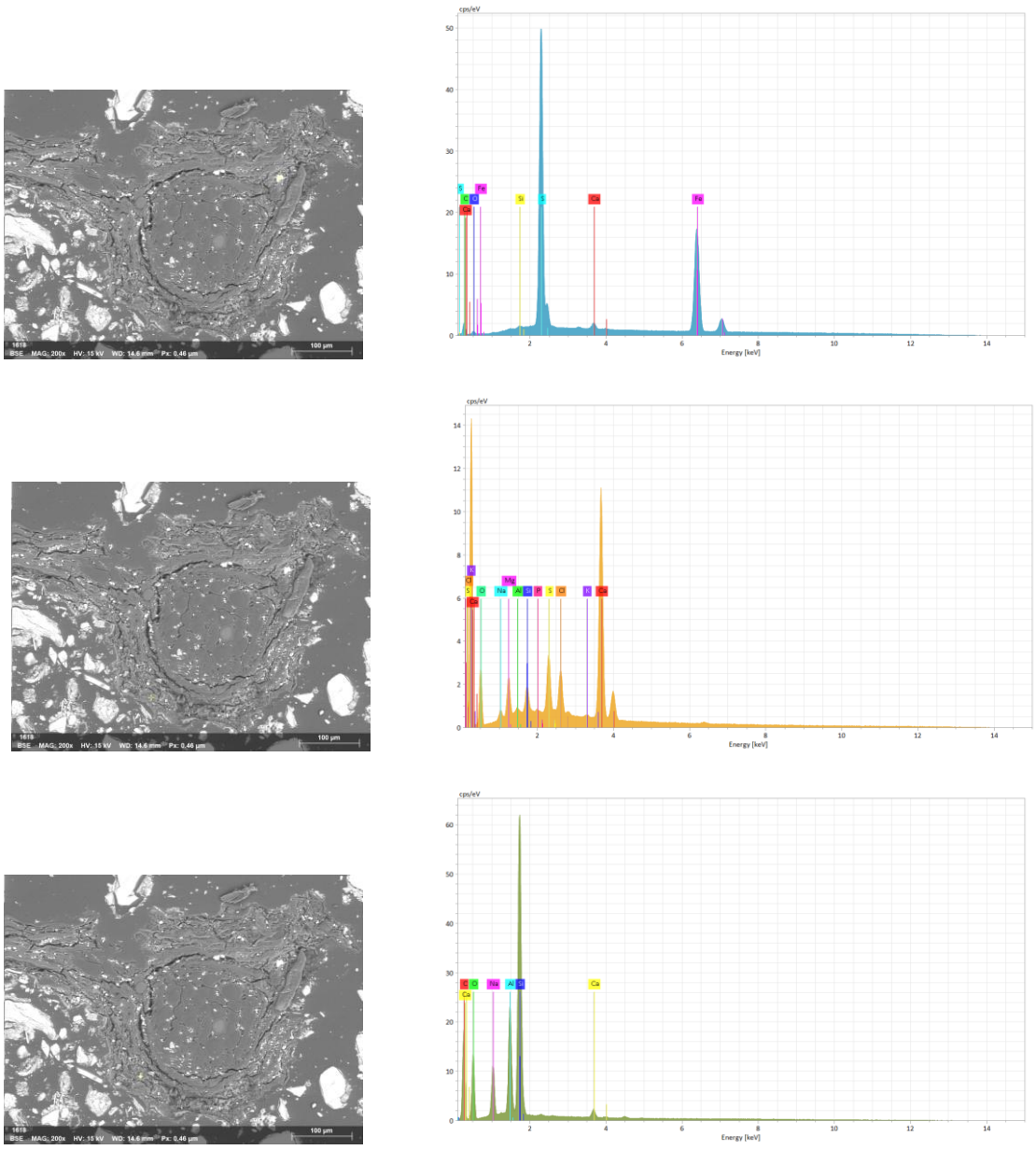

Fig. S15. Column 1: EDS locations; Column 2: Corresponding EDS

Boring 858: 2.5 ft depth (Site 1-part 2)

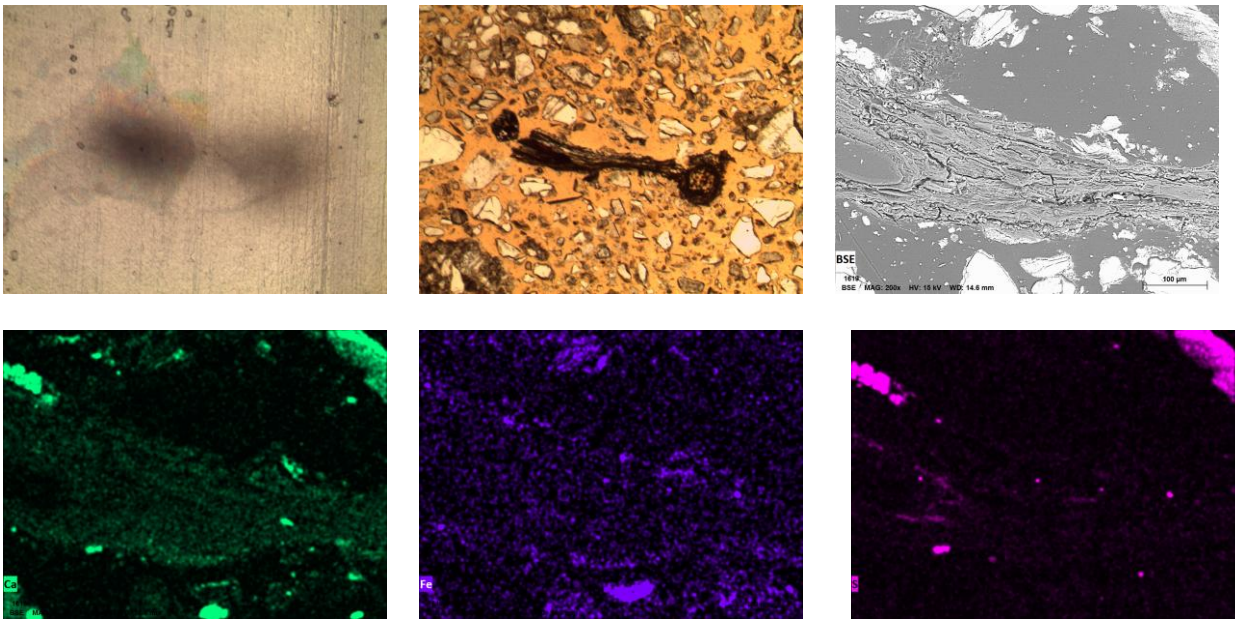

Fig. S16. Row 1: FT, Thin Section, BSE; Row 2: EM

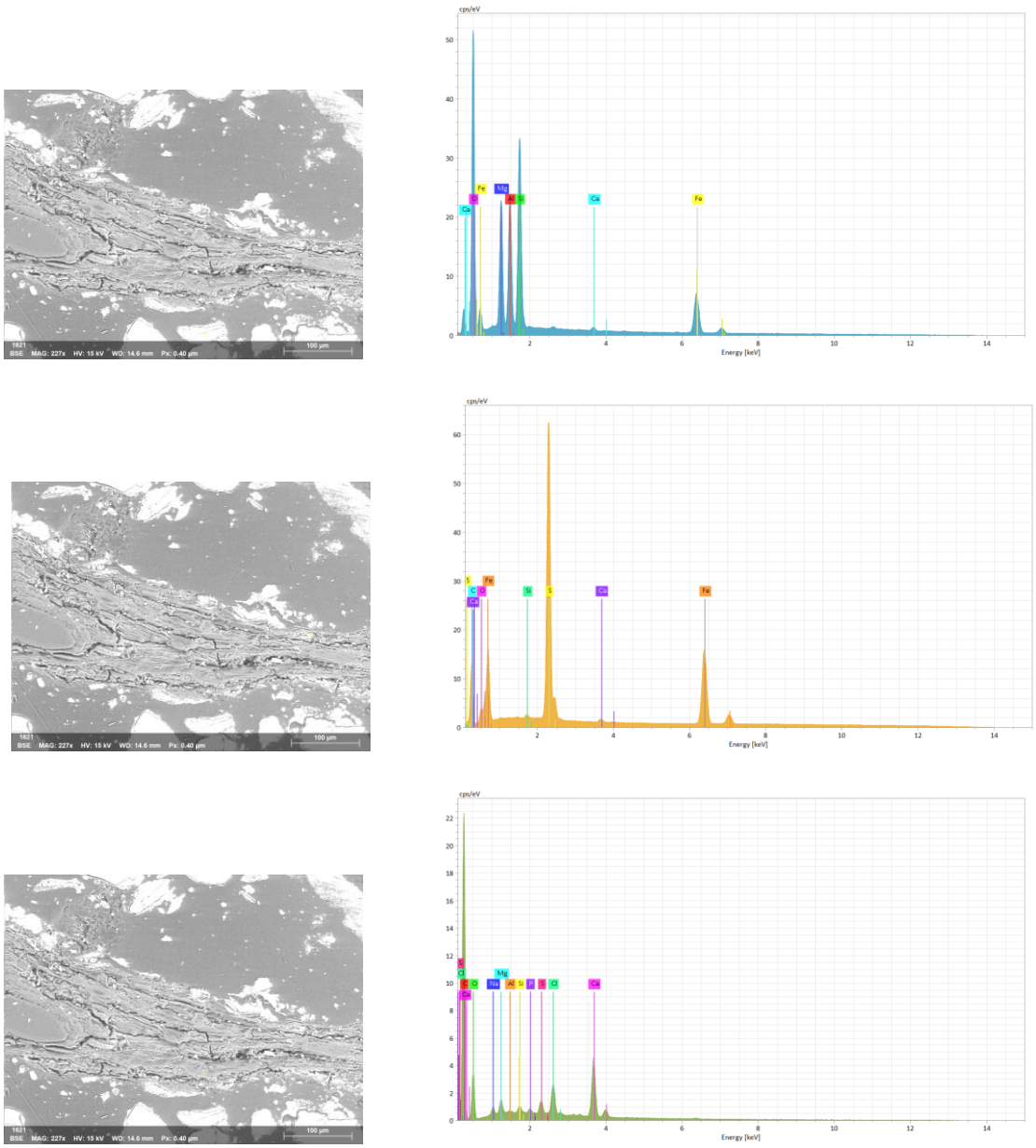

Fig. S17. Column 1: EDS locations; Column 2: Corresponding EDS

Boring 858: 2.5 ft depth (Site 2)

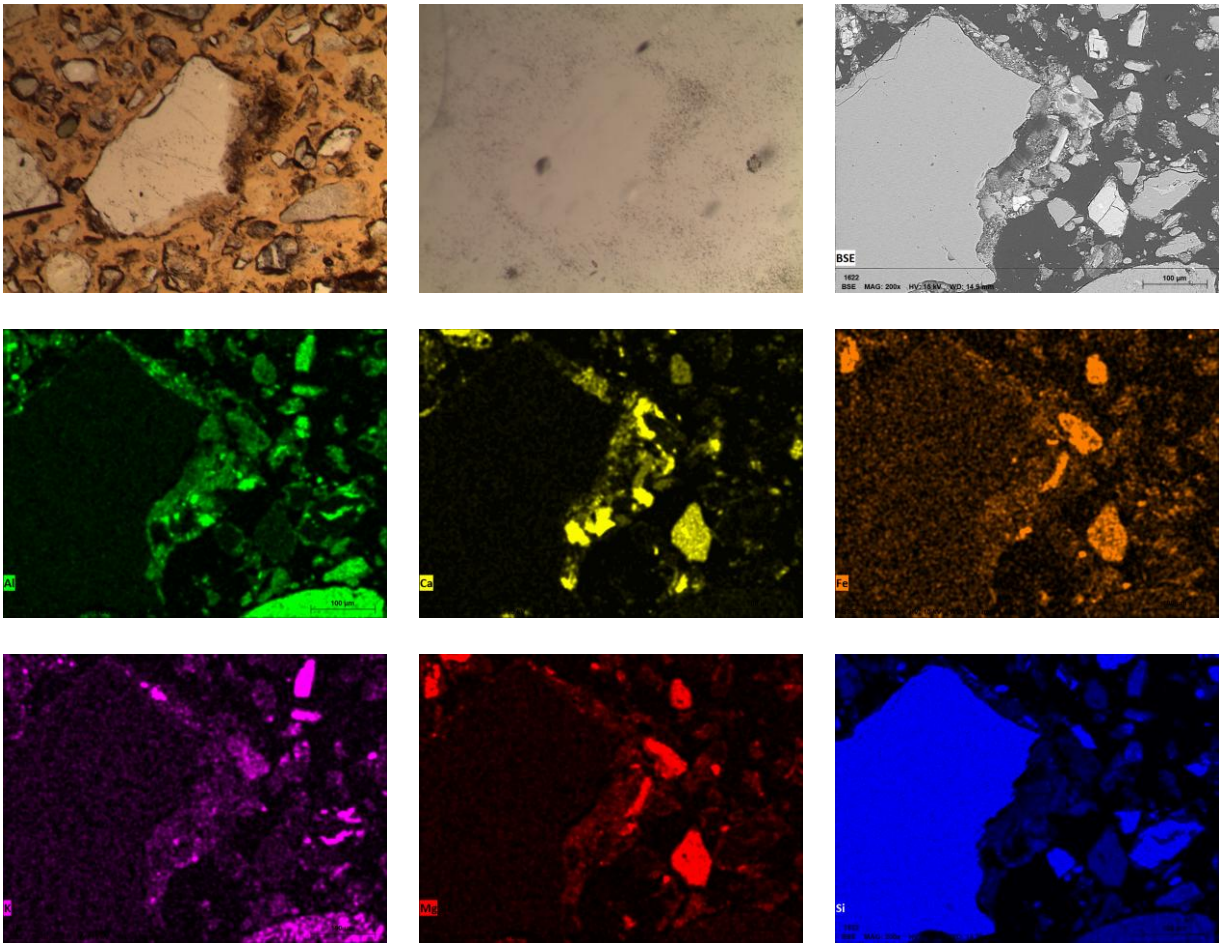

Fig. S18. Row 1: FT, Thin Section, BSE; Row 2 and Row 3: EM

Boring 858: 12.5 ft depth (Site 1)

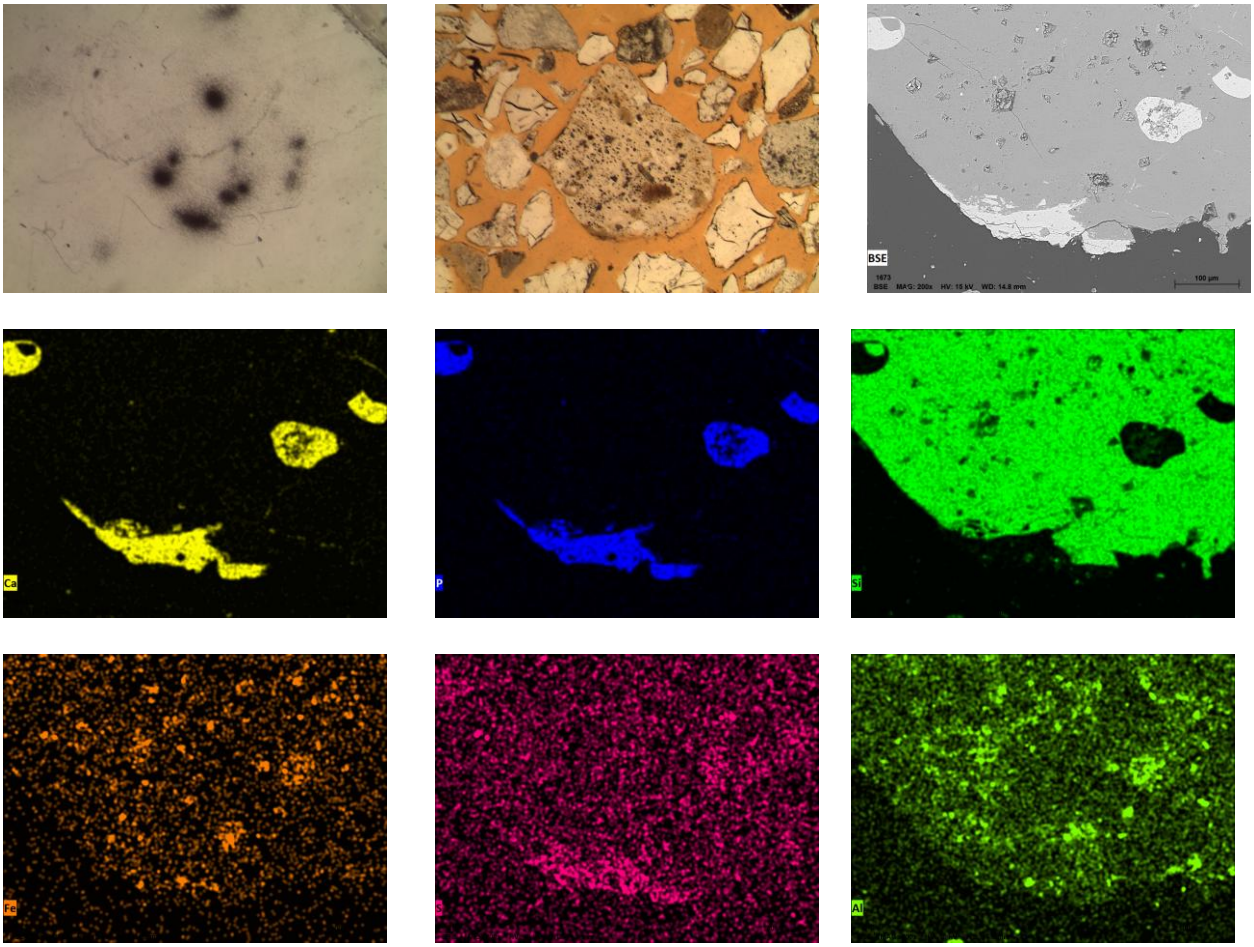

Fig. S19. Row 1: FT, Thin Section, BSE; Row 2 and Row 3: EM

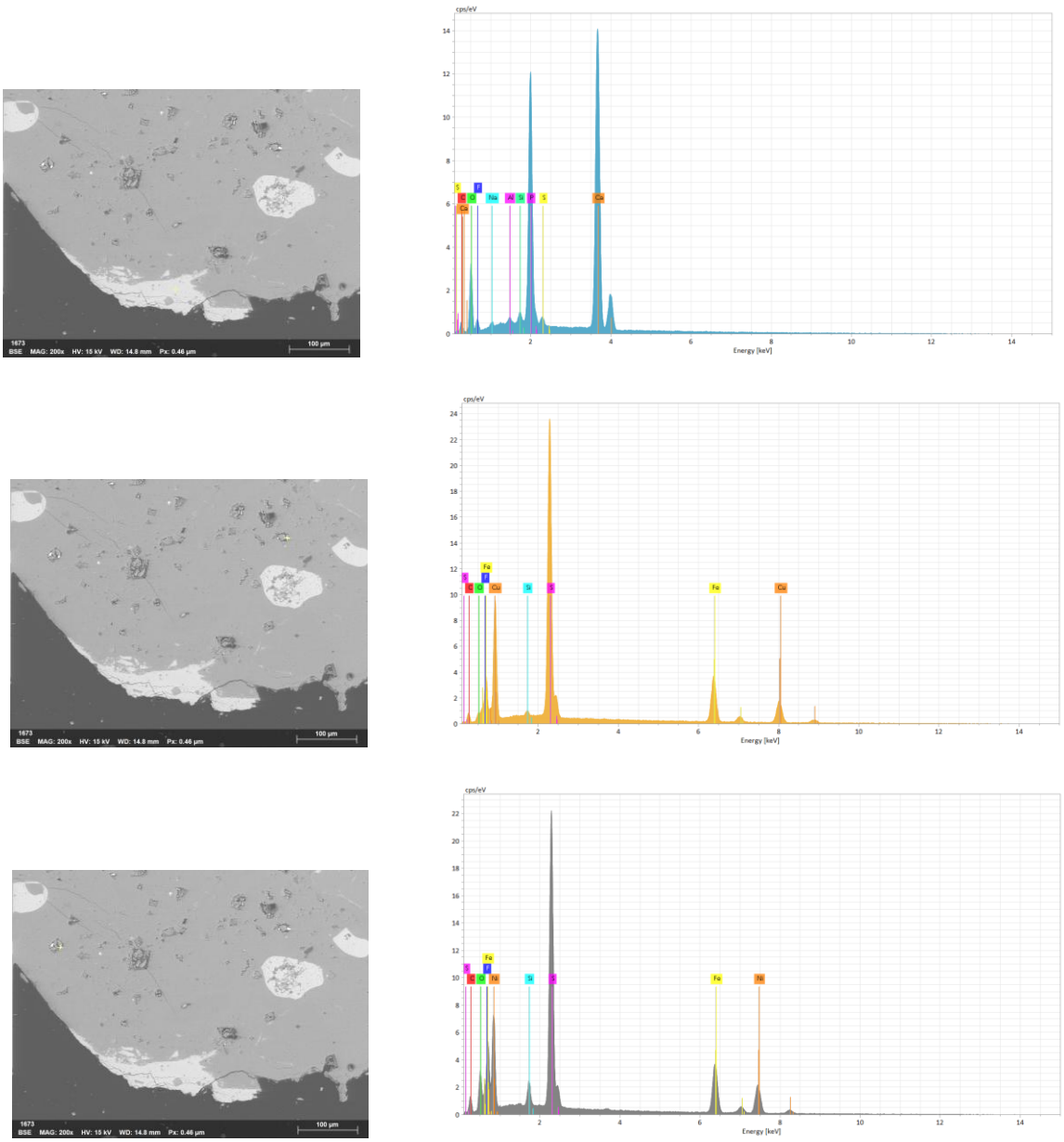

Fig. S20. Column 1: EDS locations; Column 2: Corresponding EDS

Boring 858: 12.5 ft depth (Site 2)

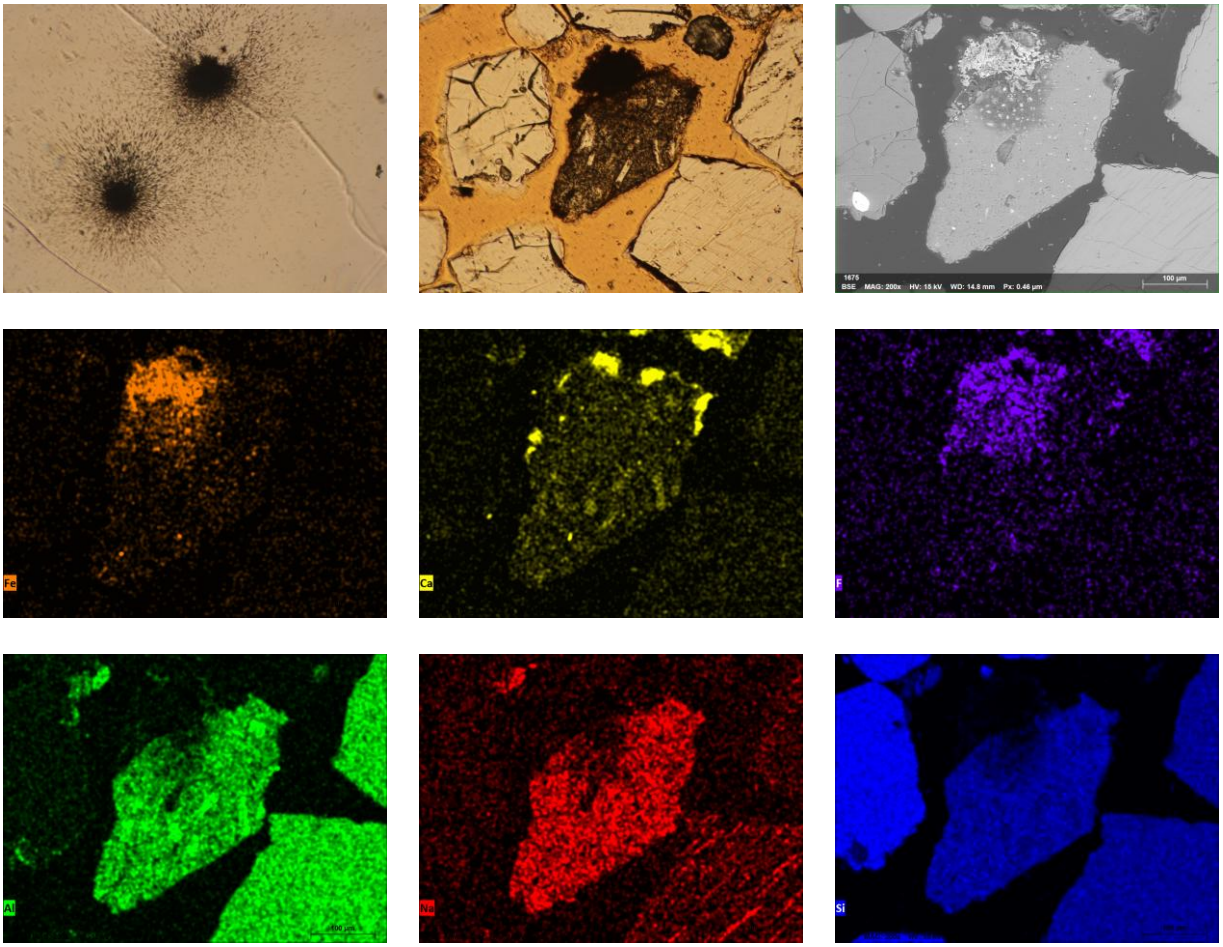

Fig. S21. Row 1: FT, Thin Section, BSE; Row 2 and Row 3: EM

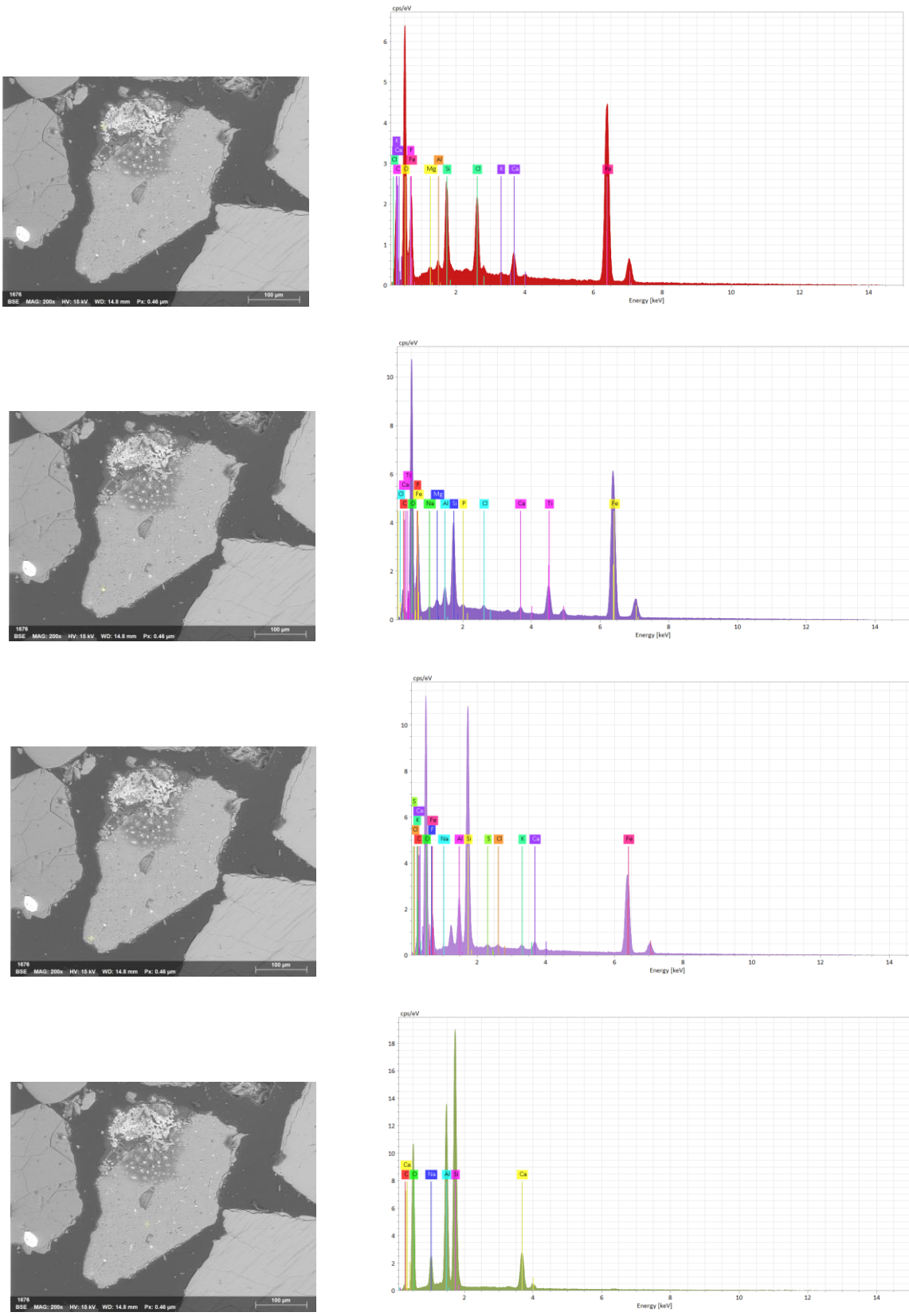

Fig. S22. Column 1: EDS locations; Column 2: Corresponding EDS

Boring 855: 2 ft depth (Site 1)

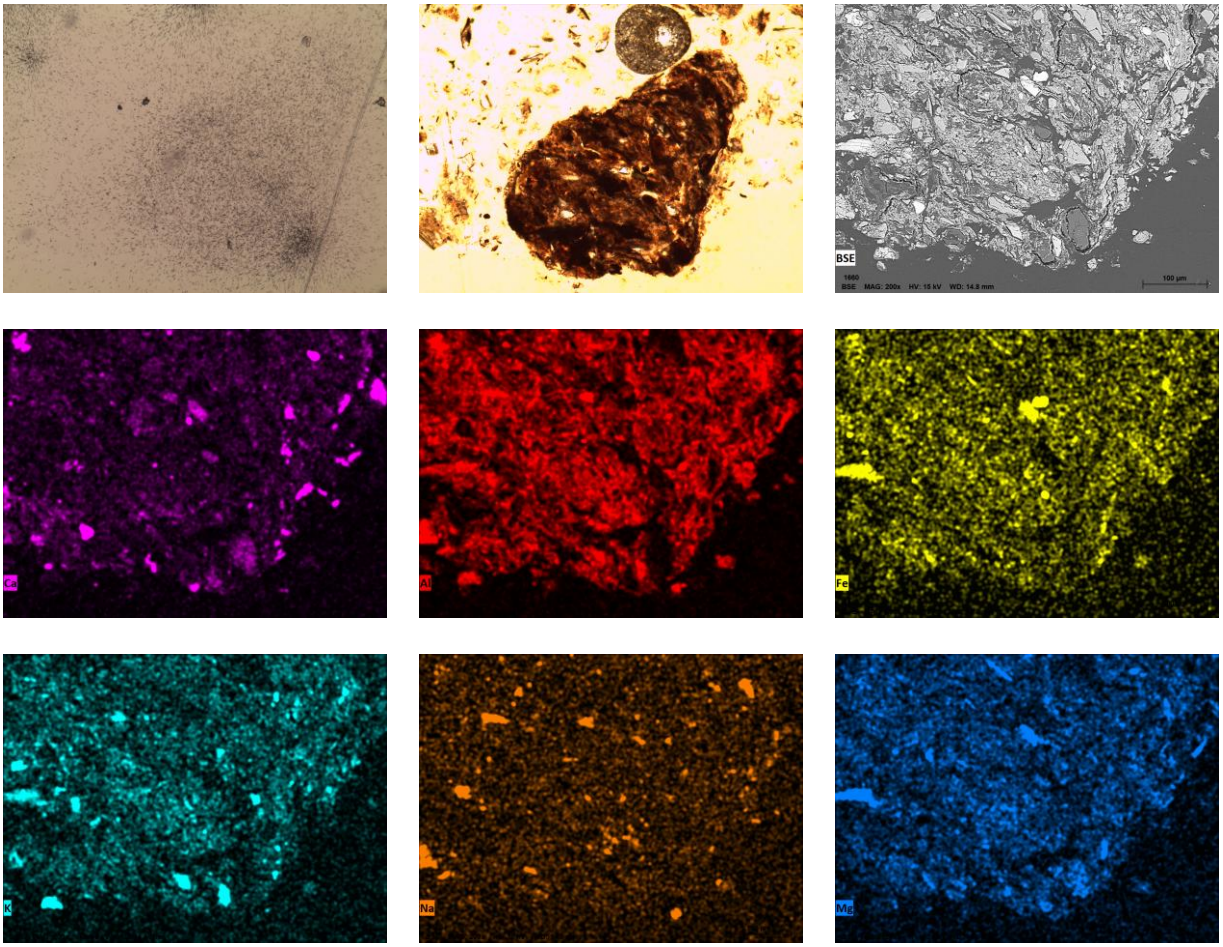

Fig. S23. Row 1: FT, Thin Section, BSE; Row 2 and Row 3: EM

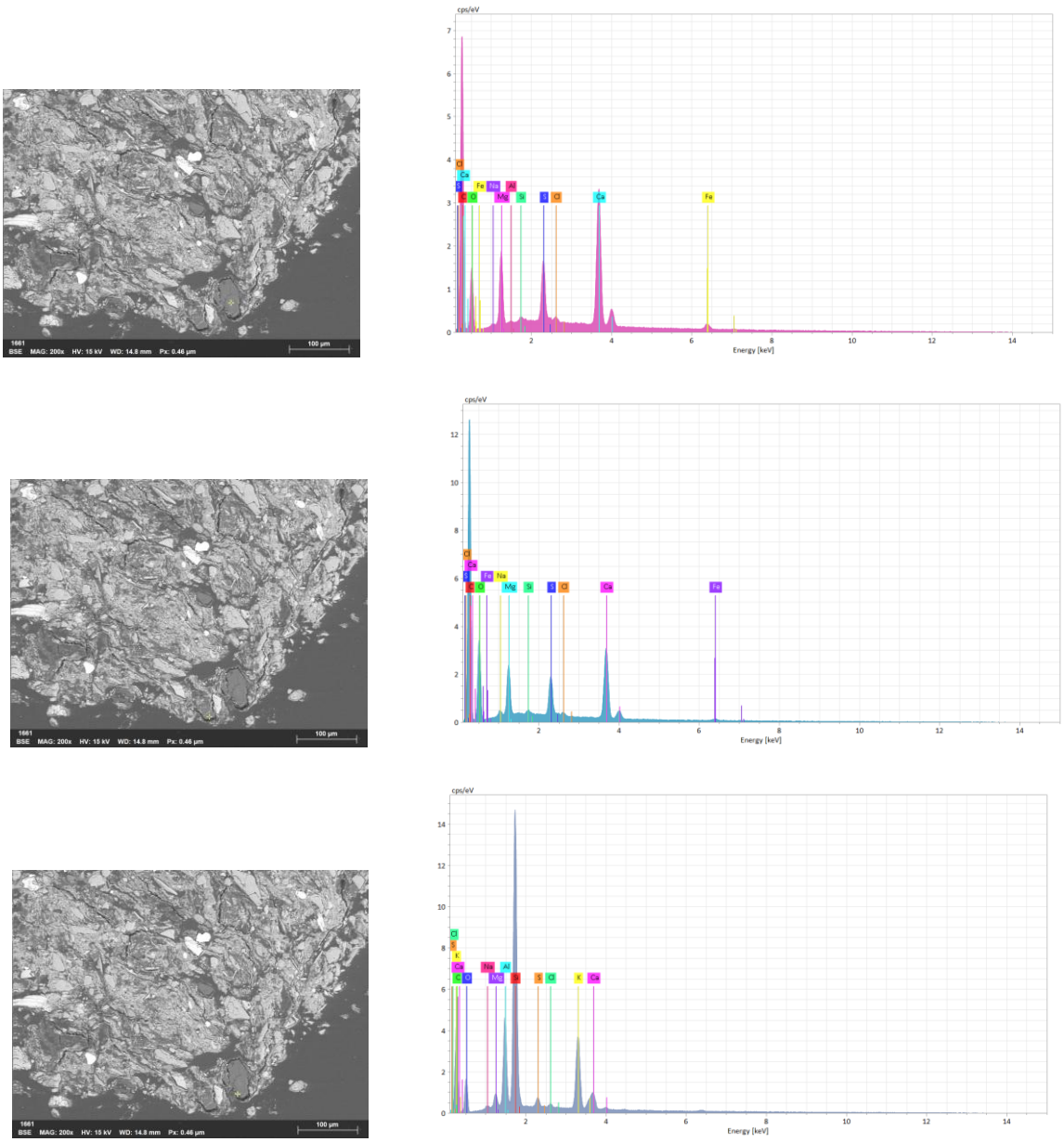

Fig. S24. Column 1: EDS locations; Column 2: Corresponding EDS

Boring 855: 2 ft depth (Site 2)

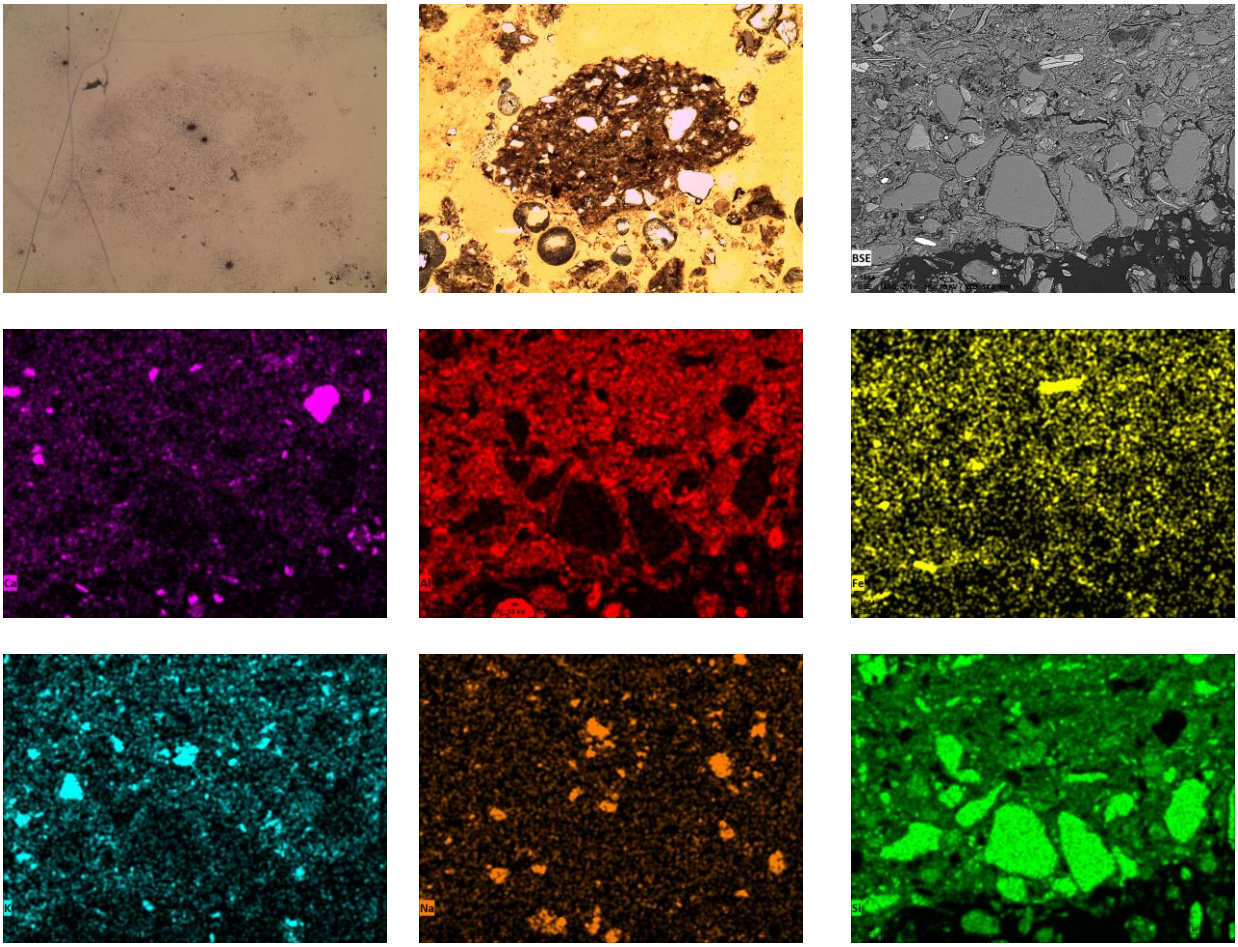

Fig. S25. Row 1: FT, Thin Section, BSE; Row 2 and Row 3: EM

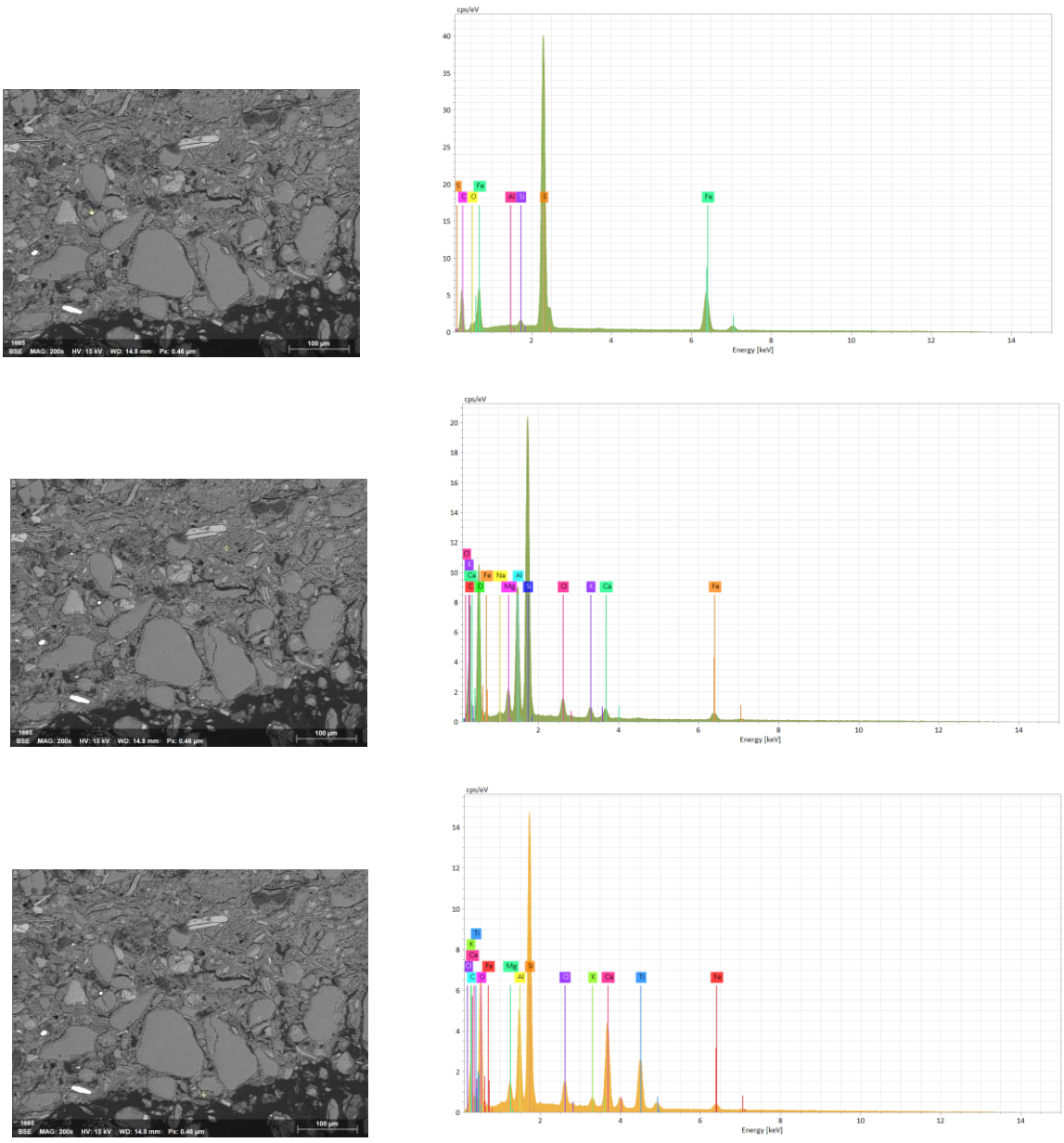

Fig. S26. Column 1: EDS locations; Column 2: Corresponding EDS

Boring 855: 2 ft depth (Site 2 - FeS)

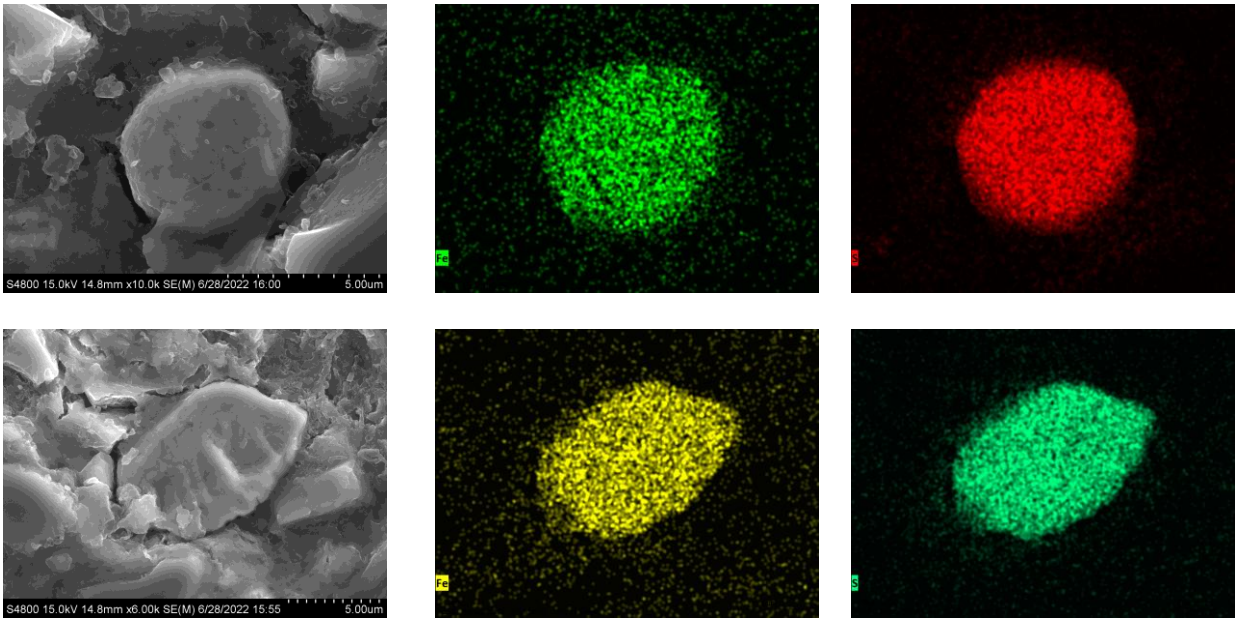

Fig. S27. Row 1 and Row 2: FeS - BSE and EM

Boring 855: 6.5 ft depth (Site 1)

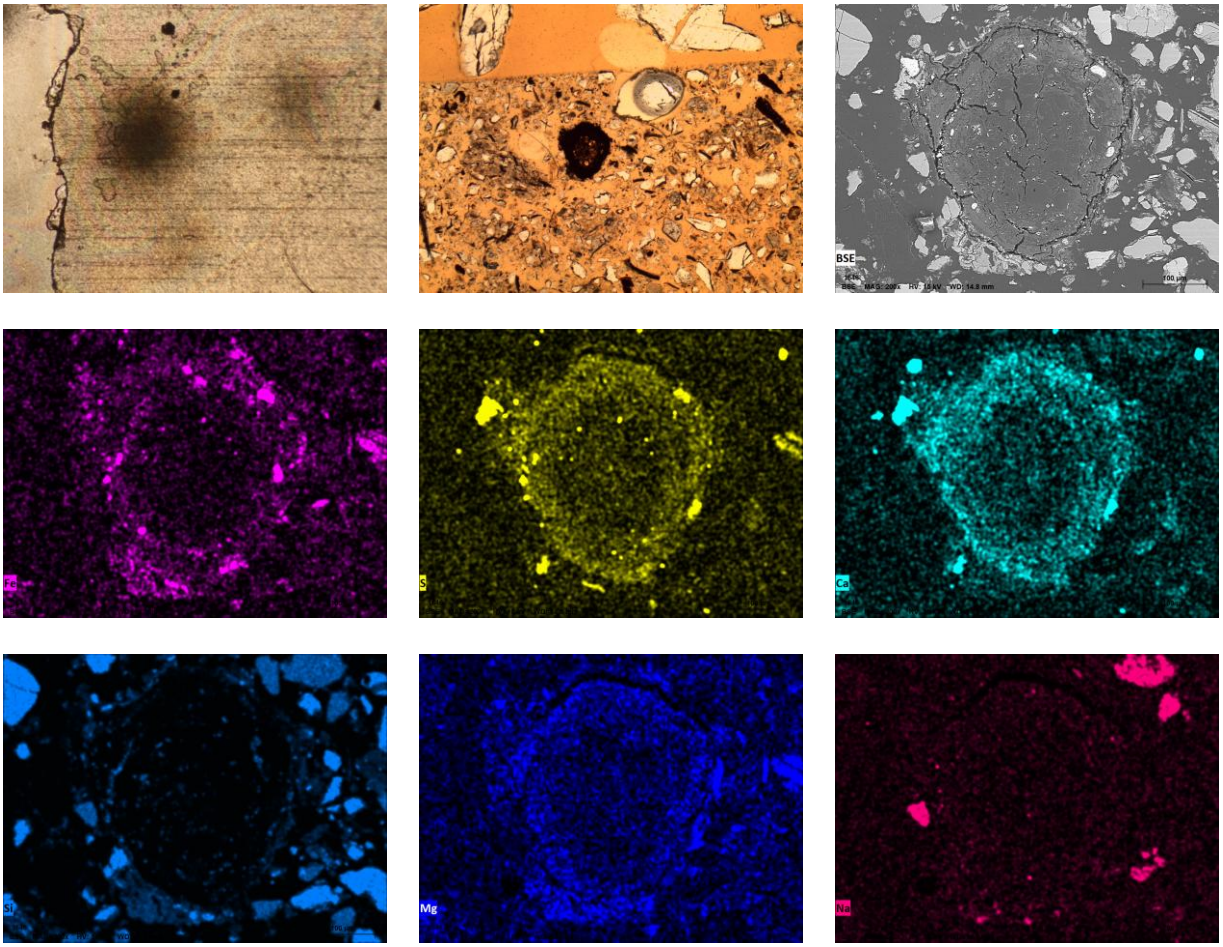

Fig. S28. Row 1: FT, Thin Section, BSE; Row 2 and Row 3: EM

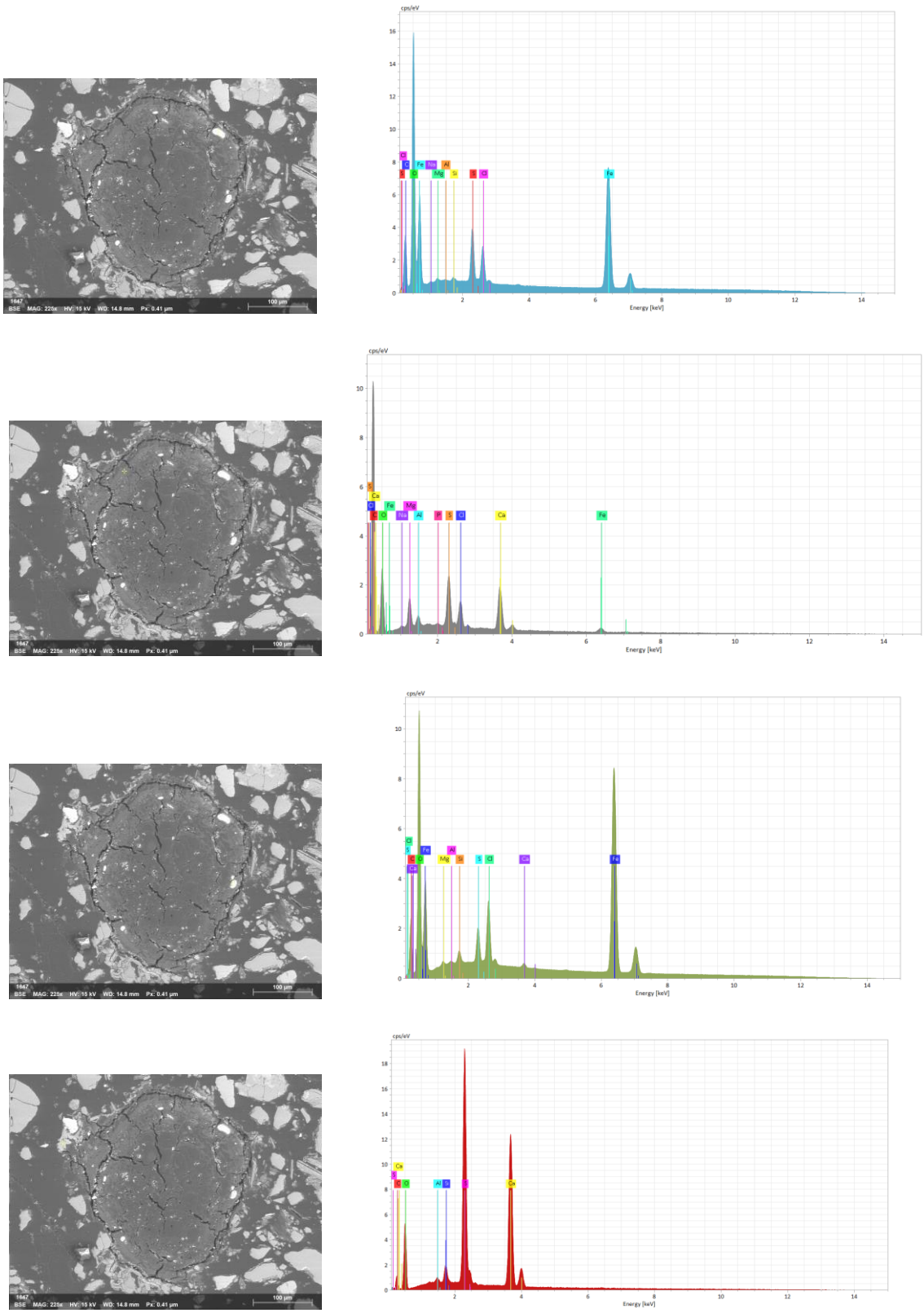

Fig. S29. Column 1: EDS locations; Column 2: Corresponding EDS

Boring 855: 6.5 ft depth (Site 1 - FeS)

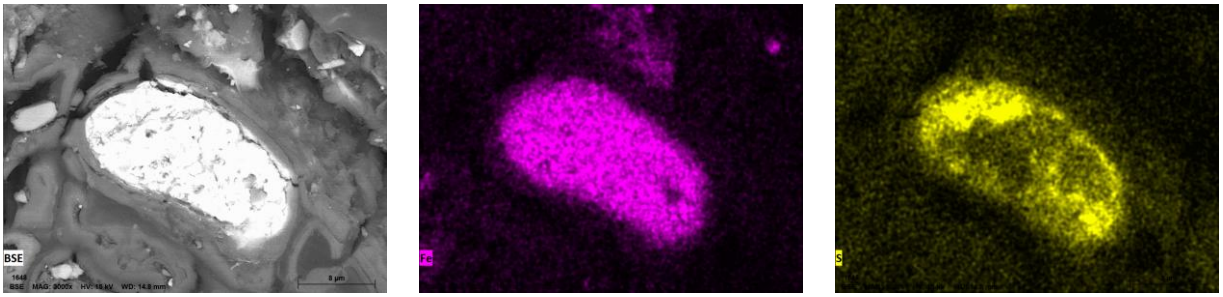

Fig. S30. Row 1: FeS - BSE and EM

Boring 855: 6.5 ft depth (Site 2)

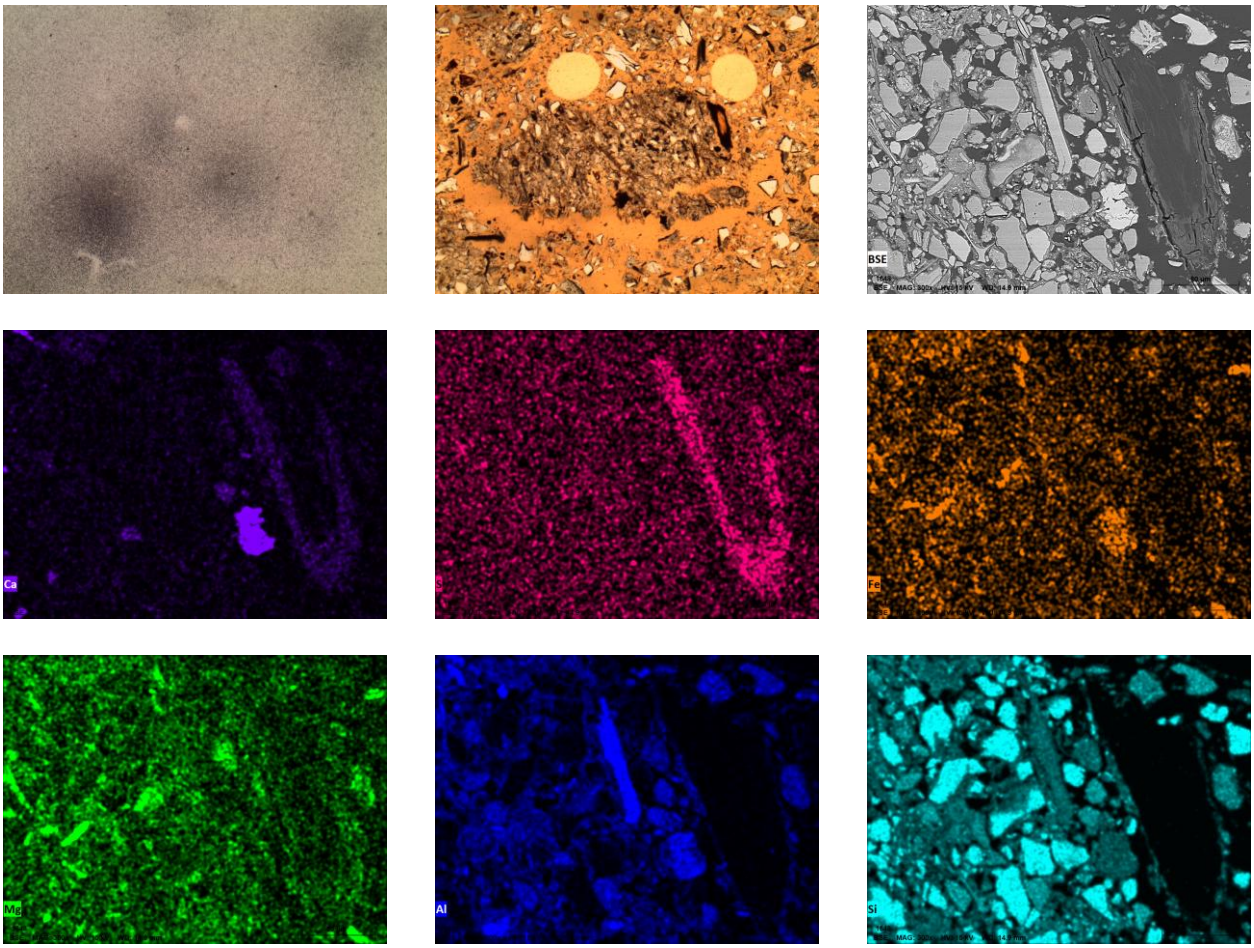

Fig. S31. Row 1: FT, Thin Section, BSE; Row 2 and Row 3: EM

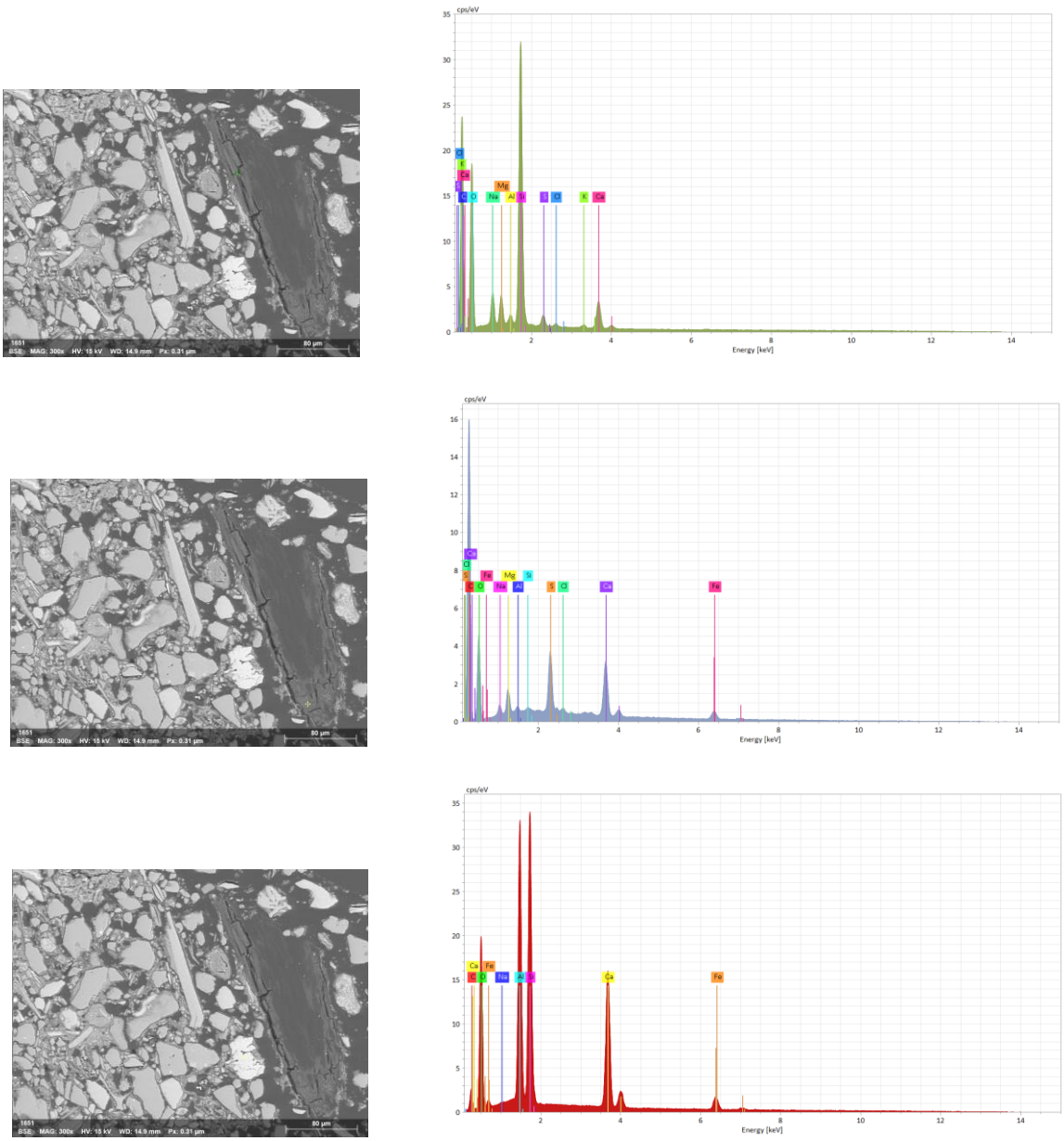

Fig. S32. Column 1: EDS locations; Column 2: Corresponding EDS

Boring 855: 6.5 ft depth (Site 3)

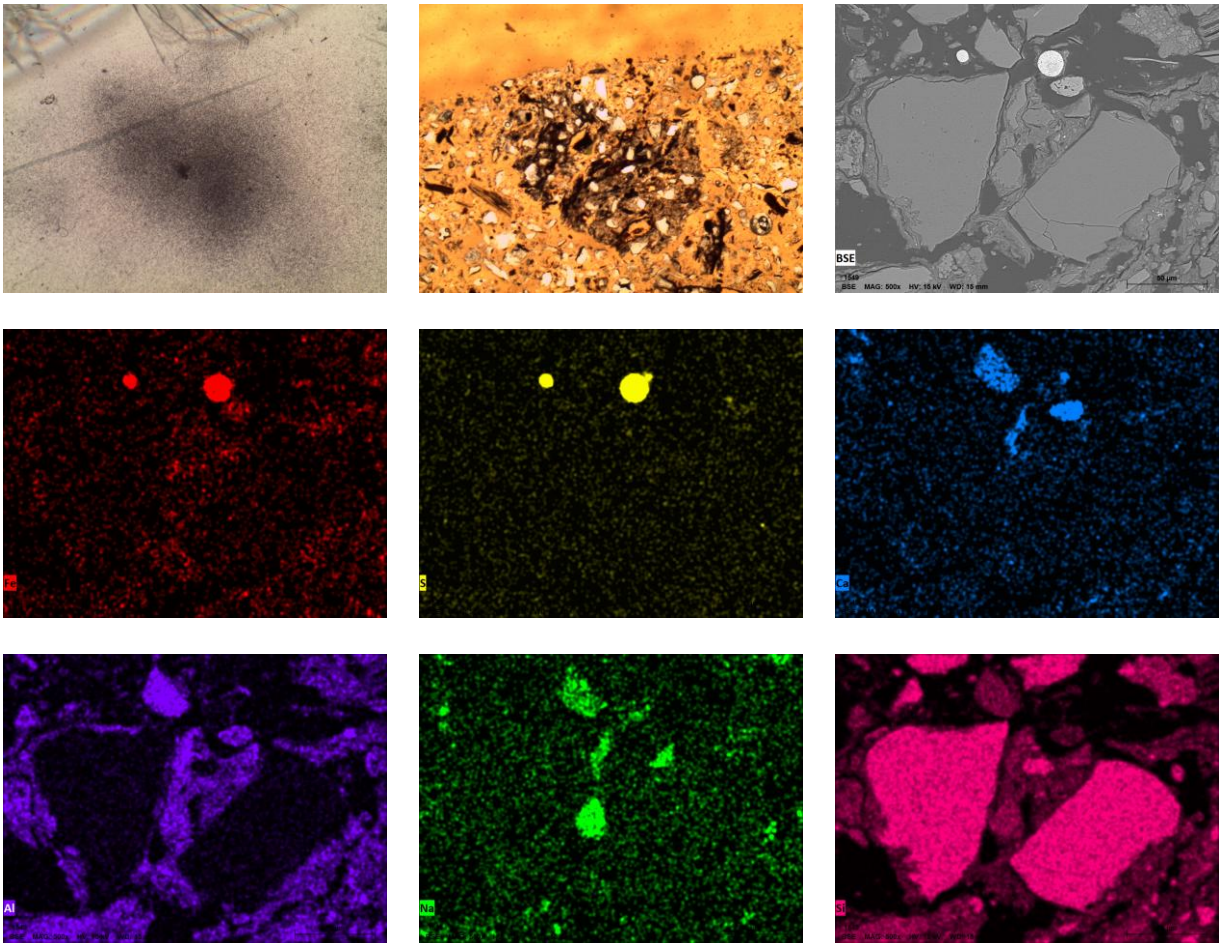

Fig. S33. Row 1: FT, Thin Section, BSE; Row 2 and Row 3: EM

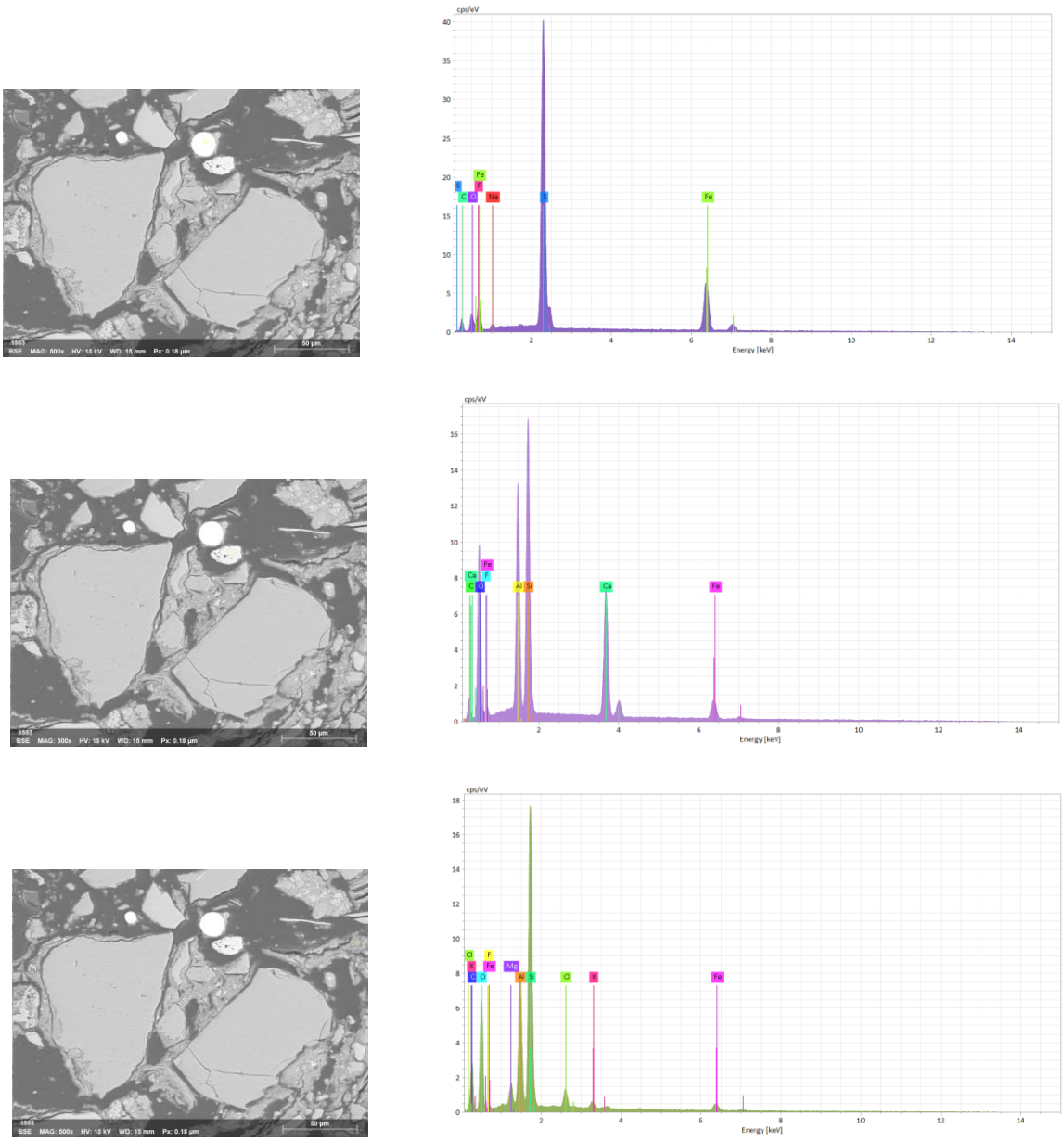

Fig. S34. Column 1: EDS locations; Column 2: Corresponding EDS

Boring 855: 6.5 ft depth (Site 3 - Pyrite)

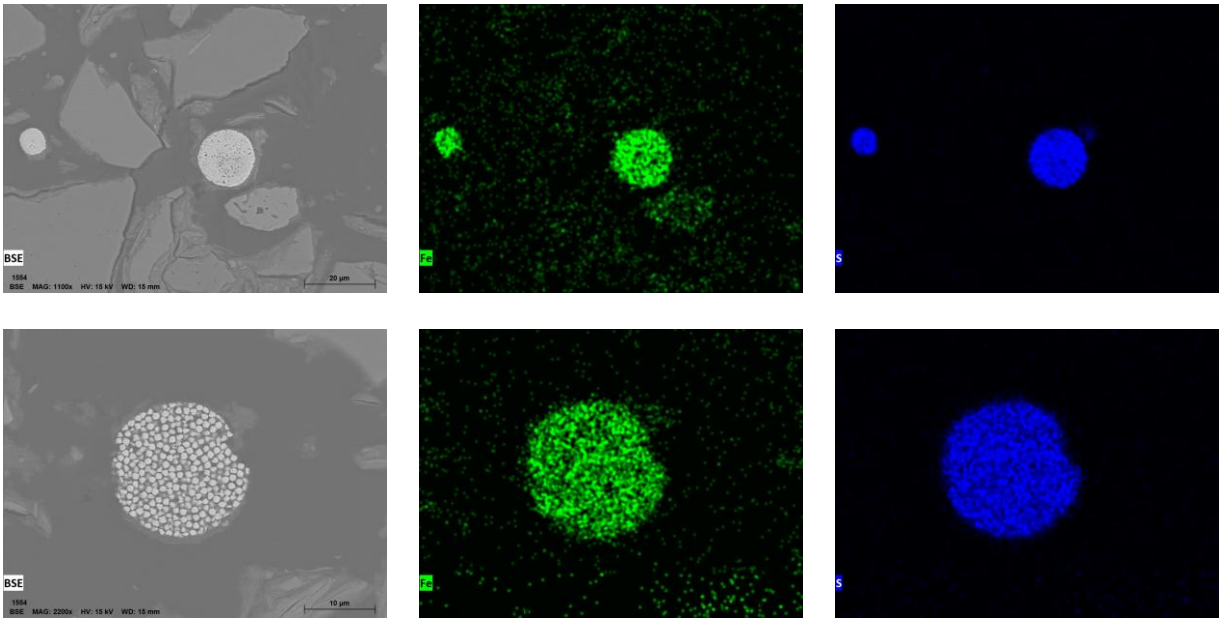

Fig. S35. Row 1 and Row 2: FeS - BSE, EM (Fe and S)

Boring 855: 6.5 ft depth (Site 4)

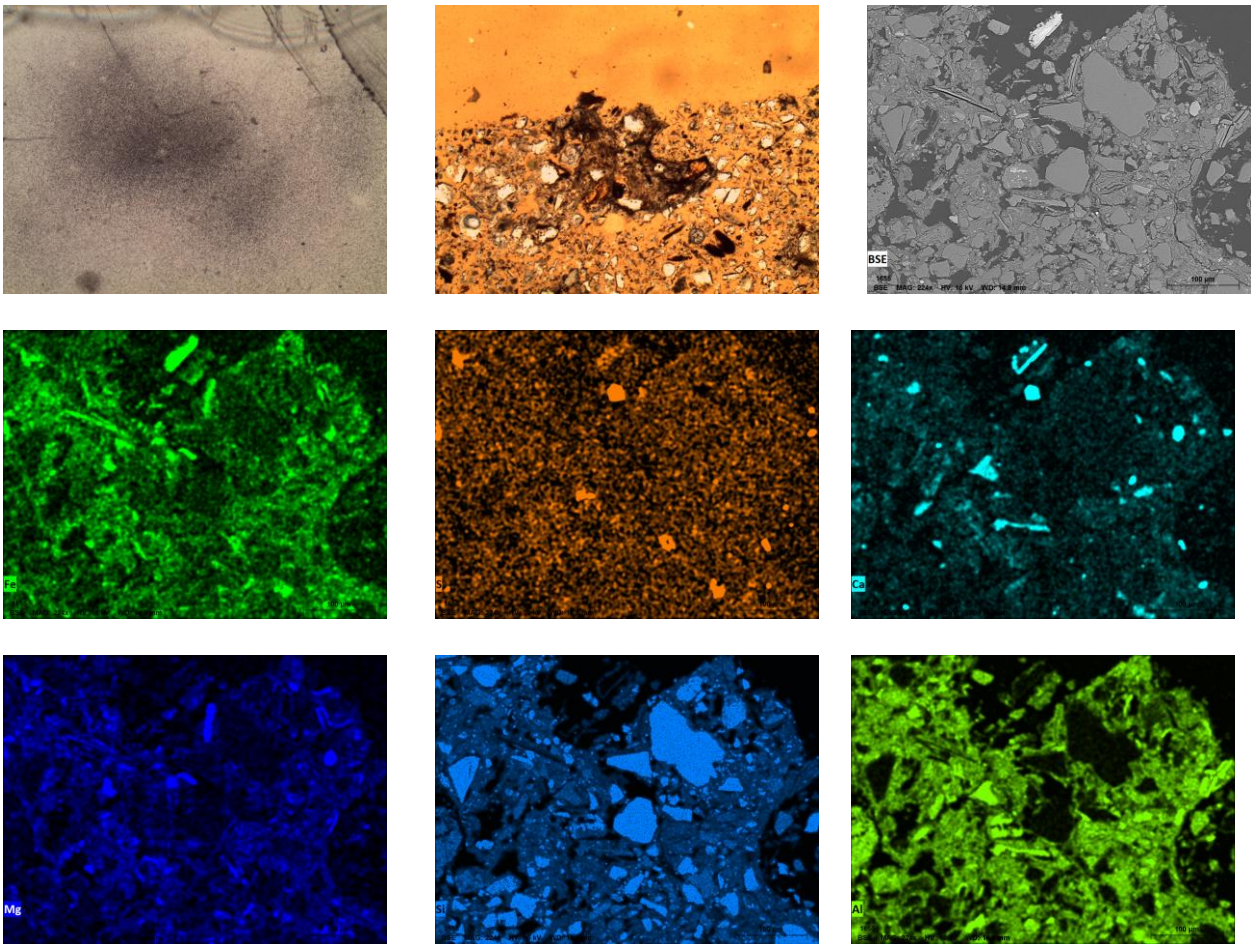

Fig. S36. Row 1: FT, Thin Section, BSE; Row 2 and Row 3: EM

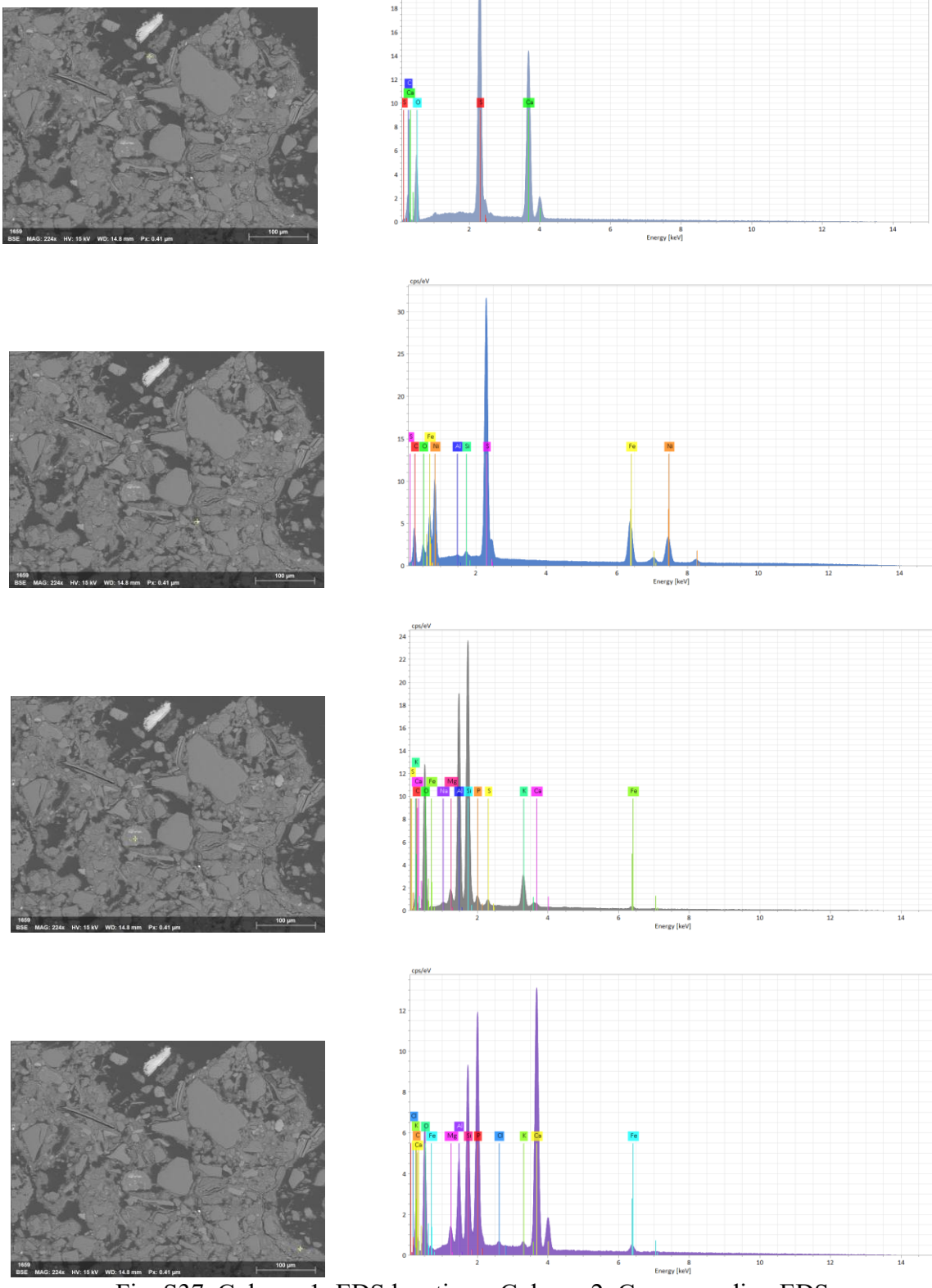

Fig. S37. Column 1: EDS locations; Column 2: Corresponding EDS

Appendix E: Numerical Modeling Input Files

Regional Model - Riverton, WY (MODFLOW 6)

Representative MODFLOW input name files (.nam) for each model are included in Appendix E. These demonstrate the file structure and configuration of the models used in this dissertation.

The complete set of input files and associated files, are archived in a public repository for reproducibility at: Regional Model-Riverton WY

Model1: A steady-state, single-layer unstructured-grid model representing an confined aquifer, with a specified-head boundary condition.

##GWF model name file

```
# File generated by Flopy version 3.8.0 on 10/09/2024 at 07:14:35.
BEGIN OPTIONS
  LIST  mf6_riv_reg.lst
  SAVE_FLOWS
  NEWTON
END OPTIONS

BEGIN PACKAGES
  disu6  mf6_riv_reg.dis
  ic6  mf6_riv_reg.ic6
  oc6  mf6_riv_reg.oc6
  npf6  mf6_riv_reg.npf
  chd6  mf6_riv_reg.chd  chd-1
  riv6  mf6_riv_reg.riv  riv-1
  ghb6  mf6_riv_reg.ghb  ghb-1
  rch6  mf6_riv_reg.rch  rch-1
  evt6  mf6_riv_reg.evt  evt-1
END PACKAGES
```

##mfsim.nam file

```
# File generated by Flopy version 3.8.0 on 10/09/2024 at 07:14:35.
BEGIN options
END options

BEGIN TIMING
  TDIS6  mf6_riv_reg.tdis
END TIMING

BEGIN MODELS
  gwf6  mf6_riv_reg.nam  mf6model
END MODELS
```

```
BEGIN EXCHANGES
END EXCHANGES

BEGIN SOLUTIONGROUP  1
  ims6  mf6_riv_reg.ims  mf6model

END SOLUTIONGROUP  1
```

Model1-wel: A steady-state, single-layer unstructured-grid model representing an confined aquifer, with a specified-head boundary condition and pumping well.

##GWF Model name file

```
# File generated by Flopy version 3.8.0 on 12/05/2024 at 20:49:00.
BEGIN OPTIONS
  LIST  mf6_riv_reg.lst
  SAVE_FLOWS
  NEWTON
END OPTIONS

BEGIN PACKAGES
  OBS6  mf6model.obs  obs_0
  WEL6  mf6model.wel  wel_0
  STO6  mf6model.sto  sto
  ghb6  mf6_riv_reg.ghb  ghb-1
  riv6  mf6_riv_reg.riv  riv-1
  chd6  mf6_riv_reg.chd  chd-1
  npf6  mf6_riv_reg.npf
  rch6  mf6_riv_reg.rch  rch-1
  ic6  mf6_riv_reg.ic6
  evt6  mf6_riv_reg.evt  evt-1
  disu6  mf6_riv_reg.dis
  OC6  mf6model.oc  oc
END PACKAGES
```

##mfsim.nam file

```
# File generated by Flopy version 3.8.0 on 12/05/2024 at 20:49:00.
BEGIN options
END options

BEGIN TIMING
  TDIS6  mf6.tdis
END TIMING
```

```
BEGIN MODELS
  gwf6  mf6_riv_reg.nam  mf6model
END MODELS

BEGIN EXCHANGES
END EXCHANGES

BEGIN SOLUTIONGROUP  1
  ims6  mf6_riv_reg.ims  mf6model

END SOLUTIONGROUP  1
```

Downscaled Model - Riverton, WY (MODFLOW 6)

Representative MODFLOW input name files (.nam) for each model are included in Appendix E. These demonstrate the file structure and configuration of the models used in this dissertation.

The complete set of input files and associated files, are archived in a public repository for reproducibility at: Downscaled Model-Riverton WY

Model1: A transient, single-layer structured-grid model representing an unconfined aquifer, with a specified-head boundary condition and a pumping well.

GWF model name file

```
# File generated by Flopy version 3.8.0 on 02/12/2025 at 20:41:13.
BEGIN options
  SAVE_FLOWS
  NEWTON  UNDER_RELAXATION
END options

BEGIN packages
  DIS6  rvt_ssma-2.1.dis  dis
  NPF6  rvt_ssma-2.1.npf  npf
  CHD6  rvt_ssma-2.1.chd  chd_0
  RCH6  rvt_ssma-2.1.rch  rch_0
  EVT6  rvt_ssma-2.1.evt  evt
  STO6  rvt_ssma-2.1.sto  sto
  WEL6  rvt_ssma-2.1.wel  wel
  OBS6  rvt_ssma-2.1.obs  obs_0
  OC6  rvt_ssma-2.1.oc  oc
  IC6  rvt_ssma-2.1.ic  ic
END packages
```

##mfsim.nam file

```
# File generated by Flopy version 3.8.0 on 02/12/2025 at 20:41:13.
BEGIN options
END options

BEGIN timing
  TDIS6  rvt_ssma-2.1.tdis
END timing

BEGIN models
  gwf6  rvt_ssma-2.1.nam  rvt_ssma-2.1
END models

BEGIN exchanges
END exchanges

BEGIN solutiongroup  1
  ims6  rvt_ssma-2.1.ims  rvt_ssma-2.1
END solutiongroup  1
```

Model1-pest: PEST control file for calibrating Model1.

```
pcf
* control data
             restart          estimation
         3        21         1         0         1
         2         1              single              point         1
   2.000000E+01  -3.000000E+00   3.000000E-01   1.000000E-02        -7
   1.000000E+01   1.000000E+01   1.000000E-03
   1.000000E-01
        10   1.000000E-02         3         3   1.000000E-02         3
         0         0         0
* singular value decomposition
         1
  10000000    1.000000E-06
1
* parameter groups
pargp                  relative             1.0000000000E-02      0.0 switch
2.0000000000E+00      parabolic            1.0000000000E-05      5.0000000000E-01
smaller
* parameter data
```

```
hk1                 log                 factor              1.0000000000E+00
1.0000000000E-02    5.0000000000E+00    pargp               1.0000000000E+00
0.0000000000E+00    1
ss                  log                 factor              1.0000000000E-07
1.0000000000E-08    1.0000000000E-03    pargp               1.0000000000E+00
0.0000000000E+00    1
sy                  log                 factor              1.0000000000E-01
1.0000000000E-05    3.0000000000E-01    pargp               1.0000000000E+00
0.0000000000E+00    1
* observation groups
obgnme
* observation data
w1006_head_01       0.0000000000E+00    1.0000000000E+00    obgnme
w1006_head_02       -1.9095000000E-02   5.0000000000E+00    obgnme
w1006_head_03       -2.4738000000E-02   5.0000000000E+00    obgnme
w1006_head_04       -3.8583000000E-02   5.0000000000E+00    obgnme
w1006_head_05       -4.4422999999E-02   5.0000000000E+00    obgnme
w1006_head_06       -5.4725000000E-02   5.0000000000E+00    obgnme
w1006_head_07       -6.5486000000E-02   5.0000000000E+00    obgnme
w1006_head_08       -7.5591000000E-02   5.0000000000E+00    obgnme
w1006_head_09       -8.4645999999E-02   5.0000000000E+00    obgnme
w1006_head_10       -9.7769000000E-02   5.0000000000E+00    obgnme
w1006_head_11       -1.0741500000E-01   5.0000000000E+00    obgnme
w1006_head_12       -9.3373000000E-02   1.0000000000E+00    obgnme
w1006_head_13       -9.3045000000E-02   1.0000000000E+00    obgnme
w1006_head_14       -9.2323000000E-02   1.0000000000E+00    obgnme
w1006_head_15       -9.1667000000E-02   1.0000000000E+00    obgnme
w1006_head_16       -9.1141999999E-02   1.0000000000E+00    obgnme
w1006_head_17       -9.1273000000E-02   1.0000000000E+00    obgnme
w1006_head_18       -9.1206999999E-02   1.0000000000E+00    obgnme
w1006_head_19       -9.1273000000E-02   1.0000000000E+00    obgnme
w1006_head_20       -9.0486000000E-02   1.0000000000E+00    obgnme
w1006_head_21       -9.0617000000E-02   1.5000000000E+01    obgnme
* model command line
run.bat
* model input/output
rvt_ssma-2.1.npf.tpl rvt_ssma-2.1.npf
rvt_ssma-2.1.sto.tpl rvt_ssma-2.1.sto
w1006-2.1.post.csv.ins w1006-2.1.post.csv
```

Model2: A transient, double-layer structured-grid model representing an unconfined aquifer, with a specified-head boundary condition and a pumping well.

GWF model name file

```
# File generated by Flopy version 3.8.0 on 02/12/2025 at 19:08:11.
BEGIN options
  SAVE_FLOWS
  NEWTON  UNDER_RELAXATION
END options

BEGIN packages
  DIS6  rvt_ssma-4.dis  dis
  IC6  rvt_ssma-4.ic  ic
  NPF6  rvt_ssma-4.npf  npf
  CHD6  rvt_ssma-4.chd  chd_0
  RCH6  rvt_ssma-4.rch  rch_0
  EVT6  rvt_ssma-4.evt  evt
  STO6  rvt_ssma-4.sto  sto
  WEL6  rvt_ssma-4.wel  wel
  OBS6  rvt_ssma-4.obs  obs_0
  OC6  rvt_ssma-4.oc  oc
END packages
```

##mfsim.nam file

```
# File generated by Flopy version 3.8.0 on 02/12/2025 at 19:08:11.
BEGIN options
END options

BEGIN timing
  TDIS6  rvt_ssma-4.tdis
END timing

BEGIN models
  gwf6  rvt_ssma-4.nam  rvt_ssma-4
END models

BEGIN exchanges
END exchanges

BEGIN solutiongroup  1
  ims6  rvt_ssma-4.ims  rvt_ssma-4
END solutiongroup  1
```

Model2-pest: PEST control file for calibrating Model2.

```
pcf
* control data
             restart          estimation
         5        21         1         0         1
         2         1              single              point         1
   2.000000E+01  -3.000000E+00   3.000000E-01   1.000000E-02        -7
   1.000000E+01   1.000000E+01   1.000000E-03
   1.000000E-01
        10   1.000000E-02         3         3   1.000000E-02         3
         0         0         0
* singular value decomposition
         1
  10000000    1.000000E-06
1
* parameter groups
pargp                relative             1.0000000000E-02      0.0 switch
2.0000000000E+00     parabolic            1.0000000000E-05      5.0000000000E-01
smaller
* parameter data
hk1                  log                  factor                1.0000000000E-01
1.0000000000E-02     5.0000000000E+00     pargp                 1.0000000000E+00
0.0000000000E+00     1
hk2                  log                  factor                1.0000000000E+00
1.0000000000E-02     5.0000000000E+00     pargp                 1.0000000000E+00
0.0000000000E+00     1
hk3                  log                  factor                5.0000000000E-02
1.0000000000E-03     5.0000000000E+00     pargp                 1.0000000000E+00
0.0000000000E+00     1
ss                   log                  factor                1.0000000000E-07
1.0000000000E-08     1.0000000000E-03     pargp                 1.0000000000E+00
0.0000000000E+00     1
sy                   log                  factor                1.0000000000E-01
1.0000000000E-05     3.0000000000E-01     pargp                 1.0000000000E+00
0.0000000000E+00     1
* observation groups
obgnme
* observation data
w1006_head_01        0.0000000000E+00     1.0000000000E+00      obgnme
w1006_head_02        -1.9095000000E-02    3.0000000000E+00      obgnme
w1006_head_03        -2.4738000000E-02    3.0000000000E+00      obgnme
w1006_head_04        -3.8583000000E-02    3.0000000000E+00      obgnme
w1006_head_05        -4.4422999999E-02    3.0000000000E+00      obgnme
```

```
w1006_head_06          -5.4725000000E-02      3.0000000000E+00       obgnme
w1006_head_07          -6.5486000000E-02      3.0000000000E+00       obgnme
w1006_head_08          -7.5591000000E-02      3.0000000000E+00       obgnme
w1006_head_09          -8.4645999999E-02      3.0000000000E+00       obgnme
w1006_head_10          -9.7769000000E-02      3.0000000000E+00       obgnme
w1006_head_11          -1.0741500000E-01      3.0000000000E+00       obgnme
w1006_head_12          -9.3373000000E-02      1.0000000000E+00       obgnme
w1006_head_13          -9.3045000000E-02      1.0000000000E+00       obgnme
w1006_head_14          -9.2323000000E-02      1.0000000000E+00       obgnme
w1006_head_15          -9.1667000000E-02      1.0000000000E+00       obgnme
w1006_head_16          -9.1141999999E-02      1.0000000000E+00       obgnme
w1006_head_17          -9.1273000000E-02      1.0000000000E+00       obgnme
w1006_head_18          -9.1206999999E-02      1.0000000000E+00       obgnme
w1006_head_19          -9.1273000000E-02      1.0000000000E+00       obgnme
w1006_head_20          -9.0486000000E-02      1.0000000000E+00       obgnme
w1006_head_21          -9.0617000000E-02      1.0000000000E+01       obgnme
* model command line
run.bat
* model input/output
rvt_ssma-4.npf.tpl rvt_ssma-4.npf
rvt_ssma-4.sto.tpl rvt_ssma-4.sto
w1006-4.post.csv.ins w1006-4.post.csv
```

Model3: A transient, double-layer structured-grid model representing an unconfined aquifer, with a general-head boundary condition and a pumping well

##GWF model name file

```
# File generated by Flopy version 3.8.0 on 06/15/2025 at 09:52:16.
BEGIN options
  SAVE_FLOWS
  NEWTON  UNDER_RELAXATION
END options

BEGIN packages
  DIS6  rvt_ssma-4.2.dis  dis
  IC6  rvt_ssma-4.2.ic  ic
  NPF6  rvt_ssma-4.2.npf  npf
  GHB6  rvt_ssma-4.2.ghb  ghb_0
  RCH6  rvt_ssma-4.2.rch  rch_0
  EVT6  rvt_ssma-4.2.evt  evt
  STO6  rvt_ssma-4.2.sto  sto
  WEL6  rvt_ssma-4.2.wel  wel
```

```
  OBS6  rvt_ssma-4.2.obs  obs_0
  OC6  rvt_ssma-4.2.oc  oc
END packages
```

##mfsim.nam file

```
# File generated by Flopy version 3.8.0 on 06/15/2025 at 09:52:16.
BEGIN options
END options

BEGIN timing
  TDIS6  rvt_ssma-4.2.tdis
END timing

BEGIN models
  gwf6  rvt_ssma-4.2.nam  rvt_ssma-4.2
END models

BEGIN exchanges
END exchanges

BEGIN solutiongroup  1
  ims6  rvt_ssma-4.2.ims  rvt_ssma-4.2
END solutiongroup  1
```

Model3-pest: PEST control file for calibrating Model3.

```
pcf
* control data
             restart          estimation
         5        21         1         0         1
         2         1              single              point         1
   2.000000E+01  -3.000000E+00   3.000000E-01   1.000000E-02        -7
   1.000000E+01   1.000000E+01   1.000000E-03
   1.000000E-01
        10   1.000000E-02         3         3   1.000000E-02         3
         0         0         0
* singular value decomposition
         1
  10000000    1.000000E-06
1
* parameter groups
pargp                  relative              1.0000000000E-02      0.0 switch
2.0000000000E+00      parabolic             1.0000000000E-05      5.0000000000E-01
smaller
```

```
* parameter data
hk1                     log                     factor                  1.0000000000E-01
1.0000000000E-02        5.0000000000E+00        pargp                   1.0000000000E+00
0.0000000000E+00        1
hk2                     log                     factor                  1.0000000000E+00
1.0000000000E-02        5.0000000000E+00        pargp                   1.0000000000E+00
0.0000000000E+00        1
hk3                     log                     factor                  5.0000000000E-02
1.0000000000E-03        5.0000000000E+00        pargp                   1.0000000000E+00
0.0000000000E+00        1
ss                      log                     factor                  1.0000000000E-07
1.0000000000E-08        1.0000000000E-03        pargp                   1.0000000000E+00
0.0000000000E+00        1
sy                      log                     factor                  1.0000000000E-01
1.0000000000E-05        3.0000000000E-01        pargp                   1.0000000000E+00
0.0000000000E+00        1
* observation groups
obgnme
* observation data
w1006_head_01           0.0000000000E+00        1.0000000000E+00        obgnme
w1006_head_02           -1.9095000000E-02       3.0000000000E+00        obgnme
w1006_head_03           -2.4738000000E-02       3.0000000000E+00        obgnme
w1006_head_04           -3.8583000000E-02       3.0000000000E+00        obgnme
w1006_head_05           -4.4422999999E-02       3.0000000000E+00        obgnme
w1006_head_06           -5.4725000000E-02       3.0000000000E+00        obgnme
w1006_head_07           -6.5486000000E-02       3.0000000000E+00        obgnme
w1006_head_08           -7.5591000000E-02       3.0000000000E+00        obgnme
w1006_head_09           -8.4645999999E-02       3.0000000000E+00        obgnme
w1006_head_10           -9.7769000000E-02       3.0000000000E+00        obgnme
w1006_head_11           -1.0741500000E-01       3.0000000000E+00        obgnme
w1006_head_12           -9.3373000000E-02       1.0000000000E+00        obgnme
w1006_head_13           -9.3045000000E-02       1.0000000000E+00        obgnme
w1006_head_14           -9.2323000000E-02       1.0000000000E+00        obgnme
w1006_head_15           -9.1667000000E-02       1.0000000000E+00        obgnme
w1006_head_16           -9.1141999999E-02       1.0000000000E+00        obgnme
w1006_head_17           -9.1273000000E-02       1.0000000000E+00        obgnme
w1006_head_18           -9.1206999999E-02       1.0000000000E+00        obgnme
w1006_head_19           -9.1273000000E-02       1.0000000000E+00        obgnme
w1006_head_20           -9.0486000000E-02       1.0000000000E+00        obgnme
w1006_head_21           -9.0617000000E-02       5.0000000000E+00        obgnme
* model command line
run.bat
* model input/output
rvt_ssma-4.2.npf.tpl rvt_ssma-4.2.npf
```

```
rvt_ssma-4.2.sto.tpl rvt_ssma-4.2.sto
w1006-4.2.post.csv.ins w1006-4.2.post.csv
```

Model4: A transient, two-layer structured-grid model representing an unconfined aquifer, incorporating a general-head boundary condition, a pumping well, and an unsaturated zone package.

GWF model name file

```
# File generated by Flopy version 3.8.0 on 06/17/2025 at 11:25:57.
BEGIN options
  SAVE_FLOWS
  NEWTON  UNDER_RELAXATION
END options

BEGIN packages
  DIS6  Riv_ssma_gwf-5.4.dis  dis
  IC6  Riv_ssma_gwf-5.4.ic  ic
  NPF6  Riv_ssma_gwf-5.4.npf  npf
  GHB6  Riv_ssma_gwf-5.4.ghb  ghb-1
  STO6  Riv_ssma_gwf-5.4.sto  sto
  OBS6  Riv_ssma_gwf-5.4.obs  obs_0
  UZF6  Riv_ssma_gwf-5.4.uzf  uzf-1
  OC6  Riv_ssma_gwf-5.4.oc  oc
END packages
```

GWT model name file

```
# File generated by Flopy version 3.8.0 on 06/17/2025 at 11:26:52.
BEGIN options
  SAVE_FLOWS
END options

BEGIN packages
  DIS6  Riv_ssma-gwt-5.4.dis  dis
  IC6  Riv_ssma-gwt-5.4.ic  ic
  ADV6  Riv_ssma-gwt-5.4.adv  adv
  DSP6  Riv_ssma-gwt-5.4.dsp  dsp-1
  MST6  Riv_ssma-gwt-5.4.mst  mst-1
  SSM6  Riv_ssma-gwt-5.4.ssm  ssm
  UZT6  Riv_ssma-gwt-5.4.uzt  uzf-1
  OC6  Riv_ssma-gwt-5.4.oc  oc
END packages
```

mfsim.nam file

```
# File generated by Flopy version 3.8.0 on 06/17/2025 at 11:25:57.
BEGIN options
END options

BEGIN timing
  TDIS6  Riv_ssma_gwf-5.4.tdis
END timing

BEGIN models
  gwf6  Riv_ssma_gwf-5.4.nam  Riv_ssma_gwf-5.4
  gwt6  Riv_ssma-gwt-5.4.nam  Riv_ssma-gwt-5.4
END models
BEGIN exchanges
  GWF6-GWT6  Riv_ssma-gwt-5.4.gwfgwt  Riv_ssma_gwf-5.4  Riv_ssma-gwt-5.4
END exchanges

BEGIN solutiongroup  1
  ims6  Riv_ssma_gwf-5.4.ims  Riv_ssma_gwf-5.4
  ims6  Riv_ssma-gwt-5.4.ims  Riv_ssma-gwt-5.4
END solutiongroup  1
```

References:

Langevin, C.D., Hughes, J.D., Banta, E.R., Niswonger, R.G., Panday, Sorab, and Provost, A.M., 2017, Documentation for the MODFLOW 6 Groundwater Flow Model: U.S. Geological Survey Techniques and Methods, book 6, chap. A55, 197 p., https://doi.org/10.3133/tm6A55.

Langevin, C.D., Provost, A.M., Panday, Sorab, and Hughes, J.D., 2022, Documentation for the MODFLOW 6 Groundwater Transport Model: U.S. Geological Survey Techniques and Methods, book 6, chap. A61, 56 p., https://doi.org/10.3133/tm6A61.

Doherty, John. 2015. *PEST: Model-Independent Parameter Estimation. User Manual. Part I: PEST, SENSAN and Global Optimisers.* 5th ed. Brisbane: Watermark Numerical Computing.

Appendix F: Analytical Pumping Test Model Calibration with PEST

Pumping test at RIverton WY calibration with Theis solution using PEST. Detailed files are available at: Analytical model-Pumptest

Pumptest model .py

```
import numpy as np
import pandas as pd
import matplotlib.pyplot as plt
from scipy.special import exp1  # Exponential integral W(u)

with open("w1005-in.dat", "r") as f:
    lines = f.readlines()
T = float(lines[0].split()[1])  # hk
S = float(lines[1].split()[1])  # storativity
# Fixed parameters
Q = -50.85
r = 3.35
t1 = 3.88 / 24

# Time array
time_days = np.logspace(np.log10(0.000931), np.log10(0.18), 2731)
def theis_superposition(Q, T, S, r, t_array, t1):
    s_total = []
    epsilon = 1e-10  # small number to avoid division by zero or tiny times

    for t in t_array:
        # Early pumping period
        u1 = (r**2 * S) / (4 * T * max(t, epsilon))
        s1 = exp1(u1)

        if t <= t1:  # during pumping
            s = (Q / (4 * np.pi * T)) * s1
        else:  # after pumping stops (rebound)
            u2 = (r**2 * S) / (4 * T * max(t - t1, epsilon))
            s2 = exp1(u2)
            s = (Q / (4 * np.pi * T)) * (s1 - s2)

        s_total.append(s)

    return np.array(s_total)

drawdown = theis_superposition(Q, T, S, r, time_days, t1)
df_model = pd.DataFrame({"Drawdown": drawdown})
```

```
df_model.to_csv("w1005-out.dat", index=False, header=False)
```

Input in.dat file

```
T 200.000
S .200000
```

Output out.dat file

out.dat #linked in repository due to file length

in.dat.tpl file

```
ptf ~
T ~  T  ~
S ~  S  ~
```

in.dat.pmt

```
t
s
```

in.dat.par file

```
single point
 t     200        1.0  0.0
 s     0.2        1.0  0.0
```

Check input files with i64tempchek.exe

```
tempchek in.dat.tpl in.dat in.dat.par
```

out.dat.ins file

out.dat.ins #linked in repository due to file length

Check output files wth inschek.exe

```
inschek out.dat.ins
inschek out.dat.ins out.dat
```

Inschek will produce a file named out.dat.obf

out.dat.obf #linked in repository due to file length

Measured output with .obf extension

measured_out.dat.obf #linked in repository due to file length

PEST control file with pestgen.exe

```
pestgen modelname in.dat.par measured_out.dat.obf
```

PEST control file

model.pst #linked in repository due to file length

Check model

```
pestchek   modelname
```

 # Run model with PEST

```
I64pest.exe    model.pst
```

Reference:

Doherty, John. 2015. *PEST: Model-Independent Parameter Estimation. User Manual. Part I: PEST, SENSAN and Global Optimisers.* 5th ed. Brisbane: Watermark Numerical Computing.

Appendix G: Post-Flooding Experimental Solid Phase Data

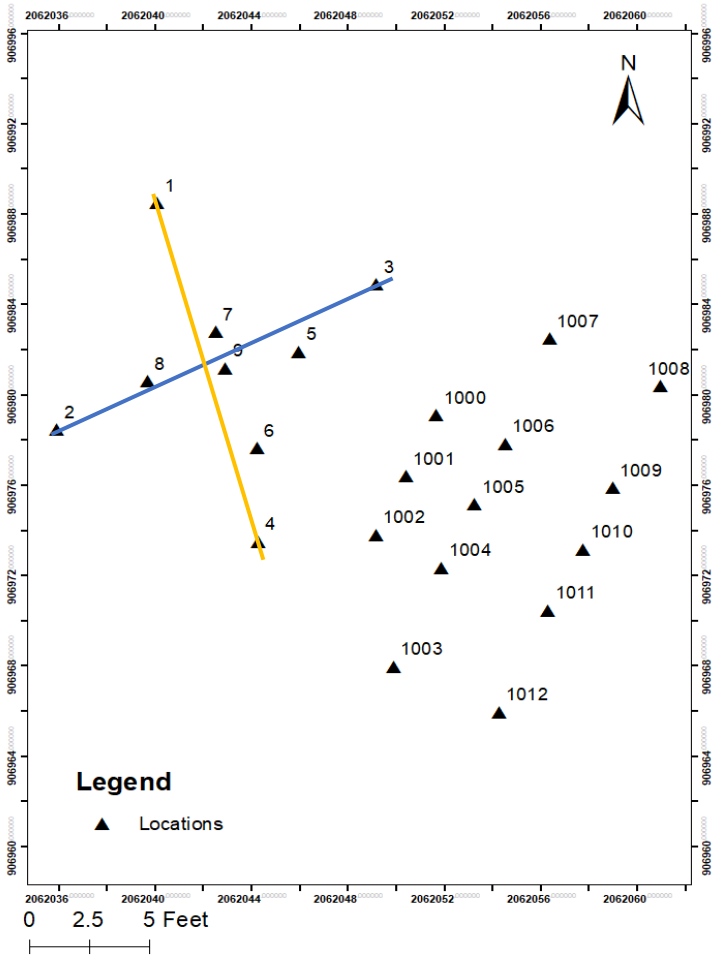

Table S1. DI Extraction Data from Infiltration Basin Area Solid Phase along blue line

Core	Blue Line	Y	Uranium (mg/kg)	Iodide (mg/kg)	Chloride (mg/kg)
2	15	3	0.0063	0.0	220.65
2	15	9	0.0263	0.0	559.89
2	15	16.5	0.0919	1.0	1081.55
2	15	24.5	0.0366	0	1531.74
2	15	32	0.0325	0	1548.35
2	15	41	0.0332	1.0	1237.71
2	15	45	0.0392	0	1170.31
2	15	52	0.0560	0	1235.09
2	15	61	0.1700	3.2	-
2	15	68.5	0.1700	5.9	-
3	181.2	3.5	0.0089	0	715.42
3	181.2	9.5	0.1539	0	635.74
3	181.2	15.5	0.3134	-	329.86
3	181.2	22	0.5931	0	118.25
3	181.2	28	0.7961	0	206.49
3	181.2	34.5	0.1595	0	475.21
3	181.2	41	0.0699	-	711.11
3	181.2	48	0.2851	0	682.17
3	181.2	54.5	0.3550	0	678.62
3	181.2	60	0.0628	0	687.20
3	181.2	65.5	0.0620	0	91.24
5	138	3	0.0597	7.2	39.38
5	138	9.5	0.1472	5.1	21.51
5	138	16	0.3484	5.1	15.57
5	138	22.5	0.6898	6.1	39.87
5	138	29.5	0.7656	4.9	24.62
5	138	36	0.2837	2.6	16.05
5	138	42.5	0.1482	2.7	13.20
5	138	48.5	0.0864	2.1	14.55
5	138	54	0.0347	1.1	7.21
6	106.8	3.5	0.0641	5.3	30.85
6	106.8	10	0.0409	5.7	15.32
6	106.8	16.5	0.0847	4.7	-
6	106.8	24	0.1861	3.1	7.37
6	106.8	31.5	0.2664	3.6	9.93
6	106.8	38	0.2806	11.8	-
6	106.8	45.5	0.2319	11.2	16.3
6	106.8	54.5	0.1700	10.6	-
6	106.8	62.5	0.1000	19.0	-
7	97.56	3	0.0608	1.8	36.79

7	97.56	9	0.0986	3.3	33.03
7	97.56	15	0.4617	5.2	-
7	97.56	21	0.7860	14.0	36.34
7	97.56	27.5	0.3570	6.7	11.64
7	97.56	34	0.2447	13.9	13.61
7	97.56	40	0.1791	8.1	-
7	97.56	46.5	0.2793	0.0	501.64
7	97.56	53	0.1129	0.0	118.86
7	97.56	58	0.0888	0.0	66.45
8	61.2	3	0.1376	3.7	31.40
8	61.2	9	0.1492	3.7	10.74
8	61.2	15	0.0767	5.0	11.01
8	61.2	21.5	0.1416	3.8	7.70
8	61.2	28.5	0.1598	2.2	8.82
8	61.2	35.5	0.3092	2.5	9.20
8	61.2	43	0.3748	3.4	-
8	61.2	51	0.2453	3.1	11.30
8	61.2	58	0.1500	16.5	-
8	61.2	62.5	0.1500	13.4	-
9	100.56	3.5	0.0000	1.6	-
9	100.56	10	0.1042	3.4	18.03
9	100.56	17	0.2300	5.6	-
9	100.56	24.5	0.5451	2.9	27.82
9	100.56	31	0.2600	1.7	-
9	100.56	37	0.2842	6.2	-
9	100.56	43	0.1800	7.2	0
9	100.56	49	0.1600	5.5	-
9	100.56	54.5	0.0600	2.7	-

Table S2. DI Extraction Data from Infiltration Basin Area Solid Phase along yellow line

Core	Yellow Line	Y	Uranium (mg/kg)	Iodide (mg/kg)	Chloride (mg/kg)
1	228.9	3	0.00606	0.00	192.84
1	228.9	9	0.01848	0.00	333.94
1	228.9	16	0.07696	4.01	52.87
1	228.9	23	0.30654	3.22	32.93
1	228.9	28	0.44581	7.39	62.43
1	228.9	33	0.44365	5.65	18.57
1	228.9	39	0.20952	2.27	47.54
1	228.9	45.5	0.15742	3.94	60.54
1	228.9	52	0.15480	0.00	96.30
1	228.9	57.5	0.07709	0.00	64.86
1	228.9	62.5	0.04969	0.00	63.88
1	228.9	65.5	0.08353	0.00	57.71
4	37.5	3	0.00854	0	939.54
4	37.5	9.5	0.01344	0	951.03
4	37.5	16.5	0.03477	0.7	589.88
4	37.5	24	0.12992	2.8	290.21
4	37.5	31.5	0.10809	0.0	858.53
4	37.5	38	0.06162	1.0	961.32
4	37.5	44.5	0.06891	0.0	641.66
4	37.5	52	0.04594	0.0	642.63
4	37.5	59.5	0.15000	0.4	-
4	37.5	67.5	0.17000	2.0	-
6	86.4	3.5	0.06415	5.3	-
6	86.4	10	0.04086	5.7	-
6	86.4	16.5	0.08467	4.7	9.4
6	86.4	24	0.18611	3.1	-
6	86.4	31.5	0.26638	3.6	-
6	86.4	38	0.28059	11.8	8.4
6	86.4	45.5	0.23194	11.2	-
6	86.4	54.5	0.17000	10.6	-
6	86.4	62.5	0.10000	19.0	-
7	153.9	3	0.06085	1.8	-
7	153.9	9	0.09855	3.3	-
7	153.9	15	0.46169	5.2	15.033
7	153.9	21	0.78596	14.0	-
7	153.9	27.5	0.35696	6.7	-
7	153.9	34	0.24470	13.9	-
7	153.9	40	0.17913	8.1	72.712
7	153.9	46.5	0.27933	0.0	-

7	153.9	53	0.11286	0.0	-
7	153.9	58	0.08879	0.0	-
9	131.4	3.5	0.00000	1.6	-
9	131.4	10	0.10416	3.4	-
9	131.4	17	0.23000	5.6	11.9
9	131.4	24.5	0.54506	2.9	-
9	131.4	31	0.26000	1.7	-
9	131.4	37	0.28422	6.2	8.86
9	131.4	43	0.18000	7.2	-
9	131.4	49	0.16000	5.5	-
9	131.4	54.5	0.06000	2.7	-

Reference:

Jena Choi, Rakiba Sultana, Charles Paradis, Publication: UWM Undergraduate Research Symposium. 2023. Funded by Support for Undergraduate Research Fellows (SURF) grant